

**Primary Vertex Finding,
b-Tagging
and
Analysis of the Channel
 $t\bar{t}H^0, H^0 \rightarrow b\bar{b}$
in the ATLAS Experiment**

Dissertation

zur Erlangung des akademischen Grades
Doktor der Naturwissenschaften

an der
Naturwissenschaftlichen Fakultät
der
Leopold-Franzens-Universität Innsbruck

eingereicht von
Mag. rer. nat. Andreas Wildauer
im September 2006

Abstract - Zusammenfassung

The discovery potential of the $t\bar{t}H$, $H \rightarrow b\bar{b}$ channel for a light Standard Model Higgs boson in the ATLAS experiment has been re-evaluated for an integrated luminosity of 30 fb^{-1} . The study has been performed on fully simulated and reconstructed Monte Carlo data sets. The significance S/\sqrt{B} has been found to be 2.45 for full simulation and 1.96 for fast simulation. The better performance of the full simulation is mostly due to the more efficient b-tagging algorithms which achieve a light jet rejection of 225 compared to the default setting of 100 in fast simulation. Influences of the trigger event selection and the high luminosity ($L = 10^{34} \text{ cm}^{-2} \text{ s}^{-1}$), at which the LHC will be operated, have been estimated to degrade the significance by up to 20%.

As a preparation, (primary) vertex fitting/finding and b-tagging algorithms, which are important for the analysis, have been implemented into the ATLAS Athena software framework. New C++ Event Data Models have been designed for both and they are now used as default in the ATLAS offline reconstruction. The performance of the vertex fitters, the primary vertex finder and the b-tagging algorithms has been studied on various input samples including pile up and a displaced primary vertex. Both algorithms have been applied to the analysis of the $t\bar{t}H$ channel.

Das Entdeckungspotential des Kanals $t\bar{t}H$, $H \rightarrow b\bar{b}$ für ein leichtes Standard Model Higgs Boson im ATLAS Detektor wurde untersucht für eine integrierte Luminosität von 30 fb^{-1} . Die Studie basiert auf voll simulierten und voll rekonstruierten Monte Carlo Daten. Eine Signifikanz S/\sqrt{B} des $t\bar{t}H$ Kanals auf voller Simulation von 2.45 und auf schneller Simulation von 1.96 wurde erzielt. Die besseren Ergebnisse auf voller Simulation werden auf den Gebrauch leistungsfähigerer b-tagging Algorithmen zurückgeführt. Sie erreichen eine Unterdrückungsrate von leichten Jets von 225 im Vergleich zu den Standardeinstellungen von 100 in der schnellen Simulation. Einflüsse der Trigger Ereignis Selektion und der hohen Luminosität von $L = 10^{34} \text{ cm}^{-2} \text{ s}^{-1}$, bei welcher der LHC betrieben werden soll, wurden abgeschätzt und verschlechtern die Signifikanz um bis zu 20%.

Als Vorbereitung wurden Algorithmen und deren Datenmodelle, welche wichtig für die Analyse des Kanals sind, in das ATLAS Software Framework Athena implementiert und ihre Leistungsfähigkeit studiert. Dazu gehören Algorithmen zur Auffindung des Primärvertex und zum Markieren von b-Jets (b-tagging). Die Algorithmen wurden für die Analyse des $t\bar{t}H$ Kanals eingesetzt. Die entwickelten Datenmodelle werden nun standarmässig in ATLAS verwendet.

Acknowledgment - Danksagung

I would like to thank Prof. Dr. Dietmar Kuhn for his broad support and advice throughout this thesis.

Many thanks to my supervisor at CERN, Dr. Markus Elsing, for his constant support and for giving me the opportunity to work in the ATLAS Computing Group.

Thanks to Dr. Per Fredrik Åkesson with whom I worked closely together on vertexing and b-tagging during his 2 years as a fellow at CERN.

Special thanks to Dr. Wolfgang Liebig for acting as the “1st level trigger” in correcting my thesis.

Special thanks to Prof. Dr. hab. Elzbieta Richter-Was for her many advices on the analysis of the $t\bar{t}H$ channel.

Special thanks to Dr. Martin Siebel for reading through the theory chapter and for many valuable discussions and suggestions.

Thanks to all the people in the ATLAS Computing Group for their help on all sorts of topics from grid computing to physics analysis.

Thanks also to all people from the High Energy Physics group of Innsbruck University.

And last but not least thanks to many many people in the ATLAS collaboration:
<enter your name here> :-)

Private thanks to Mirijam and my whole family!

Contents

1	Introduction and Motivation	1
2	The Large Hadron Collider (LHC)	3
2.1	Luminosity	4
2.2	Injector Chain	5
2.3	Expected Integrated Luminosity	6
2.4	Expected Total Event Rate for the $t\bar{t}H^0$ channel	6
3	The ATLAS Detector	9
3.1	ATLAS Coordinate System and System of Units	10
3.2	The Magnetic Fields	11
3.3	Inner Detector	11
3.3.1	Pixel Detector	13
3.3.2	Semi Conductor Tracker (SCT)	13
3.3.3	Transition Radiation Tracker (TRT)	13
3.4	Calorimeters	14
3.4.1	Electromagnetic Calorimeter	14
3.4.2	Hadron Calorimeter	15
3.5	Muon Detector	15
4	Theoretical Overview	17
4.1	The Standard Model	17
4.1.1	Electro-weak Theory	19
4.1.2	The Higgs Mechanism and the Higgs Boson	21
4.1.3	Strong Interactions - QCD	27
4.2	Physics at the LHC	32
4.2.1	QCD Processes	32
4.2.2	Electro-weak Gauge Bosons	33
4.2.3	B-Physics	33
4.2.4	Heavy Quarks and Leptons	33
4.2.5	Higgs Boson	34
4.2.6	Super Symmetry and Beyond	39
4.3	Characteristics of B Hadrons and b jet Topology	40

5	Trigger Event Selection	43
5.1	Trigger Overview	44
5.2	Trigger Levels and Data Flow	46
5.3	Selection Signatures and Trigger Menu	46
5.4	The e/γ Trigger	47
5.4.1	The e/γ Framework	49
5.4.2	Results for the High Level Trigger TDR	49
5.5	The μ Trigger	51
6	Track Reconstruction	53
6.1	Perigee Parameters	53
6.2	Track Selection	54
6.3	Impact Parameter Resolutions	56
7	Vertex Finding and Fitting	59
7.1	Vertex Finding	60
7.2	Vertex Fitting: The Billoir Method	60
7.2.1	General Method	60
7.2.2	Vertex Constraint	62
7.2.3	Full Vertex Fit	62
7.2.4	Fast Vertex Fit	63
7.2.5	Parametrisation of Track Parameters	63
7.2.6	Internal Iterations	65
7.2.7	Performance of the Billoir Fitters	67
7.3	Primary Vertex Finder	70
7.3.1	Finding Strategies	70
7.3.2	Data Sets	72
7.3.3	Track Selection	73
7.3.4	Performance Variables	73
7.3.5	Performance on $WH^0(120) \rightarrow l\nu b\bar{b}$ and $WH^0(120) \rightarrow l\nu u\bar{u}$	74
7.3.6	Performance on $t\bar{t}H$ and $t\bar{t}$ events	79
7.3.7	Summary	80
8	Jet Finding	83
8.1	Recombination Schemes	83
8.2	Jet Algorithms	84
8.2.1	Cone Algorithm	84
8.2.2	K_t Algorithm	85
8.3	Jet Energy Calibration	85
8.4	Settings and Jet Selection Cuts	86
9	b-Tagging	89
9.1	General Jet-Tagging Process	90
9.2	b-Tagging Methods	90
9.2.1	Impact Parameter Tagging	91
9.2.2	Secondary Vertex Tagging	92

9.3	Tagging Preparation	93
9.3.1	Association of Tracks to Jets	93
9.3.2	Truth Matching	93
9.4	Discriminating Variables	94
9.4.1	Likelihood	94
9.4.2	Weight	95
9.4.3	Weight and Likelihood for the Secondary Vertex Tagger	95
9.5	b-Tagging Performance	96
9.5.1	Performance Variables: Efficiency and Rejection	96
9.5.2	Track and Jet Selection Cuts	97
9.5.3	Tagging Methods and Reference Histograms	97
9.5.4	Performance on $WH^0(120) \rightarrow l\nu b\bar{b}$ and $WH^0(120) \rightarrow l\nu u\bar{u}$	100
9.5.5	Performance on $t\bar{t}H^0$, $H^0 \rightarrow b\bar{b}$ and $t\bar{t}$ background	105
9.6	Summary	108
10	Analysis of the Channel $t\bar{t}H$, $H \rightarrow b\bar{b}$	111
10.1	Description of the Signal and Background Channels	112
10.2	Event Selection	115
10.3	Parton-Jet Matching	116
10.4	Jet Energy Calibration	116
10.5	Reconstruction of the Final State	118
10.5.1	Reconstruction of $W \rightarrow l\nu$	119
10.5.2	Reconstruction of $W \rightarrow jj$	121
10.5.3	Simultaneous Reconstruction of the 2 Top Quarks	122
10.5.4	Reconstruction of the Higgs Boson	124
10.6	Results	125
10.6.1	Event Selection Cut Flow	125
10.6.2	Event Reconstruction Cut Flow	127
10.6.3	Significance	129
10.6.4	Uncertainties	130
10.7	Summary	132
11	Conclusion	133
Appendices		
A	Design of the Vertexing Software	137
A.1	Terminology	137
A.2	Event Data Model	138
A.3	Vertex Fitter Interface and Implementations	140
A.4	Primary Vertex Finder	141
A.5	Configuration	142
A.5.1	Billoir Fast and Full Vertex Fitters	142
A.5.2	Primary Vertex Finder	142
A.6	Location of the Vertexing Software	143

B	Design of the Jet-Tagging Software	145
B.1	Jet-Tagging Event Data Model	146
B.2	Algorithms and Data Flow	149
B.2.1	Jet-Tagging Process	149
B.2.2	Individual Tag Tools	151
B.2.3	Reference Histograms	151
B.3	Implementation of Helper Tools	151
B.4	Access to Tagging Results	154
B.5	Changing the Reference Histogram Input Files	155
B.6	Location of the Jet-Tagging Software	156
	Bibliography	157
	Curriculum Vitae	161

List of Figures

2.1	The Large Hadron Collider at CERN.	3
2.2	Preaccelerator and injector chain for the LHC.	5
3.1	The ATLAS Detector.	9
3.2	The ATLAS Inner Detector.	12
3.3	The inner most Pixel Detector.	12
4.1	Feynman diagrams for two possible decays of the Higgs boson.	26
4.2	Branching ratios of the Higgs boson as a function of its mass.	26
4.3	Schematic representation of the contributions to the QCD Lagrangian.	28
4.4	Schematic representation of the process $t\bar{t}H^0(120), H^0(120)\rightarrow b\bar{b}$	29
4.5	The physical vertex as a sum of the perturbative orders.	30
4.6	Parton cascade in the final state.	31
4.7	Feynman diagrams of the four Higgs boson production channels at the LHC.	35
4.8	Cross sections of various Higgs boson production processes at the LHC.	35
4.9	Feynman diagrams for the $t\bar{t}H$ channel.	37
4.10	Discovery potential of various Higgs channels in ATLAS.	38
4.11	$r\phi$ projection of a $t\bar{t}H^0(120), H^0(120)\rightarrow b\bar{b}$ event using ATLANTIS.	42
5.1	Cross section and rates for various processes in pp collisions.	43
5.2	Overview of the trigger and data flow systems.	45
5.3	The graphical user interface of the e/γ analysis framework.	49
5.4	Trigger Level 2 and Event Filter e^- selection efficiencies for $W \rightarrow e\nu$ samples.	50
5.5	Efficiency vs. rate for the trigger Level 2 cut optimisation procedure.	51
6.1	Schematic view of the ATLAS Perigee Parameters	54
6.2	Track selection variables.	55
6.3	Resolution of the transverse and longitudinal impact parameters.	57
7.1	General sequence diagram of the vertex finding and fitting process.	60
7.2	Schematic illustration of the iterative process to fit a vertex.	65
7.3	Iterative calculation of the vertex position.	66
7.4	Residuals and pulls for the fast Billoir fitter on $H\rightarrow 4l$	68
7.5	Residuals and pulls for the full Billoir fitter on $H\rightarrow 4l$	68
7.6	Residuals and pulls for the fast Billoir fitter on $H\rightarrow 4\mu$	69
7.7	Residuals and pulls for the full Billoir fitter on $H\rightarrow 4\mu$	69

7.8	d_0 perigee parameter for events with shifted vertex before and after extrapolation to the vertex region.	71
7.9	Track multiplicity in WH events before and after track selection cuts.	73
7.10	Residuals of the primary vertex on pure WH events.	74
7.11	Reconstructed primary vertex in WH events with pile up.	76
7.12	Track multiplicity in WH events with pile up before and after track selection cuts.	76
7.13	Residuals of the primary vertex on WH events with pile up.	77
7.14	Track multiplicity in WH events with shifted vertex before and after track selection cuts.	78
7.15	Residuals of the primary vertex on WH events with shifted vertex.	78
7.16	Track multiplicity in $t\bar{t}H$ and $t\bar{t}$ events before and after track selection cuts.	79
7.17	Residuals of the primary vertex on $t\bar{t}H$ and $t\bar{t}$ events.	80
7.18	Summary of the impact of the track selection cuts on the track multiplicity.	80
7.19	Summary of the performance of the primary vertex finder.	81
8.1	p_t and η distribution of the Cone4, Cone7 and K_t jet algorithms.	87
8.2	Jet and track multiplicities before and after jet selection cuts.	88
9.1	Information flow and execution order of the jet-tagging process.	90
9.2	Impact parameter of a particle originating from a B hadron decay.	91
9.3	Distribution of the transverse impact parameter and significance.	92
9.4	Weight/Likelihood for the combined 3D b-tagging algorithm on WH events.	96
9.5	Reference histograms for the 1D and 2D impact parameter taggers.	98
9.6	Reference histograms for the secondary vertex tagger.	99
9.7	Impact of truth matching and jet finding on the b-tagging performance.	100
9.8	Performance of the impact parameter taggers on WH events.	102
9.9	Performance of the 3D impact parameter and the secondary vertex tagger on WH events.	102
9.10	η and p_t dependence of the light jet rejection rate for the combined 3D and 3D+SV taggers.	103
9.11	Performance on pure events, events with pile up and events with shifted primary vertex.	104
9.12	Comparison of jet quantities important for b-tagging in $t\bar{t}H$ and WH events.	106
9.13	Performance of the 3D and the secondary vertex tagger on $t\bar{t}H$ events.	107
9.14	Summary of the b-tagging performance.	109
10.1	Event characteristic on generator level for signal and background processes.	114
10.2	Reconstruction efficiency of electrons and muons for $t\bar{t}H$ CSC events in full simulation.	115
10.3	Number of jets and b jets in CSC samples in full simulation.	117
10.4	Jet energy calibration constants.	118
10.5	Single jet energy calibration of light and b jets in full simulation.	119
10.6	Reconstructed neutrino momenta in full and fast simulation for CSC samples.	120
10.7	Mass spectrum of $W \rightarrow jj$ for all jet-jet pairs for the CSC signal sample.	121
10.8	Reconstructed mass of $t \rightarrow l\nu b$ for the CSC signal sample.	123
10.9	Reconstructed mass of $t \rightarrow jjb$ for the CSC signal sample.	123
10.10	Mass spectrum of the reconstructed Higgs boson in $t\bar{t}H$ events.	124

10.11	Mass spectrum of all events with correctly assigned b jets from the Higgs decay. .	125
10.12	Scale dependence and NLO corrections of the $t\bar{t}H$ cross section.	130
A.1	The design of the Vertex and RecVertex classes	138
A.2	The VxCandidate class	139
A.3	Interface design of the vertex fitters.	140
A.4	Data flow between vertex finding and fitting.	141
B.1	Inheritance structure, data members and methods of the JetTag object.	147
B.2	Inheritance structure of the jet-tagging info objects.	149
B.3	Jet-tagging TruthInfo class to store relevant truth matching information.	149
B.4	Sequence diagram of the jet-tagging process.	150
B.5	Interface structure of the tagging algorithms.	151

List of Tables

2.1	Expected $t\bar{t}H$ and background event rate at the LHC for an integrated luminosity of 30 fb^{-1}	7
4.1	Fundamental fermions of the Standard Model.	18
4.2	Fundamental interactions and their relative strength.	18
4.3	Coupling constants for the neutral current.	21
4.4	Predicted and measured masses of electro-weak gauge bosons	24
4.5	Standard Model and their supersymmetric partners in the Minimal Supersymmetric Standard Model.	39
4.6	Properties of B and D mesons.	41
5.1	Selection signatures of the physics trigger.	47
5.2	Selection cuts applied by trigger Level 1.	48
5.3	Selection cuts applied by trigger Level 2.	48
5.4	Combined Inner Detector and Calorimeter selection cuts applied by trigger Level 2.	48
5.5	Selection cuts applied on Event Filter Level.	48
5.6	Rates and efficiencies for low luminosity single electron events ($p_t=25 \text{ GeV}/c$).	50
5.7	Trigger rates for the $\mu 20i$ trigger.	52
7.1	ATLAS and Billoir perigee parameters.	63
7.2	Residuals and pulls for the fast and the full vertex fitter on $H \rightarrow 4l$	67
7.3	Monte Carlo data sets to study the performance of the primary vertex finder.	72
7.4	Track selection cuts.	73
7.5	Performance of the primary vertex finder on WH events.	75
7.6	Performance of the primary vertex finder on WH events with pile up.	75
7.7	Performance of the primary vertex finder on WH events with shifted vertex.	78
7.8	Performance of the primary vertex finder on $t\bar{t}H$ and $t\bar{t}$ events.	79
7.9	Summary of the resolution, reconstruction efficiency and outliers of the primary vertex finder on various data sets.	81
8.1	Parameter settings for the cone jet algorithms in Athena.	86
8.2	Parameter settings for the K_t jet algorithm in Athena.	86
9.1	Track selection cuts for b-tagging.	97
9.2	Performance of the impact parameter and secondary vertex taggers on WH events.	103

9.3	Performance of the 3D impact parameter and secondary vertex taggers on events with pile up and vertex shift.	105
9.4	Performance of the 3D impact parameter and secondary vertex taggers on $t\bar{t}H$	108
9.5	Summary of the b-tagging performance.	109
10.1	Description of data sets.	112
10.2	Mean of the p_t distribution of true particles in the $t\bar{t}H$ channel.	114
10.3	Average jet multiplicity in signal and background samples.	116
10.4	Resolution of the reconstructed neutrino momenta in signal samples.	121
10.5	Resolution of top mass reconstruction.	123
10.6	Event selection cut flow for the CSC samples.	126
10.7	Expected number of events at 30 fb^{-1} after the event selection.	127
10.8	Reconstruction cut flow.	128
10.9	Expected number of events at 30 fb^{-1} after reconstruction.	129
10.10	S/B and S/\sqrt{B} for the $t\bar{t}H$ channel.	130
A.1	Configuration of the full/fast vertex fitter.	142
A.2	Configuration of the primary vertex finder.	143

Chapter 1

Introduction and Motivation

The aim of particle physics is to describe the fundamental building blocks of the universe. The most successful particle physics theory up to date is the so called Standard Model (SM). It describes the fundamental particles and the forces that act among them.

According to the Standard Model, our entire universe consists of 12 fundamental fermions. They are divided into two groups of 6 leptons and 6 quarks and further organised in three families: (e, ν_e) leptons and (u, d) quarks, (μ, ν_μ) and (s, c) and finally (τ, ν_τ) and (t, b) . All matter (nuclei, atoms) are made of these fundamental building blocks.

In addition, we know of four different forces which can act between these 12 fermions. They are in order of increasing strength: gravity, weak force, electromagnetism and strong force. All four but one - gravitation - are described by the Standard Model. The messenger particles which mediate these forces are the photon (electric force), the W^\pm and Z bosons (weak force) and the gluon (strong force). The underlying mathematical theories to describe these particles and forces are so called gauge-theories.

The big success of the Standard Model was its prediction of many of these fundamental particles before their discovery. A very prominent example is the discovery of the W^\pm and Z bosons in 1983 at the Super Proton Synchrotron collider at CERN. Other ones are the discoveries of the bottom quark at Fermilab in 1977, the top quark in 1995 and the ν_τ - the last missing fermion - at Fermilab in 2000.

One of the biggest questions in high energy physics, however, is the origin of mass itself. The SM successfully describes interactions between fundamental particles by means of messenger bosons but it cannot explain the origin of mass of the particles. In 1964 a British physicist named Peter Higgs used the concept of spontaneous breaking of the gauge symmetry to generate masses for the quarks and leptons and also for the massive messenger particles W^\pm and Z^0 of weak interactions. The mechanism is widely known in High Energy Physics as the *Higgs Mechanism*. However, applying the Higgs mechanism in the context of the Standard Model predicts yet another particle: the Higgs boson.

The search for the Higgs boson is considered the biggest challenge of modern particle physics and lead to the development and construction of the biggest and most powerful particle accelerator ever being build: the Large Hadron Collider (LHC). The LHC is a 27 km long circular accelerator that is currently constructed 100 m below ground at the European Laboratory for High Energy Physics (CERN) in Geneva, Switzerland. Its purpose is to accelerate two counter rotating proton beams to an energy of 7 tera electron volts each and either collide them 40 million times per second or shoot them on a fixed target. At four interaction points along the

ring, four large particle detectors stand ready to measure the remnants of these collisions.

This thesis has been carried out in the ATLAS collaboration which currently builds the biggest of these four detectors. The front most goal of the ATLAS experiment is the discovery of the Higgs boson. This thesis depicts the analysis of the discovery potential of a Standard Model Higgs boson in the so called $t\bar{t}H^0(120)$, $H^0(120)\rightarrow b\bar{b}$ channel and covers the full spectrum starting with a study of the electron/ γ trigger which is important for the online selection of $t\bar{t}H$ events to the (software) development and study of reconstruction algorithms which are important for the analysis of this channel (i.e. vertex finding/fitting and b-tagging) and finally to the actual analysis itself.

In the $t\bar{t}H$ channel under study, the Higgs boson is produced in association with a $t\bar{t}$ pair which in 29% of all cases leaves a final state of a lepton with high transverse momentum, 2 b jets and 2 light jets. The Higgs boson itself decays into a pair of $b\bar{b}$ adding 2 b jets to the final state. Given 4 b jets in the final state, efficient b-tagging is crucial to successfully reconstruct the signal and efficiently reject the overwhelming background. The latter arises from $t\bar{t}$ pairs which are vastly produced at the LHC, from $t\bar{t}b\bar{b}$ events and from events where a Z/γ boson is produced in association with the $t\bar{t}$ pair and the boson decays into $b\bar{b}$.

The analysis re-evaluates the discovery potential of the $t\bar{t}H^0(120)$, $H^0(120)\rightarrow b\bar{b}$ channel in the ATLAS experiment using fully simulated and fully reconstructed Monte Carlo data sets from the recent Computing System Commissioning production and compares results to recent studies in ATLAS on fast simulation by Jochen Cammin and to results from CMS. Given the time consuming full simulation, many events have been produced in a private effort using the resources of the new world wide LHC Computing Grid (LCG) [1] of which the University of Innsbruck is part.

This thesis is structured as follows: Chapter 1 (this chapter) gives an introduction. Chapter 2 gives an overview of the Large Hadron Collider which is currently under construction at CERN. The third chapter describes the ATLAS detector with all its subsystems and puts emphasis on detector parts that are important for this thesis. The fourth chapter gives a general theoretical overview of the Standard Model and describes Higgs boson production and decay channels which are important for the discovery of the Higgs boson at the LHC. Chapter 5 depicts the ATLAS trigger system which is of great importance because it decides which collisions are written to tape and which are rejected (and lost forever). Performance studies of the e/γ trigger carried out during this thesis are presented. Chapter 6 gives a short overview of the tracking software and its performance. Reconstructed tracks are the main ingredient for primary vertex reconstruction and also play a central role in the performance of b-tagging algorithms. Chapter 7 describes in great detail the vertex fitting and finding methods which have been implemented and used for this thesis. It compares various vertex fitting mechanisms and ends with a general performance section of the primary vertex finder on different Monte Carlo data sets including the $t\bar{t}H$ sample. Chapter 8 gives a brief introduction to the jet finding algorithms used in the ATLAS detector. Jets are, next to tracks, a very important ingredient for b-tagging. In addition they (and their energy calibration) play a major role in the analysis of the $t\bar{t}H$ channel. Chapter 9 discusses the conceptual design of the b-tagging software and concentrates on various b-tagging methods and algorithms which have been implemented. The performance of the b-tagging algorithms is studied on various samples including the $t\bar{t}H$ and its background channels. Chapter 10 describes the analysis of the $t\bar{t}H$ channel and presents results and comparisons to earlier studies by J. Cammin and CMS. The two appendices describe the software design and implementation of the vertexing and b-tagging software.

Chapter 2

The Large Hadron Collider (LHC)

The Large Hadron Collider (LHC) is a ring of superconducting magnets with the sole purpose to accelerate and collide particles (see Fig. (2.1)). It has a circumference of 26.7 km and is currently under construction as an international project of many countries at the European Laboratory for Particle Physics (CERN) in Geneva, Switzerland. To cut costs and construction time the existing underground tunnel of the former Large Electron Positron collider (LEP) - which was switched off in late 2000 after more than a decade of operation - is reused for the LHC. It is located about 100m below ground, underneath the border of France and Switzerland. The LHC is foreseen to be operational in 2007.

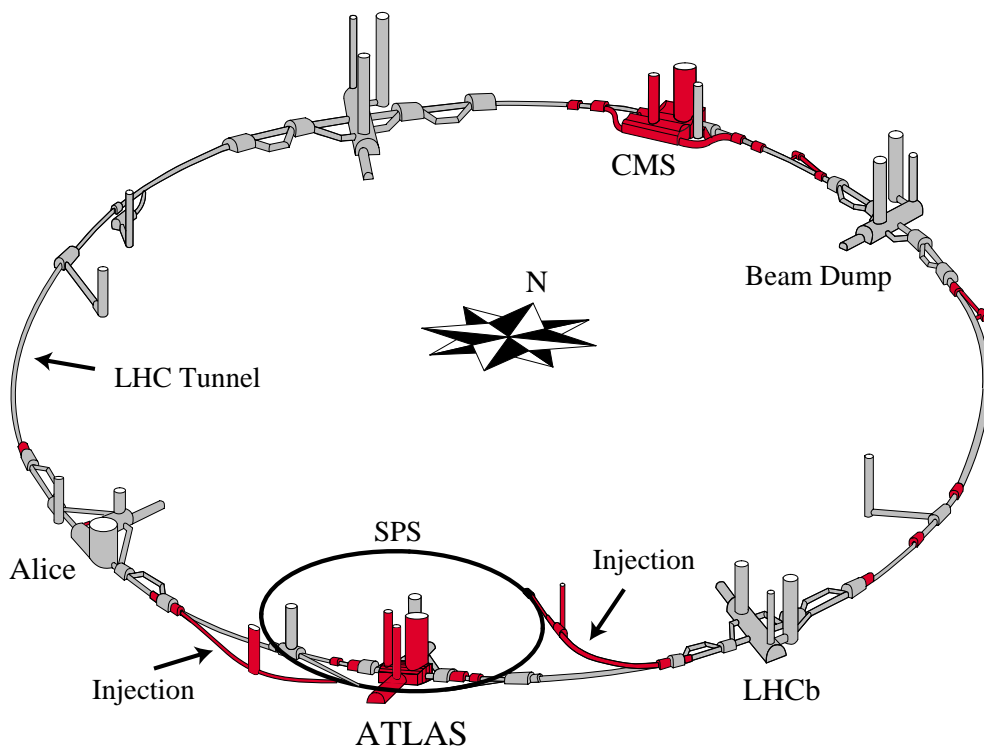


Figure 2.1: Schematic figure of the Large Hadron Collider. Structures in grey have been in use for the Large Electron Positron collider, red structures are newly built for the LHC.

The Large Hadron Collider is designed to cover an energy range that enables particle physics to answer some of its most fundamental questions. One is the hunt for the yet undiscovered Higgs boson. The LHC accelerates two proton beams in opposite directions along two separated circular beam pipes up to a center of mass energy E_{cm} of 14 TeV before collision. The two counter rotating beams will be brought to collision at two points and will be shot on a fixed target at one point along the ring. A fourth experiment is specialised on heavy ion collision which will take place in the LHC at a later stage.

The particle detectors are:

- ATLAS and CMS: two multi-purpose detectors to measure the remnants of pp collisions. They are designed to cover a wide range of physics.
- LHCb: a fixed target experiment with focus on B hadron physics.
- ALICE: a detector for heavy ion collisions which are planned at a later stage of the LHC.
- TOTEM: an experiment to measure the total pp cross section. Detectors for this experiment are integrated into the CMS detector.

This chapter gives an overview of the Large Hadron Collider in general and puts emphasis on its performance for physics measurements in terms of luminosity and total event rate. If not stated otherwise the information in this chapter is taken out of the recently published LHC Technical Design Reports [2, 3, 4].

2.1 Luminosity

The key quantity of every collider is the so called luminosity. It only depends on machine (i.e. beam) parameters and not on the physics process under consideration. However, the rate N_i at which a certain physics process i occurs is directly proportional to the luminosity of the machine

$$N_i[s^{-1}] = \sigma_i L \quad (2.1)$$

where σ_i is the cross section of the process under study and L the luminosity. This relation makes it desirable for every collider to have an as high luminosity as possible in order to give higher event rates.

The luminosity itself is proportional to

$$L \propto \frac{n_b N_b^2}{\epsilon_n} \quad (2.2)$$

where N_b is the number of particles in each bunch¹ and n_b the number of bunches per beam. ϵ_n is the normalised transverse beam emittance and corresponds to the area of the beam in the transverse plane ($\epsilon_n \sim A^2$). At start up and for the first few years the LHC is foreseen to run with a luminosity of $L = 2 \cdot 10^{33} \text{cm}^{-2} \text{s}^{-1}$ - so called *low* luminosity runs. The anticipated *high* luminosity is $L = 10^{34} \text{cm}^{-2} \text{s}^{-1}$, a value no collider has reached before.

¹a *bunch* is a cloud of particles which are accelerated together

In terms of Eq. (2.2) high luminosity requires from the beam to have

- a small normalised transverse emittance ϵ_n , i.e. the beam has to be squeezed together at the point of collision. This is limited by the LHC aperture since more squeezing means also that it has to be bigger elsewhere along the ring.
- a high brightness of the beam, which is limited by beam-beam effects.
- a high total intensity which is limited by the thermal energy caused due to synchrotron radiation that has to be absorbed by the cryogenic system.

To meet these requirements and reach low and especially high luminosity the proton beams have to be prepared in terms of bunch spacing, emittance energy etc. before being injected into the LHC. This is accomplished via a so called injector chain. It serves the purpose of preacceleration which decreases ϵ_n tremendously (by a factor of 1500 going from 50 MeV to 450 GeV) and also prepares the right bunch spacing and intensity.

2.2 Injector Chain

The protons for the LHC are produced in a so called Duoplasmatron Proton Source. Atoms of hydrogen gas are ionised via electron bombardment and then accelerated to 90 keV. This low energy proton beam is brought to injection energy by a chain of 5 accelerators: Radio Frequency Quadrupole (750 keV), Linac2 (50 MeV), Proton Synchrotron Booster (1.4 GeV), Proton Synchrotron (25 GeV) and Super Proton Synchrotron (450 GeV). These accelerators have already been in use for many decades either stand alone with their own experiments or as part of an injector chain for, e.g., the Large Electron Positron collider. Given their age they had to be modified and substantially upgraded to meet the requirements of the LHC (high beam intensity, high bunch frequency, small transverse emittance).

The beams are injected into the LHC with an energy of 450 GeV each and are then brought to an energy of 7 TeV before collision. A schematic picture of the injector chain is shown in Fig. (2.2).

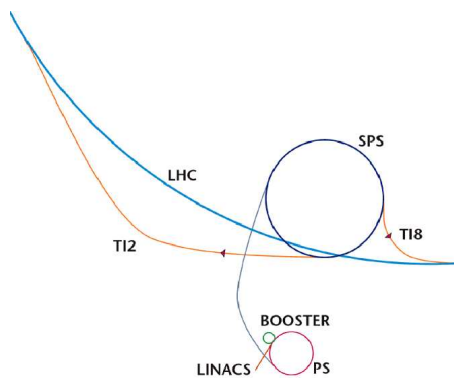


Figure 2.2: Preaccelerator and injector chain for the LHC.

2.3 Expected Integrated Luminosity

In the planning phase of an accelerator, the expected integrated luminosity is used to calculate the absolute number of expected events per physics process which will occur over a given period of time (usually a year of data taking). It is important to estimate the expected integrated luminosity for calculating the final number of events available for a certain physics analysis. This does not take into consideration any trigger rate or detector efficiency but still provides important information if an analysis of a channel is feasible or not. On the other hand, cross sections of important channels, e.g. Higgs boson discovery channels and their main backgrounds, define the requirements on the machine performance.

The integrated luminosity depends on the luminosity itself, the turnaround time of the machine (i.e. the time it takes to bring it down and restart) and the time window looked at. Since the LHC is not operational yet, these numbers have to be approximated using the experience from other colliders. Estimated figures are that from proton production to injection into the LHC it takes about 16 minutes for both beams. It takes another 20 minutes to accelerate both up to the nominal 7 TeV. At the end of the beam lifetime (i.e. several hours) the bending magnets have to be brought down to the 450 GeV initial state which takes another 20 minutes. Finally, 10 minutes are taken into account for a check of all systems before the next injection. This gives an approximate total turnaround time of 70 minutes.

The beam lifetime is directly related to the dependence of the luminosity on the beam age. Due to several effects, where the most stringent one is the collision itself, the initial luminosity goes down until it reaches an unusably low value (defined as $1/e$ of the initial one). The beam lifetime can be calculated as about 15 hours. Since the luminosity gets worse with time one has to decide when to dump the beam and restart in order to get a maximum integrated luminosity. The best combination has been calculated as 5.5 hours of run with 1.2 hours of turnaround time. Recent experience from the HERA collider however states that the average turnaround time is about 6 times bigger than the theoretical value which leads to a best combination of 12 hours of run with 7 hours of turn around. With the assumption that the LHC will be operational 200 days per year this gives an integrated luminosity of 80 fb^{-1} (7 hours turn around) to 120 fb^{-1} (1.2 hours turn around) for high luminosity and one fifth of that for low luminosity.

In ATLAS it is common to quote results for an integrated luminosity of 30 fb^{-1} which corresponds roughly to two years of data taking at low luminosity. With these numbers total event rates of certain physics processes can be estimated to get an idea about the expected sizes of the data sets available for analysis.

2.4 Expected Total Event Rate for the $t\bar{t}H^0$ channel

The total event rate per year for a process of interest can be calculated as

$$N_i = \sigma_i L_{int} \tag{2.3}$$

where σ_i is the cross section of the process and L_{int} the integrated luminosity.

To get an idea about the total event rates for signal and background channels some numbers for the $t\bar{t}H$ channel under study in this thesis are presented in Table (2.1). The $t\bar{t}H$ channel has an inclusive cross section of about 0.52 pb (for $m_H=120 \text{ GeV}/c^2$) [5]. For an integrated luminosity of 30 fb^{-1} this yields a total event rate of $0.52 \text{ pb} \times 30 \text{ fb}^{-1} = 15600$. For the

Process	σ (pb)	30 fb^{-1}
$t\bar{t}H(120) \rightarrow Wb Wbbb$	0.52	15600
$gg \rightarrow t\bar{t}b\bar{b}$	8.1	243000
$qq \rightarrow t\bar{t}b\bar{b}$	0.5	15000
$gg \rightarrow Z/\gamma/W \rightarrow t\bar{t}b\bar{b}$	0.9	27000
$t\bar{t}q\bar{q}$	833	26 million

Table 2.1: Expected $t\bar{t}H$ and background event rate at the LHC for an integrated luminosity of 30 fb^{-1} .

dominant $t\bar{t}$ background with $\sigma = 833 \text{ pb}$ [6] one can expect of the order of 26 million events for the same integrated luminosity.

Chapter 3

The ATLAS Detector

The ATLAS¹ detector is a multi purpose particle detector designed to cover a wide range of high energy physics measurements including Standard Model physics (SM Higgs, B-physics, QCD), Super Symmetry and possible new physics signatures (technicolor, extra dimensions). Key aspects of the detector layout are excellent tracking capabilities, pattern recognition and lepton identification of the tracking detectors (Inner Detector and Muon Spectrometer) and high resolution energy/position measurements in the Electromagnetic and Hadron Calorimeters.

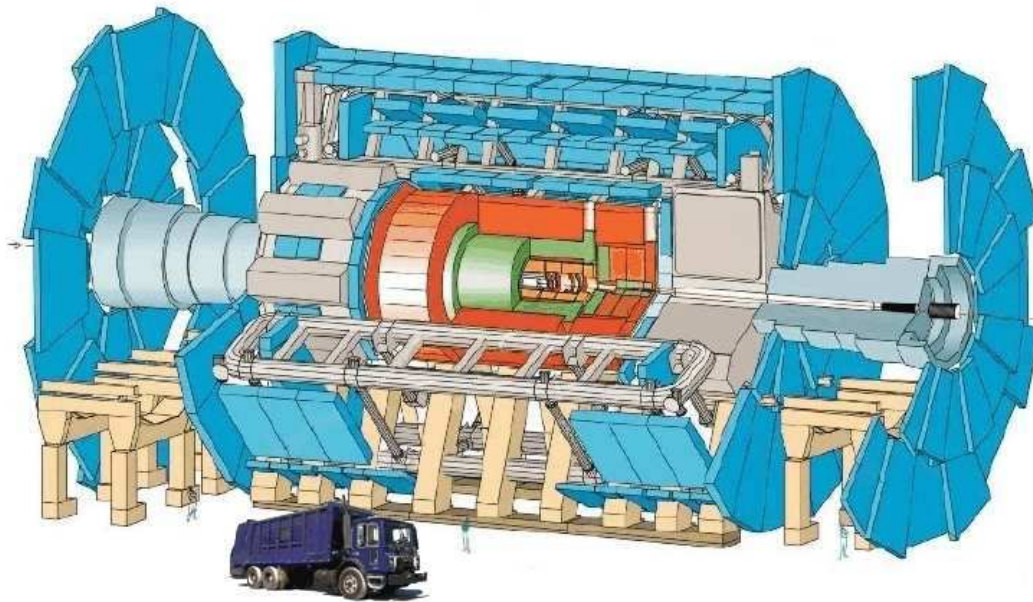


Figure 3.1: Schematic figure of the ATLAS detector.

The ATLAS detector is the biggest of the four LHC detectors. It is about 46m long, 22m in diameter and weighs roughly 7000 tons. A new underground area along the LHC ring has been excavated to host the detector and the required infrastructure like cooling and electronics. The various detector parts are constructed and tested in different countries and then shipped to

¹A Toroidal Lhc ApparatuS

CERN where they are being lowered into the cavern and assembled. Given that the detector is almost the size of the cavern, assembling the detector underground is a highly complex task in itself.

The detector has four main subsystems: two tracking detectors (Inner Detector and Muon System) and two calorimeters (Electromagnetic and Hadron Calorimeter). From inside to outside (see also Fig. (3.1)) it consists of the Inner Detector (orange), the Electromagnetic Calorimeter (green), the Hadron Calorimeter (red) and the Muon Spectrometer (blue).

The overall detector layout - in detail and in general - has been optimised and changed several times over the past years due to various reasons. The vertexing and b-tagging studies in this thesis have been done in 2005 where the detector layout misses the middle pixel layer because problems in the elaborate production of the pixel modules seemed to prevent the completion of three pixel layers in time. The analysis of the $t\bar{t}H$ channel has been carried out in 2006 where it was known that the final detector will have three pixel layers after all and hence it was reintroduced in the simulation of the detector.

The ATLAS detector has been described in great detail in the Technical Design Reports of each subsystem: Inner Detector [7, 8], Electromagnetic Calorimeter [9], Tile Calorimeter [10], Muon Spectrometer [11], Magnet System [12] and an overview of all detectors can be found in the ATLAS Physics Performance TDR [13]. This chapter will give a summary of the main detector subsystems and the magnet system. It will also introduce the ATLAS coordinate system and the system of units which is used throughout this thesis.

3.1 ATLAS Coordinate System and System of Units

The origin of the global ATLAS coordinate system is the geometrical center of the ATLAS detector. The positive x axis points to the center of the LHC ring. The positive y axis points upward. The x and y axes define the transverse plane. The z axis points along the LHC ring. Its direction is determined by the rules for a right handed coordinate system: when looked at ATLAS from above (i.e. from an aircraft) then the positive z axis points towards Geneva.

Another common representation is in spherical coordinates where

$$\begin{aligned} r &= \sqrt{x^2 + y^2} \\ \phi &= \tan^{-1}(y/x) \\ \theta &= \cos^{-1}(z/r) \end{aligned} \tag{3.1}$$

and therefore the transverse plane is often referred to as the $r\phi$ plane. ϕ is in the range $[-\pi, \pi[$ and $\theta \in [0, \pi]$.

All global parameters are expressed in this coordinate system and variables are often split into a transverse part (the projection of the x, y, z coordinates on to the $r\phi$ plane) and a longitudinal part (the projection on to the z axis).

The pseudo-rapidity η defined as

$$\eta = -\log \tan \theta/2 \tag{3.2}$$

is used instead of the polar angle θ because the number of particles produced in rapidity intervals of the same size is roughly constant over a wide range. The pseudo-rapidity is in the range $]-\infty, +\infty[$.

The system of units is a mixture of SI² [14] units and of so called *natural* or Planck units [15] where many quantities are expressed in electron volts ($1 \text{ eV} = 1.6 \cdot 10^{-19} \text{ joules}$). The base unit in ATLAS is MeV ($= 10^6 \text{ eV}$).

3.2 The Magnetic Fields

The ATLAS detector consists of two different magnetic systems: a 2 Tesla solenoid field in the Inner Detector and a toroidal field in the Muon Spectrometer with a maximum field strength of ~ 4 Tesla.

The superconducting coils to generate the field for the Inner Detector (ID) are located in front of the calorimeter. Any additional material before the calorimeter reduces its performance and hence the central solenoid is constructed as thin as mechanically possible. The Electromagnetic Calorimeter and the central solenoid also share the same vacuum chamber, thus avoiding two extra vacuum walls in front of the calorimeter. The ID magnetic field is generated by an 8 kA current.

The toroidal field for the Muon Spectrometer is generated by 3 huge air-core toroids, one for the muon barrel region and two for the end cap regions. Each air-core toroid consists of 8 coils mounted symmetrically in ϕ distances of 45° around the beam axis. The magnetic field strength is 3.9 Tesla in the barrel toroid which covers a region of $0 < |\eta| < 1.3$ and 4.1 Tesla in the end cap region which covers $1.6 < |\eta| < 2.7$. The end cap coils are rotated by 22.5 degrees with respect to the barrel ones in order to minimise degradation of the field in the overlap region of $1.3 < |\eta| < 1.6$. The bending power in terms of $\int \vec{B} d\vec{l}$ (with B in azimuthal and l in radial direction) is 2-6 Tm in the barrel region, 4-8 Tm in the end caps and a bit lower in the overlap region. The toroidal field is generated by a current of 21 kA.

3.3 Inner Detector

The Inner Detector is a tracking detector with three different subsystems (see Fig. (3.2)): Pixel Detector, Semi-Conductor Tracker (SCT) and Transition Radiation Tracker (TRT). Requirements from physics are excellent momentum and impact parameter measurements (good pattern recognition) in conjunction with radiation hardness in the very high particle multiplicity environment of the LHC which gives high radiation doses especially to the detectors close to the beam pipe.

The three systems consist of two high resolution pixel and silicon strip detectors and one straw tube detector with transition radiation capabilities for electron identification and pion rejection.

Each detector is divided into one central barrel region and two end cap regions with full hermetic coverage in an η region of $|\eta| < 2.5$. Each particle produces an average of 3 pixel, 8 SCT and 36 TRT hits. A higher number of pixel and SCT layers can improve the tracking and pattern recognition performance of the Inner Detector, however, it also introduces more material which can degrade the detector performance because of more multiple scattering. In addition each extra layer increases the cost of the Inner Detector dramatically.

²Systeme International d'unités

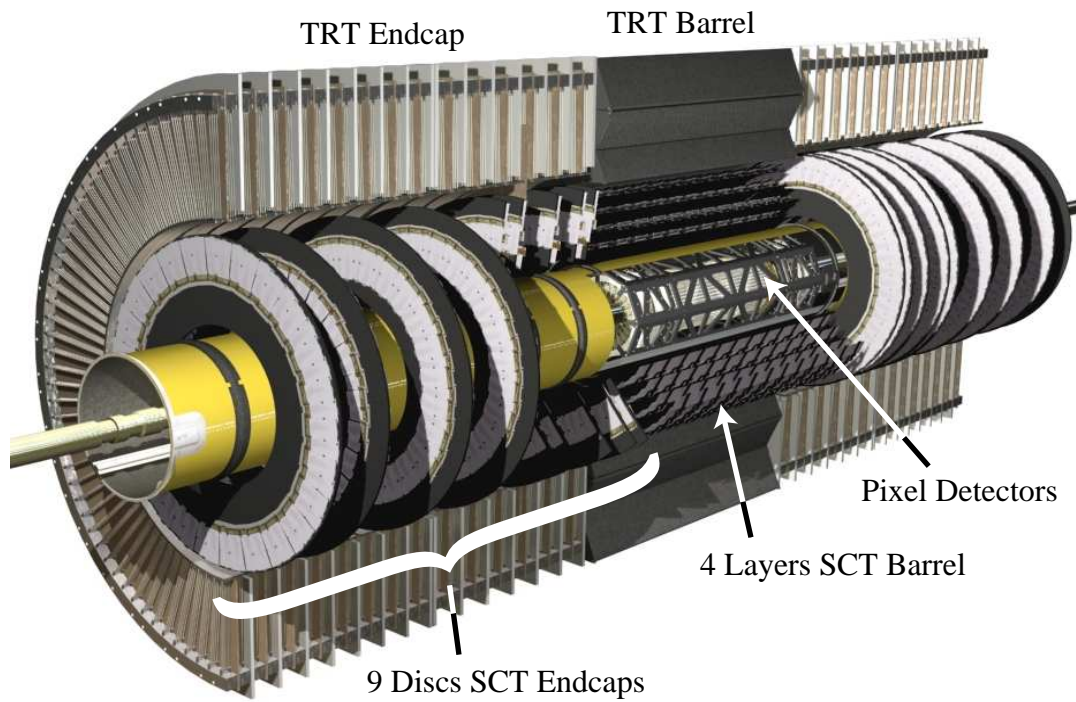


Figure 3.2: The ATLAS Inner Detector. From inside to outside it consists of the Pixel Detector, the Semi-Conductor Tracker and the Transition Radiation Tracker. It is about 6 m long and 2 m in diameter.

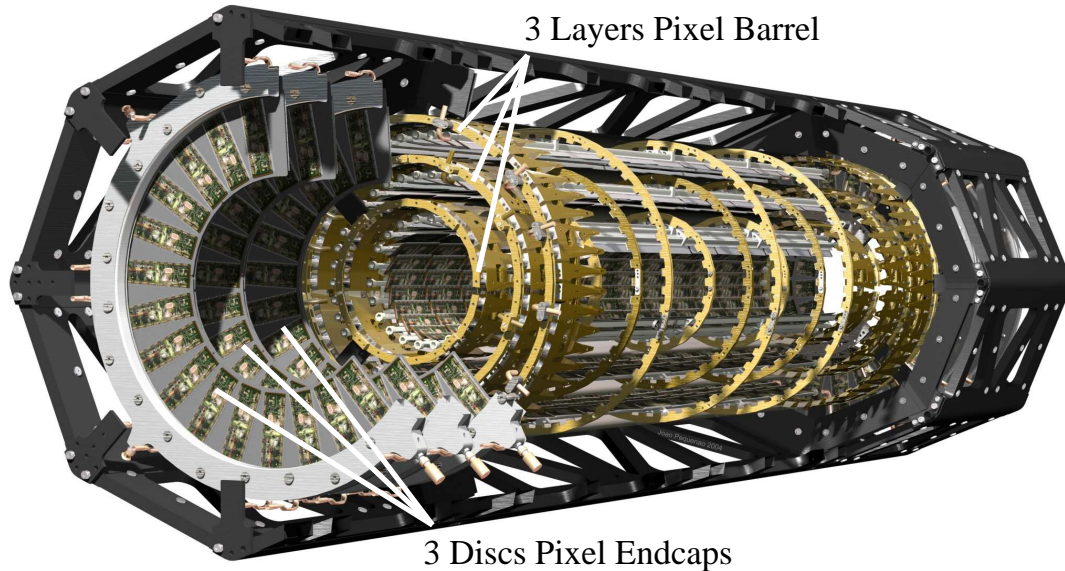


Figure 3.3: The inner most Pixel Detector consists of 3 layers in the barrel and 3 discs in each endcap. It is about 1.6 m long and 50 cm in diameter.

3.3.1 Pixel Detector

The Pixel Detector is the innermost detector (see Fig. (3.3)). It has three layers in the barrel and three discs in each end cap assuring at least 3 measurements over the whole acceptance. The barrel layers are located at radial distances of 50.5, 88.5 and 122.5 mm and the discs at z distances of $\pm 495, 580, 650$ mm. The system covers a region of $|\eta| < 2.5$.

The Pixel detector has a very high granularity with a total of 80 million pixel elements mounted on 1456 modules in the barrel and 144 in each endcap. Each module has 46080 pixels. The high precision measurements in the Pixel Detector guarantee good pattern recognition and determine mostly the performance of the whole Inner Detector in terms of impact parameter resolution and the ability to find short lived particles (B's, τ 's). The first layer is especially important for primary vertex finding and b-tagging.

The pixel elements have a size of $50 \mu\text{m}$ in $r\phi$ and $400 \mu\text{m}$ in z direction. Each module is 62.4 mm long and 21.4 mm wide. The readout chip is mounted directly on the module. It is analogue to allow for charge weighted clustering (for the resolution) and noise reduction. The information is buffered on the module until the Level 1 trigger decision is taken.

The first layer - being closest to the beam pipe - has to withstand high radiation levels of 300 kGy ³ of ionising radiation and $5 \cdot 10^{14}$ neutrinos per cm^2 over 10 years of operation. Due to an insertable design it is possible and foreseen to exchange the innermost layer after a few years of operation in order to maintain an excellent performance.

3.3.2 Semi Conductor Tracker (SCT)

The semi conductor tracker is the middle detector of the three Inner Detector subsystems. It consists of 4 layers in the barrel region and 9 discs in each end cap region. The layers consist of two detector modules mounted back-to-back at a small angle of 40 mrad to obtain the z measurement. There are 4224 back-to-back modules in the barrel and 1976 in each endcap. The 4 double layers are mounted at radial distances of 301, 373, 445 and 516 mm. The 9 discs at z distances between ± 85 cm and 272 cm. It covers a region of $\eta < 2.5$.

Each module has a size of 6.3 times 6.4 cm and holds 780 readout strips each with $80 \mu\text{m}$ pitch. It covers a total area of 61 m^2 and has about 6.2 million readout channels. It is a high granularity tracking detector which adds a maximum of 8 precision measurements to the 3 hits of the Pixel Detector. It contributes significantly to the pattern recognition abilities and momentum and impact parameter resolution of the Inner Detector. The read out chips are again mounted on the modules and the digital hit information is buffered until the Level 1 trigger has drawn its decision.

High precision measurements in the Pixel Detector and SCT require a high mechanical stability, cold operation of detectors and efficient removal of heat generated by electronics and the detector leakage currents.

3.3.3 Transition Radiation Tracker (TRT)

The TRT is the third and outermost subsystem of the Inner Detector (besides the central solenoid for the magnetic field). It consists of a barrel and two identical end caps. It adds on average 36 hits to the measurements of the Pixel and SCT.

³One Gray is the absorption of one joule of radiation energy by one kilogram of matter.

In the barrel, the straws are parallel to the beam axis whereas in the end cap they are aligned radially. Each straw is 4 mm in diameter and with a maximum length of 144 cm in the barrel. The gold plated wire in the center has a diameter of 30 μm . The TRT has about 50000 straws in the barrel which are divided into two at the center and 320000 radial straws in each endcap. The straws are filled with a non flammable gas mixture of 70% Xe, 20% CO_2 and 10% CF_4 giving the TRT the capability of electron identification (and pion rejection) by detecting transition radiation of photons created in the radiator between straws. Two different thresholds are used to distinguish between tracking hits (lower threshold) and transition radiation hits (higher threshold).

Given the high number of particles per event and the relatively big size of the tubes (compared to pixels and strips) the TRT needs to have very good performance in terms of resolving low(high) threshold hits. It was tested to be stable up to a rate of 6-18 MHz in the barrel and 7-19 MHz in the end caps for low threshold hits and up to 1 MHz for high threshold hits.

The tracking performance of the Inner Detector in terms of transverse and longitudinal impact parameter resolutions is presented in chapter 6.3.

3.4 Calorimeters

The calorimeters measure the energy and position (in $r\phi$) of particles with high precision. ATLAS uses two different calorimeters: the Electromagnetic Calorimeter (LAr) for energy measurements of mainly electrons and photons and the Hadron Calorimeter for energy measurements of hadrons. The calorimeters cover a range of up to $\eta = 5$ and have an overall weight of about 4000 tons.

3.4.1 Electromagnetic Calorimeter

The Electromagnetic Calorimeter surrounds the Inner Detector and shares a vacuum chamber with the ID central toroid. It is a high granularity liquid argon sampling calorimeter with excellent energy and position resolution. It covers a range of $|\eta| < 3.2$ for the barrel and $|\eta| < 4.9$ for the end caps. The outer radius is 2.25 m and it is 12.2 m long. The active material in the Electromagnetic Calorimeter is liquid argon inside an accordion structure of Kapton electrodes and lead as absorber. Particles pass through the calorimeter and loose energy in the lead absorber which causes them to radiate bremsstrahlung (photons). These photons convert into electron-positron pairs which initiate a cascade/shower. The secondary particles ionise the liquid argon and free electrons from the ionisation are drawn off by the high voltage field and the produced signal is measured. The Inner Detector, the cryostat and the coils of the central solenoid are in front of the Electromagnetic Calorimeter and with a radiation length of about $2.3 X_0$ at $\eta = 0$ they absorb energy before the particles hit the calorimeter. This energy loss is corrected with a LAr presampler of 1.1 cm thickness in the barrel and 0.5 cm in the end cap region.

The anticipated design resolution of the Electromagnetic Calorimeter is

$$\frac{\sigma_E}{E} = \frac{0.1}{\sqrt{E}} \oplus \frac{0.3}{E} \oplus 0.01. \quad (3.3)$$

3.4.2 Hadron Calorimeter

The Hadron Calorimeter surrounds the Electromagnetic Calorimeter. It has an outer radius of 4.25 m and a length of 12.2 m. In the barrel region ($|\eta| < 1.7$) it uses a novel approach with plastic scintillators embedded in an iron absorber. The incoming particles initiate showers in the absorber and the secondary particles excite atoms in the scintillators which then radiate light. These photons are transmitted to photo multipliers which convert the light into an electric signal. In the end caps ($1.5 < |\eta| < 3.2$) the hadron calorimeter makes also use of the more radiation-hard liquid argon as active material. The calorimeters extend to an η region of 4.9 to cover the very forward regions. To achieve this, additional calorimeters are mounted at a distance of 4.7 m from the interaction point in z and as close as possible in $r\phi$ (some centimeters). This region is under high exposure to radiation and therefore the LAr technology has been used for both the Electromagnetic and Hadronic Calorimeter. To cover very high η regions is important for the measurement of missing energy and for Higgs discovery channels involving Higgs production via vector boson fusion. The parton remnants of the protons cause jets in the very forward regions of the detector.

The design energy resolution of the hadron calorimeter is

$$\frac{\sigma_E}{E} = \frac{0.5}{\sqrt{E}} \oplus 0.03. \quad (3.4)$$

3.5 Muon Detector

The Muon Detector is the biggest of all detector subsystems covering a large magnetic field volume with strong bending power in a light and open structure. It is designed to trigger on and to measure the momentum of muons and therefore consists of dedicated trigger chambers and high precision tracking chambers. The size of the Muon Spectrometer defines the overall dimensions of the ATLAS detector with an outer radius of 11m and a length of 25m. The third forward end cap layers are mounted at either end of the cavern wall at a distance of $z=\pm 23$ m giving the detector an overall length of 46m. Magnetic bending is provided by the large air-core barrel toroid magnets for $\eta < 1$ and for $1.4 < \eta < 2.7$ by the two end cap magnets. In the transition region the magnetic field is a complex superposition of both.

There are two types of tracking chambers namely Monitored Drift Tubes (MDT) and Cathode Strip Chambers (CSC). The MDTs cover an η range up to 2.7 with three layers in the barrels at radii of 5, 7.5 and 10 meters and end cap wheels at $z=\pm 7, 10, 14$ and 23 meters. The CSCs have higher granularity and are used in the region $2 < \eta < 2.7$. The MDTs are single wire drift chambers with a single wire precision of about $80 \mu\text{m}$. CSCs are multi wire chambers with a resolution of up to $\sim 60 \mu\text{m}$. The tubes are aligned toroidal (i.e. in the same direction as the magnetic field) in the barrel and parallel to the transverse plane in the end caps.

The muon trigger is made of Resistive Plate Chambers (RPC) in the barrel and Thin Gap Chambers (TGC) in the end caps which together cover a region of up to $\eta = 2.4$. The trigger chambers actually serve three purposes. The first is the identification of the bunch crossing which requires a time resolution of better than the 25 ns bunch crossing rate. The second is the efficient triggering with a well defined transverse momentum cut off in the moderate magnetic field of the muon system. The third purpose is to provide an additional position measurement orthogonal to that of the precision chambers. The RPCs are mounted on both sides of the

the middle MDT and inside of the outer MDT barrel layers. The TGCs are mounted on three separate end cap layers which are located near the middle MDT layer.

The RPCs are made of two resistive plate chambers with a $C_2H_2F_4$ gas filled gap in between. A high voltage of several kV/mm between the plates results in an avalanche of ionised particles as soon as a muon passes the chamber. The chambers have a very high time resolution (order of nanoseconds). The TGCs are similar in design but filled with a different gas mixture and operated in saturation mode. They achieve a time resolution of about 5 ns.

The muon system consists of 32 CSC, 1194 MDT, 596 RPC and 192 TGC chambers resulting in a total number of 1.2 million readout channels and covering an area of more than 12000 square meters.

Chapter 4

Theoretical Overview

The Standard Model (SM) describes fundamental particles of matter and their interaction with each other. The basis of the SM are gauge theories which exploit that physical observables of quantum mechanical wave functions are invariant under certain transformations of the wave function. Therefore, the Lagrangian involving the fermion fields has to be gauge invariant under a local symmetry transformation with respect to the underlying gauge symmetry. To achieve this, so called gauge fields are introduced which can be identified with the “messenger” bosons which mediate a force. In this approach interactions among fermions enter the theory in a natural way.

Section 1 of this chapter gives an overview of the Standard Model and shows in detail how the force mediating bosons of electro-weak theory (γ , W^\pm , Z^0) are introduced by using gauge invariance. The origin of the masses of the fermions and the massive gauge bosons is a yet unsolved problem in particle physics. It is shown that the concept of spontaneously breaking the electro-weak gauge symmetry can generate masses of fermions and bosons. The consequence is that a new - yet undiscovered - particle enters the theory: the Higgs boson. This Higgs boson is meant to give particles of the Standard Model their masses and its discovery (or proof against) is highest priority at the LHC. An overview of the theory of quantum chromo-dynamics which describes the strong force between quarks ends section 1.

Section 2 of this chapter gives an overview of the rich physics program at the Large Hadron Collider at CERN. The high energy and luminosity at the LHC will allow for a wide range of physics measurements front most being the discovery of the Higgs boson. Numerous measurements in the QCD sector, in the field of electro-weak gauge bosons, B-physics and also the search for effects from new physics beyond the Standard Model like Super Symmetry or other theories are planned.

Section 3 explains the special topology of b jets and characteristics of B hadrons which make b jets different from lighter jets. This differences are used in b-tagging algorithms to separate b jets from light jets which is important in many physics analyses such as the $t\bar{t}H$ channel which is subject of this thesis.

4.1 The Standard Model

The Standard Model is currently considered the most appropriate theory in particle physics. It describes fundamental particles and their interactions with very high accuracy and is in good

agreement with measurements which have been boosted in precision by orders of magnitude over the last 3 decades.

According to the Standard Model 12 fundamental fermions with spin $\frac{1}{2}$, and 5 messenger bosons (photon, W^\pm , Z^0 , gluon) with spin 1 exist. Fermions are further divided into 3 families of 2 leptons and 2 quarks as shown in Table (4.1).

Generation	I	II	III	Electric Charge
Leptons	$\begin{pmatrix} \nu_e \\ e^- \end{pmatrix}$	$\begin{pmatrix} \nu_\mu \\ \mu^- \end{pmatrix}$	$\begin{pmatrix} \nu_\tau \\ \tau^- \end{pmatrix}$	0 -1
Quarks	$\begin{pmatrix} u \\ d \end{pmatrix}$	$\begin{pmatrix} c \\ s \end{pmatrix}$	$\begin{pmatrix} t \\ b \end{pmatrix}$	2/3 -1/3

Table 4.1: The fundamental fermions of the Standard Model are divided into 3 families of 2 leptons and 2 quarks each.

Of the 4 known fundamental forces - electromagnetic, weak, strong and gravitational - the first 3 are described by the Standard Model with gauge theories. The gravitational force, which dominates on a large scale throughout the universe, is not included in the Standard Model. This is seen as a weakness of the theory and many attempts were/are made to develop a more inclusive theory (\rightarrow Grand Unified Theories [16]). However, since gravity is by far the weakest of all forces (see Table (4.2)), it does not play a role for the outcome of present particle physics experiments and can therefore be neglected in the study of the other three interactions..

Of these three forces only the weak force is felt by all fermions (meaning that all fermions have *flavour* charge). The electromagnetic force is only felt by particles with electrical charge (i.e. all but the neutrinos) and only quarks interact via the strong force (because quarks are the only particles which carry *colour* charge).

The theoretical basis of the Standard Model to describe the fundamental particles and their interaction are gauge theories. Requiring the Lagrangian of a certain force to be gauge invariant under a local transformation introduces new fields which can be interpreted as the messenger particles of this force. The electromagnetic, the weak and the strong force are all described by a gauge theory where the first two have been formally unified into an electro-weak theory.

interaction	mediator(s)	range [m]	relative strength
strong	gluon	10^{-15}	1
electromagnetic	photon (γ)	∞	1/137
weak	W^\pm , Z^0	10^{-17}	10^{-5}
gravitational	graviton (postulated)	∞	10^{-39}

Table 4.2: Fundamental interactions and their relative strength [17, 18].

4.1.1 Electro-weak Theory

Electro-weak theory describes the interaction of particles via the weak and electromagnetic forces. The formal unification of *quantum electro dynamics* (QED) and the theory of *weak interactions* into a theory of *electro-weak interactions* including massive gauge bosons was done by Glashow, Salam and Weinberg in 1967. This section describes electro-weak theory as a Yang-Mills theory where the masses of the electro-weak gauge bosons are not taken into account. The masses of gauge bosons will be introduced in the next section using the Higgs mechanism of spontaneous breaking of a gauge symmetry. This section and section 4.1.3 are written in analogy to [17, 18].

The underlying gauge symmetry of electro-weak theory is the gauge group $SU(2)_L \times U(1)_Y$. The Lagrangian has to be invariant under such transformations which are part of this group. Starting from the free Lagrangian for electrons and neutrinos, both represented by Dirac spinors Ψ_e and Ψ_ν , respectively,

$$\mathcal{L} = i(\bar{\Psi}_e \gamma^\mu \partial_\mu \Psi_e) + i(\bar{\Psi}_\nu \gamma^\mu \partial_\mu \Psi_\nu) \quad (4.1)$$

the requirement of gauge invariance can be used to generate the gauge bosons and identify them as the mediator particles of the electromagnetic force (the photon) and the weak force (Z^0 , W^\pm). For massless neutrinos no right-handed term exists¹ but the electron spinor can be split into a right and a left handed part

$$\Psi_e = \Psi_{eR} + \Psi_{eL} \quad (4.2)$$

and Eq. (4.1) can be rewritten in a more symmetric form

$$\mathcal{L} = i(\bar{\Psi}_{\nu L}, \bar{\Psi}_{eL}) \gamma^\mu \partial_\mu \begin{pmatrix} \Psi_{\nu L} \\ \Psi_{eL} \end{pmatrix} + i(\bar{\Psi}_{eR} \gamma^\mu \partial_\mu \Psi_{eR}). \quad (4.3)$$

First, we require the first part of Eq. (4.3) to be gauge invariant under a transformation $U(x) \in SU(2)$ and this can be achieved by replacing ∂_μ with the covariant derivative D_μ defined as

$$\partial_\mu \rightarrow D_\mu = \partial_\mu + ig \frac{1}{2} W_\mu^k \sigma_k \quad (4.4)$$

which makes Eq. (4.3) gauge invariant again, but introduces a new interaction term

$$\mathcal{L}_W = -\frac{g}{2} (\bar{\Psi}_{\nu L}, \bar{\Psi}_{eL}) \gamma_\mu W_\mu^k \sigma_k \cdot \begin{pmatrix} \Psi_{\nu L} \\ \Psi_{eL} \end{pmatrix} \quad (4.5)$$

where $\sigma_{k=1,2,3}$ denote the three generators of the $SU(2)$ symmetry group (i.e. Pauli matrices) and $W_\mu^{k=1,2,3}$ are the three new gauge fields with gauge bosons $W^{1,2,3}$. These three gauge bosons cannot yet be identified with the known mediators of the electro-weak force. However, with $W^\pm := \frac{1}{\sqrt{2}}(W^1 \mp iW^2)$ and substitution of the Pauli matrices a preliminary expression for the

¹In 1998 the Super-Kamiokande Collaboration announced the discovery of oscillations of atmospheric neutrinos and hence give evidence that neutrinos are massive particles [19].

electro-weak Lagrangian can be given by

$$\begin{aligned} \mathcal{L}_W = & \quad -\frac{g}{2} \cdot (W_\mu^3 (\bar{\Psi}_{\nu L} \gamma^\mu \Psi_{\nu L} - \bar{\Psi}_{eL} \gamma^\mu \Psi_{eL})) \\ & \underbrace{-\frac{g}{\sqrt{2}} \cdot W_\mu^+ (\bar{\Psi}_{\nu L} \gamma^\mu \Psi_{eL}) - \frac{g}{\sqrt{2}} \cdot W_\mu^- (\bar{\Psi}_{eL} \gamma^\mu \Psi_{\nu L})}_{=: \mathcal{L}_{CC}} \end{aligned} \quad (4.6)$$

The coupling of W^\pm in \mathcal{L}_{CC} is identical to the charged-current coupling in weak theory, and hence W^\pm are identified as the two charged gauge bosons of weak interactions.

To get a connection to Z^0 and the gauge boson A of QED, Eq. (4.3) is also made invariant under a $U(1)$ transformation.

Again D_μ is replaced and, with the following currents

$$\begin{aligned} j_\nu^\mu &= \bar{\Psi}_{\nu L} \gamma^\mu \Psi_{\nu L} \\ j_{eL}^\mu &= \bar{\Psi}_{eL} \gamma^\mu \Psi_{eL} \\ j_{eR}^\mu &= \bar{\Psi}_{eR} \gamma^\mu \Psi_{eR} \\ j_{em}^\mu &= \bar{\Psi}_e \gamma^\mu \Psi_e = j_{eL}^\mu + j_{eR}^\mu \end{aligned}$$

it is possible to write down the complete interaction term of the electro-weak Lagrangian

$$\begin{aligned} \mathcal{L}_W = & \quad \mathcal{L}_{CC} - \frac{1}{2}(gW_\mu^3 - g'B_\mu)j_\nu^\mu \\ & + \frac{1}{2}(gW_\mu^3 + g'B_\mu)j_{eL}^\mu - Y_R g' B_\mu j_{eR}^\mu \end{aligned} \quad (4.7)$$

where Y_R is the so called hypercharge.

Since both, W^3 and B , couple to the neutrino, none can be the photon. However, the linear combination $(gW_\mu^3 - g'B_\mu)$ couples to the neutrino only and since the neutrino feels nothing but a weak force this term can be identified with the Z^0 boson. The gauge field A_μ for the photon is an orthogonal linear combination to the Z^0

$$\begin{aligned} A_\mu &= B_\mu \cos \theta_W + W_\mu^3 \sin \theta_W \\ Z_\mu^0 &= -B_\mu \sin \theta_W + W_\mu^3 \cos \theta_W \end{aligned} \quad (4.8)$$

with $\cos(\theta_W) = \frac{g}{\sqrt{g^2+g'^2}}$ and $\sin(\theta_W) = \frac{g'}{\sqrt{g^2+g'^2}}$.

The observed gauge bosons Z^0 and A are a mixture of the gauge fields obtained by requiring gauge invariance of Eq. (4.3). The mixing angle θ_W is called Weinberg angle. It needs to be determined by experiment and has been measured to $\sin^2 \theta_W = 0.2324 \pm 0.0012$ [20]. With the new fields Z_μ^0 and A_μ , Eq. (4.7) becomes

$$\begin{aligned} \mathcal{L}_W = & \quad \mathcal{L}_{CC} \\ & -\sqrt{g^2+g'^2} \cdot Z_\mu \cdot \left\{ \frac{1}{2}j_\nu^\mu - \frac{1}{2}j_{eL}^\mu - \sin^2 \theta_W (-j_{eL}^\mu + Y_R j_{eR}^\mu) \right\} \\ & -\sqrt{g^2+g'^2} \cdot \sin \theta_W \cos \theta_W \cdot A_\mu (-j_{eL}^\mu + Y_R j_{eR}^\mu) \end{aligned} \quad (4.9)$$

It is possible to convert the last term to the well known interaction term of electromagnetism by choosing the (up to now) arbitrary hypercharge Y_R to -1 and identifying the electric charge with $e = \sqrt{g^2+g'^2} \cdot \sin \theta_W \cdot \cos \theta_W$.

So, at length, the interaction term of the final Lagrangian of electro-weak theory is

$$\mathcal{L}_W = \mathcal{L}_{CC} + eA_\mu \cdot j_{em}^\mu - \frac{e}{\sin \theta_W \cos \theta_W} \cdot Z_\mu j_{NC}^\mu \quad (4.10)$$

with $j_{NC}^\mu = (\frac{1}{2}j_\nu^\mu - \frac{1}{2}j_{eL}^\mu) + \sin^2 \theta_W j_{em}^\mu$.

This Lagrangian is valid for the 3 lepton isospin-doublets (ν_e, e^-) , (ν_μ, μ^-) and (ν_τ, τ^-) . In order to expand this scheme to suit the 3 quark generations as well, the first part of j_{NC} is rewritten as a sum of a left and a right handed part

$$j_{NC} = (I_3 - Q \sin^2 \theta_W)j_L - Q \sin^2(\theta_W)j_R \quad (4.11)$$

$$= C_L j_L + C_R j_R. \quad (4.12)$$

If the three quark generations are also understood as weak isospin doublets, i.e. $I_3(u) = 1/2$ and $Q(u) = 2/3$, one can easily calculate the appropriate neutral current j_{NC} and \mathcal{L}_W for all quarks (see Table (4.3)).

fermion	charge Q	isospin I_3	$C_L =$ $I_3 - Q \sin^2 \theta_W$	$C_R =$ $-Q \sin^2 \theta_W$
ν_e, ν_μ, ν_τ	0	1/2	1/2	0
e^-, μ^-, τ^-	-1	-1/2	$-1/2 + \sin^2 \theta_W$	$\sin^2 \theta_W$
u, c, t	2/3	1/2	$1/2 - (2/3) \sin^2 \theta_W$	$-(2/3) \sin^2 \theta_W$
d, s, b	-1/3	-1/2	$-1/2 + (1/3) \sin^2 \theta_W$	$(1/3) \sin^2 \theta_W$

Table 4.3: Coupling constants for the neutral current. The hypercharge Y_R is related to Q and I_3 via $Q = I_3 + Y_R/2$.

Alternatively, v_f and a_f can be defined as

$$\begin{aligned} v_f &= C_L + C_R \\ a_f &= C_L - C_R \end{aligned} \quad (4.13)$$

The above procedure is often presented as a unification of weak and electromagnetic theory. It is rather a unified formulation of both theories. The value of the parameter Y_R was set to -1 to convert the last term of Eq. (4.9) to the known interaction term of electromagnetism. It is not an outcome of electro-weak theory. Neither is θ_W - it has to be determined by experiment.

It was shown that a theory which is gauge invariant under a local transformation is capable of describing the fundamental fermions and their electro-weak interactions through gauge bosons. However, in this theory the three gauge bosons W^\pm , Z^0 are massless, just like the photon. To give the fermions and gauge bosons mass, new parts have to be added to the theory: spontaneous symmetry breaking and the *Higgs mechanism* [17, 18].

4.1.2 The Higgs Mechanism and the Higgs Boson

The gauge theories of the SM describe the interaction between fermions via gauge bosons in great detail. However, other than the fermions and gauge bosons in these theories the fermions

and bosons of electro-weak theory (except the photon) have mass. To include these masses into the theory an additional assumption has to be made. This assumption is known as the Higgs mechanism [17, 18]. It uses the concept of spontaneous breaking of the (electro-weak) gauge symmetry, which introduces a new particle into the theory: the Higgs boson.

First, the basic spontaneous breaking of a gauge symmetry is shown by the example of a complex scalar field. Second, the full mechanism is demonstrated by generating a mass for a gauge boson of a $U(1)$ local gauge symmetry. Finally, the results for the more complex $SU(2)_L \times U(1)_Y$ symmetry of electro-weak theory and its gauge bosons are presented. At the end Higgs decay channels will be discussed which play an important role for discovery at the LHC.

Spontaneous Breaking of a Global $U(1)$ Symmetry

Consider a complex scalar field Φ described by a Lagrangian

$$\mathcal{L} = (\partial_\mu \Phi)^* (\partial^\mu \Phi) - V \quad (4.14)$$

with the potential V as

$$V = \mu^2 (\Phi^* \Phi) + \lambda (\Phi^* \Phi)^2 \quad (4.15)$$

where $\mu^2 < 0$ and $\lambda > 0$. The Lagrangian Eq. (4.14) is invariant under a global $U(1)$ gauge transformation $\Phi \rightarrow e^{i\alpha} \Phi$. With $\Phi = 1/\sqrt{2}(\Phi_1 + i\Phi_2)$, Eq. (4.14) becomes

$$\mathcal{L} = \frac{1}{2}(\partial_\mu \Phi_1)^2 + \frac{1}{2}(\partial_\mu \Phi_2)^2 - \frac{1}{2}\mu^2(\Phi_1^2 + \Phi_2^2) - \frac{1}{4}\lambda(\Phi_1^2 + \Phi_2^2)^2. \quad (4.16)$$

There is an infinite number of minima for the potential $V(\Phi)$ which fulfil

$$\Phi_1^2 + \Phi_2^2 = -\frac{\mu^2}{\lambda} =: v^2. \quad (4.17)$$

Without loss of generality it is possible to move the field Φ to one arbitrary minimum, say $\Phi_1 = v$ and $\Phi_2 = 0$ and expand \mathcal{L} around this minimum with two new fields η and ξ

$$\Phi(x) = \sqrt{\frac{1}{2}} \{v + \eta(x) + i\xi(x)\}. \quad (4.18)$$

This translation of the field to one arbitrary minimum spontaneously breaks the symmetry of the Lagrangian. Substitution of Eq. (4.18) into Eq. (4.16) yields

$$\mathcal{L} = \frac{1}{2}(\partial_\mu \xi)^2 + \frac{1}{2}(\partial_\mu \eta)^2 + \mu^2 \eta^2 + \text{const.} + \text{higher terms.} \quad (4.19)$$

Even though this Lagrangian describes the same physics as the original one, it has a field η with a mass term μ^2 . If compared to the familiar Klein Gordon equation, the mass of the particle described by η is $m_\eta = \sqrt{-2\mu^2}$. Unfortunately a second field ξ is also present which describes a massless particle. By the attempt of generating a massive boson by spontaneous symmetry breaking we also got an unwanted massless gauge boson, the so called *Goldstone Boson*. A hint for a solution to this problem can be seen if we choose the gauge symmetry to be local instead of global.

Higgs Mechanism for a Local U(1) Symmetry

If the Lagrangian in Eq. (4.14) shall be invariant under a local gauge transformation like $\Phi \rightarrow e^{i\alpha(x)}\Phi$, the derivative ∂_μ has to be replaced by the covariant form D_μ

$$\partial_\mu \rightarrow D_\mu = \partial_\mu - ieA_\mu \quad (4.20)$$

and the gauge field A_μ by

$$A_\mu \rightarrow A_\mu + \frac{1}{e}\partial_\mu\alpha(x). \quad (4.21)$$

The gauge invariant Lagrangian then becomes

$$\mathcal{L} = (\partial^\mu + ieA^\mu)\Phi^*(\partial_\mu - ieA_\mu)\Phi - \mu^2\Phi^*\Phi - \lambda(\Phi^*\Phi)^2 - \frac{1}{4}F_{\mu\nu}F^{\mu\nu}. \quad (4.22)$$

With the same procedure as before a massless Goldstone particle enters the scene. This time, however, an unusual off-diagonal term $A_\mu\partial_\mu\xi$ appears which gives a hint that not all fields which appear in \mathcal{L} give rise to an observable particle. Further on, the gauge boson A_μ acquires a mass $m_A = ev$, which means it can be polarised longitudinally as well and its degrees of freedom increase from 2 to 3.

With a different set of real fields (h, Θ), instead of (η, ξ), the field Φ is expanded around one minimum of the potential in Eq. (4.15)

$$\Phi = \sqrt{\frac{1}{2}}(v + h(x))e^{i\Theta(x)/v}. \quad (4.23)$$

This and an additional transformation of the gauge field are substituted

$$A_\mu \rightarrow A_\mu + \frac{1}{ev}\partial_\mu\Theta \quad (4.24)$$

into the original Lagrangian of Eq. (4.22) and lead to

$$\mathcal{L} = \frac{1}{2}(\partial_\mu h)^2 - \lambda v^2 h^2 + \frac{1}{2}e^2 v^2 A_\mu^2 + (\text{h - selfint.}) + (\text{hA - higher order}). \quad (4.25)$$

At last, no Goldstone boson appears in this Lagrangian. It describes two massive particles, one gauge boson A_μ and the so called *Higgs boson* h . The Goldstone boson has been turned into the longitudinal polarisation of the massive particle A_μ .

Higgs Mechanism for Electro-Weak Theory

To generate the masses of W^\pm and Z^0 , the Higgs mechanism is applied on the $SU(2)_L \times U(1)_Y$ symmetry of electro-weak theory. The procedure is the same as presented in the preceding section, but more complicated in detail due to the more complex symmetry.

The basic potential is given by Eq. (4.14) with $\mu^2 < 0$ and $\lambda > 0$. Φ is a $SU(2)$ doublet of complex scalar fields

$$\Phi = \frac{1}{\sqrt{2}} \begin{pmatrix} \Phi_1 + i\Phi_2 \\ \Phi_3 + i\Phi_4 \end{pmatrix}. \quad (4.26)$$

This Φ is the original one used by Weinberg in 1967. The potential in Eq. (4.14) has minima at

$$\Phi_1^2 + \Phi_2^2 + \Phi_3^2 + \Phi_4^2 = -\frac{\mu^2}{\lambda} =: v^2. \quad (4.27)$$

The choice of a certain minimum Φ_0 is arbitrary since any will break the symmetry and create masses for the gauge bosons. Knowing that the photon is massless, Φ_0 is taken as

$$\Phi_0 = \frac{1}{\sqrt{2}} \begin{pmatrix} 0 \\ v \end{pmatrix}. \quad (4.28)$$

This choice breaks both symmetries $SU(2)_L$ and $U(1)_Y$, but leaves the subgroup $U(1)_{em}$ unbroken and therefore the corresponding gauge boson γ massless.

The masses of W^\pm and Z^0 are obtained by substituting Eq. (4.28) into the Lagrangian of electro-weak theory and come out as

$$\begin{aligned} M_\gamma &= 0 \\ M_{Z^0} &= \frac{1}{2}v\sqrt{g^2 + g'^2} \\ M_{W^\pm} &= \frac{1}{2}vg \end{aligned} \quad (4.29)$$

where v is called the vacuum expectation value of the Higgs boson.

With $v = 246$ GeV, $\sin(\theta_W)^2 = 0.2315$, $e = \sqrt{4\pi\alpha_{e.m.}(M_Z)}$, $\alpha_{e.m.}(M_Z) \approx 1/128$ and $e = g \sin(\theta_W) = g' \cos(\theta_W)$, numerical values for the masses are $M_{Z^0} \approx 91$ GeV/ c^2 and $M_{W^\pm} \approx 80$ GeV/ c^2 and hence there is a good agreement between experiment and masses predicted by the Higgs mechanism (see Table (4.4)). With this mechanism it is also possible to generate the masses of leptons and quarks [18]. However, it is also important to state that the Higgs mechanism gives mass to the particles but does not explain the hierarchy in masses between the families; or why there are three lepton and quark families at all.

	Z^0	W^\pm
Higgs	≈ 91 GeV/ c^2	≈ 80 GeV/ c^2
experiment	91.1875 ± 0.0021 GeV/ c^2	80.392 ± 0.029 GeV/ c^2

Table 4.4: Predicted and measured masses of electro-weak gauge bosons [20].

Since the Standard Model Higgs boson is a postulated particle and has not yet been discovered its properties are not all known. A big mystery is the mass of the Higgs boson itself. Experimental constraints at LEP2 set a lower limit at about 114 GeV/ c^2 , theoretical constraints set an upper limit at about 1 TeV. However, the SM only stays renormizable to the scale of grand unified theories ($M_{GUT} \sim 10^{16}$) if the Higgs mass is below 170 GeV/ c^2 [21]. If the Higgs mass is higher than 170 GeV/ c^2 then the SM is not a valid candidate for a grand unified theory because it does not remain perturbative up to the GUT scale. The production processes and decay branching ratios strongly depend on the actual Higgs mass and therefore many different potential discovery channels exist depending on the assumed mass of the Higgs boson.

Masses of Fermions and Cabibbo-Kobayashi-Maskawa Matrix

The masses of the fermions in the Standard Model can be generated by the same Higgs field which is used to generate masses of the electro-weak gauge bosons W^\pm and Z . However, the quark mass eigenstates are not the same as the weak eigenstates which couple to the weak gauge bosons. The Cabibbo-Kobayashi-Maskawa (CKM) matrix describes the mixing of quark mass eigenstates $|q\rangle$ and eigenstates of the weak interaction $|q'\rangle$. It is a 3×3 matrix which can be expressed by three real parameters and one complex phase. The relation of mass eigenstates to weak eigenstates is given by

$$\begin{pmatrix} V_{ud} & V_{us} & V_{ub} \\ V_{cd} & V_{cs} & V_{cb} \\ V_{td} & V_{ts} & V_{tb} \end{pmatrix} \begin{pmatrix} |d\rangle \\ |s\rangle \\ |b\rangle \end{pmatrix} = \begin{pmatrix} |d'\rangle \\ |s'\rangle \\ |b'\rangle \end{pmatrix}. \quad (4.30)$$

The transition probability for e.g. $u \rightarrow Wd$ is proportional to the squared matrix element $\propto |V_{ud}|^2$. Many precision measurements of the CKM matrix have been carried out and measurements are also planned at the LHC. Latest values of the elements of the CKM matrix are [22]

$$\begin{pmatrix} 0.97377 \pm 0.00027 & 0.2257 \pm 0.0021 & (4.31 \pm 0.3)10^{-3} \\ 0.23 \pm 0.011 & 0.957 \pm 0.017 \pm 0.093 & (41.6 \pm 0.6)10^{-3} \\ (7.4 \pm 0.8)10^{-3} & (40.6 \pm 2.7)10^{-3} & > 0.78 \end{pmatrix}. \quad (4.31)$$

Decays within one family like $u \rightarrow Wd$ happen very frequently while flavour changing transitions from one family to another are highly suppressed in the CKM matrix (off-diagonal terms). This is also the reason for the special lifetimes of hadrons containing b quarks and c quarks.

Decay of the SM Higgs Boson

The Higgs boson can decay directly into all possible massive particles. Through loop diagrams it can also decay into massless photons and gluons. Figure (4.1) shows two possible Feynman diagrams of Higgs boson decays: (a) direct decay of the Higgs boson into a pair of fermions, (b) possible Feynman diagram of a Higgs decay into a pair of photons via a top quark loop. The branching ratios of the most important decays are shown in Fig. (4.2) as a function of the Higgs mass. For a Higgs with mass below $120 \text{ GeV}/c^2$ the dominant decay channel is into a pair of b quarks. For masses over $120 \text{ GeV}/c^2$ a decay into two on-mass-shell W 's becomes kinematically accessible and this decay becomes the dominant channel. At a Higgs boson mass of about $180 \text{ GeV}/c^2$ the decay into $Z^0 Z^0$ becomes the second dominant decay channel. Its branching ratio is about half of that of the decay into $W^+ W^-$. Branching ratios of other decays are significantly smaller but are also of interest because they can have a clear signature in the final state and might be experimentally observable in gluon fusion channels. Among them are $H \rightarrow \gamma\gamma$ or $H \rightarrow \tau\tau$.

In the channel under consideration in this thesis the Higgs boson decays into a pair of b quarks. This decay will be looked at in more detail in the next paragraph. Details about other decay modes can be found in [23].

Decay $H \rightarrow b\bar{b}$

The branching ratio of the Higgs boson into fermions is directly proportional to their masses. The coupling to the top quark is the strongest. However, for Higgs masses below $2m_t$ the decay

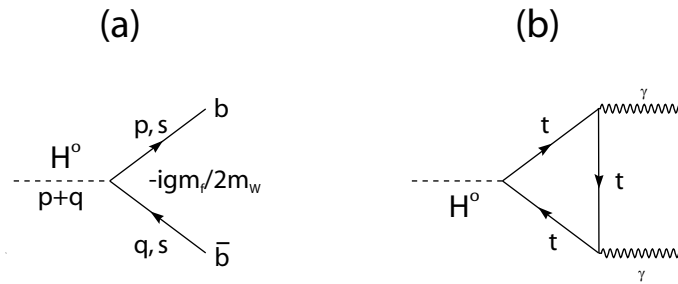


Figure 4.1: Feynman diagrams for two possible decays of the Higgs boson. (a) Decay into a pair of fermions with the Feynman rule for the vertex. (b) Decay into a pair of photons via a top quark loop.

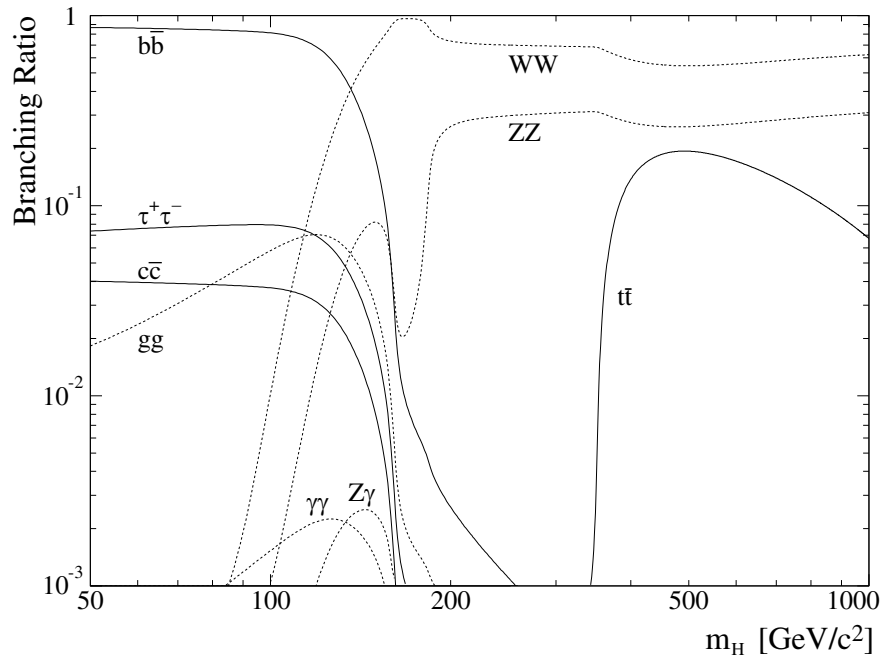


Figure 4.2: Branching ratios of the Higgs boson as a function of its mass. For masses below 120 GeV/c^2 $H \rightarrow b\bar{b}$ is the dominant decay process. For higher masses the decay into a W^+W^- pair becomes dominant.

into a pair of b quarks is the dominant decay channel to fermions. According to Fig. (4.1) the amplitude for this decay is

$$iM_{H \rightarrow f\bar{f}} = i \frac{gm_f}{2m_W} \bar{u}(p)v(q). \quad (4.32)$$

To calculate the decay width, the amplitude has to be squared and integrated over full space $d\Omega$. The result is

$$\Gamma_{H \rightarrow f\bar{f}} = \frac{N_c g^2 m_f^2 m_H}{32\pi m_W^2} \left(1 - \frac{4m_f^2}{m_H^2}\right)^{3/2} \quad (4.33)$$

where N_c is a colour factor which is 3 for quarks and 1 for leptons.

Equation (4.33) gives the decay width of the Higgs boson into fermions at lowest order. In the Higgs mass region of interest (around 120 GeV/c²) first order corrections are large (up to a factor of two reduction in the width) as shown in [24]. Remaining higher order corrections are estimated to be of the order of 5%. The high branching ratio to b quark pairs at lower Higgs mass makes this decay mode a very interesting one as we will see in the next section.

4.1.3 Strong Interactions - QCD

The strong interaction between quarks is described by *Quantum Chromo Dynamics* (QCD) [18]. In its basic concept it resembles QED, which means it is also a gauge theory. However, the underlying symmetry group is more complex and has properties which makes QCD very different from QED.

The QCD analogy to the QED electric charge is colour charge. Three types of colour charges exist: red, green and blue. The symmetry group is the non-Abelian group $SU(3)_C$. By requiring the QCD Lagrangian to be gauge invariant under a SU(3) transformation, 8(= 3² - 1) gauge fields need to be introduced. They are referred to as gluons, and since SU(3) is non-Abelian, quarks *and* gluons carry colour charge.

The Lagrangian of QCD is

$$\mathcal{L}_{QCD} = \bar{q}(i\gamma^\mu \partial_\mu - m)q - g(\bar{q}\gamma^\mu T_a q)G_\mu^a - \frac{1}{4}G_{\mu\nu}^a G_a^{\mu\nu} \quad (4.34)$$

with g the coupling constant, T_a the generators of SU(3) and G_a the eight colour fields (gluons). The last term stands for gluon self interaction. This becomes more clear if the Lagrangian is rewritten with

$$G_{\mu\nu}^a = \partial_\mu G_\nu^a - \partial_\nu G_\mu^a - gf_{abc}G_\mu^b G_\nu^c \quad (4.35)$$

in a more symbolic way (see also Fig. (4.3))

$$\mathcal{L}_{QCD} = \bar{q}q + G^2 + g \cdot \bar{q}qG + g \cdot G^3 + g^2 \cdot G^4. \quad (4.36)$$

The first three terms, free quark/gluon propagation and quark-gluon interaction, have QED analogies. The three- and four-gluon vertices reflect the fact that gluons themselves carry colour charge.

This has a deep impact on the behaviour of quarks and gluons. As long as the particles are close together (high Q^2), they hardly feel the strong force because the coupling constant

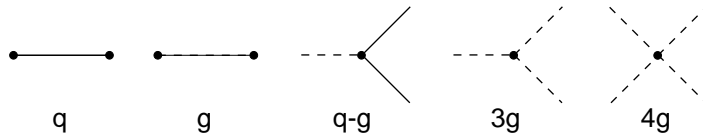


Figure 4.3: Schematic representation of the contributions to the QCD Lagrangian. From left to right: quark and gluon propagator, q-g vertex and 3g/4g self-coupling.

α_S is small ($\alpha_s(Q^2 = M_Z^2) = 0.12$) and it is possible to compute colour interactions using the perturbative techniques familiar from QED. At larger distances, however, α_S becomes bigger ($\alpha_s \approx 1$) and perturbation theory fails at all or becomes too complicated and elaborate for practical use. This behaviour is called *asymptotic freedom* and is a necessary attribute for confinement of the quarks.

Due to the confinement it is not possible to observe a single quark/gluon. Only colourless formations of quarks are observed: mesons ($q\bar{q}$), baryons (qqq) and anti-baryons ($\bar{q}\bar{q}\bar{q}$).

In leading order the dependence of α_S on the energy scale Q^2 of a process is

$$\alpha_S(Q^2) = \frac{12\pi}{(33 - 2n_f) \log(Q^2/\Lambda^2)} \quad (4.37)$$

where n_f is the number of flavours which are kinematically accessible. α_S is small as long as Q is large compared to Λ and gets large when Q is of the order of Λ . The scale Λ can be seen as marking a boundary between quasi-free quarks/gluons and the world of hadrons. It is a free parameter of QCD to be determined by experiment ($\Lambda = 217 \pm 25$ MeV [22]).

When simulating physical processes such as the associated production of a Higgs boson with a $t\bar{t}$ pair as shown in Fig. (4.4), the QCD behaviour of confinement and asymptotic freedom causes computational problems not known from QED or weak processes in the final state of the event. The transition of final state quarks and gluons to the final colourless hadrons (also known as fragmentation and/or hadronisation) has to be artificially divided into two regimes, namely the perturbative region (see 4.4b), where quarks and gluons can be treated as free particles and perturbative calculations can be used, and the non-perturbative region (see 4.4c), where the strong force gets *really* strong and starts to bind the partons into colourless hadrons.

In contrary to lepton colliders, the initial state of a proton-proton collider is described by QCD and is not very well known. The protons are made up of three quarks each (uud) and the actual deep inelastic process arises mostly from the collision of two gluons which are radiated off the quarks inside the protons. Knowledge of the structure functions of the quarks and gluons inside the protons is therefore important to describe the initial state.

In this thesis, the final state of the $t\bar{t}H$ channel is of interest. The transition from the regime of perturbative processes after the initial gluon-gluon hard interaction to the final state/observable hadrons can be described in four consecutive phases:

- (a) Split of two gluons from the proton-proton collision into $t\bar{t}$ with subsequent annihilation of two top quarks into the Higgs boson and decay of the other two t quarks into Wb .
- (b) Fragmentation (perturbative region): radiation of gluons from the primary quark pair, gluon splitting. This process is mostly described by perturbative theory (matrix element calculations) or by parton shower models.

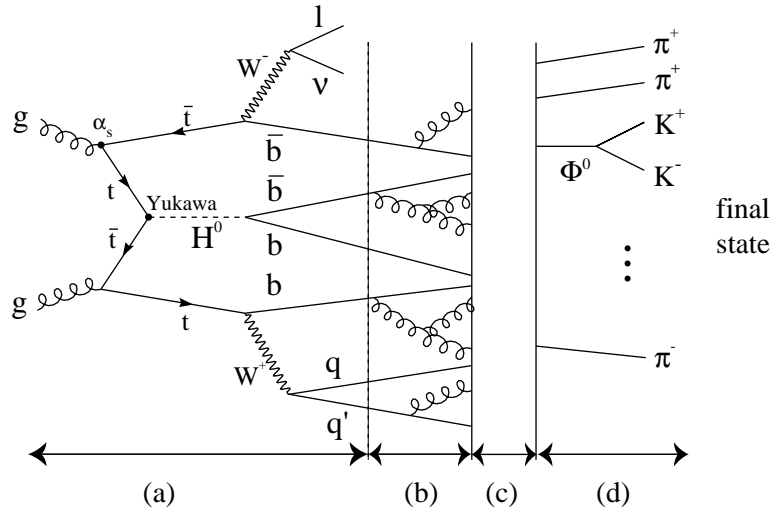


Figure 4.4: Schematic representation of the process $t\bar{t}H^0(120), H^0(120) \rightarrow b\bar{b}$.

(c) Fragmentation (non-perturbative region): transition of partons (i.e. quarks and gluons) into colourless hadrons. This process is still not very well understood in the Standard Model and can only be described by phenomenological theories.

(d) Decay of short lived particles. This is also well described by the Standard Model.

In the next two sections common approaches to simulate the perturbative and non-perturbative regions of the fragmentation process are discussed.

Fragmentation: Perturbative Region

The principle of perturbation theory is to express a physical quantity T (i.e. a solution to an equation which cannot be solved exactly) in terms of a power expansion in a small parameter. The QED coupling constant $\alpha_{e.m.}(M_Z^2) \simeq 1/128$ of QED is a good example. The (approximated) solution is then given by

$$T(\alpha) = T_0 + \alpha T_1 + \frac{\alpha^2}{2} T_2 + \dots \quad (4.38)$$

If α is small compared to unity the series might converge rapidly and already the first term only is a very good approximation of the real solution.

Two QCD motivated common methods are in use to simulate the perturbative region:

(i) Matrix Element Method

The matrix element method [25] is based on exact calculations of Feynman diagrams to fixed order of perturbation theory. As an example one can look at Fig. (4.5) which shows the process $Z^0 \rightarrow \text{hadrons}$ which was a very important process at LEP. The physical vertex is made up of a sum of perturbative orders which start from the basic process $Z^0 \rightarrow q\bar{q}$ and add higher order

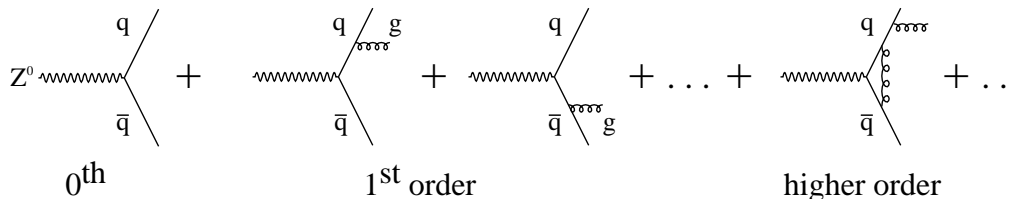


Figure 4.5: The physical vertex as a sum of the perturbative orders.

corrections to it. For the total cross section of $Z^0 \rightarrow \text{hadrons}$ in terms of a perturbation series in α_S this means

$$\sigma = \sigma_0 \left(1 + \frac{\alpha_S}{\pi} + \dots \right) \quad (4.39)$$

Since the matrix element method cannot be calculated to all orders of perturbation theory other models have been developed to simulate the fragmentation process. A quite successful one which is also used for the generation of simulated events in this thesis is the parton shower model.

(ii) Parton Shower Model

The parton shower model [25] is a different approach to simulate the perturbative region of fragmentation. It is simulated by a successive (independent) branching of partons, starting from the primary pair. The basic structure of the shower is made up by three branching processes: $q \rightarrow qg$, $g \rightarrow gg$ and $g \rightarrow q\bar{q}$. Each process is characterised by the so called Altarelli-Parisi splitting kernels

$$\begin{aligned} P_{q \rightarrow qg} &= C_F \frac{1+z^2}{1-z} \\ P_{g \rightarrow gg} &= C_A \left(\frac{z}{1-z} + \frac{1-z}{z} + z(1-z) \right) \\ P_{g \rightarrow q\bar{q}} &= \frac{n_f}{2} (z^2 + (1-z)^2). \end{aligned} \quad (4.40)$$

The branching rate is proportional to $\int P_{1 \rightarrow 23}(z) dz$. The z value of the branching describes the energy sharing among daughter partons 2 and 3. Parton 2 gets a fraction z of the mother energy, parton 3 gets $(1-z)$. The two daughter partons can then split again, and so on. The splitting to c or b quarks in terms of the energy distribution is quite different than for light quarks resulting in more energetic c or b quarks than light quarks. This causes, as will be shown in section 9.5.3, the energy fraction in the secondary vertex of a b jet to be substantially higher than in a light jet. With this parton shower higher orders in α_S can be simulated. In addition to z , each parton is characterised by a virtuality scale Q^2 , where the very first parton in the shower has a virtuality of Q_{max} . In final state showers, Q^2 decreases at each branching (see Fig. (4.6)).

In PYTHIA, Q^2 is associated with m^2 of the branching parton. Starting from Q_{max} , the first parton evolves down in Q^2 until a branching occurs. The selected Q^2 defines the mass of the branching parton, and the z of the splitting kernel the energy sharing among the daughters. These daughters also evolve down in Q^2 separately, where their starting virtuality scale

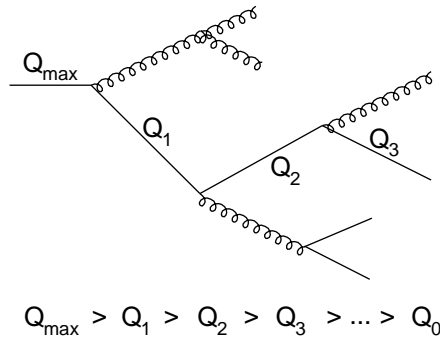


Figure 4.6: Parton cascade in the final state.

is given by kinematics. When Q reaches Q_0 the parton shower is stopped. From this point on perturbative calculations are no longer valid, due to the rise in α_S .

Often the matrix elements method is mixed with the parton shower model. The problem here is that the final partons of the matrix elements method have no virtuality anymore (i.e. they are on the mass shell). However, in the parton shower model the partons need to have a certain virtuality in order to split into two other partons. This virtuality has to be given to them artificially before the parton shower can take over after the matrix element method.

Fragmentation: Non-Perturbative Region

After the parton shower is stopped the set of coloured partons needs to be evolved into the final observable colourless hadrons. In this lower energy region α_S becomes larger (order of 1 or bigger) and the series 4.38 does not converge at all and a perturbative expansion of the solution is not possible. Since the underlying physics, i.e. QCD in the strongly interacting region, is not yet completely understood, several phenomenological models have been developed. Two of them are widely used: string fragmentation and cluster fragmentation. Only string fragmentation [25] will be discussed in the following since it is the default fragmentation model of the event generator PYTHIA used in this study.

The partons delivered by the parton shower are connected via a colour field due to the strong force. To explain the basics, consider an initial parton configuration made up of two quarks only. The string stretches from quark to antiquark. Coulomb forces are neglected and the approximation is made that the energy in the string increases linearly with the separation of the two quarks. The amount of energy per unit length of the string is $1 \frac{\text{GeV}}{fm}$. On further separation of the partons, energy increases and the string may break up into a new $q'\bar{q}'$ pair. The choice of flavour and energy/momentum sharing of the newly created partons is made by probabilistic functions. The quarks are created at the same point in space and separate from each other via quantum mechanical tunnelling. This sudden separation leaves them with free energy from the string between them which is used to give them transverse momenta and mass. The latter also explains the suppression of heavy quark production (b, t) in string fragmentation. The p_t of the final hadron is just a sum of the p_t of the quark constituents. After the breaking there are two new string pieces $q\bar{q}'$ and $q'\bar{q}$. Further breakups may occur if the invariant mass of the newly created string pieces is large enough. In the Lund string model [26] implemented

in PYTHIA, breakups occur until only on-mass-shell hadrons remain.

The treatment of a multi-parton configuration is complicated due to the number of string pieces moving in different directions and due to different possibilities to connect the partons. Calculable matrix elements of perturbative QCD contain interference terms between the possibilities and they are found to be down in magnitude by a factor $\frac{1}{N_c^2} = \frac{1}{9}$ [25]. Hence, approximations with no interference terms can be used.

Meson production is directly understood by this breaking of strings into lower energy pieces. Baryons, however, are made up of three quarks and the simple picture of $q\bar{q}$ string pieces does not lead to three quark colourless hadron production. Different models for baryon production are used, an overview is given in [25].

When the energy of the string pieces is too low for further breakups the (almost) final state of the simulation of the process of associated Higgs production is reached. The last step is the decay of resonances into *stable* particles.

At the end of this section it should be said that nature does not distinguish between the two steps (b) and (c) of Fig. (4.4). To handle the problem by means of a perturbative and then a non-perturbative approach is a purely artificial separation of the whole process. The boundaries between the regions are not fixed, but given by model parameters (Λ_{QCD}, Q_0) which need to be tuned to describe data. Many aspects of this process are not yet understood and therefore some observable effects are not reproduced by the simulation.

4.2 Physics at the LHC

With its high energy and luminosity the LHC covers a wide range of high energy physics measurements. This section gives an overview of physics measurements which will be done at the LHC using data from the ATLAS detector. A very detailed overview of the ATLAS physics program can be found in the ATLAS Physics TDR [13].

4.2.1 QCD Processes

Measurement of QCD processes at the LHC serve different purposes:

1. test of predictions from perturbative QCD and precision measurements of QCD variables
2. detailed understanding of QCD processes since they play an important role in many signal and background channels
3. understanding of the minimum bias collisions and the underlying event

Precision measurements of the important strong coupling constant α_S of QCD at different scales are planned as well as the measurement of parton probability density functions of e.g. the gluons in the protons and alike. Precise knowledge of these variables is also important for the understanding of many signal and background channels since QCD processes dominate the production cross section of almost all signal and background processes.

Another important role of QCD studies at the LHC is the understanding and correct simulation of so called minimum bias collisions. These minimum bias events come from inelastic proton-proton collisions that take place in the same bunch crossing as the interesting deep inelastic collision. They are not very well understood so far. However, at high luminosity

about 23 minimum bias proton-proton collisions will underlay the interesting signal event per bunch crossing. The influence of these events on the physics generator and the detector and reconstruction performance needs to be understood in detail. It needs to be stressed that minimum bias events are not to be confused with the so called underlying event. The latter is caused by the interaction among partons of the same two protons which cause the signal. Minimum bias collisions are additional proton-proton collisions which, in more general terms, make up or better *are* the so called *pile up*.

4.2.2 Electro-weak Gauge Bosons

Electro-weak gauge bosons will be vastly produced at the LHC. Measurements with Z^0 and W^\pm gauge bosons serve two main goals: additional constraints on the Higgs boson mass by a very precise measurement of the W^\pm mass and alignment and calibration of the detector using leptonic Z^0 decays.

As of today the W^\pm mass has been measured with a precision of 29 MeV [20]. The W^\pm mass itself is a free parameter of the Standard Model and is connected to other SM parameters like the electro-weak coupling constant α_{ew} , the Fermi constant G_F and the Weinberg angle $\sin\theta_W$. Via radiative corrections (which amount to 4% for the W^\pm mass) m_W also depends quadratically on the top mass m_t^2 and logarithmically on the mass of the Higgs boson $\log(m_H)$. This dependence sets a constraint on the Higgs boson mass if the top and the W^\pm masses are known very precisely. It is anticipated to measure the top mass at the LHC with a precision better than 2 GeV/c². This means that the W^\pm mass has to be known to ± 15 MeV otherwise it becomes the dominant error for the Higgs mass prediction.

The huge production rate of the Z^0 boson is very important for the calibration of the ATLAS detector. Calibration can be done by constraining the two measured leptons from a leptonic $Z^0 \rightarrow l^+l^-$ decay to the well known mass ($m_Z = 91.1874 \pm 0.0021$ GeV/c² [20]) of the Z^0 boson.

4.2.3 B-Physics

The production rate of B hadrons at the LHC is enormous and hence the ATLAS B-physics program covers a wide range of measurements. One major goal is the precision measurement of B hadron decays to test the Standard Model, in particular the Cabibbo-Kobayashi-Maskawa matrix. This matrix gives the transition probability of one quark type into another during an electro-weak process (e.g. $t \rightarrow Wb$). These studies involve precise measurements of CP violation in B meson decays, of flavour oscillations in the B_s^0 system and relative decay rates. Other studies involve the measurements of very rare B decays like $B \rightarrow \mu\mu\rho^0$ where indirect evidence for new physics could be seen.

4.2.4 Heavy Quarks and Leptons

The study of heavy quarks and leptons includes high precision measurements of the top quark and the search for a possible fourth generation of quarks and leptons.

The LHC is also a top quark factory with about 8 million top quark pairs per year. Precise measurement of top quark properties are important and interesting for various reasons. First the top quark is the only quark whose mass is at the electro-weak scale and hence can be used to probe electro-weak symmetry breaking and fermion mass generation. Secondly, the high precision of the top mass measurement (along with the W^\pm mass measurement - as discussed

in section 4.2.2) constrains the mass of the Standard Model Higgs boson and any new physics effects in electro-weak loops. As of today the top mass will be known as $171.4 \pm 2.1 \text{ GeV}/c^2$ [27] but it needs to be known to $\pm 2 \text{ GeV}/c^2$ to constrain the Higgs mass to a level of 30% (given that the W^\pm mass is known to $\pm 15 \text{ MeV}$ or better). Thirdly, detailed understanding of top quark production cross sections and decay channels is important because events stemming from top quarks in the final state are the dominant background in searches for new physics at the TeV scale.

4.2.5 Higgs Boson

The hunt for the yet undiscovered Higgs boson is the most important goal of the ATLAS experiment at the LHC. This section gives an overview of the Higgs boson production mechanisms at the LHC and the most promising Higgs boson discovery channels in ATLAS in the whole Higgs boson mass range.

Higgs Boson Production

There are four Higgs boson production mechanisms which are relevant at the LHC. The one with the highest cross section is the production via gluon fusion. Cross sections of other processes are by a factor of 10 to 100 smaller. However, three other mechanisms are still of great interest at the LHC because their production process leads to final states with advantageous signatures concerning triggering or background rejection, which the gluon fusion process does not have. These three processes are: vector boson fusion (VBF), associated production with a W^\pm or Z^0 boson and associated production with a $t\bar{t}$ pair. Figure (4.7) shows example Feynman diagrams for the four production mechanisms. In Fig. (4.8) the cross section as a function of the standard model Higgs boson mass is plotted. The direct production via gluon fusion is dominant over almost the whole mass range. VBF becomes competitive only for Higgs boson masses above $800 \text{ GeV}/c^2$.

Gluon Fusion The process of gluon fusion is shown in Fig. (4.7a). Since the coupling of the Higgs is proportional to the mass of a particle, the loop is dominated by the top quark. The cross section of this process can be calculated by knowledge of the decay $H \rightarrow gg$ and the gluon structure function. The cross section for $gg \rightarrow H$ is given by

$$\sigma(gg \rightarrow H) = \frac{8\pi^2 \Gamma_{H \rightarrow gg}}{N_g^2 m_H} \delta(S - m_H^2) \quad (4.41)$$

where S is the squared energy of the initial gluon pair and $N_g = 8$ (the number of different gluons). Since the two gluons are constituents of the colliding protons, Eq. (4.41) has to be integrated using the gluon structure function to obtain the total cross section

$$\sigma(pp \rightarrow H) = \int \int dx_1 dx_2 x_1 g(x_1, m_H^2) x_2 g(x_2, m_H^2) \sigma(gg \rightarrow H) \quad (4.42)$$

This is the cross section calculated in lowest order perturbation theory. The effect of higher order calculations is expressed as the so called K factor ($K := \frac{\sigma_{HO}}{\sigma_{LO}}$). In a next to leading order calculation it turns out that for gluon fusion the K factor is about 1.5 over the whole Higgs mass range [28].

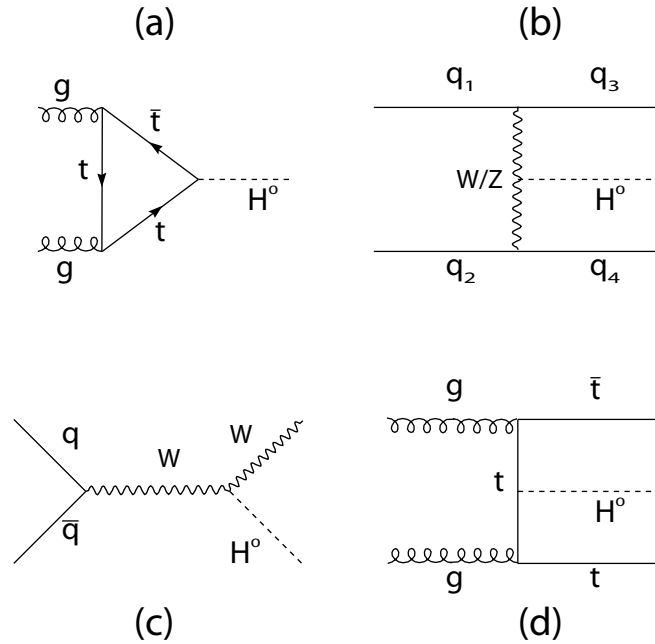


Figure 4.7: Feynman diagrams of the four relevant Higgs boson production channels at the LHC: (a) gluon fusion, (b) vector boson fusion (VBF), (c) associated production with a W or Z boson, (d) associated production with a $t\bar{t}$ pair.

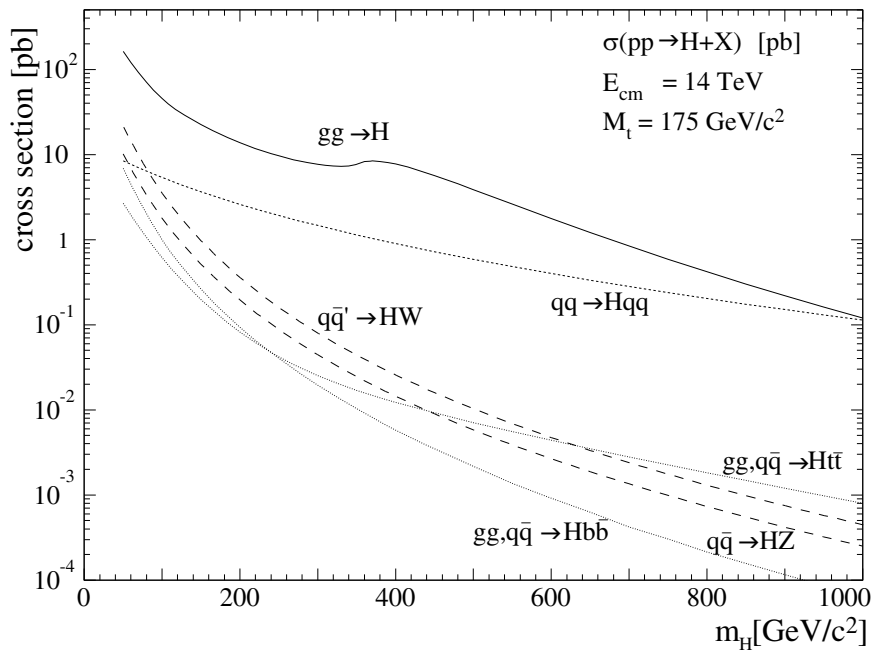


Figure 4.8: Cross sections of various Higgs boson production processes at the LHC as a function of the Higgs mass. Gluon fusion is the dominant Higgs production mechanism over the whole mass range. Only vector boson fusion production becomes competitive for a Higgs mass of more than 800 GeV/c^2 .

For this production channel it is important to state that its cross section is sensitive to the existence of a fourth generation of leptons and quarks. The coupling of the Higgs boson is proportional to the mass of the fermion in the loop of Fig. (4.7a). A heavy fourth generation quark would not be suppressed in this loop. The cross section of the gluon fusion process would increase by a factor of 2 to 4 (depending on the Higgs mass) if a fourth generation of fermions exists.

Vector Boson Fusion (VBF) Figure (4.7b) shows the production of a Higgs boson via vector boson fusion. The Higgs boson is produced via fusion of two W^\pm or two Z^0 bosons which were radiated off by incoming quarks. If a heavy Higgs is created, the vector bosons act essentially as massless particles and hence can be treated as constituents of the colliding protons rather than as being radiated off quarks inside the proton. This way it is possible to separate the cross section calculation similar to the gluon fusion process into production of the Higgs in the collision of two incoming particles (the vector bosons) and the usage of the vector boson structure functions inside the protons. This approach is called the effective W approximation.

The production cross section turns out to be always about a factor of 10 smaller than for gluon fusion. It becomes competitive to gluon fusion for Higgs boson masses above $800 \text{ GeV}/c^2$. This production mode nevertheless is of interest because it will always have the signature of two high p_t jets in the forward region and little jet activity apart from the Higgs decay in the central region of the detector.

Associated Production with a W^\pm or Z^0 Boson Figure (4.7c) shows the associated production of a Higgs boson with a W^\pm or Z^0 vector boson. The cross section of associated production is compatible to the VBF production for low Higgs masses around $100 \text{ GeV}/c^2$ but then drops rapidly as the mass of the Higgs increases and becomes about 2 orders of magnitude smaller than production via VBF. Associated production with a vector boson can still be of interest since the possible presence of a lepton with high transverse momentum in the final state from the decay of the W^\pm or Z^0 gives a good trigger signature.

Associated Production with a $t\bar{t}$ pair Figure (4.7d) shows one possible Feynman graph of the associated production of a Higgs boson with a $t\bar{t}$ pair. This production mechanism is the one of interest in this thesis. This production mode also leads to final states with a special signature which makes it still possible to extract the signal from the overwhelming QCD background despite the small production cross section. The final state of interest contains 2 b jets from the $t \rightarrow Wb$ decay (which has a branching ratio of more than 99% [22]) and requires at least one W^\pm to decay semileptonically to have a high p_t lepton for triggering.

The lowest order calculation of the cross section already involves 10 Feynman diagrams (Fig. (4.9) shows a subset) and hence it is rather complex and no detailed derivative is given here. It was first calculated by Kunszt [29] in 1984, more details can also be found in [30]. The production cross section is comparable to the associated production with a vector boson.

Potential Discovery Channels

At LHC several combinations of Higgs boson production and decay modes can lead to a potential Higgs boson discovery channel. This section gives an overview of possible discovery channels

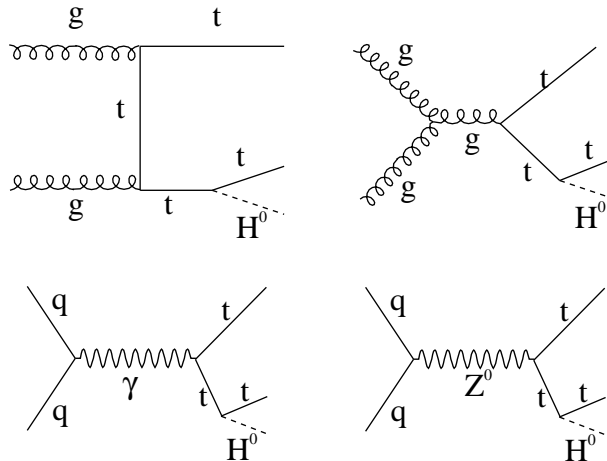


Figure 4.9: A subset of Feynman diagrams for the $t\bar{t}H$ channel.

and emphasises on the first few years of low luminosity data taking with an expected integrated luminosity of 30 fb^{-1} .

The discovery potential of a certain channel depends strongly on the Higgs boson mass itself. Therefore the discovery potential of the Higgs boson in the ATLAS detector is split into several mass ranges starting from the lower exclusive bound of $114 \text{ GeV}/c^2$ (which was set by LEP2) up to the upper bound of about 1 TeV which is set by theoretical constraints. Figure (4.10) shows potential discovery channels and their significances in the ATLAS detector as a function of the Higgs mass.

For a Higgs mass between $110\text{-}130 \text{ GeV}/c^2$ the decay into a pair of bottom quarks is dominant. A Higgs boson which was produced via gluon fusion and decays into $b\bar{b}$, however, cannot be detected because the overwhelmingly large QCD two jet background cannot be separated from the signal and consequently there is no trigger condition for this channel. Associated production via a W or Z boson with subsequent decay into $b\bar{b}$ has a trigger lepton from the vector boson decay. However, also in this channel the jet background (e.g. Z +jets, W +jets) is too large and the signal cannot be separated sufficiently well from the background. The channel significance was found to be less than 2σ [31]. The cross section of associated production with a $t\bar{t}$ pair is comparable to the associated production with a W or Z vector boson. The $t\bar{t}H$ final state, however, can be better separated from the background because (in addition to a trigger lepton) four jets tagged as b jets are required. The channel is especially interesting for a Higgs mass close to the direct lower limit and it reaches the 5σ discovery limit as shown in [32].

Another channel which is taken into consideration as a discovery channel for a light Higgs boson is the decay of the Higgs into two photons. The branching ratio for this decay is only about $1/1000$ but since the channel has a quite unique signature it is possible to observe it in direct production (gluon fusion). Even before combination with other channels the $H \rightarrow \gamma\gamma$ channel reaches a maximum significance of about 4σ [31]. This channel needs very good energy and angular resolutions in the electromagnetic calorimeter.

The intermediate mass region ($130 - 180 \text{ GeV}/c^2$) is covered by VBF production with subsequent decay into W^+W^- or gluon fusion with decays $H \rightarrow ZZ^* \rightarrow 4l$ and $H \rightarrow WW^* \rightarrow l\nu l\nu$.

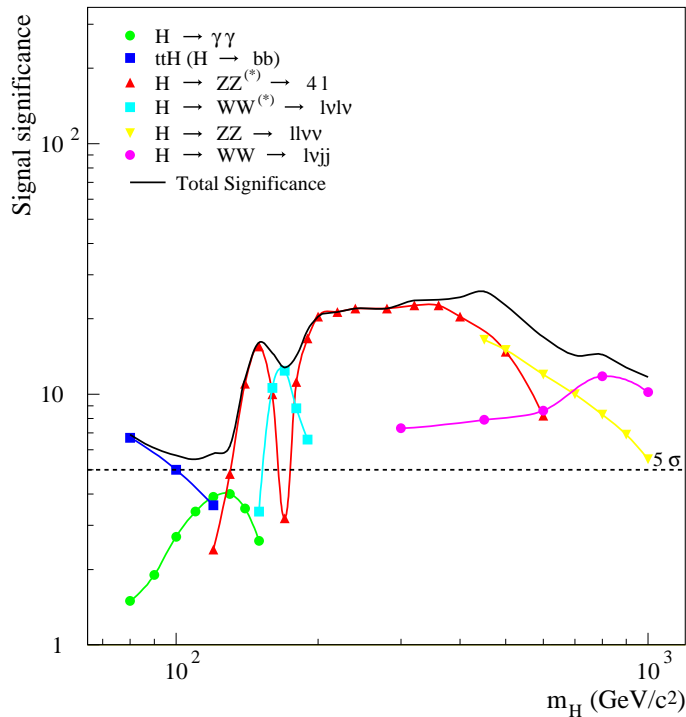


Figure 4.10: Discovery potential of various Higgs channels for an integrated luminosity of 30 fb^{-1} at the ATLAS detector [31].

The VBF channels are characterised by two opposite jets in the forward region with high transverse momentum. They stem from the original quarks that radiate the vector bosons. In addition there is only little jet activity in the central region because of the lack of colour exchange between the quarks [33]. It is shown in [33] that the VBF channels have a discovery significance above 5σ in this intermediate mass range.

When the Higgs boson mass is higher than $180 \text{ GeV}/c^2$ the decay into two on-shell Z^0 bosons becomes accessible. The subsequent decay of the two Z 's into four leptons with high transverse momentum is the "Golden Higgs Discovery Channel" of the LHC. Four isolated leptons with large transverse momentum in the final state can be easily triggered on and separated from the large QCD background. This channel has the highest significance of all channels at the LHC and stays above 10σ for a Higgs mass up to $500 \text{ GeV}/c^2$. The decay width of the Higgs boson increases rapidly with its mass and for $m_H > 300 \text{ GeV}/c^2$ the width starts to dominate the experimental resolution. This sets a Higgs discovery limit for the 4 lepton channel to a Higgs boson mass of $800 \text{ GeV}/c^2$. Above this the signal rate is too low and other decay channels of the Z pair have to be taken into consideration. One of them is the decay into $ll\nu\nu$ which has a rate 6 times larger than the four lepton one. Still others are $lljj$ (25 times larger) or if a pair of W 's is produced a decay into $l\nu\nu jj$ (150 times larger). All these channels are more difficult to reconstruct and to separate from the background. In this mass range the production via vector boson fusion becomes comparable to the gluon fusion and also contributes to the discovery of the Higgs boson.

In total, for an integrated luminosity of 30 fb^{-1} , the full Higgs mass range can be covered

by ATLAS with a significance exceeding 5σ [31, 33] (see also Fig. 4.10). It is also foreseen that the results of ATLAS and CMS will be combined to achieve the 5σ confidence level with less integrated luminosity,

4.2.6 Super Symmetry and Beyond

Super Symmetry is an extension of the Standard Model which tries to overcome some of its shortcomings. Super Symmetry - or short SUSY - introduces a new symmetry which relates bosons to fermions and vice versa. This symmetry is called *supersymmetry* and gives every lepton, quark and gauge boson a supersymmetric partner. Supersymmetric leptons are called sleptons and supersymmetric quarks are called squarks. The yet unobserved SUSY partners of the SM particles must act on a completely different mass scale and hence Super Symmetry is a broken symmetry as well. The number of new particles which are introduced by the new symmetry depends on the underlying supersymmetric model. The most common one - the "Minimal SUSY Standard Model" (MSSM) is discussed here. A general introduction to SUSY theories, including MSSM, can be found in [34].

In SUSY theories no spontaneous symmetry breaking of the Lagrangian is possible with only one Higgs doublet. The reason for that is that the SUSY partner to the Higgs boson (the Higgsino) introduces gauge anomalies. These gauge anomalies can only be resolved with an additional Higgs doublet leading to 5 Higgs bosons plus SUSY partners in the MSSM Table (4.5).

Quarks (u, d, c, s, t, b)	Leptons (e, μ , τ)	Neutrinos (ν_e , ν_μ , ν_τ)	g	W $^\pm$, H $^\pm$	γ , Z 0 , h 0 , H 0	A 0
(\tilde{u} , \tilde{d} , \tilde{c} , \tilde{s} , \tilde{t} , \tilde{b})	(\tilde{e} , $\tilde{\mu}$, $\tilde{\tau}$)	($\tilde{\nu}_e$, $\tilde{\nu}_\mu$, $\tilde{\nu}_\tau$)	\tilde{g}	\tilde{W}^\pm , \tilde{H}^\pm	$\tilde{\gamma}$, \tilde{Z}^0 , \tilde{h}^0 , \tilde{H}^0	\tilde{A}^0

Table 4.5: Standard Model particles (upper row) and supersymmetric partners (lower row) in the Minimal Supersymmetric Standard Model. There are counterparts to each SM quark and lepton. The partners to the charged gauge bosons and to the charged Higgs bosons are called charginos $\chi_{1,2}^\pm$. The partners of the neutral gauge bosons and the CP-even Higgs bosons are called neutralinos $\chi_{1,2,3,4}^0$.

The MSSM introduces yet another new symmetry: R-parity which is defined as

$$R := (-1)^{3B+L+2S} \quad (4.43)$$

where B is the baryon number, L the lepton number and S the spin. Standard Model particles all have an even, MSSM particles an odd value of R. The R quantum number conservation was originally introduced to prohibit the decay of the proton. However, it has some implications on the phenomenology of the theory:

1. SUSY particles are only produced in pairs;
2. a decay of a SUSY particle always results in an odd number of SUSY particles in the decay channel;
3. a stable lightest SUSY particle exists.

The advantage of Super Symmetry is that it overcomes some shortcomings of the Standard Model. For example, SUSY does not need any fine tuning to keep the Higgs mass on the scale of electro-weak interactions. It unifies the gauge couplings at a scale close to the Plank scale and SUSY theories lead to a particle which is similar to the Graviton and hence points the way to a Grand Unified Theory. Another big advantage of the R-parity conserving SUSY theories is that if the lightest stable particle (LSP) is electrically neutral it can be a candidate to make up the dark matter in the universe. However, it is not a must that R-parity is conserved and in the most general SUSY theories this is in fact not the case. At LEP and also at HERA studies were done to search for R-parity violating decays [35, 36].

Unconstrained SUSY theories (including MSSM) have more than 100 free parameters and an experimental scan over the whole parameter space is impossible. SUSY breaking scenarios like GMSB (Gauge Mediated Supersymmetry Breaking) [37] or mSUGRA (minimal Super Gravity) [38] have less parameters. Only a few scenarios with a reduced number of parameters have been studied in detail in ATLAS (see e.g. the ATLAS TDR [31]). Decays which involve SUSY particles have some special characteristics: high amount of missing energy due to the lightest SUSY particle which does not interact with the detector, leptons with high transverse momenta, lepton pairs with same charge in the final state and spherical events. It was shown that the ATLAS detector at the LHC is sensitive to supersymmetric extensions of the Standard Model up to a SUSY scale of 1 TeV.

The ATLAS detector is also designed to be sensitive to other conceivable new phenomena. Parts of the exciting physics program are tests of models which can generate masses for fermions and bosons without the need of a Higgs boson (Technicolor), search for extra dimensions, search for magnetic monopoles or the generation of mini black holes [31].

4.3 Characteristics of B Hadrons and b jet Topology

Jets stemming from b quarks play a central role in many analyses like the potential Higgs boson discovery channel $t\bar{t}H^0(120)$, $H^0(120)\rightarrow b\bar{b}$. b jets are also present in every analysis involving top quarks because the top quark almost exclusively decays into Wb ($> 99\%$ [22]). This section describes characteristics of b quarks and B hadrons which cause b jets to have a different topology than jets coming from lighter quarks or gluons and make it possible to separate b jets from others.

The b quark is the second heaviest known quark with a pole mass between 4 and 4.4 GeV/c^2 [22]. It will be produced in large numbers at the LHC via all sort of mechanisms (gluon splitting, top decay). Jets which come from b quarks will contain one or more B hadrons in their final state after fragmentation/hadronisation and it is the properties of some B hadrons which give b jets their special topology with a reconstructable secondary vertex and tracks with large impact parameters. The most important B hadrons are the B^\pm , B^0 and B_s mesons which decay via the electro-weak force and have lifetimes of the order of 10^{-12} seconds. The only hadrons with constituent quarks lighter than b's which have comparable lifetimes and therefore can fake the topology of b jets are hadrons containing c quarks (e.g. D mesons). Their lifetimes is in general about 1/3 to 2/3 of the ones of B mesons and they are hardest to separate from b jets in an analysis. Lifetimes of hadrons containing lighter quarks are either several orders of magnitude shorter or longer. In the first case the particles decay via the strong or electromagnetic force and the lifetime is of the order of 10^{-23} (10^{-16}) seconds. These particles decay

more or less instantly without travelling a measurable distance (e.g. π^0 , resonances). In the second case they decay, just like the B and D mesons, via the electro-weak force but have a very much longer lifetime of the order of 10^{-8} seconds. They therefore either decay very late (several meters away from the primary vertex) in the detector or can be regarded as stable, i.e. leave the detector before they decay. Kaons and π^\pm are prominent examples. The reason for the large (order 10^4) lifetime difference for light mesons and B/D mesons is found in the different weak process $q \rightarrow Wq'$ via which they decay. For a B^\pm meson, e.g., the decay $b \rightarrow Wt$ is kinematically not accessible and it decays through the suppressed channel $b \rightarrow Wc$ or Wu . The same is true for a meson containing s quarks where $s \rightarrow Wc$ is not accessible. In this case however the suppressed channel $s \rightarrow Wu$ has a very much smaller phase space compared to the suppressed $b \rightarrow Wc$ due to the smaller mass difference of s and u compared to b and c. Therefore mesons containing light s quarks live much longer than B/D mesons.

Another difference between light quarks and c/b quarks is their fragmentation function. In the fragmentation process b and c quarks (due to their higher masses) take a much larger energy fraction from the string than light quarks do. The produced B/D hadrons therefore carry a large amount of the jets' energy which gives the produced secondary vertex a different signature than that of (if any) secondary vertices in light jets.

Table 4.6 compares masses, lifetimes and decay length (in the laboratory frame) of B and D mesons as given in the latest issue of the Particle Data Group booklet [22].

meson	mass [MeV/c ²]	lifetime τ [10^{-12} s]	appr. decay length [mm]
B^\pm	5279.0 ± 0.5	1.638 ± 0.011	4.9
B^0	5279.4 ± 0.5	1.532 ± 0.009	4.6
B_s^0	5369.6 ± 2.4	1.466 ± 0.059	4.4
D^\pm	1869.3 ± 0.4	1.040 ± 0.007	3.1
D^0	1864.5 ± 0.4	0.4103 ± 0.0015	1.2

Table 4.6: Properties of B and D mesons [22]. The decay length is calculated assuming an average energy of the B(D)meson of 50(20) GeV yielding a relativistic γ factor of about 10 and a decay length in the laboratory frame of $l = \gamma c\tau$.

B (and often D) mesons therefore cause a jet topology consisting of a reconstructable secondary vertex which is several millimeters away from the primary one. The tracks which come from this secondary vertex also have a higher impact parameter with respect to the primary vertex. Another property of b jets is that they have more tracks on average compared to light jets (but not to gluon jets which usually have as many tracks - depending on the initial parton energy - but with softer spectrum). Figure (4.11) illustrates the different topologies of light jets and b jets using Atlantis [39, 40], a program to visualise events in the Atlas detector. The plot shows the $r\phi$ projection of a $t\bar{t}H$ event. Two b jets with a secondary vertex a few millimeters away from the primary vertex can clearly be identified. Tracks coming from these secondary vertices also have larger impact parameters than the ones from the primary vertex. In light jets there is nothing alike - no reconstructable secondary vertex and all tracks originate from the primary vertex region. This difference in topology between light and b jets is used to construct discriminating variables to separate them.

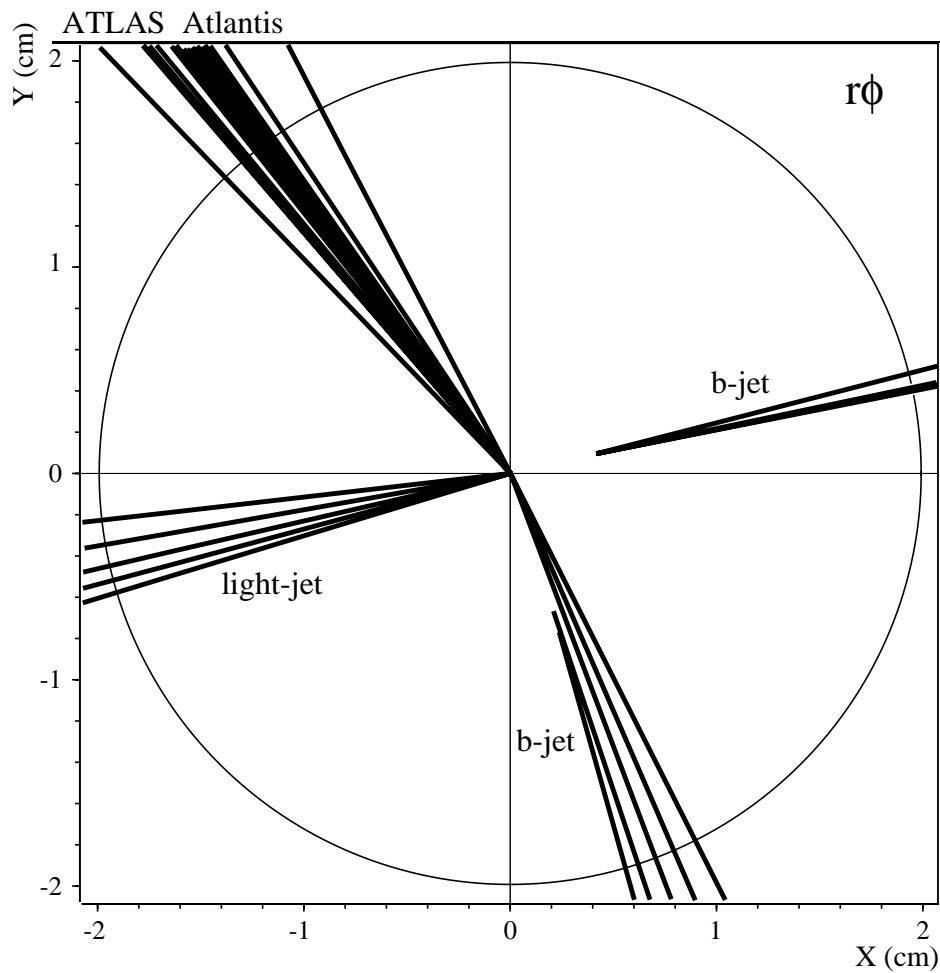


Figure 4.11: $r\phi$ projection of a $t\bar{t}H^0(120)$, $H^0(120)\rightarrow b\bar{b}$ event using the ATLAS event display Atlantis. In this event two b jets with a secondary vertex a few millimeters away from the primary vertex (simulated at the ATLAS origin) can clearly be identified. Jets which stem from light quarks have no such signature - all tracks are coming from the primary vertex. The track multiplicity in this plot is reduced for better visibility with a track cut of $p_t > 3$ GeV/c. The black circle denotes the beam pipe.

Chapter 5

Trigger Event Selection

At design luminosity two proton bunches will collide in the center of the ATLAS detector every 25 nanoseconds. With an anticipated event size of 1.5 megabyte this would imply a data flow of roughly 60 terabyte per second! It is the task of the Trigger and Data Acquisition Systems (TDAQ) to read out the detector and filter out those events which are thought to be of interest and store them on disk for later analysis. The trigger system is therefore a very crucial part of the ATLAS experiment because it exclusively decides which events are kept and which are lost forever. The physics events of interest in ATLAS are hereby defined by the ATLAS physics goals (see section 4.2) which put emphasis on the understanding of electro-weak symmetry breaking (i.e. discovery of the Higgs boson) and the search for new physics (e.g. Super Symmetry). Figure (5.1) shows cross sections for various processes in proton-proton collisions and the challenge of this selection task can be stressed with an example: The cross section for inelastic collisions is about 70 mb whereas the cross section for the Higgs discovery channels like $t\bar{t}H^0(120)$, $H^0(120)\rightarrow b\bar{b}$ is in the region of 0.1 pb (0.52 pb inclusive cross section times branching ratios 70% for $H\rightarrow b\bar{b}$ and 29% for $t\bar{t}\rightarrow l\nu bj\bar{j}b$, with $l = e^\pm$ or μ^\pm). This means that on average there will be one interesting $t\bar{t}H$ event in 660 million uninteresting events! Event selection strategies have to be tight enough to reduce the event rate accordingly but general enough not to lose these very rare physics events. This issue becomes particularly delicate in the search for new physics where appropriate trigger conditions might not be known. The general ATLAS trigger approach is

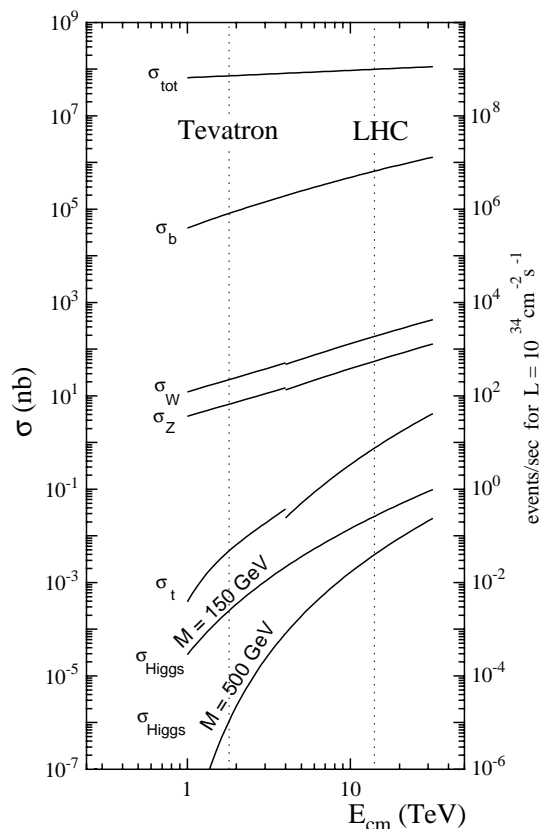


Figure 5.1: Cross section and rates for a luminosity of $10^{34}\text{cm}^{-2}\text{s}^{-1}$ for various processes in pp collisions as a function of the center of mass energy .

therefore to use very inclusive triggers on mainly high transverse energy/momentum deposits in the detectors (e.g. signatures from e^\pm , μ^\pm , photons, jets and similar with high transverse momentum) which define regions of interest (RoI) in the detector rather than very exclusive triggers which would look for special signatures of certain event types which would be suitable e.g. for pure B-physics studies.

This chapter gives an overview of the ATLAS trigger system putting emphasis on the performance of the electron/photon and the muon trigger. Both contribute a significant amount to the overall trigger rate. The performance of the e/γ trigger has been studied as part of this thesis. Results have been published in the HLT/TDAQ TDR [41] and are summarised in section 5.4.2. This work included the development of a ROOT [42] software framework to analyse the performance of the e/γ part of the trigger system. The framework is also presented in section 5.4.2. The muon and the e/γ triggers are equally important for the study of the potential Higgs discovery channel $t\bar{t}H^0(120)$, $H^0(120)\rightarrow b\bar{b}$. A semileptonic decay of one of the W's from the top decays into either $e^\pm\nu$ or $\mu^\pm\nu$ gives a good signature to trigger on. Relevant results from the High Level Trigger TDR for the muon trigger are therefore summarised at the end of this chapter.

5.1 Trigger Overview

The ATLAS Trigger system is shown in Fig. (5.2). It is split into 3 separate levels called Level 1 (LVL1), Level 2 (LVL2) and Event Filter (EF). The terminology further divides into triggers which only use information from certain subdetectors such as the LVL1Calo which is the Level 1 trigger that is purely based on information from the Calorimeter or the LVL2ID for Level 2 Inner Detector decisions. These levels consecutively lower the event rate with increasingly refined event selection cuts from the initial 40 MHz to an anticipated final output rate of 100 events per second. On each trigger level more processing time and event data is available than on the previous level to apply more sophisticated selection cuts, thus refining the selection strategy gradually. The LVL1 trigger has a maximum of $2.5\ \mu\text{s}$ per event to decide to delete it or to pass it on, LVL2 has 10 ms and the Event Filter has one second. Given the stringent time constraint, the LVL1 trigger is designed as a pure hardware trigger and it is directly integrated into the detector readout system. The data which comes out of the detectors' Read Out Drivers (ROD) has therefore already undergone a LVL1 event selection. The output of the RODs and the input to the read out buffers (ROB, where the data is stored until the LVL2 decision is made) marks the boundary of the detector read out system and the ATLAS High Level Trigger and Data Acquisition system (HLT/TDAQ) [41] of which the LVL2 and EF triggers are part. LVL2 and EF are software triggers and they are integrated in the ATLAS Athena framework.

The HLT/TDAQ system further consists of four major components:

1. Data Flow System
2. High Level Trigger (LVL2, EF)
3. Online System
4. Detector Control System (DCS)

The Data Flow System is responsible for event building and moving data from the detector RODs to the High Level Trigger system and also transports events which have finally been selected for mass storage. The HLT consists of the second and third trigger stage, LVL2 and

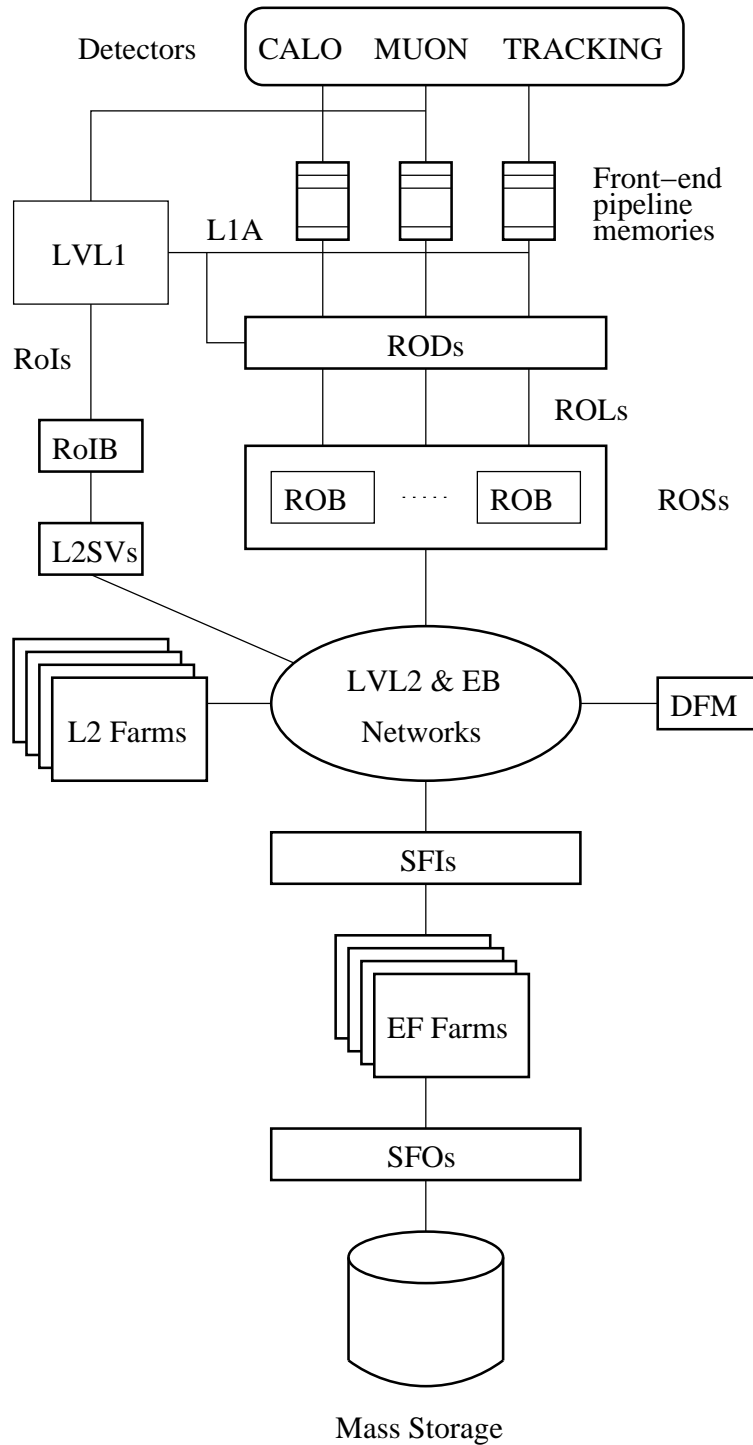


Figure 5.2: Overview of the trigger and data flow systems. Acronyms not mentioned in the text are: Read Out System (ROS), Read Out Link (ROL), Sub Farm Output (SFO) and Level 2 Super Visor (L2SV).

EF, respectively. The Online System is responsible for the control and monitoring of all trigger and data acquisition systems and the DCS monitors the safe and correct operation of the ATLAS detector. It also is the interface to external systems like the LHC.

5.2 Trigger Levels and Data Flow

The LVL1 trigger decisions are based on information from the calorimeter and the muon system. In the calorimeters the LVL1Calo trigger looks for regions which exceed a certain E_t threshold. The LVL1Muon trigger uses the muon trigger chambers, the RPCs in the barrel and TGCs in the endcaps (see section 3.5), to trigger on muons with low and high transverse momentum at 6 GeV/c and 20 GeV/c threshold, respectively. LVL1Calo and LVL1Muon send their information to the Central Trigger Processor (CTP) which draws the LVL1 trigger decision. If the event is accepted then all detector systems send their data to the Region of Interest Builder (RoIB) which prepares the data and passes it on to the second level trigger (LVL2). The LVL1 trigger reduces the initial event rate from 40 MHz to 75 kHz and from there on the HLT/TDAQ system takes over. The initial data flow from the LVL1 trigger to the read out buffers (ROBs) is about 160 gigabyte per second. The amount of data the LVL2 trigger has to look through to draw a decision is extremely reduced (to a few % of the whole event) by giving the LVL2 trigger Regions of Interest (RoIs) containing event fragments to look at. The data is stored for 10 ms in the ROBs and by looking only at the RoIs the LVL2 trigger can do more elaborate event selection strategies to draw a decision. In addition to the calorimeter and muon spectrometer, the LVL2 trigger can make use of tracking information from the Inner Detector. The LVL2 trigger also has the possibility to request additional event fragments which are not part of the LVL1 RoIs. The full event information is stored in fragments in the ROBs until the LVL2 decision has been made. If the event passes, the Data Flow Manager (DFM) initiates the building of the full event. This is done in the Sub Farm Input (SFI) of the EF which consists of the order of 100 ordinary PCs. The bandwidth of the LVL2 trigger into the event building farms is of the order of 5 GByte/s. When the event is built it is passed on to the Event Filter. Similar to the LVL2 the Event Filter receives regions of interests from the previous level. The Event Filter has about 1 second to draw a decision and does more elaborate selection cuts based on information from the whole event. In addition, the Event Filter does a first event classification and writes out different streams to facilitate offline reconstruction. The final output rate of the event filter has to be in the range 100 to 200 events per second resulting in a data flow of about 320 MB/s.

5.3 Selection Signatures and Trigger Menu

Trigger decisions are based on signatures in the detectors which are defined by the physics goals of the ATLAS experiment. For the ATLAS physics program the most important signatures of interesting physics events are high transverse energy deposits in the calorimeters or tracks with high transverse momentum in the tracking detectors. ATLAS defines a variety of these signatures for various physics objects including

- electron/positron with $|\eta| < 2.5$: very concentrated high E_t area in the calorimeter with a specific shower shape. At LVL2 and EF also a high p_t track in the Inner Detector.
- photon with $|\eta| < 2.5$: similar to electron but with no matching track in the Inner Detector.

- μ^\pm with $|\eta| < 2.4$: identified as a high p_t track in the muon spectrometer. Track match with Inner Detector possible but not necessary for decision.
- Jets with $|\eta|$ up to 4.9: identified as cluster in the calorimeter. Charged tracks from ID can be used for better identification.
- missing transverse energy E_t^{miss} and total energy $\sum E_T$: their definition will be based on full calorimeter information.

Selection signatures are combinations of one or more of these trigger conditions. For example the selection signature e25i which is used to trigger on semileptonic W decays or Z decay into electrons requires one isolated electron object with transverse momentum of 25 GeV/c or bigger. ATLAS uses various trigger signatures which consist of combinations of certain selection signatures such as the e25i one. A small list of selection criteria with emphasis on triggering on Higgs discovery channels is listed in Table (5.1). To trigger on the $t\bar{t}H$ channel the e25i and $\mu 20i$ are used.

Other trigger types are the prescaled physics triggers which extend the physics coverage of the ATLAS detector by extending the kinematic reach of various measurements toward smaller values (e.g. less p_t required). The exclusive physics triggers search for very special signatures of certain event types (e.g. for B-physics) and the monitor and calibration triggers are used for alignment and other issues. Another trigger type, especially for the beginning of data taking, is the minimum bias trigger. It uses two scintillator plates in the forward directions and triggers as soon as particle traverse both plates. This trigger is a very simple one which is meant to produce an un-biased data sample and basically just triggers as soon as a collision takes place in the detector. It will be used for timing studies but also to test other triggers because it can be checked later on if a more specialised trigger (on leptons with large transverse momentum for example) would have accepted some of these events.

Selection Signature	Example of Physics Coverage
e25i	$W \rightarrow e\nu, Z \rightarrow ee$, top production
$\mu 20i$	$W \rightarrow \mu\nu, Z \rightarrow \mu\mu$, top production
$2\gamma 20i$	$H \rightarrow \gamma\gamma$
$\tau 35i + xE46$	associated Higgs production with $H \rightarrow \tau\tau$

Table 5.1: Variety of selection signatures of the physics trigger with emphasis on triggers for Higgs boson discovery channels.

5.4 The e/γ Trigger

The e/γ trigger selects events with high p_t electrons and photons and is therefore very important to select $t\bar{t}H$ events where one W from the decay $t \rightarrow Wb$ decays into $e\nu$. The e/γ trigger contributes to a large fraction to the overall trigger rate at each level and is a very important trigger also for estimating the total costs of computing power needed for the trigger farms. It starts at the LVL1 trigger which looks for isolated clusters in the electromagnetic calorimeter above a certain E_t threshold (LVL1 Calo). The clusters also have to satisfy certain isolation criteria. Events which pass LVL1 are transferred along with regions of interest to LVL2.

LVL1	E25i	E30i
E_t (GeV) >	19	20
e.m. ring isol. (GeV) <	3	5
had. ring isol. (GeV) <	2	3
had. core isol. (GeV) <	2	2

Table 5.2: Selection cuts applied by LVL1 Calo.

LVL2		E25i	E30i
Calo	E_t (GeV) >	22.5	25.5
	R_η^{shape} >	0.90	0.90
	R_η^{strip} >	0.72	0.75
	E_t^{had} (GeV) <	1.0	2.2
ID	p_t^{track} (GeV/c) >	8	8

Table 5.3: Selection cuts applied by LVL2 Calo and LVL2 ID. R_η^{shape} and R_η^{strip} are variables which describe the shape of the shower produced by the incoming particle(s). Their purpose is to distinguish e/γ particles from jets.

LVL2 ID-Calo	e25i				e30i			
η -ranges	0.-1.	1.-1.5	1.5-2.	2.-	0.-1.	1.-1.5	1.5-2.	2.-
$ \Delta\Phi <$	0.035	0.035	0.030	0.025	0.05			
$ \Delta\eta <$	0.07	0.06	0.05	0.05	0.05			
$E_t/p_t \in$	[0.2,3.]		[0.2,3.5]		[0.2,4.]	[0.2,5.]	[0.2,7.]	

Table 5.4: Selection cuts applied by LVL2 ID-Calo.

EF		e25i	e30i
Calo	E_t (GeV) >	20	27
ID	# precision hits \geq	7	7
	# pixel hits \geq	1	2
	# B-layer hits \geq	1	1
	$a_0^{vert} <$	0.2	0.2
ID-Calo	if $\eta < 1.37 \rightarrow E_t/p_t \in$	[.8,1.3]	[.7,1.7]
	if $\eta \geq 1.37 \rightarrow E_t/p_t \in$	[.7,2.5]	[.7,2.7]
	$ \Delta\Phi <$	0.02	0.02
	$ \Delta\eta <$	0.01	0.01

Table 5.5: Selection cuts applied by EF Calo, ID and ID-Calo.

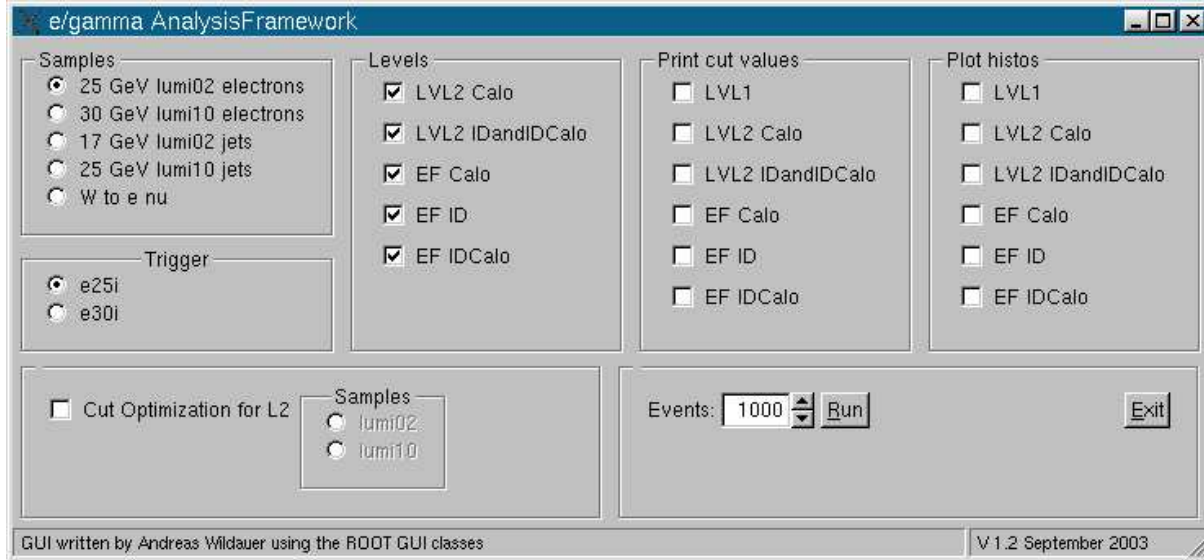


Figure 5.3: The graphical user interface of the e/γ analysis framework.

The LVL2 trigger looks at the LVL1 RoIs using the full granularity of the electromagnetic calorimeter. It can use a sharper E_t threshold and tighter isolation criteria. Shower shape variables in the calorimeter are used to distinguish between “electromagnetic” objects (electron, photon) and jets. The LVL2 trigger also uses tracking information from the Inner Detector. Tracks are reconstructed in the regions of interest with dedicated track finders which mainly use the two innermost detectors (Pixel and SCT). If an ID track matches to a calorimeter cluster the object is labelled an electron candidate and the event is passed on to the Event Filter along with regions of interest. The main difference between LVL2 and EF is that the EF has more time, can look at the event as a whole and better calibration data is available. The EF uses the same algorithms as the Athena offline software. Table (5.2) to Table (5.5) give an overview of the selection variables used at each level and their values for the e25i and e30i trigger menus.

5.4.1 The e/γ Framework

The e/γ framework [43] was developed to analyse the performance of the e/γ trigger and to produce results for the High Level Trigger Data Acquisition and Controls Technical Design Report [41]. It offers a graphical user interface Fig. (5.3) to activate/deactivate various trigger levels, to change the input set of simulated data, to set the number of events to run on and finally to run the trigger study. The output is a set of histograms of the selection variables as well as detailed selection efficiencies and rates after the different trigger steps. The framework was written in ROOT.

5.4.2 Results for the High Level Trigger TDR

The performance of the trigger is measured in terms of a selection efficiency, e.g. for electrons, and the expected event rate after the trigger. The efficiency is measured using truth information and the rate is estimated with di-jet events. For the e/γ studies, 25 GeV single electron events

Trigger Step	Rate [Hz]	Efficiency [%]
LVL1 Calo	12000	100
LVL2 Calo	2114±48	95.9±0.3
LVL2 ID-Calo	137±12	86.6±0.6
EF Calo	56±8	84.4±0.6
EF Calo-ID	30±5	79.0±0.7

Table 5.6: Rates and efficiencies for low luminosity single electron events ($p_t=25$ GeV/c).

have been generated and fully simulated. For more realism also $W \rightarrow e\nu$ processes have been generated with the electron having a transverse momentum of at least 25 GeV/c. For the results presented in the TDR the events were fed into the trigger simulation assuming the LHC runs at low luminosity ($L = 2 \times 10^{33} \text{ cm}^{-2} \text{ s}^{-1}$).

Table (5.6) shows results for the e/γ trigger as obtained by the e/γ framework. The efficiency after LVL1 is tuned to be 95% giving an event rate of ~ 12 kHz where the anticipated overall aimed event rate after LVL1 is ~ 75 kHz. The results for LVL2 and EF are split into two levels to see the influence of the calorimeter and track selection cuts. All LVL2 and EF efficiencies are given with respect to LVL1 (i.e. LVL1 = 100%). The errors on the rates are purely statistical. The rate after LVL2 is about 137 Hz which means a reduction from LVL1 by a factor of ~ 87 . The drop in efficiency from after LVL1 to after LVL2 is 13.4%. The Event Filter brings the rate down to 30 Hz with an efficiency of 79.0%. These results are in good agreement with earlier studies [31] and satisfy the anticipated requirement of 30 Hz output rate with 80% efficiency.

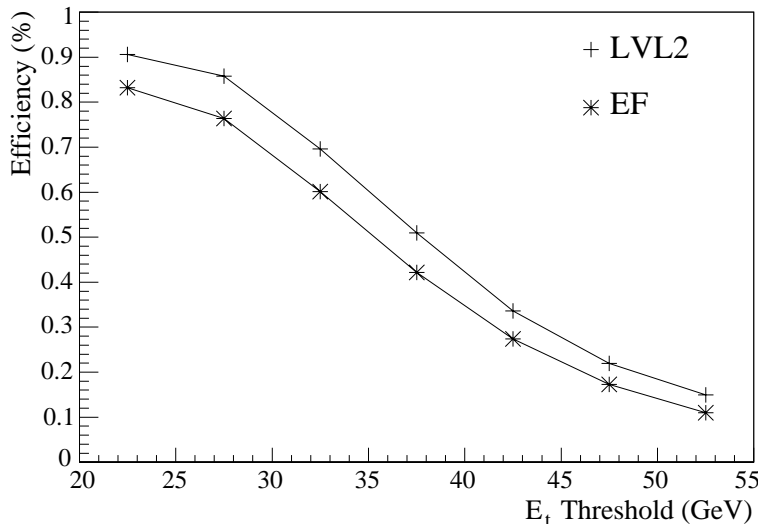


Figure 5.4: LVL2 and EF e^- selection efficiencies for $W \rightarrow e\nu$ samples as a function of the E_t threshold.

For cross checks selection efficiencies have also been studied with 10000 $W \rightarrow e\nu$ events using the same cuts as for the 25 GeV single muon samples. The efficiency is $90.6 \pm 0.8\%$ after LVL2 and $83.2 \pm 1.0\%$ after EF level. The better performance with respect to the single electron sample is due to the fact that only electrons from the W decay with at least 25 GeV/c transverse

momentum have been looked at. The impact of the E_t threshold on the selection efficiency has also been studied on the W sample. Figure (5.4) shows the selection efficiency as a function of the LVL2 and EF E_t thresholds.

For the HLT TDR a very preliminary study of efficiencies and rates at design luminosity of the LHC has been done. For a 30 GeV single electron sample the efficiency was 72% with a rate of 165 Hz. Because of software problems LVL2 was not activated.

Cut optimisation on LVL2 Calo

For the four cuts on LVL2 Calo (E_t , R_η^{shape} , R_η^{stripe} and E_t^{had}) a cut optimisation can be performed with the e/γ framework. The optimisation helps to choose an optimal set of cut values for a desired combination of efficiency and rate. Figure (5.5) shows a two dimensional plot of the efficiency versus rate. In general all points which are close to the upper left limit of the scatter plot are a good choice since they represent the maximum efficiency possible for a desired rate.

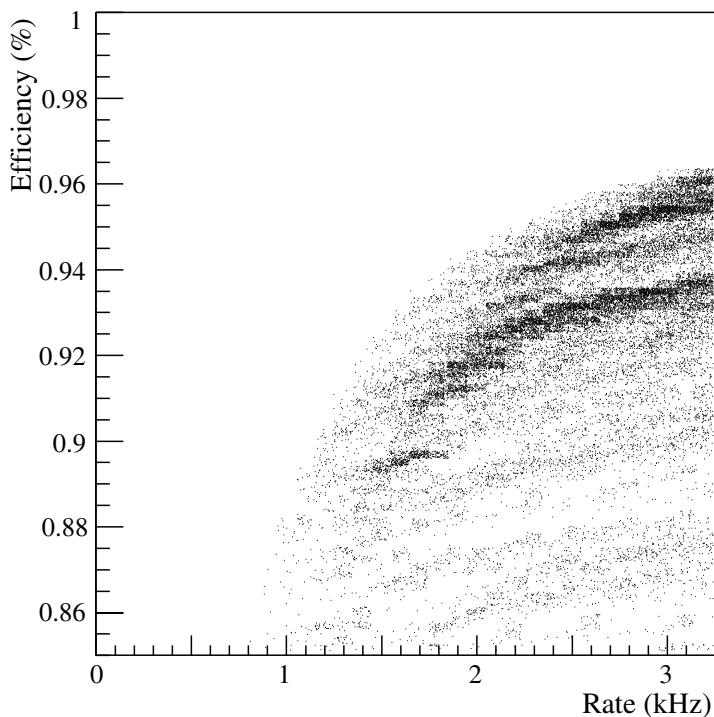


Figure 5.5: Efficiency vs. rate for the cut optimisation procedure on LVL2 Calo. Each point in the plot corresponds to the efficiency and rate of a certain set of selection cuts: E_t , R_η^{shape} , R_η^{stripe} and E_t^{had} .

5.5 The μ Trigger

The $\mu 20i$ trigger is the second trigger which is sensitive to $t\bar{t}H^0(120)$, $H^0(120) \rightarrow b\bar{b}$ events in case one W decays leptonically into $\mu\nu$. The stringent timing constraint at LVL1 ($< 2.5\mu s$) does not allow the use of elaborate tracking algorithms to trigger on muons and hence the LVL1

muon trigger uses a special fast approach without track reconstruction. In the barrel, the trigger starts from the hit in the middle one of the 3 RPC layers. It extrapolates the track to the vertex region in a straight line. Around the intersection point of this line with the inner most RPC layer a coincidence window is created. The muons are bent in the presence of the solenoid field and hence the size of this window is proportional to the trigger p_t threshold. Low (and high) p_t tracks have a measured hit in the inner most RPC layer which is inside this coincidence window. High p_t tracks in addition have a measured hit in the third layer which is inside its coincidence window. For the TGCs in the end caps the situation is similar.

After LVL1 the strategy of the μ trigger is similar to the e/γ trigger. With the guidance of the LVL1 RoIs it starts to reconstruct tracks in the muon spectrometer. Reconstructed muon tracks can be matched to an Inner Detector track or to energy clusters in the calorimeters which enhances the selection efficiency and the rejection power. As for the e/γ trigger, the difference between LVL2 and EF is the time available to process one event and the resulting possibility to use more refined algorithms with better calibration on EF level. The main sources of failure arise from secondary muons from Kaon or Pion decays which can fake an interesting physics event (e.g. can look like a muon coming from a W decay from the $t\bar{t}H$ process) and from fake muon tracks which arise from hits due to the cavern background. However, the probability that a fake muon that passed LVL1 also passes LVL2 is below 1% [41].

In general, sources of muons which need to be triggered on consist mainly of prompt muons from c, b and leptonic W decays where the latter are important for the $t\bar{t}H$ channel. The μ trigger is split into triggering on μ with low transverse momentum (around 6 GeV/c) and on μ with high transverse momentum (above 20 GeV/c). The first is important for B-physics studies and the latter is important for the $t\bar{t}H$ channel and will be looked at in a bit more detail. Table (5.7) shows trigger rates of the LVL1, LVL2 and EF muon trigger for high p_t (20 GeV/c) μ at high luminosity ($10^{34}cm^{-2}s^{-1}$). The rate after LVL1 is 1.9 kHz and 0.24 after LVL2. This means a reduction of a factor of 8. The efficiencies for the muon triggers are $\sim 83\%$ after LVL1, $\sim 96\%$ after LVL2 with respect to LVL1 and $\sim 98\%$ after EF with respect to LVL2 [44] giving an overall efficiency of 78% which is comparable to the e/γ trigger.

Physics Process	LVL1	LVL2	EF
π/K decays	0.97	0.07	0.054
b decays	0.65	0.1	0.077
c decays	0.28	0.04	0.030
$W \rightarrow \mu\nu$	0.027	0.03	0.022
Total	1.9	0.24	0.18

Table 5.7: Muon trigger rates in kHz for the $\mu 20i$ trigger at LHC design luminosity ($10^{34}cm^{-2}s^{-1}$).

The trigger threshold for the e/γ and μ are set to 25 and 20 GeV, respectively. Setting up trigger thresholds too high can introduce a bias on physics analyses because the expected signal (or background) event rate of a physics channel might be altered. A study of the trigger influence on the Higgs discovery potential of the $t\bar{t}H$ channel was done in [31]. It was shown that the loss of significance (i.e. S/\sqrt{B}) degrades by about 2% if the p_t threshold is set to 25(20) GeV for electrons(muons) and that degradation gets up to 8% if the selection criteria were raised to 35(25) GeV. A detailed understanding of the trigger is necessary to minimise such degradations.

Chapter 6

Track Reconstruction

Tracks are a basic ingredient for vertex fitting/finding and b-tagging. In the ATLAS Inner Detector two track finding/fitting algorithms have been available since a long time: xKalman [45] and iPatRec [46]. Within the development of the new ATLAS Event Data Model these two (software wise) completely separate tracking algorithms are merged into a common tracking software framework, the so called “new tracking”, which will be the default ATLAS tracking in the near future. For this thesis iPatRec was used. A comparison between iPatRec and xKalman can be found in [47]. The performance of both algorithms is very comparable. A description of iPatRec in this chapter is avoided, details can be found in [46].

This chapter starts with a summary of the common ATLAS perigee representation of the track parameters. Second, track selection variables as used by the vertexing and b-tagging algorithms are presented. The chapter ends with an overview of the performance of iPatRec on the transverse and longitudinal impact parameter resolutions which are especially important for vertexing and b-tagging.

6.1 Perigee Parameters

A track reconstructed in the Inner Detector can be approximated as a helix (charged particle in a magnetic field) with 5 parameters given to some arbitrary reference point. In ATLAS the reference point is usually the global origin of the coordinate system as described in section 3.1. The track parameters themselves are given in the so called perigee parametrisation, which is one possible representation of a helix, where the perigee $P = (x_p, y_p, z_p)$ of a track is defined as the closest approach to the z axis of the coordinate system. The ATLAS perigee parameters are defined in [48] and consist of (see also Fig. (6.1))

- d_0 : signed transverse impact parameter, closest distance to z-axis in transverse plain
- z_0 : longitudinal impact parameter, z coordinate of the track at closest distance in the transverse plain
- ϕ_0 : azimuthal angle of the track at the perigee
- θ : polar angle of the track at the perigee
- $\frac{q}{p}$: charge over momentum of the track.

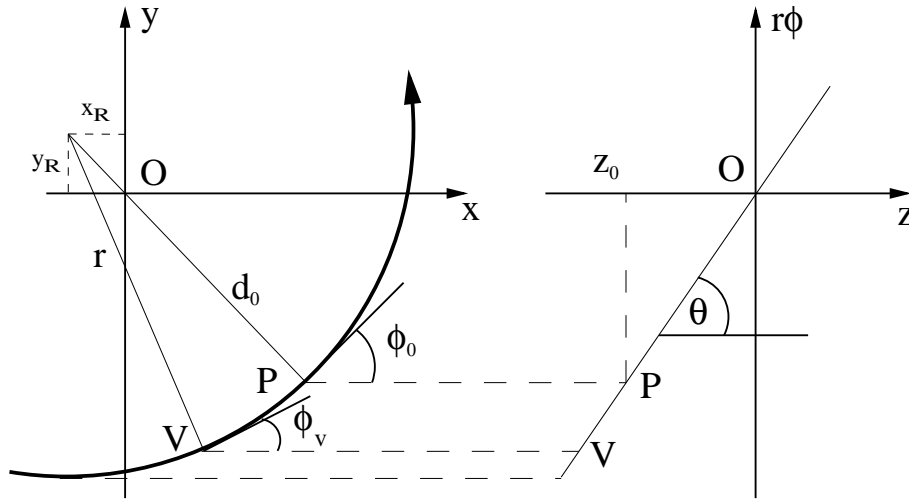


Figure 6.1: Schematic view of the ATLAS Perigee Parameters

The impact parameter d_0 is signed following the convention:

- positive, if the angle between the vector \overrightarrow{OP} and the direction of the track is $-\pi/2$ (or in other words: the origin is to the right side of the track)
- negative, if the angle is $+\pi/2$

In mathematical terms, this means the sign is positive if the following statement

$$\phi - \phi_0 = \frac{\pi}{2} + n2\pi \quad (6.1)$$

is true, where ϕ is the azimuthal angle of the perigee P ($\tan \phi = \frac{y_p}{x_p}$) and $n \in \mathbb{Z}_0$. Otherwise it is negative.

6.2 Track Selection

The track selection variables used for vertex finding are the same which are later used for the b-tagging studies and are listed already here because most of the variables are the same and only differ in the cut value and/or the reference point to which they are given.

Common cuts for vertexing and b-tagging are on the transverse momentum of the track which is required to be at least 1 GeV and on the number of hits in the subdetectors (Pixel, SCT, TRT) of the Inner Detector. The tracks need to have at least one hit in the b-layer (i.e. innermost pixel layer) and two hits altogether in the pixel detector. For b-tagging the total number of precision hits (i.e. Pixel and SCT) has to be at least nine.

The selection cuts on the impact parameters differ a bit for vertexing and b-tagging. For the first, the tracks are required to have a transverse impact parameter d_0 of less than 0.25 mm and a longitudinal z_0 of less than 150 mm. Both are given with respect to the ATLAS global origin and hence the one for z_0 has to be sufficiently large to allow for the z vertex spread of the beamspot which has a σ_z of several centimeters. Both cuts are meant to reject tracks which

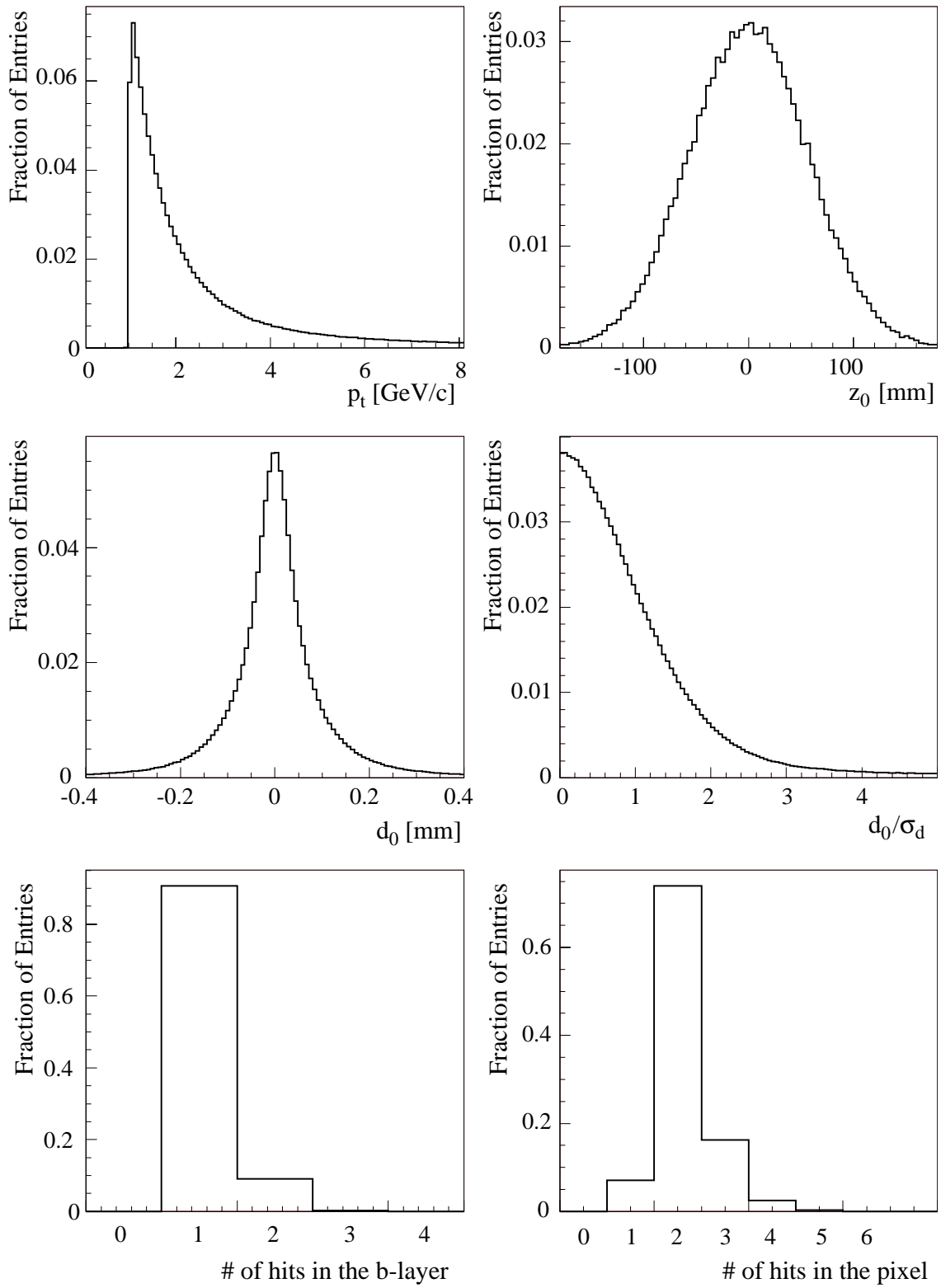


Figure 6.2: Track selection variables for $WH^0(120) \rightarrow l\nu u\bar{u}$ events.

more likely stem from the decay of longer lived particles. For b-tagging, also cuts on d_0 and z_0 are used but this time the primary vertex is known already and cuts can be done with respect to the primary vertex position. Therefore tracks need to have a d_0 of less than 1 mm and a z_0 of less than 1.5 mm. The cut on d_0 is looser than in the case of vertexing even though d_0 is given with respect to the primary vertex because the track selection cuts for b-tagging are not meant to reject tracks which come from a secondary vertex as in the case of primary vertex finding - especially those tracks carry valuable tag information.

Tracks which pass these selection cuts will hereafter be referred to as *good* tracks. Figure (6.2) shows the track selection variables.

6.3 Impact Parameter Resolutions

The performance of the tracking software, especially the resolution of the transverse and longitudinal impact parameters d_0 and z_0 , is very important for vertex finding/fitting and b-tagging. In general, the resolutions of the impact parameters are parametrised as a function of momentum and pseudo-rapidity as [7]

$$\sigma_{IP} = a_0 \oplus \frac{b_0}{p_t} \quad (6.2)$$

where a_0 and b_0 can be considered to be functions of $|\eta|$. a_0 is the intrinsic resolution and b_0 accounts for multiple scattering.

The plots in figure (6.3) show the resolution of the transverse (left plots) and longitudinal (right plots) impact parameter as a function of η and for tracks with $p_t = 1-2, 2-5, 5-10, 10-50$ and above 50 GeV for data sets of increasing complexity (see section 7.3.2 for a description of the data sets). In general the resolution of the transverse impact parameters is better than for the longitudinal one and ranges from 12 μm for small η and high p_t to about 180 μm for large η and small p_t . The longitudinal resolution varies from 200 μm for small η and high p_t to about 800 μm for large η and small p_t . The tracking performance with respect to impact parameter resolution is comparable in all the samples and an earlier study [47] yields impact parameter resolutions similar to the ones shown here. For single muons with true p_t of 1 GeV σ_{d_0} was found to be between $\sim 90 \mu\text{m}$ for tracks with $|\eta| < 0.1$ going up 200 μm for tracks with $|\eta|$ around 2. The same numbers for the samples studied here are about 85 μm and 170 μm for the same η regions. The numbers are a bit better in this study because the tracks had p_t between 1 and 2 GeV where as in the paper it was 1 GeV (true) p_t . Comparisons for different p_t and η regions and for z_0 give similar results. Earlier studies on b-tagging report similar performances [49] as well.

The track reconstruction efficiency of iPatRec is given in [47] and yields an efficiency of $\sim 99\%$ for single μ with $|\eta| < 0.8$ and more than 97% for tracks with $1.6 < |\eta| < 2.5$. For π^\pm these figures drop to 92% and 82% for the same η regions.

The overall tracking performance in terms of impact parameter resolution and track reconstruction efficiency is satisfying and sufficient for efficient vertexing and b-tagging algorithms and the analysis of the $t\bar{t}H$ channel. Only for events with shifted primary vertex a serious drop of the b-tagging performance to 50% of its normal value has been observed. This is however due to the default setting of the tracking software used and can be regarded as a pure software problem (see also 9.5.4).

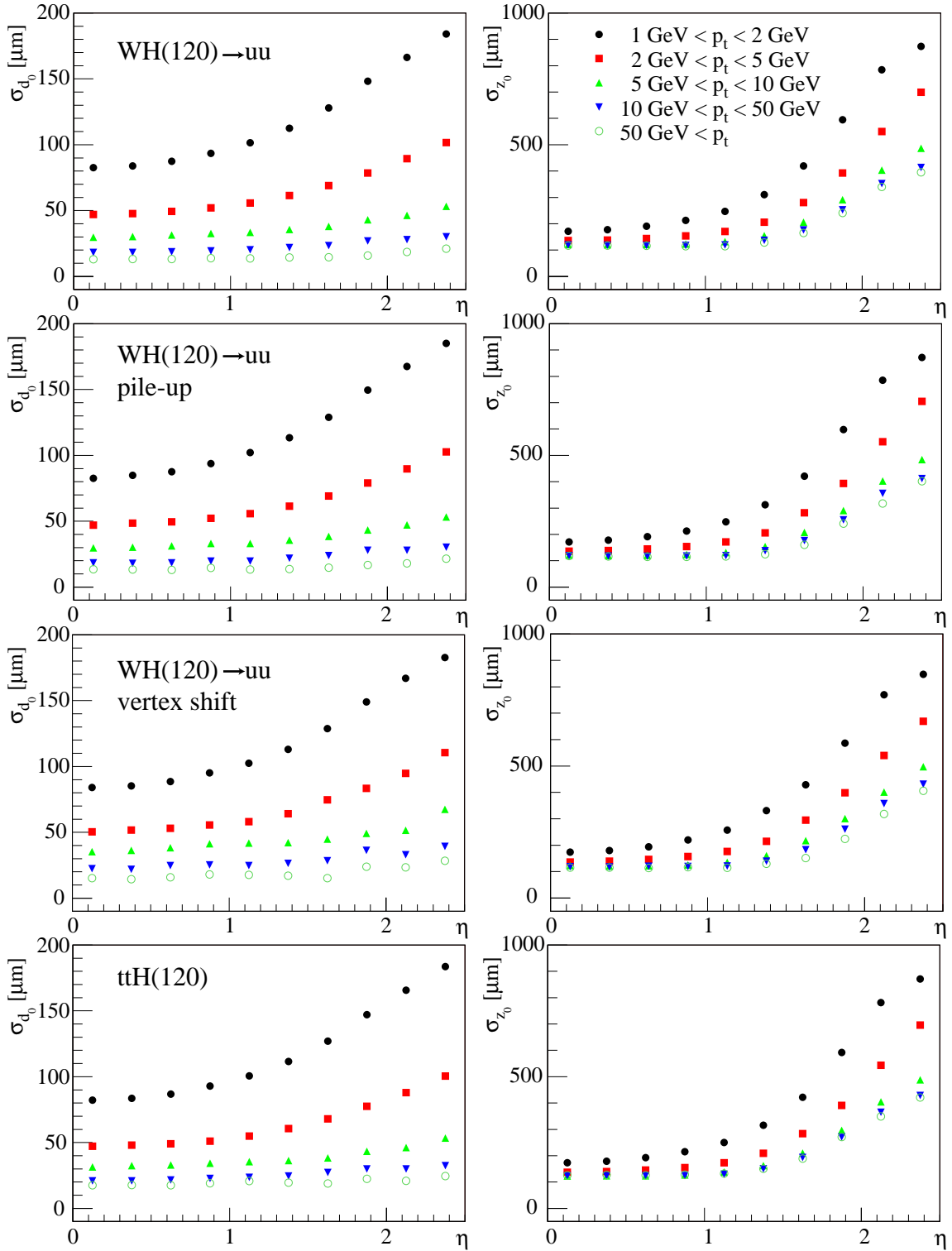


Figure 6.3: Resolution of the d_0 (left plots) and z_0 (right plots) perigee parameters for pure $\text{WH}^0(120) \rightarrow \ell \nu u \bar{u}$ events (top), with pile up (second row), with shifted vertex (third row) and for $\text{ttH}^0(120)$, $\text{H}^0(120) \rightarrow b \bar{b}$ events (bottom row) as a function of η and p_t .

Chapter 7

Vertex Finding and Fitting

The knowledge of the primary vertex position is needed for many physics studies and by algorithms like b-tagging. At the LHC an average of 5(23) minimum bias events at low(high) luminosity will overlay the interesting signal event and it is therefore important for the primary vertex finder to correctly reconstruct and identify *the* primary vertex of the collision. In addition there are many secondary vertices in an event which arise from conversions, V0 decays or long lived (B-)hadrons. For b-tagging, e.g., reconstruction of secondary vertices in jets greatly improves the tagging performance.

The vertex finding strategy can be different among these use cases and also the type of vertex fitter needed does vary. For primary vertex finding it is sufficient to use a fast vertex fitter which only calculates the vertex position and leaves the parameters of the associated tracks unchanged in order not to bias downstream reconstruction algorithms. For B-physics and conversions it is important that the fitter can deal with certain constraints like the decay vertex of a (neutral) particle whose track has to point back to the primary vertex.

From a technical point of view it is therefore desirable to split the two processes of vertex fitting and finding into two separate levels. The fitter is on the mathematical level just a tool which takes some input tracks and eventual additional information and returns a vertex. A vertex finder is a client of a vertex fitter. It gives tracks to the fitter and receives a reconstructed vertex. An important aspect here is that it has to be possible for one vertex finder to use different vertex fitters without the need of changes to the code of the finder.

These different requirements and use cases have inspired the development of a modular and flexible vertex fitter package as part of this thesis work. In addition a primary vertex finder has been developed which is a client of the vertex fitter software. This primary vertex finder is used as the default primary vertex finder in the ATLAS event reconstruction process.

This chapter will start with a short introduction on how the process of vertex finding is understood and how finders and fitters should work together. It is followed by the description of the Billoir method, one mathematical method for vertex fitting, which has been first to be implemented in the vertex software and is also used by the primary vertex finder. A comparison of the performance of the two variations of the Billoir fitter on exclusive $H \rightarrow 4$ lepton decays is then presented. The second part of this chapter is dedicated to the primary vertex finder. The performance of the primary vertex finder has been studied on data sets with increasing complexity including low luminosity pile up and events where the proton-proton interaction point was shifted by 1 cm in the $r\phi$ plane.

7.1 Vertex Finding

The general interplay of vertex finder and fitter is illustrated in Fig. (7.1). The input to the vertex finder is a set of reconstructed tracks which are retrieved from StoreGate, the Athena transient event store. The finder might apply certain track selection cuts and then give a subset of tracks to the vertex fitter. The role of the latter is simply to take the tracks as input and return a vertex. This vertex candidate is then written to StoreGate from where it can be retrieved by other algorithms (e.g. b-tagging) and from where it will eventually be written to persistent storage (i.e. disk).

This is the most basic scenario and illustrates how a vertex finder and a fitter should work together. In the case of the primary vertex finder, for example, the fitter is called twice where the vertex finder uses the vertex information of the first call to further reject tracks which might not belong to the primary vertex.

In this concept the rather specialised vertex finders are always separated by an interface from the purely mathematical tool - the vertex fitters. This creates the advantage for different vertex finders to share common vertex fitting tools and to pick the fitting algorithm which gives the best performance in a given physics environment. The design of the vertexing software and its Event Data Model implements this modular concept and a very detailed description on how this is accomplished is given in appendix A.

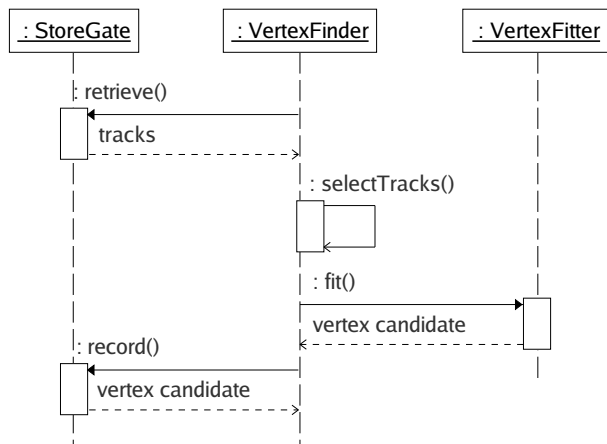


Figure 7.1: General sequence diagram of the vertex finding and fitting process. The vertex finder retrieves input tracks, applies selection cuts on them, feeds the vertex fitter with remaining tracks and writes the results back to the general storage area from where they are available to other algorithms.

7.2 Vertex Fitting: The Billoir Method

The Billoir method [50, 51] is an analytical method using a least-squares ansatz to estimate the vertex position and the momenta of tracks at this position.

7.2.1 General Method

For a vertex fitter the input is a set of measurements \vec{q}_i of $i = 1$ to N tracks plus the covariance matrices C_i (or weight matrices $W_i = C_i^{-1}$) given at an arbitrary but fixed reference surface.

The output is the vertex position $\vec{V} = (x_v, y_v, z_v)$ plus errors and the momentum \vec{p}_i of each track i at the vertex.

With the dependence of the measured parameters \vec{q}_i on the vertex position \vec{V} and the track momentum \vec{p}_i represented by $\vec{F}(\vec{V}, \vec{p}_i)$ a least-squares ansatz can be written as

$$M(\vec{V}, \vec{p}_1, \dots, \vec{p}_N) = \chi^2 = \sum_{i=1}^N (\vec{q}_i^{meas} - \vec{F}(\vec{V}, \vec{p}_i))^T W_i (\vec{q}_i^{meas} - \vec{F}(\vec{V}, \vec{p}_i)). \quad (7.1)$$

The dimension of \vec{q} and \vec{F} depends on the chosen parametrisation of the input tracks. For ATLAS this will be the five perigee parameters of chapter 6.1. In order to get unique results for \vec{V} and \vec{p}_i , $\vec{F}(\vec{V}, \vec{p}_i)$ has to be linear. This can always be achieved if \vec{F} is approximated by a first order Taylor expansion of the form

$$\vec{F}(\vec{V}^0 + \delta\vec{V}, \vec{p}_i^0 + \delta\vec{p}_i) = \vec{F}(\vec{V}^0, \vec{p}_i^0) + \frac{\partial \vec{F}(\vec{V}, \vec{p}_i)}{\partial V_n} \delta V_n + \frac{\partial \vec{F}(\vec{V}, \vec{p}_i)}{\partial p_{in}} \delta p_{in} \quad (7.2)$$

where \vec{V}^0 and \vec{p}_i^0 denote starting points (i.e. expansion points) and $\delta\vec{V}$ and $\delta\vec{p}_i$ are small variations around them. n is an index over the three space or momentum coordinates. For convenience the following abbreviations will be used

$$(D_i)_{jn} := \frac{\partial F_j(V, p_i)}{\partial V_n} \quad (7.3)$$

$$(E_i)_{jm} := \frac{\partial F_j(V, p_i)}{\partial p_{im}}. \quad (7.4)$$

For illustrative reasons (and to avoid confusion) the generic form of the D matrix is given explicitly for the case of a track i with 5 parameters:

$$(D_i) := \begin{pmatrix} \frac{\partial F_1(\vec{V}, \vec{p}_i)}{\partial x} & \frac{\partial F_1(\vec{V}, \vec{p}_i)}{\partial y} & \frac{\partial F_1(\vec{V}, \vec{p}_i)}{\partial z} \\ \frac{\partial F_2(\vec{V}, \vec{p}_i)}{\partial x} & \frac{\partial F_2(\vec{V}, \vec{p}_i)}{\partial y} & \frac{\partial F_2(\vec{V}, \vec{p}_i)}{\partial z} \\ \vdots & \vdots & \vdots \\ \frac{\partial F_5(\vec{V}, \vec{p}_i)}{\partial x} & \frac{\partial F_5(\vec{V}, \vec{p}_i)}{\partial y} & \frac{\partial F_5(\vec{V}, \vec{p}_i)}{\partial z} \end{pmatrix}. \quad (7.5)$$

Minimising Eq. (7.1) wrt. \vec{V} and \vec{p}_i :

$$\frac{\partial}{\partial \vec{V}} M(\vec{V}, \vec{p}_1, \dots, \vec{p}_N) = 0 \quad \text{and} \quad \frac{\partial}{\partial \vec{p}_i} M(\vec{V}, \vec{p}_1, \dots, \vec{p}_N) = 0 \quad (7.6)$$

gives the solution for the vertex position $\delta\vec{V}$

$$\delta\vec{V} = (A - \sum_i B_i C_i^{-1} B_i^T)^{-1} (T - \sum_i B_i C_i^{-1} U_i) \quad (7.7)$$

and the track momentum $\delta\vec{p}_i$

$$\delta\vec{p}_i = C_i^{-1} (U_i - B_i^T \delta\vec{V}) \quad (7.8)$$

where the following substitutions have been made

$$\begin{aligned}
A &= \sum_i D_i^T W_i D_i \\
B_i &= D_i^T W_i E_i \\
C_i &= E_i^T W_i E_i \\
T &= \sum_i D_i^T W_i (\vec{q}_i - \vec{F}(\vec{V}^0, \vec{p}_i^0)) \\
U_i &= E_i^T W_i (\vec{q}_i - F(\vec{V}^0, \vec{p}_i^0)).
\end{aligned} \tag{7.9}$$

The covariance matrices for the vertex position δV and for each track δp_i are given by

$$\begin{aligned}
C_V &= (A - \sum_i B_i C_i^{-1} B_i^T)^{-1} \\
C_{p_i} &= (C_i^{-1} + (B_i C_i^{-1})^T C_V (B_i C_i^{-1}))
\end{aligned} \tag{7.10}$$

Covariance matrices for track-vertex and track-track correlations can also be obtained.

7.2.2 Vertex Constraint

If the vertex position is approximately known (e.g. because the beam-spot is given) then it is also possible to take this information into account as an additional measurement \vec{B} with covariance matrix C_B . One therefore only needs to add a line to the least-squares ansatz of Eq. (7.1). The dependence of the vertex position \vec{V} on this additional measurement is trivial since it is a vertex estimation itself $\vec{B} = \vec{F}(\vec{V}, \vec{p}_i) = \vec{V}$ and the additional term is then:

$$(\vec{B} - \vec{V})^T C_B^{-1} (\vec{B} - \vec{V}) \tag{7.11}$$

This additional measurement modifies A and T of Eq. (7.9) to

$$\begin{aligned}
A &= \sum_i (D_i^T W_i D_i) + C_B^{-1} \\
T &= \sum_i D_i^T W_i (\vec{q}_i - F(\vec{V}^0, \vec{p}_i^0)) + C_B^{-1} (\vec{B} - \vec{V}^0)
\end{aligned} \tag{7.12}$$

and the results Eq. (7.7) and Eq. (7.8) accordingly.

A vertex constraint can not only be used as an additional measurement to improve the overall vertex fit but also gives the possibility to perform a fit if only one track is present.

7.2.3 Full Vertex Fit

The full vertex fit method uses the formalism as described in the previous section and calculates the vertex position as well as the track momenta at the vertex using equations Eq. (7.7) and Eq. (7.8). It has been implemented in the vertexing software as a vertex fitter tool with the name `FullVertexFitter`.

7.2.4 Fast Vertex Fit

In the fast fit method the momentum of the track is taken as constant when going from $\vec{V}^0 \rightarrow \vec{V}^0 + \delta\vec{V}$. This reduces the perigee from 5 parameters to $q'_i = \{d_0, z_p\}$ and the D matrix from 5x3 to a 2x3 submatrix D' holding only the derivatives of d_0 and z_0 wrt. (x_v, y_v, z_v)

$$D' = \begin{pmatrix} -\sin \phi_v & \cos \phi_v & 0 \\ -\cos \phi_v \cot \phi_v & -\sin \phi_v \cot \phi_v & 1 \end{pmatrix}. \quad (7.13)$$

The error matrix is reduced from 5x5 to a 2x2 matrix (for d_0 and z_0). Equation (7.13) already uses the track parametrisation which will be presented in the next section. Since \vec{p}_i^0 is taken as constant the E matrix is not needed at all.

V^0 is taken to be the origin of the coordinate system to which the perigee parameters have to be extrapolated. With \vec{V}^0 as the center, $\delta\vec{V}'$ turns into \vec{V}' and $\delta\vec{q}'_i$ into \vec{q}'_i . With $\vec{x}_{pi} = (x_p, y_p, z_p)$ the position of the perigee and

$$\vec{x}_{pi} = D_i'^{-1} \vec{q}'_i \quad (7.14)$$

the χ^2 in Eq. (7.1) and the solution for V in Eq. (7.7) can be written as

$$\begin{aligned} \chi^2 &= \sum_i (\vec{x}_{pi} - V)^T w_i (\vec{x}_{pi} - \vec{V}) \\ \vec{V} &= \left(\sum_i w_i \right)^{-1} \left(\sum_i w_i \vec{x}_{pi} \right) \end{aligned} \quad (7.15)$$

where $w_i := D_i'^T W_i' D_i'$. The error on \vec{V} is given by $(\sum_i w_i)^{-1}$.

The fast vertex fitter has been implemented as a vertex fitter tool with the name `FastVertexFitter`.

7.2.5 Parametrisation of Track Parameters

To apply the Billoir method, the dependence of the measured track parameters on the vertex position and the track momenta needs to be known in order to calculate the D and E matrices of Eq. (7.2). This linearisation of track parameters in the vicinity of the vertex position is not special for the Billoir vertex fitting method. Almost all fitting algorithms (Kalman fitter, adaptive fitter) depend on it. However, track parameters can be given in many different representations which all require their specific linearisation. For the case of the Billoir fitter the perigee representation has been chosen but the perigee parameters which are used in the original Billoir papers [50, 51] are different from the ones used in ATLAS (see table 7.1 and section 6.1). This section describes the D and E matrices in their special form for the ATLAS definition of the perigee.

ATLAS	d_0	z_0	ϕ_0	θ	$\frac{q}{p}$
Billoir	ϵ	z_0	θ	ϕ_0	curvature C
	$\epsilon = -d_0$				$C_{Billoir}(q/p) = -\frac{B_z q/p}{\sin \theta}$

Table 7.1: ATLAS and Billoir perigee parameters. C is the transverse curvature of rotation and $\rho = \frac{1}{C}$ the transverse radius of rotation. Both are signed but due to other sign conventions of d_0 and C in ATLAS the dependence of C_{ATLAS} and $\frac{1}{\rho_{ATLAS}}$ on $\frac{q}{p}$ has the opposite sign. In the calculation in the text the suffix ATLAS is omitted because all calculations are done in ATLAS parameters only.

First, the ATLAS perigee parameters $\{d_0, z_0, \phi_0, \theta, q/p\}$ need to be expressed as a linear parametrisation in terms of \vec{V} and \vec{p}_i in the vicinity of the vertex region. Let $\vec{V} = (x_V, y_V, z_V)$ and $\vec{p} = (\phi_V, \theta, q/p)$ then the perigee \vec{q} can be expressed as

$$\begin{aligned} d_0 &= \rho - hS, \\ z_0 &= z_V + z_R + \rho(\phi_V - \phi_P) \frac{1}{\tan \theta}, \\ \phi_0 &= (-h \cdot \text{sgn}(Y)) \cdot \arcsin\left(h \frac{X}{S}\right) + \begin{cases} 0, & \text{if } h \cdot \text{sgn}(Y) < 0 \\ \pi \cdot h \cdot \text{sign}(X), & \text{if } h \cdot \text{sgn}(Y) > 0 \end{cases} \end{aligned} \quad (7.16)$$

with X, Y and S defined as

$$\begin{aligned} X &= x_V + x_R + \rho \sin \phi_V \\ Y &= y_V + y_R - \rho \cos \phi_V \\ S &= \sqrt{X^2 + Y^2}. \end{aligned} \quad (7.17)$$

ρ is the transverse radius of the helix and $h = \text{sign}(\rho)$. The parameters θ and q/p stay constant along the helix. X and Y can be understood geometrically as the distances between the reference point and the center of rotation of the helix along the x and y axis respectively. Thus S is the full distance between the origin of the coordinate system and the center of rotation.

The D and E matrices as the derivatives of Eq. (7.16) to \vec{V} and \vec{p} , respectively, can then be calculated to first order of the curvature $\frac{1}{\rho}$ as

$$D = \begin{pmatrix} -\sin(\phi_V) & \cos(\phi_V) & 0 \\ -\cos(\phi_V)\cot(\theta) & -\sin(\phi_V)\cot(\theta) & 1 \\ \frac{1}{\rho}\cos(\phi_V) & \frac{1}{\rho}\sin(\phi_V) & 0 \\ 0 & 0 & 0 \\ 0 & 0 & 0 \end{pmatrix} \quad (7.18)$$

and

$$E = \begin{pmatrix} -R & \frac{1}{2}\cot(\theta)R^2\frac{1}{\rho} & -\frac{1}{2\frac{q}{p}}R^2\frac{1}{\rho} \\ \cot(\theta)Q & \frac{R}{\sin^2(\theta)} & \frac{\cot(\theta)}{2\frac{q}{p}}\tau\frac{1}{\rho} \\ 1 & -\cot(\theta)R\frac{1}{\rho} & \frac{1}{\frac{q}{p}}R\frac{1}{\rho} \\ 0 & 1 & 0 \\ 0 & 0 & 1 \end{pmatrix} \quad (7.19)$$

where the quantities R, Q and τ are defined as

$$\begin{aligned} R &= X \cos \phi_V + Y \sin \phi_V, \\ Q &= X \sin \phi_V - Y \cos \phi_V, \\ \tau &= -2x_V y_V \cos(2\phi) + (x_V^2 - y_V^2) \sin(2\phi). \end{aligned} \quad (7.20)$$

These matrices are used in the implementation of the fast and the full Billoir vertex fitters to calculate the vertex position and track momenta.

7.2.6 Internal Iterations

The Billoir fitting methods are based on a Taylor expansion of the track parameters around the vertex position $\vec{V} = \vec{V}^0 + \delta\vec{V}$ and track momenta $\vec{p}_i = \vec{p}_i^0 + \delta\vec{p}_i$. Therefore, the software implementations of the fast/full fitting methods execute the Billoir mechanism in an iterative way where the fitted vertex of the previous iteration serves as starting point for the next iteration and so forth, assuming that every successive iteration is closer to the true vertex and hence the approximated track parameters are more accurate. Figure (7.2) illustrates this procedure. The very first starting point can be the ATLAS global origin or the beam spot. The fitter extrapolates all perigee parameters of the input tracks to this starting point (in case it is not the ATLAS global origin), runs on the input tracks and calculates a vertex position δV_1 with respect to the starting point. All tracks are extrapolated to this new position and the fit is repeated, giving a new vertex position $\delta V_1 + \delta V_2$. The tracks are always extrapolated from perigee p_j^0 which is given with respect to the global ATLAS origin.

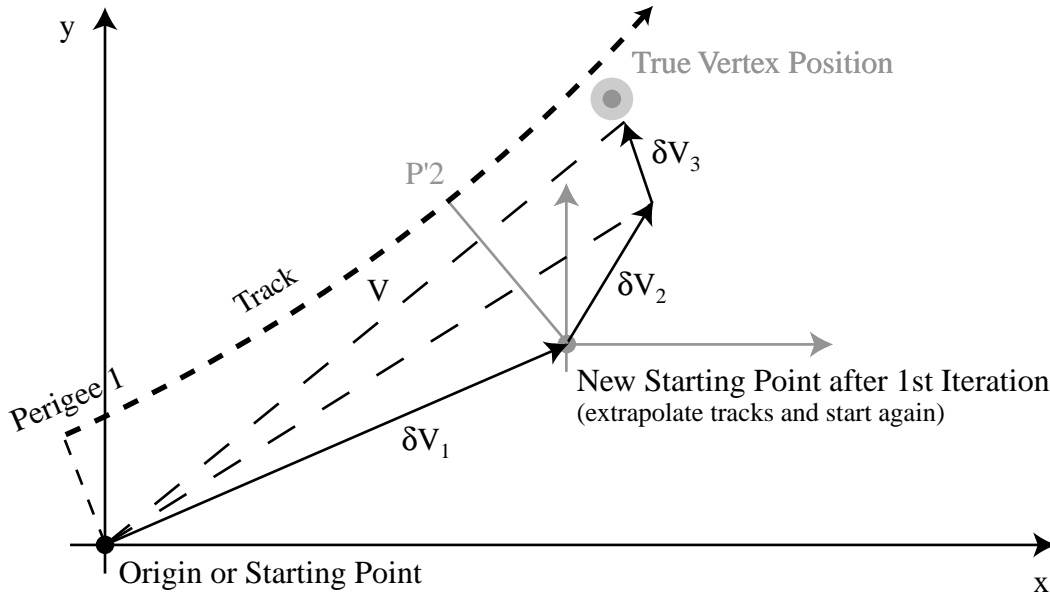


Figure 7.2: Schematic illustration of the iterative process to fit a vertex.

As an example, Fig. (7.3) illustrates the impact of these iterations on the primary vertex finder. It shows the calculated vertex position updates δV_1 , δV_2 and δV_3 with respect to the starting point of the iterations in the $r\phi$ plane and for the z direction separately. The upper plots show the results of the internal iterations during the first call of the Billoir vertex fitter by the primary vertex finder. As described in section 7.1 the primary vertex finder performs two external iterations to improve the vertex resolution further. The lower plots are for the second call where the vertex position of the first call is used as starting point and tracks with a χ^2 contribution bigger than 5 have been removed. One can clearly see that the correction in position with respect to the previous vertex strongly decreases after the second iteration. The effect of the third internal iteration is about $5 \mu\text{m}$ in xy and $10 \mu\text{m}$ in z which is smaller than the precision of the fitted vertex ($10\text{-}20 \mu\text{m}$ in xy , about $50 \mu\text{m}$ in z) and hence the maximum number of internal iterations of the vertex fitter for the case of primary vertex finding is set to three.

For the z direction during the first call of the tool (upper right plot) δV_z converges extremely fast from the first to the second iteration due to the fact that the initial vertex uncertainty in z is about ± 56 mm and the starting point is at $z=0$ mm for the first call. After the first iteration the starting point is much closer to the true primary vertex and δV_2 is smaller than δV_1 by a factor of 1000 and therefore not shown in the top plot of Fig. (7.3). The effect of the iterations on δV is much smaller during the second call of the fitter because the vertex position of the first call serves as starting point of the second call.

The default number of iterations of the vertex fitters is set to 3 and all plots shown hereafter use this default setting.

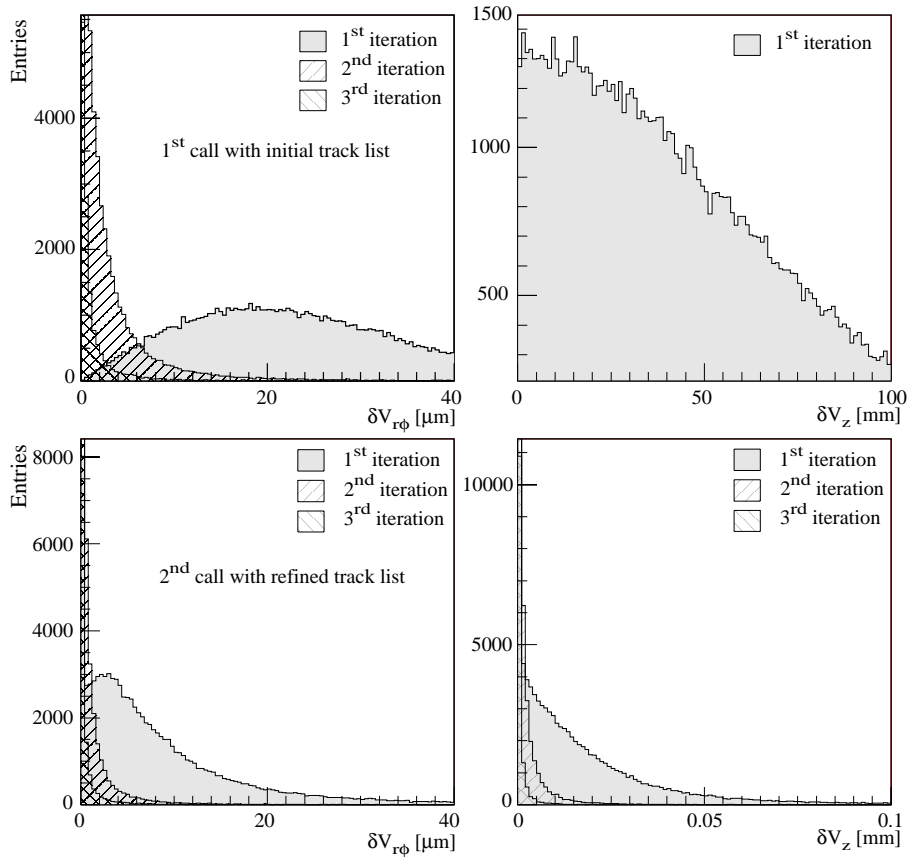


Figure 7.3: The plots show the distance δV between the fitted vertex position after each iteration with respect to the starting point of this iteration. The left plots show the distance in $r\phi$ the right plots in z direction. The upper plots show the three iterations of the first call of the fitter by the primary vertex finder, the lower plots those of the second call. Starting point for the first iteration in the first call of the fitter is the beam spot (normally the ATLAS global origin). The result of the first call of the fitter serves as starting point of the first iteration of the second call of the fitting algorithm. In addition, tracks with a χ^2 contribution of more than 5 have been removed before the second call.

7.2.7 Performance of the Billoir Fitters

This section is dedicated to the performance of the fast and the full Billoir vertex fitters using different reference data sets. The two fitters are tested under equal conditions using tracks coming from the exclusive decay of a Higgs boson with mass $130 \text{ GeV}/c^2$ which decays into four leptons. The reconstructed tracks are matched to the Monte Carlo truth information to assure that the input tracks really stem from the exclusive decay. Events where not all true decay particles could be matched to a reconstructed track are skipped. This procedure assures that both fitters receive the same input and that their performance can be compared directly.

The two cases $H \rightarrow 4l$ and $H \rightarrow 4\mu$ are looked at separately because the vertexing should perform better on the $H \rightarrow 4\mu$ channel where no electrons are present which undergo bremsstrahlung and interact more with the detector material.

The performance of the Billoir vertex fitters is measured using the width of residual and pull distributions. The residual distribution is defined as the difference between the reconstructed and the true vertex position in x, y and z and the pull distribution is the residual divided by the error of the vertex position. The performance in x and y direction (i.e. the $r\phi$ plane) is very much alike and hence plots are only shown for x and z directions.

Figure (7.4) and Fig. (7.5) show the residuals and pulls for the fast and full vertex fitter on $H \rightarrow 4l$, Fig. (7.6) and Fig. (7.7) show the according plots for the Higgs decay into four muons. A Gauss fit has been applied to the residuals in the range $[-30\mu\text{m}, 30\mu\text{m}]$ for x and y and in the range $[-90\mu\text{m}, 90\mu\text{m}]$ for the z direction to estimate the width of the distributions. For the pulls the Gauss fit covers the range $[-2, 2]$. The ranges have been chosen to fit the core Gaussian region of the distribution only. Table (7.2) summarises the results.

Residuals [μm]	Full		Fast	
	$H \rightarrow 4l$	$H \rightarrow 4\mu$	$H \rightarrow 4l$	$H \rightarrow 4\mu$
$\sigma_{r\phi}$	13.93	11.47	13.92	11.46
σ_z	51.08	47.84	51.07	47.84
Pulls	$H \rightarrow 4l$	$H \rightarrow 4\mu$	$H \rightarrow 4l$	$H \rightarrow 4\mu$
$\sigma_{r\phi}$	1.14	0.94	1.14	0.94
σ_z	0.94	0.91	0.94	0.91

Table 7.2: Residuals and pulls for the fast and the full vertex fitter on exclusive $H \rightarrow 4l$ and $H \rightarrow 4\mu$ decays.

The performance of the fast and the full vertex fitting algorithms is very comparable. The resolution on $H \rightarrow 4l$ for both fitters is about $13.9 \mu\text{m}$ in the $r\phi$ plane and about $51 \mu\text{m}$ in z direction. The resolution on $H \rightarrow 4\mu$ is $11.9 \mu\text{m}$ in the $r\phi$ plane and about $47.8 \mu\text{m}$ in z direction and is slightly better than for the decay into four leptons. The difference comes from the decay into electrons which interact more with the material than muons and also radiate bremsstrahlung. In the residuals this can be observed as tails towards higher $x^{rec} - x^{truth}$ values ($> 45 \mu\text{m}$). The tails of the $H \rightarrow 4l$ distribution in the x direction are more pronounced than for the $H \rightarrow 4\mu$ case. In numbers, 6.2% of all fitted four lepton vertices are outside the core gaussian region. For the decay into four muons it is only about 0.5% of all vertices.

The performance of the two fitters concerning the position of the fitted vertex is very comparable. For the purpose of finding and fitting of the primary vertex where only the position

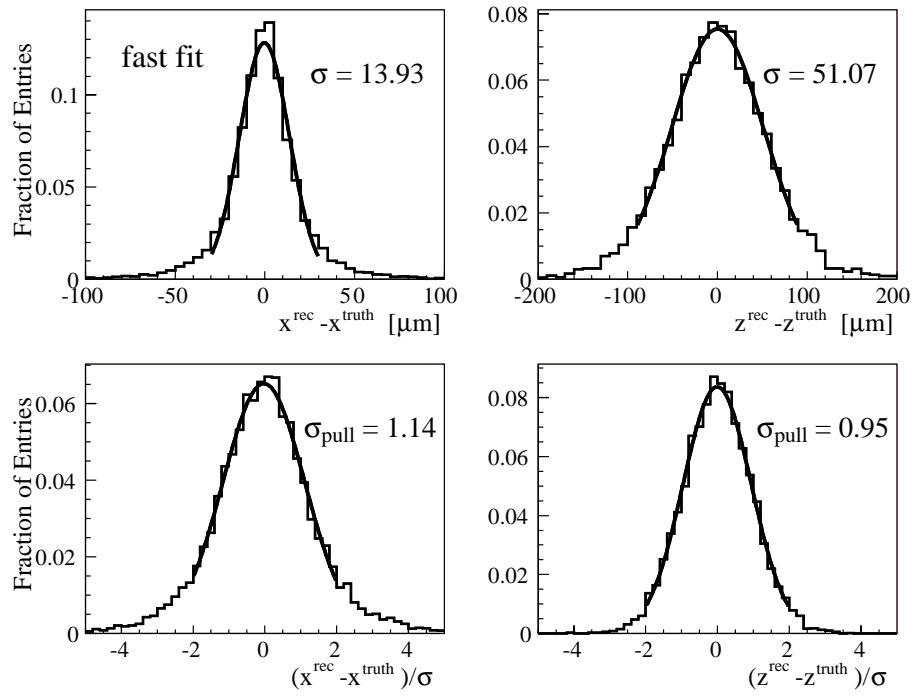


Figure 7.4: Residuals (top) and pulls (bottom) for the fast Billoir vertex fitter on exclusive $H \rightarrow 4l$ decays.

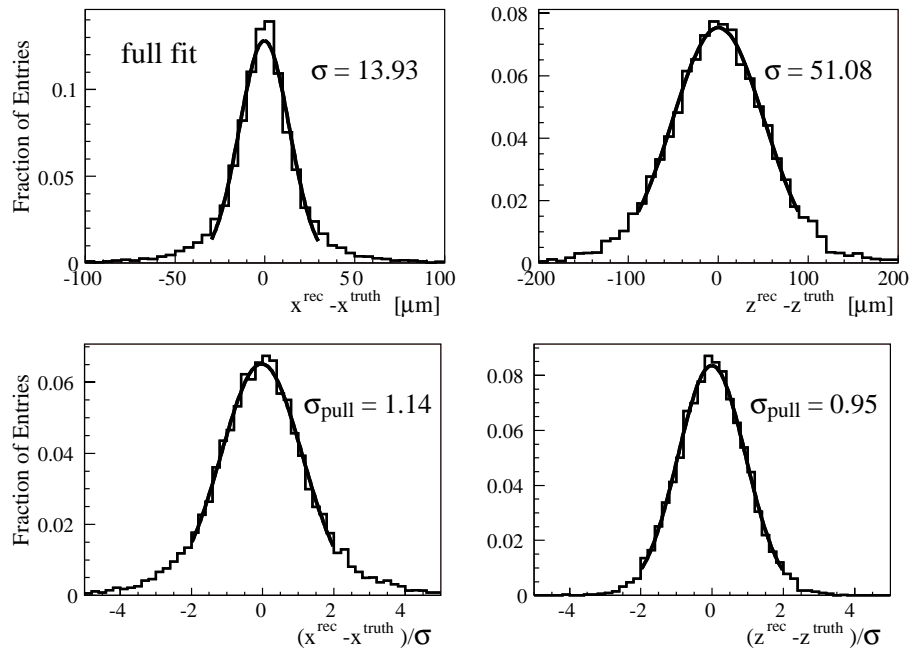


Figure 7.5: Residuals (top) and pulls (bottom) for the full Billoir vertex fitter on exclusive $H \rightarrow 4l$ decays.

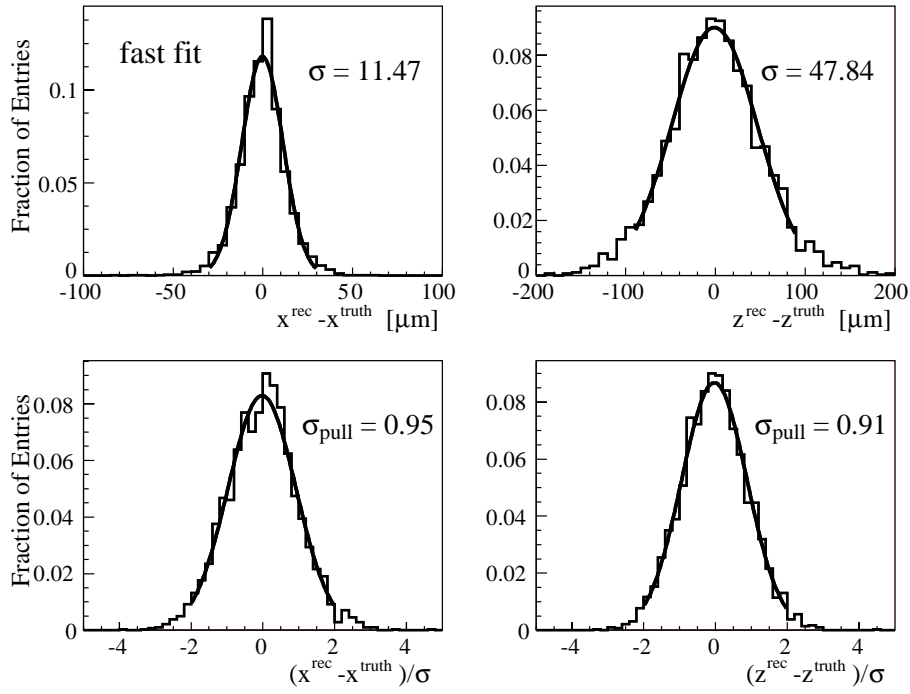


Figure 7.6: Residuals (top) and pulls (bottom) for the fast Billoir vertex fitter on exclusive $H \rightarrow 4\mu$ decays.

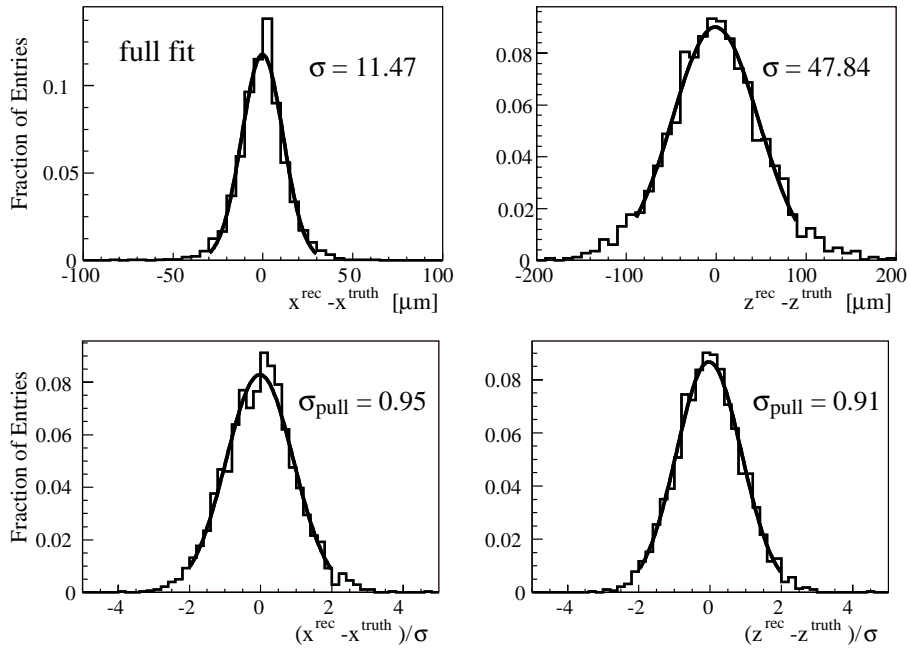


Figure 7.7: Residuals (top) and pulls (bottom) for the full Billoir vertex fitter on exclusive $H \rightarrow 4\mu$ decays.

is of great importance it has therefore been decided to only use the quicker fast Billoir vertex fitting algorithm.

7.3 Primary Vertex Finder

To study the performance of the primary vertex finder a vertex finding strategy has been first implemented to find vertices in *pure* events, i.e. events centered around the ATLAS global origin and with only the generated signal process. It has then been enhanced to include more realistic events with pile up and also with a displaced primary vertex. The main difference in the vertex finding strategies for these three event types is the track selection and track preparation process. The former is important to select tracks which come from the primary vertex and to reject the ones which stem from a secondary, pile up or some other vertex (e.g. conversions). The latter is needed because the parameters of the reconstructed tracks are always given with respect to the ATLAS global origin. However, some of these variables can be very different if the actual primary vertex is some millimeters away in the $r\phi$ plane from this global origin and hence the track parameters have to be propagated to the vertex region before the track cuts can be applied. This of course requires knowledge of the vertex region which can be obtained from the beam spot or by doing a blind vertex fit without track selection cuts.

7.3.1 Finding Strategies

Pure Signal Events For the case of *pure* signal events the track selection strategy is straight forward. On all input tracks so called standard “good track” selection cuts (see section 7.3.3) are applied and the remaining tracks are passed to the vertex fitter tool. The tool returns a vertex position and the finder applies cuts on the maximum χ^2 contribution a track is allowed to make. The fitter is called again (with the first found vertex as starting point) and the final primary vertex is returned to the finder.

Events with Pile Up In events with pile up the vertex finding strategy of the primary vertex finder has to be modified substantially. The primary vertices in an event with low luminosity pile up are spread over several centimeters along the z axis but will all be in the very confined region of the beam spot in the $r\phi$ plane. It is therefore sensible to use the z position of input tracks to separate and reconstruct all potential primary vertices in the event. This is done using a sliding z window approach where tracks are bundled according to their z coordinate. A varying (i.e. sliding) cut for a maximum cluster length in z direction is used to separate vertices from each other.

First, tracks are ordered according to their z coordinate. Then clusters of tracks are put together as long as the distance in z to the next track is lower than a certain cut value - or - as long as the total length of the cluster stays within a certain limit. After this procedure there is a certain number of track clusters, well separated in z direction, with which separate vertex fits are done (in the same manner as done for *pure* signal events). The vertices are ordered according to their transverse momentum p_t , i.e. the sum of p_t of the tracks used to fit them.

Events coming from uninteresting (low p_t) minimum bias collisions mostly have tracks with low transverse momentum. Therefore, the sum of p_t of all tracks used in the vertex fit serves as a variable to define the primary vertex of the event as the one with highest p_t . As will be shown

in Table (7.6) this definition properly identifies the vertex which stems from the interesting deep-inelastic collision in about 98% of all events.

Events With Displaced Vertex In the vertex finding context, events with a displaced primary vertex are mostly a problem for the track selection cuts. The perigee parameters are always given with respect to the z axis of the ATLAS global coordinate system. A shift of the vertex position of 1 cm in the $r\phi$ plane changes the distribution of some measured perigee parameters like d_0 dramatically and a cut on them would reject almost all tracks and leave the vertex finder with very few or no input tracks.

The solution to this problem is to extrapolate the perigee parameters to a position closer to the primary vertex. An estimate of this position can be obtained from the beam condition database or by a “blind vertex fit” with all available input tracks on which only selection cuts are applied which are not much affected by a shifted vertex position (e.g. p_t or θ).

The left plot in Fig. (7.8) shows the distribution of the transverse impact parameter d_0 of tracks in an event where the primary vertex was shifted to (1 cm, 0, 0). The distribution is, as expected, not centered around zero but peaks at ± 1 cm. A track selection cut of 0.25 mm rejects most of the tracks in this event and leaves the fitter with only a couple of (actually bad) tracks. The right plot shows the d_0 distribution after extrapolation to the vertex region using the input of the beam condition database. It is very much comparable to the d_0 distribution of events with the primary vertex around (0, 0, 0). After all tracks have been propagated to the vertex

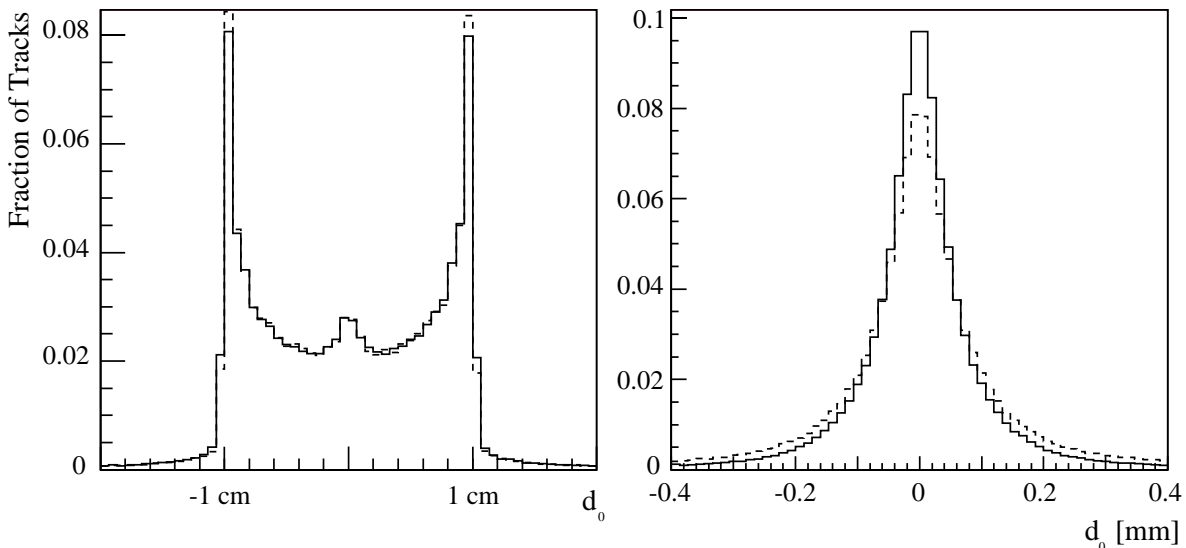


Figure 7.8: The d_0 perigee parameter as obtained from the tracking software(left plot) in events with primary vertex shifted to (1 cm, 0, 0) and propagated to the beam spot region(right plot). The continuous line is for $WH^0(120) \rightarrow l\nu u\bar{u}$ events, the dashed line for $WH^0(120) \rightarrow l\nu b\bar{b}$.

region, the standard track selection cuts are applied and the vertex finder proceeds as in the case of centralised events. The propagation is only done for track selection reasons - the input to the vertex fitter is always the original ATLAS perigee because the vertex fitters work relative to the ATLAS global coordinate system and have their own internal extrapolation/iteration scheme (see section 7.2.6).

Vertex Finding on Real Data On real data it is of course impossible to categorise the vertex finding into different event classes. Primary vertex finding on real data will always involve pile up, a displaced primary vertex and other effects such as misalignment of the detector which are not considered in this thesis. The general vertex finding strategy on real data is a mixture of the steps described above. All input tracks are clustered in z direction using a sliding window approach. They are then extrapolated to the beam spot position (given by the beam condition database) and track selection cuts are applied. These will be less strict than the ones applied on the simulated samples from above because of detector misalignment and other detector imperfections. For each z cluster a vertex is then fitted, tracks with too high χ^2 contribution rejected and the vertices fitted again. All vertices are ordered according to their p_t and stored. The primary vertex is defined as the one with highest p_t .

7.3.2 Data Sets

The data samples used to study the performance of the primary vertex finder are:

- $WH(120) \rightarrow l\nu u\bar{u}$
- $WH(120) \rightarrow l\nu b\bar{b}$
- $t\bar{t}H(120), H \rightarrow b\bar{b}$

The first two have been chosen because they are also commonly used to study the performance of b-tagging algorithms. The $t\bar{t}H$ channel is the potential Higgs boson discovery channel of interest in this thesis. The WH samples are available as pure signal events, events with low luminosity pile up ($L = 2 \cdot 10^{33} cm^{-2}s^{-1}$, 4-5 pile up vertices added) and events with shifted primary vertex. The first two have been taken from the official production and the latter has been privately produced on the GRID.

All samples were generated with Pythia 6.221 and contain initial and final state radiation and an underlying event. Simulation and digitisation has been done with Athena 9.0.4, reconstruction with Athena 10.0.1. Table (7.3) gives an overview about the generated samples and the number of events that were available.

Sample	Data Set	# of Events
$WH(120) \rightarrow l\nu u\bar{u}$	4861	93.549
$WH(120) \rightarrow l\nu b\bar{b}$	4860	18.505
$t\bar{t}H(120), H \rightarrow b\bar{b}$	4020	58.134
With vertex shift to (10 mm, 0, 0)		
$WH(120) \rightarrow l\nu u\bar{u}$	4861	21.666
$WH(120) \rightarrow l\nu b\bar{b}$	4860	14.733
With low luminosity pile up		
$WH(120) \rightarrow l\nu u\bar{u}$	4861	20.753
$WH(120) \rightarrow l\nu b\bar{b}$	4860	3.837

Table 7.3: Monte Carlo data sets to study the performance of the primary vertex finder.

7.3.3 Track Selection

Tracks are selected according to the track selection cuts in Table (7.4). A description was given in section 6.2 of the tracking chapter which also shows plots of the selection variables. The average

p_t	$>$	1 GeV/c
z_0	$<$	150 mm
d_0	$<$	0.25 mm
$\frac{d_0}{\sigma_{d_0}}$	$<$	3
b-layer hits	\geq	1
pixel hits	\geq	2

Table 7.4: Track selection cuts. Tracks which pass these cuts are selected and referred to as “good” tracks.

numbers of reconstructed and selected tracks are shown in Fig. (7.9). In $WH^0(120) \rightarrow l\nu b\bar{b}$ ($WH^0(120) \rightarrow l\nu u\bar{u}$) on average 31.75(29.78) tracks are reconstructed and 22.16(23.55) pass the track selection cuts. This is a decrease in track multiplicity of about 30%(20%). Due to the presence of b-jets in the $WH^0(120) \rightarrow l\nu b\bar{b}$ samples the d_0 and $\frac{d_0}{\sigma_{d_0}}$ distributions are broader and less tracks pass the selection cuts than in $WH^0(120) \rightarrow l\nu u\bar{u}$ events.

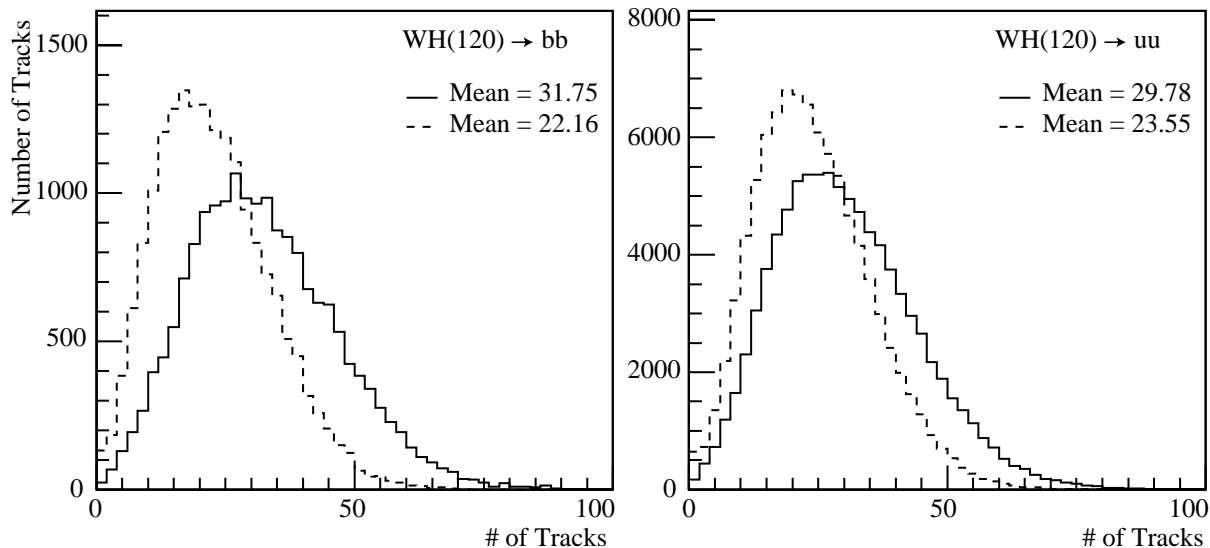


Figure 7.9: The total number of tracks in $WH^0(120) \rightarrow l\nu b\bar{b}$ (left) and $WH^0(120) \rightarrow l\nu u\bar{u}$ (right) events before (continuous line) and after (dashed line) the good track selection.

7.3.4 Performance Variables

In addition to the important residual and pull distributions for the fitted vertex position wrt. the truth the following variables define the performance of the primary vertex finder:

1. reconstruction efficiency

2. percentage of outliers
3. pile up: number of misidentified primary vertices

The reconstruction efficiency is defined as the number of found primary vertices divided by all primary vertices, i.e. by the total number of events. A primary vertex which is further away than a certain distance in z (normally set to $250 \mu\text{m}$) from the truth vertex is referred to as an outlier. The ratio of outliers to all reconstructed primary vertices is of interest. For pile up the misidentification rate of a pile up vertex as the primary one is important. The reconstructed vertex is labelled as misidentified if the distance in z to the true primary vertex is larger than $500 \mu\text{m}$.

7.3.5 Performance on $\text{WH}^0(120) \rightarrow l\nu b\bar{b}$ and $\text{WH}^0(120) \rightarrow l\nu u\bar{u}$

The performance of the primary vertex finder using the fast vertex fitter on the event types described in section 7.3.1, namely *pure* events, events with pile up and events with shifted (i.e. displaced) primary vertex is studied in this section using mainly $\text{WH}^0(120) \rightarrow l\nu b\bar{b}$ and $\text{WH}^0(120) \rightarrow l\nu u\bar{u}$ samples. The performance on the $t\bar{t}H$ channel is also looked at.

Performance on *pure* Signal Events

The resolution of the primary vertex on *pure* $\text{WH}^0(120) \rightarrow l\nu b\bar{b}$ and $\text{WH}^0(120) \rightarrow l\nu u\bar{u}$ events is shown in Fig. (7.10) and Table (7.5). The resolutions are about $14.4(12.3) \mu\text{m}$ in the $r\phi$ plane and $48.6(42.5) \mu\text{m}$ in z direction. The $r\phi$ resolution is comparable to the (expected) beam resolution of $15 \mu\text{m}$. The z resolution is much better than the (expected) 5.6 cm which the LHC monitoring aims to provide.

The resolution is worse for the $\text{WH}^0(120) \rightarrow l\nu b\bar{b}$ sample due to various reasons: tracks with higher impact parameters from decays of secondary vertices which can slip through the track selection cuts increase the spread of the vertex distribution. The somewhat lower track multiplicity after cuts and slightly worse reconstruction quality of tracks in $\text{WH}^0(120) \rightarrow l\nu b\bar{b}$ events degrade the resolution further.

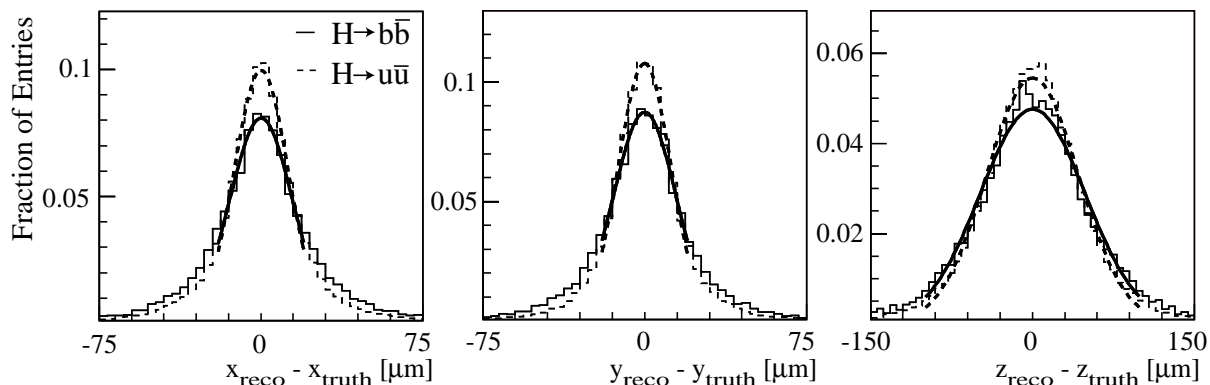


Figure 7.10: Residuals of the primary vertex in x , y and z direction for $\text{WH}^0(120) \rightarrow l\nu b\bar{b}$ (continuous line) and $\text{WH}^0(120) \rightarrow l\nu u\bar{u}$ (dashed line) events.

The reconstruction efficiency, i.e. number of reconstructed primary vertices over total number of events, is $99.3\%(99.3\%)$. The percentage of outliers, i.e. number of reconstructed primary

	x [μm]	y [μm]	z [μm]	Efficiency[%]	Outliers[%]
$\text{WH}^0(120)\rightarrow l\nu b\bar{b}$	$14.5 \pm$	$14.3 \pm$	$48.6 \pm$	99.3%	1.63%
$\text{WH}^0(120)\rightarrow l\nu u\bar{u}$	$12.5 \pm$	$12.1 \pm$	$42.5 \pm$	99.3%	0.85%

Table 7.5: Resolution, reconstruction efficiency and outliers of the primary vertex finder on $\text{WH}^0(120)\rightarrow l\nu u\bar{u}$ and $\text{WH}^0(120)\rightarrow l\nu b\bar{b}$ events.

vertices further away than 0.25 mm from the true primary vertex over all reconstructed primary vertices, is 1.63%(0.85%) for $\text{WH}^0(120)\rightarrow l\nu b\bar{b}$ ($\text{WH}^0(120)\rightarrow l\nu u\bar{u}$).

Performance on Events with Pile Up

In events with low luminosity pile up, on average 4-5 collisions overlay the signal per bunch crossing so that more than one vertex can be found by the primary vertex finder. These reconstructed vertices are ordered according to their transverse momentum and the primary vertex is defined as the one with the highest p_t .

The left plot of Fig. (7.11) shows the number of reconstructed vertices in the event. Even though 4 to 5 pile up vertices are overlaid on the interesting primary vertex only on average about 2 vertices can be reconstructed in each event. This is because tracks from pile up vertices have very low momenta and are either not reconstructed by the tracking software or are rejected during the selection cuts. The right plot in Fig. (7.11) shows the p_t distribution of all reconstructed vertices (histogram with grey area) and shows the contribution of the identified primary vertex and that of all other vertices. The p_t distribution of all vertices clearly shows two regions: vertices with very low transverse momenta and a tail with vertices of higher momentum. The ones with higher transverse momenta are the identified primary vertices of each event.

The effect of the track selection cuts on the average number of tracks can be seen in Fig. (7.12) which shows the total number of reconstructed tracks (continuous line), the number of tracks that survive the track selection cuts (dashed line) and the amount of tracks which pass the χ^2 cut after the first vertex fit.

The total number of reconstructed tracks is about 14%(15%) higher in $\text{WH}^0(120)\rightarrow l\nu b\bar{b}$ ($\text{WH}^0(120)\rightarrow l\nu u\bar{u}$) events with pile up compared to those without. After the track selection pile up events only have about 11% more tracks and after the χ^2 cut about 10% more tracks than the events without pile up. Given that the track reconstruction quality in events with and without pile up is the same it is expected that the performance of the primary vertex finder on pile up events is comparable to the performance on the pure samples.

The resolution is shown in Table (7.6) and Fig. (7.13) and is about 15(12) μm in the $r\phi$ plane and about 46(42) μm in z for $\text{WH}^0(120)\rightarrow l\nu b\bar{b}$ ($\text{WH}^0(120)\rightarrow l\nu u\bar{u}$) events. This is comparable to the performance on events without pile up (see also summary plots in section 7.3.7).

	x [μm]	y [μm]	z [μm]	Eff [%]	Outliers[%]	MisID [%]
$\text{WH}^0(120)\rightarrow l\nu b\bar{b}$	15.0 ± 6.1	14.7 ± 6.1	46.1 ± 4.9	99.35%	3.8%	2.8%
$\text{WH}^0(120)\rightarrow l\nu u\bar{u}$	12.6 ± 2.4	11.9 ± 2.1	42.7 ± 4.3	99.53%	2.1%	1.5%

Table 7.6: Resolution, reconstruction efficiency, outliers and misidentification rate of the primary vertex finder on $\text{WH}^0(120)\rightarrow l\nu u\bar{u}$ and $\text{WH}^0(120)\rightarrow l\nu b\bar{b}$ events with pile up.

The reconstruction efficiency is 99.3%(99.5%) and the percentage of outliers is 3.8%(2.1%)

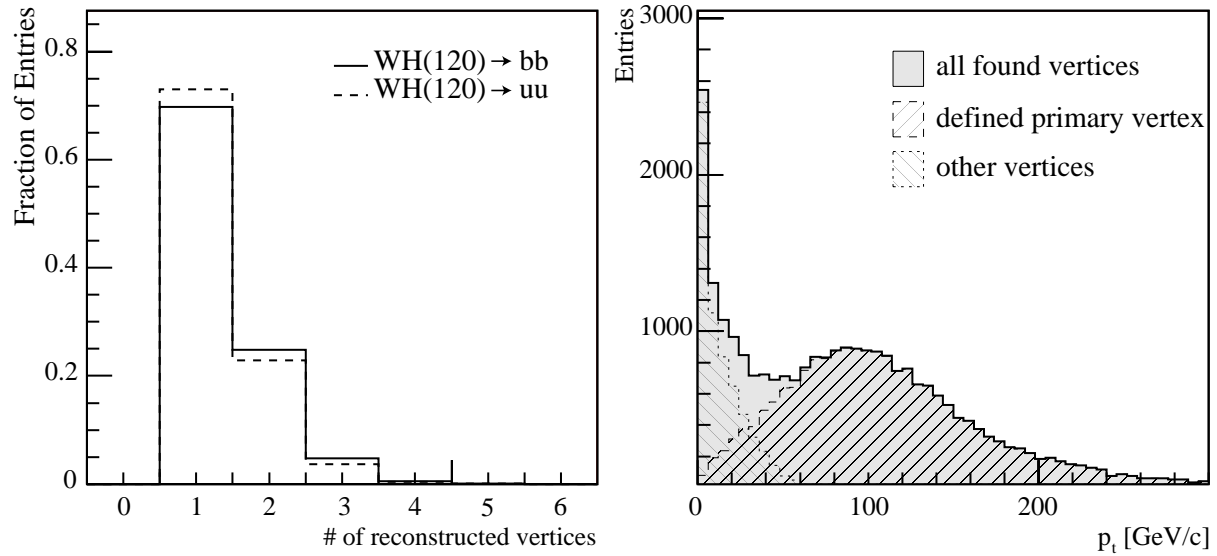


Figure 7.11: Left plot: number of reconstructed vertices in $WH^0(120) \rightarrow l\nu b\bar{b}$ (continuous line) and $WH^0(120) \rightarrow l\nu u\bar{u}$ (dashed line) events with pile up. Right plot: p_t distribution of all reconstructed vertices in $WH^0(120) \rightarrow l\nu u\bar{u}$ events.

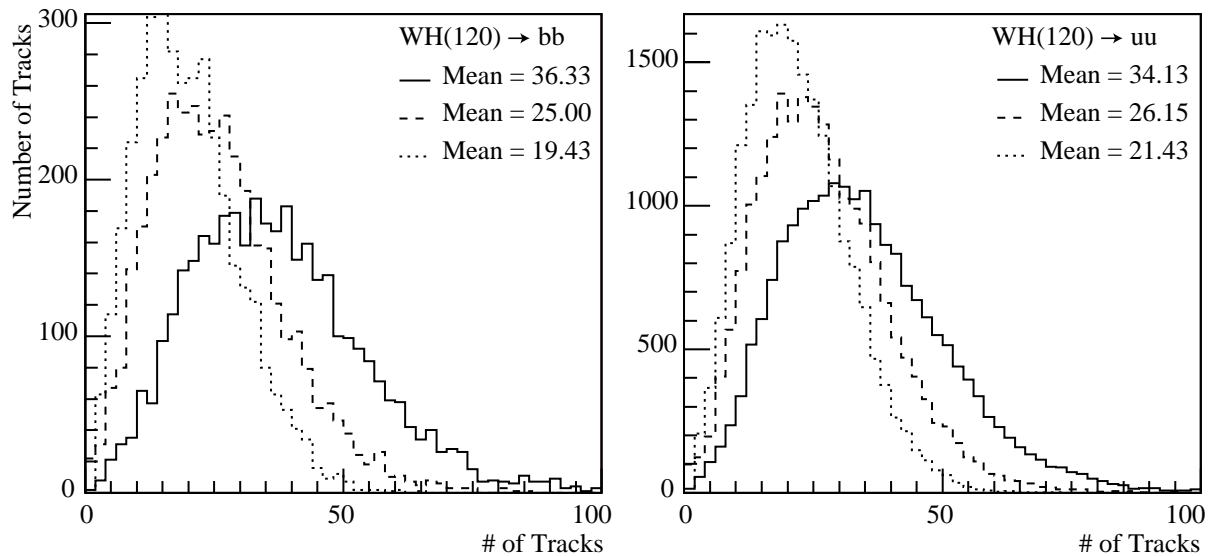


Figure 7.12: The total number of reconstructed tracks in $WH^0(120) \rightarrow l\nu b\bar{b}$ (left plot) and $WH^0(120) \rightarrow l\nu u\bar{u}$ (right plot) events with pile up before (continuous line) and after (dashed line) applying good track selection cuts. The dotted line is the number of tracks finally used in the primary vertex fit after tracks with too high χ^2 have been rejected.

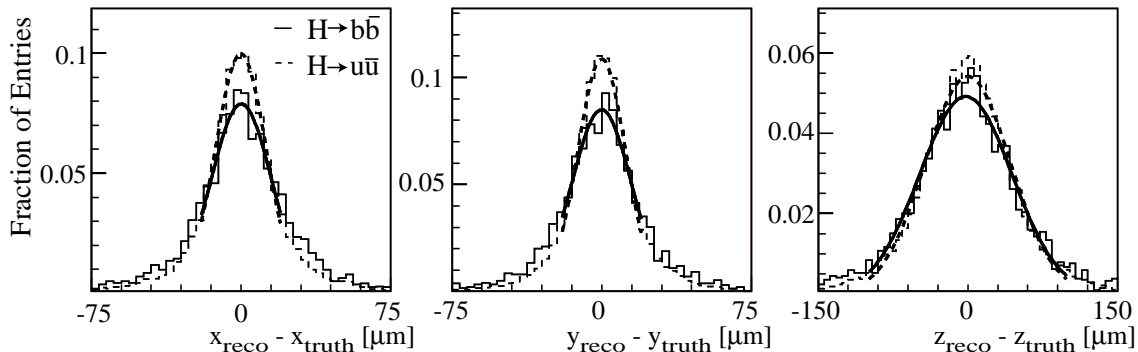


Figure 7.13: Resolution of the primary vertex in x, y and z direction for $WH^0(120) \rightarrow l\nu b\bar{b}$ (continuous line) and $WH^0(120) \rightarrow l\nu u\bar{u}$ (dashed line) events with low luminosity pile up.

for $WH^0(120) \rightarrow l\nu b\bar{b}$ ($WH^0(120) \rightarrow l\nu u\bar{u}$). The numbers of outliers are two to three times as high as for events without pile up. This is because of the contribution of misidentified primary vertices. The misidentification rate is 2.8%(1.5%) for $WH^0(120) \rightarrow l\nu b\bar{b}$ ($WH^0(120) \rightarrow l\nu u\bar{u}$). This is very comparable to earlier results on samples from “Data Challenge 0” (DC0) and DC1 where the misidentification rate was 1.8%(2.5%) and 3.3%(3.6%) for DC0 and DC1 respectively [52].

Performance on Events with Displaced Primary Vertex

The primary vertex finder needs to extrapolate the perigee parameters of the input tracks to the approximated vertex location given by the beam spot or by a “blind fit” before applying the track selection cuts. Figure (7.14) shows the track multiplicity for $WH^0(120) \rightarrow l\nu b\bar{b}$ (left plot) and $WH^0(120) \rightarrow l\nu u\bar{u}$ (right plot). The total number of tracks found by the tracking software (continuous line) is 27.9(25.9). This is about 12% less than in the unshifted case. The reason for that difference is believed to be in the tracking software used: iPatRec’s pattern recognition is tuned to look for tracks emerging from the global center. In case of a shift of 1cm in x-direction fewer tracks are found. After the good track selection cuts (dashed line) 16.7(17.9) tracks are left. This is a reduction of 40%(31%) which is significantly higher than for the unshifted case where the reduction due to the track selection cuts was about 30%(20%). A comparison of the track selection variables uncovers that more reconstructed tracks are rejected in the shifted case because of slightly broader d_0 and z_0 distributions as well as fewer hits in the pixel detector compared to centered events. The number of tracks which have finally been used in the vertex fit (dotted line) after the χ^2 cut is 14.8(16.6). The effect of the χ^2 cut is comparable with that on *pure* and pile up events. The number of tracks used in the final vertex fit is about 24% less than for the exact same events with the primary vertex spread around (0, 0, 0). The track quality is comparable to the unshifted case but due to the fewer tracks the resolution of the primary vertex finder on $WH^0(120) \rightarrow l\nu b\bar{b}$ ($WH^0(120) \rightarrow l\nu u\bar{u}$) events with displaced primary vertex is expected to be slightly worse.

The resolution is shown in Fig. (7.15) and Table (7.7) and is about 15.7(13.3) μm in the $r\phi$ plane and about 52.3(45.6) μm in z for $WH^0(120) \rightarrow l\nu b\bar{b}$ ($WH^0(120) \rightarrow l\nu u\bar{u}$) events. This is slightly worse but competitive to the performance on events with and without pile up. The reconstruction efficiency is 98.6%(98.9%). The percentage of outliers is 2.89%(1.81%). Both numbers are a bit worse than for the unshifted case which is due to the smaller track multiplicity.

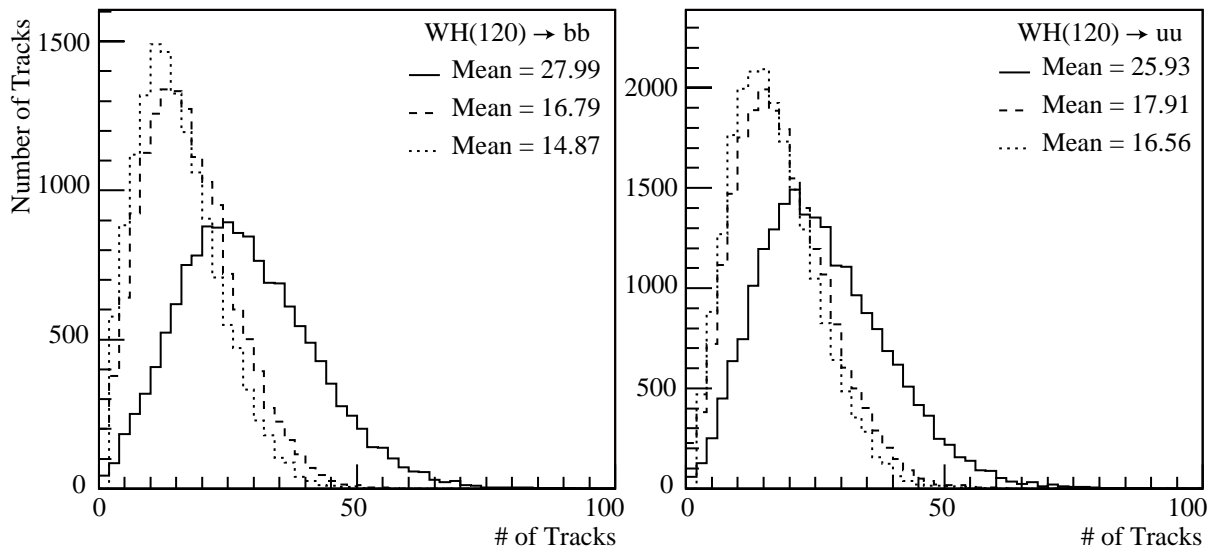


Figure 7.14: The total number of reconstructed tracks in $\text{WH}^0(120) \rightarrow l\nu b\bar{b}$ (left plot) and $\text{WH}^0(120) \rightarrow l\nu u\bar{u}$ (right plot) events with displaced vertex before (continuous line) and after (dashed line) applying good track selection cuts. The dotted line is the number of tracks finally used in the primary vertex fit after tracks with too high χ^2 have been rejected.

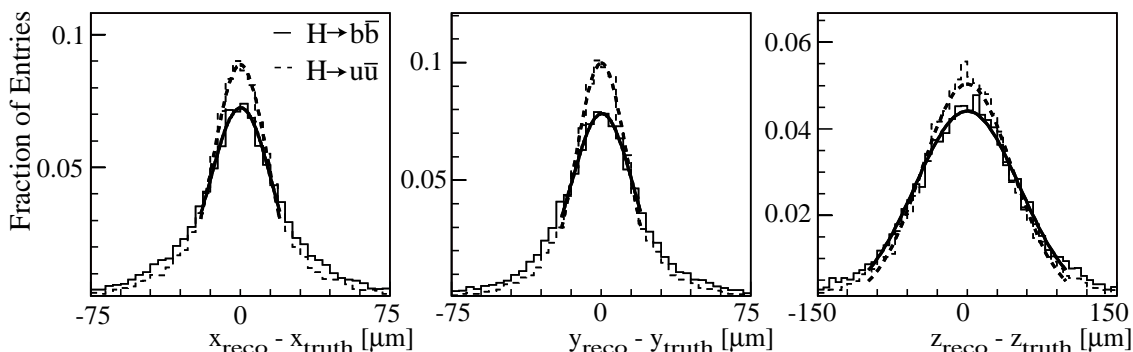


Figure 7.15: Resolution of the primary vertex in x, y and z direction for $\text{WH}^0(120) \rightarrow l\nu b\bar{b}$ (continuous line) and $\text{WH}^0(120) \rightarrow l\nu u\bar{u}$ (dashed line) events with displaced primary vertex around $(10 \text{ mm}, 0, 0) \pm (15 \mu\text{m}, 15 \mu\text{m}, 56 \text{ mm})$.

	x [μm]	y [μm]	z [μm]	Efficiency[%]	Outliers[%]
$\text{WH}^0(120) \rightarrow l\nu b\bar{b}$	15.7 ± 5.9	15.7 ± 6.0	52.3 ± 6.3	98.65%	2.89%
$\text{WH}^0(120) \rightarrow l\nu u\bar{u}$	13.6 ± 2.8	12.9 ± 2.4	45.6 ± 4.8	98.94%	1.81%

Table 7.7: Resolution, reconstruction efficiency and outliers of the primary vertex finder on $\text{WH}^0(120) \rightarrow l\nu u\bar{u}$ and $\text{WH}^0(120) \rightarrow l\nu b\bar{b}$ with shifted primary vertex at $(10 \text{ mm}, 0, 0) \pm (15 \mu\text{m}, 15 \mu\text{m}, 56 \text{ mm})$.

7.3.6 Performance on $t\bar{t}H^0$, $H^0 \rightarrow b\bar{b}$ and $t\bar{t}$ events

The reconstruction of the $t\bar{t}H$ channel and the rejection of background events like $t\bar{t}$ with additional jets is of great importance in this thesis. The performance of the primary vertex finder on these events has therefore been studied and compared to the results from the $WH^0(120) \rightarrow l\nu b\bar{b}$ and $WH^0(120) \rightarrow l\nu u\bar{u}$ samples.

The total number of reconstructed tracks is given in Fig. (7.16). On average it is 65.8 tracks for the $t\bar{t}H$ events and therefore more than two times higher than for $WH \rightarrow l\nu b\bar{b}$ or $WH \rightarrow l\nu u\bar{u}$. The multiplicity after the track selection cuts is 45.2 for $t\bar{t}H$ and 27.6 for the $t\bar{t}$ background samples. After the χ^2 selection cut 38.7(24.1) tracks are finally used in the reconstruction of the primary vertex in $t\bar{t}H$ ($t\bar{t}$) events. The track reconstruction quality (see section 6.3) is comparable to the ones in $WH^0(120) \rightarrow l\nu b\bar{b}$ and $WH^0(120) \rightarrow l\nu u\bar{u}$ events. Due to the much higher track multiplicity in $t\bar{t}H$ events the resolution of the primary vertex is expected to be significantly better. The resolution of the primary vertex is shown in Table (7.8) and Fig. (7.17).

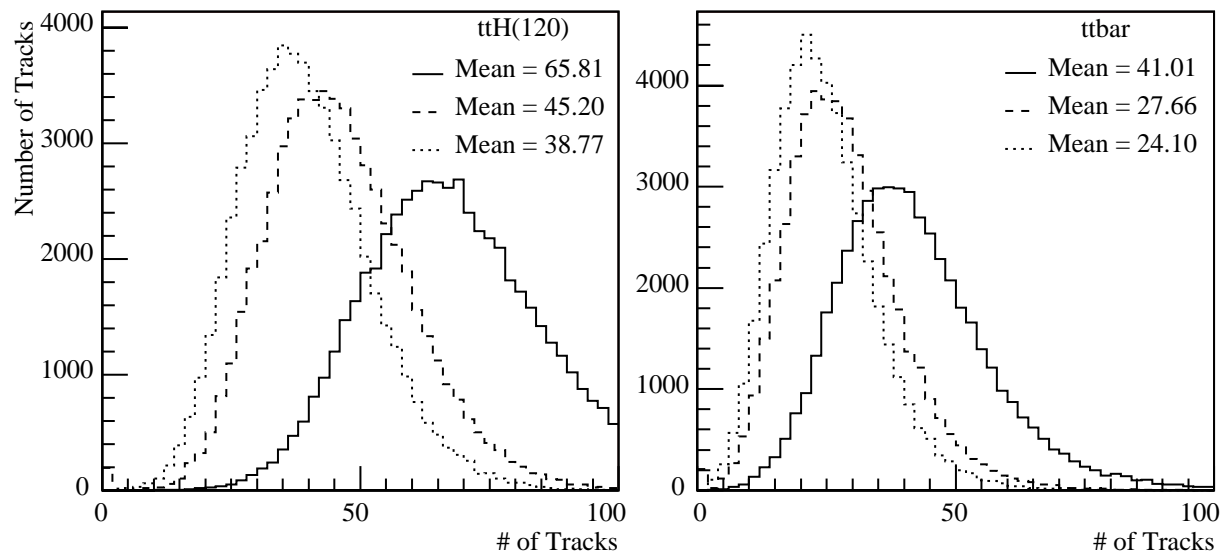


Figure 7.16: The total number of tracks in $t\bar{t}H$ and $t\bar{t}$ events before and after track selection cuts.

For the $t\bar{t}H$ sample it is about $10.3 \mu\text{m}$ in the $r\phi$ plane and $31.5 \mu\text{m}$ in the z direction. For the $t\bar{t}$ events it is slightly larger. This resolution is about 20% better than for $WH^0(120) \rightarrow l\nu b\bar{b}$ events and 14% better than for $WH^0(120) \rightarrow l\nu u\bar{u}$.

	x [μm]	y [μm]	z [μm]	Efficiency[%]	Outliers[%]
$t\bar{t}H$	10.6 ± 1.5	10.0 ± 1.3	31.5 ± 2.7	99.6%	0.13%
$t\bar{t}$	12.1 ± 2.1	11.7 ± 1.9	39.4 ± 3.7	99.5%	0.39%

Table 7.8: Resolution, reconstruction efficiency, outliers and misidentification rate of the primary vertex finder on $t\bar{t}H$ and $t\bar{t}$ events.

The reconstruction efficiency is 99.6%(99.5%) and is the same as for $WH^0(120) \rightarrow l\nu b\bar{b}$ ($WH^0(120) \rightarrow l\nu u\bar{u}$). The percentage of outliers is 0.13%(0.39%) which is much better than for the $WH^0(120) \rightarrow l\nu b\bar{b}$ ($WH^0(120) \rightarrow l\nu u\bar{u}$) case with 1.63%(0.85%) due to the higher track multiplicity.

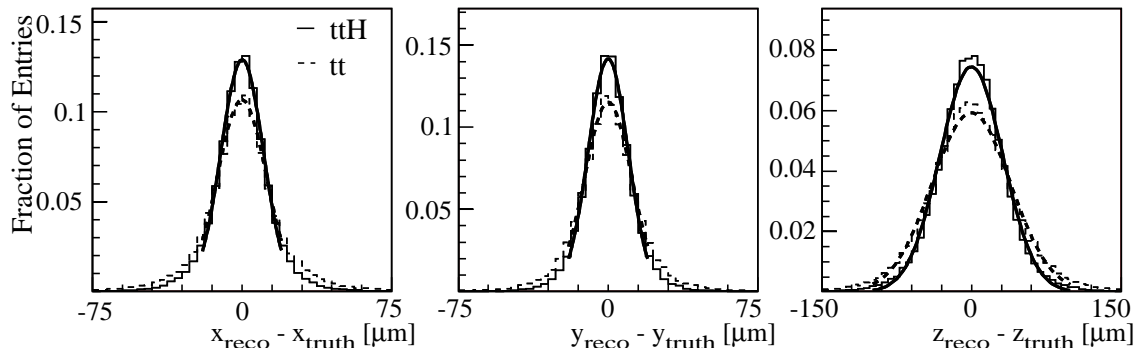


Figure 7.17: Resolution of the primary vertex in x, y and z direction for $t\bar{t}H$ (continuous line) and $t\bar{t}$ (dashed line) events.

7.3.7 Summary

The performance of the primary vertex finder is summarised in this section. Figure (7.18) shows the average total number, selected number and χ^2 selected number of tracks in all used samples. The number of tracks used in the fit is highest for $t\bar{t}H$ events (38.7) and lowest for $WH^0(120) \rightarrow l\nu b\bar{b}$ events with shifted vertex (14.8). Fig. (7.19) and Table (7.9) show the resolution in x, y and z as well as the reconstruction efficiency and outliers for all used samples. The performance is good for all data sets and ranges between $10.6 \mu\text{m}$ in $r\phi$ to $52.3 \mu\text{m}$ in z direction. Differences in resolution come mainly from differences in track multiplicities since the overall performance of the tracking software in terms of track quality is stable over all input samples. The reconstruction efficiency is above 99% for most samples with a minor and expected drop to around 98% for samples with shifted primary vertex which also have the lowest track multiplicity. Outliers are below 1% for *pure* samples and around 2-3% for samples with vertex shift or pile up. The primary vertex misidentification rate in pile up samples is below 3% which is in accordance with earlier studies [52].

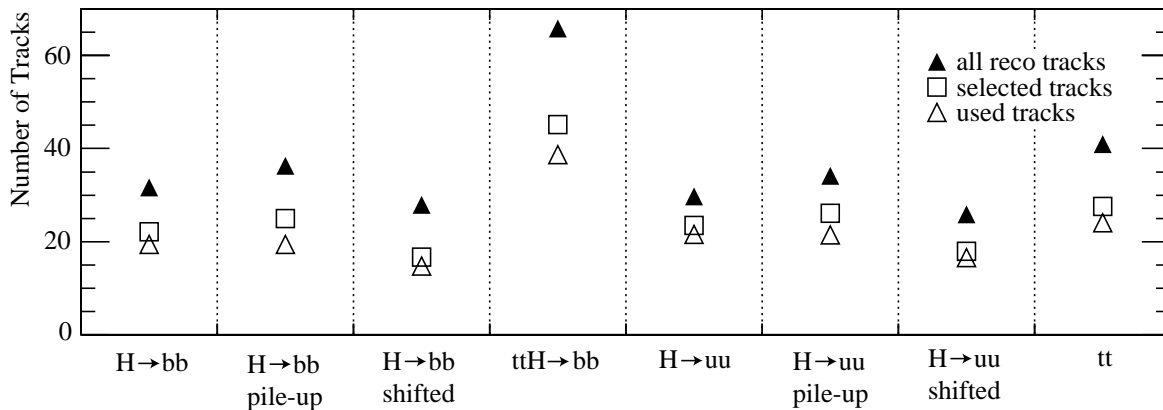


Figure 7.18: Average number of reconstructed, selected and used (after χ^2 cut) tracks in the primary vertex finder for various samples, with and without pileup and displaced primary vertex.

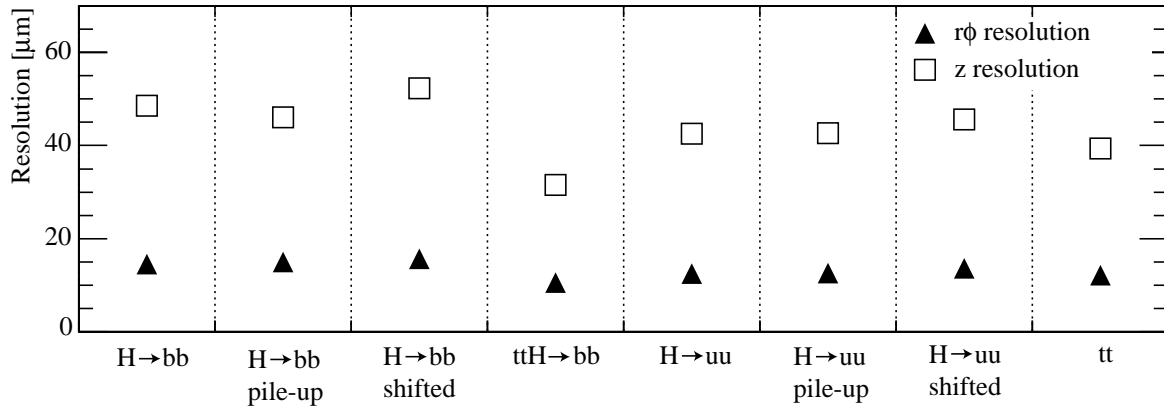


Figure 7.19: Overview of the performance of the primary vertex finder in $r\phi$ and z direction for various samples, with and without pileup and displaced primary vertex.

	x [μm]	y [μm]	z [μm]	Efficiency[%]	Outliers[%]
WH→ $l\nu b\bar{b}$	14.5 ± 6.1	14.3 ± 6.1	48.6 ± 5.6	99.3%	1.6%
WH→ $l\nu u\bar{u}$	12.5 ± 2.3	12.1 ± 2.1	42.5 ± 4.2	99.3%	0.8%
WH→ $l\nu b\bar{b}$ pile up	15.0 ± 6.1	14.7 ± 6.1	46.1 ± 4.9	99.3%	3.8%
WH→ $l\nu u\bar{u}$ pile up	12.6 ± 2.4	11.9 ± 2.1	42.7 ± 4.3	99.5%	2.1%
WH→ $l\nu b\bar{b}$ vertex shift	15.7 ± 5.9	15.7 ± 6.0	52.3 ± 6.3	98.6%	2.9%
WH→ $l\nu u\bar{u}$ vertex shift	13.6 ± 2.8	12.9 ± 2.4	45.6 ± 4.8	98.9%	1.8%
$t\bar{t}H$	10.6 ± 1.5	10.0 ± 1.3	31.5 ± 2.7	99.6%	0.1%
$t\bar{t}$	12.1 ± 2.1	11.7 ± 1.9	39.4 ± 3.7	99.5%	0.4%

Table 7.9: Summary of the resolution, reconstruction efficiency and outliers of the primary vertex finder on various data sets.

Chapter 8

Jet Finding

Jets are an observable manifestation of the quark/gluon structure of matter. When the protons collide, partons from the hard interaction fly apart. Due to the nature of the strong interaction hadrons are produced in bundles, so called jets, when the partons separate further. Their existence was one of the main proofs of the theory that protons and neutrons are made up of smaller particles called quarks and gluons. Jets are a basic input to b-tagging algorithms and play an important role in the analysis of the $t\bar{t}H$ channel.

The concept of parton-hadron duality in QCD states that the dynamics in the high energy/momentum region of the partons which cause the jets is closely and continuously linked with the dynamics of the resulting hadrons in the low energy/momentum region. The purpose of jet finding algorithms is to reconstruct these bundles and combine them in a way that the kinematic properties of the found jets correspond to the kinematic properties of the energetic partons which have been produced in the hard scattering process.

This chapter describes the jet finding algorithms which are used in ATLAS. It puts emphasis on the algorithmic side of the jet finding. Theoretical aspects and properties of an ideal jet finding algorithm such as infrared and collinear safeness and a more detailed description of jet finding algorithms in general can be found in [53].

The standard input to jet finding in ATLAS when running on (simulated) data are calorimeter towers from the electromagnetic calorimeter, but it is also possible to use reconstructed tracks. Both input types are hereafter referred to as particles.

The process of jet finding can be split into two logically separated steps:

- selection process: which particles are part of a jet? This step is done by so called jet algorithms.
- recombination process: how are the momenta of the particles combined to define the final jet kinematics?

The recombination process is explained first since the variables of a certain selection algorithm can already be expressed in quantities unique to the recombination process chosen.

8.1 Recombination Schemes

There are various recombination schemes used in high energy physics [53] but only the one used by default in ATLAS is described here in more detail. It is the so called E-Scheme or 4-vector

recombination. It is used by most hadron-hadron colliders because by definition the resulting jet kinematic variables (e.g. energy-momentum 4-vector) have the desired Lorentz properties like invariance under longitudinal boost.

The recombination of the jet constituents is defined as follows:

1. energy-momentum 4-vector:

$$p^J = (E^J, p^J) = \sum_{i \in J=C} (E^i, p_x^i, p_y^i, p_z^i) \quad (8.1)$$

2. transverse momentum:

$$p_T^J = \sqrt{(p_x^J)^2 + (p_y^J)^2} \quad (8.2)$$

3. rapidity:

$$y_T^J = \frac{1}{2} \ln \frac{E^J + p_z^J}{E^J - p_z^J} \quad (8.3)$$

4. azimuthal angle:

$$\phi^J = \tan^{-1} \frac{p_y^J}{p_x^J} \quad (8.4)$$

where i denotes one constituent (i.e. a particle) of the jet and J indicates that it is a final jet property (e.g. p^J is the energy-momentum 4-vector of the final jet).

8.2 Jet Algorithms

In general there are two different jet algorithms used in ATLAS: Cone and K_t . The cone jet algorithm is the standard one used in hadron-hadron collisions. The K_t jet algorithm is mainly used in lepton colliders but is also implemented in the Athena jet reconstruction software.

8.2.1 Cone Algorithm

The first cone jet algorithm was the so called Snowmass algorithm [54]. The algorithm starts to look for particles (e.g. energy clusters in the calorimeter) within a cone of radius R in $\eta \times \phi$ space. The center of the first cone is arbitrary and one has to make sure that during the processing of a full event the whole detector range is scanned. All particles i which (expressed in E-Scheme variables) fulfil

$$\sqrt{(y^i - y^C)^2 + (\phi^i - \phi^C)^2} \leq R \quad (8.5)$$

are clustered together (using the E-Scheme). The center of this protojet, which is somewhere else than the geometric center (y^C, ϕ^C) of the cone, serves as a new geometric center of a new cone with radius R . Again all particles within this cone are clustered together and the next cone is calculated. This is done iteratively until the geometric center of the cone coincides with the center (y^J, ϕ^J) found by the recombination scheme. The resulting cone is called a jet. This process is repeated until the whole $\eta \times \phi$ range of the detector is scanned and all jets are found.

Two obvious problems are that it is very time consuming to go blindly through the whole detector and look for stable cones and that there is no protection against overlaps of the final jets, resulting in particles which are associated to more than one jet.

The first problem is solved by using seeds. A seed is a calorimeter tower with an energy above a certain threshold $E^{tower} > E^{seed}$. All seeds are ordered in energy and the jet algorithm starts with the cell with highest energy deposit as the geometric center of the cone. It is important that the cut value E^{seed} is chosen large enough to significantly improve the computation time but small enough so that little variations of the seed energy only insignificantly change observables (like the jet kinematics). E^{seed} values range from several hundred MeV to some GeV. The ATLAS default is 2 GeV.

The second problem is minimised by running split and merge algorithms over all found jets. Two jets that overlap are split or merged depending on the amount of overlap. A simple 50% rule is used here. If the two jets overlap more than 50% they are merged into one. If they overlap less they are split. This procedure also minimizes the problems that cone algorithms are usually not collinear or infrared safe. The first can cause the jet algorithm to reconstruct two jets instead of one if the seed energy is distributed between towers due to the radiation of a collinear parton. The second causes the cone jet algorithm to merge two jets in the presence of soft radiation of a gluon between the two jets (for more information see [53]).

8.2.2 K_t Algorithm

K_t algorithms work on the basis of clustering two particles into one. This procedure is repeated until no particle can be clustered anymore and the remaining clusters are regarded as the jets. The K_t algorithm used in Athena is theoretically described in [55], the software implementation can be found in [56].

For every final state object k (e.g. calorimeter towers) and for every pair of two objects k, l two resolution variables

$$\bar{d}_k = (p_t^2)_k \quad (8.6)$$

$$d_{kl} = \min(\bar{d}_k, \bar{d}_l) \cdot R_{kl}^2 \quad (8.7)$$

with $R_{kl}^2 := (\eta_k - \eta_l)^2 + (\phi_k - \phi_l)^2$ are computed. The parameter R defines the extent of the jet similar to the R parameter of the cone algorithms. In ATLAS it is set to 1.0.

Now \bar{d}_k of the single object is scaled with R^2 , defining a new quantity

$$d_k = \bar{d}_k R^2 \quad (8.8)$$

If d_k itself is the smallest value of all d variables $d_k, d_{k1} \dots d_{kn}$, then the object cannot be combined and is regarded as a jet itself. If d_{kl} of a pair kl of two final state objects gives the smallest value then the two are combined according to a given combination scheme. The whole process is continued until all objects have been included into jets.

The big advantage of this type of jet finding is that by definition there cannot be overlaps of jets. All final state objects are assigned to one jet only. In addition this scheme is infrared safe and collinear safe with respect to the initial parton state topology (again see [53] for details). The big disadvantage of this algorithm is the calibration. K_t jets have no fixed shape and it is therefore difficult to subtract energy which does not belong to the jet (e.g. from spectator fragments or from pile up of multiple hadron-hadron collisions).

8.3 Jet Energy Calibration

The goal of jet energy calibration is to relate the measured energy of the reconstructed jet to the one of the original parton which caused the jet. Calibration is necessary since various

effects change the measured energy of the reconstructed jet. One of them is that the jet energy is originally measured at the electromagnetic scale in the LAr calorimeter. A jet is mainly composed of hadrons, however, and the response of the calorimeter to hadrons is different ($e/h \neq 1$) and has to be corrected for. In addition the calibration is η and ϕ dependent since the presence of dead materials, cracks and the use of different technologies in different η regions change the energy measurement.

The standard calibration approach in ATLAS is based on a method developed by the H1 experiment [57]. The idea is to compute a weight for each individual calorimeter cell which corrects for the various effects mentioned above. These weights are then applied on reconstructed jets to estimate their true energy. Using this calibration the ratio of reconstructed to true jet energy (from Monte Carlo truth) $\Delta E_T/E_{TMC}$ is less than 1% over the whole jet energy range.

8.4 Settings and Jet Selection Cuts

In Athena two cone jet algorithms and one K_t jet algorithm are in use. They all use the E-Scheme as the recombination scheme and are referred to as Cone7, Cone4 and K_t . Their ATLAS default settings are given in Table (8.1) and Table (8.2).

Algorithm	Cone4	Cone7
ΔR	0.4	0.7
E^{seed}	2 GeV	
Reco Scheme	E-Scheme	
Calibration	H1-Style	

Table 8.1: Parameter settings for the cone jet algorithms in Athena.

Algorithm	K_t
ΔR	1.
Dist Scheme	ΔR
Reco Scheme	E-Scheme
Calibration	H1-Style

Table 8.2: Parameter settings for the K_t jet algorithm in Athena.

For all b-tagging studies the standard ATLAS jet selection cuts have been used. They consist of two kinematic cuts on $|\eta| < 2.5$ and $p_t > 15$ GeV. For the analysis of the $t\bar{t}H$ channel the jet selection variables are the same but the cut values are different. Distributions of the cut variables for $t\bar{t}H^0(120)$, $H^0(120) \rightarrow b\bar{b}$ events for all three jet finders and their default settings are shown in Fig. (8.1). Cone7 jets have as expected a higher average transverse momentum than Cone4 jets (76 GeV over 62 GeV) due to the bigger cone size ΔR . Their η distributions are very comparable. The K_t jet algorithm has the smallest average transverse momentum with 54 GeV. Its η distribution is also broader than for the cone jet algorithms.

Figure (8.2) shows the jet multiplicity and the number of associated tracks to the jets before and after the selection cuts. The expected number of signal jets in $t\bar{t}H$ events is around 6. Cone4 reconstructs on average 7.17 and Cone7 5.89 jets. The difference comes from the smaller cone size of the Cone4 algorithm. The K_t algorithm reconstructs on average 9.57 jets per event

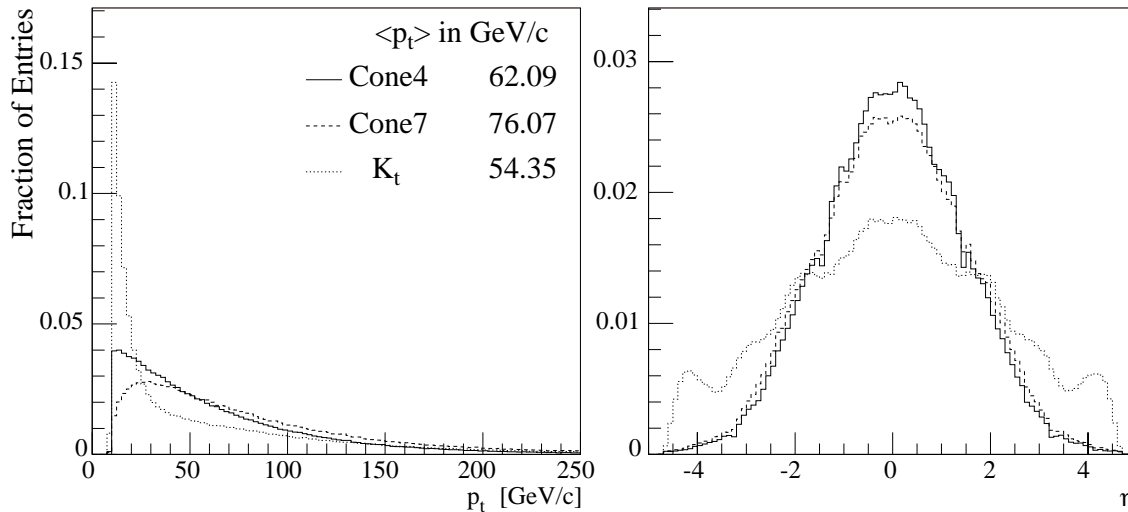


Figure 8.1: Jet selection variables p_t and η for $t\bar{t}H$ events for the three jet algorithms which are used in ATLAS: Cone4, Cone7 and K_t .

where a significantly large fraction of these jets have none or only one associated track from the Inner Detector. This is also the reason for the smaller average transverse momentum of K_t jets. The average number of tracks associated to K_t jets for b-tagging reasons is 2.93 whereas Cone4(Cone7) have on average 4.56(4.68) tracks. Using different settings for the K_t algorithm could force it to produce on average 6 jets (which would be more suitable for the $t\bar{t}H$ analysis). However, a tuning of ATLAS jet parameters has not been performed in this thesis but rather the most suitable of the three default ATLAS jet finders for the $t\bar{t}H$ analysis in terms of jet multiplicity and b-tagging performance has been chosen.

After the kinematic and the b-tagging cuts (at least one associated track) the average number of jets per event decreases to 5.97(5.01) for the Cone4(Cone7) jet algorithm and to 5.36 for the K_t algorithm. The average number of associated tracks after the selection cuts is about 5 for all jet algorithms. For the analysis of the $t\bar{t}H$ channel in this thesis the Cone4 jet algorithm is used. One reason for this choice is the higher jet multiplicity compared to Cone7 and K_t after selection cuts which rejects significantly less events during the event selection. Concrete numbers obtained in this thesis are that $\sim 70\%$ of all events have 6 reconstructed Cone4 jets (without the b-tagging requirement of at least one track associated) whereas this figure drops down below 50% for Cone7 jets. The b-tagging software performs also better on Cone4 jets than on Cone7 or K_t jets (see section 9.5.4) which further increases the percentage of events which have 4 jets tagged as b jets in the final state.

A disadvantage of using Cone4 jets is that it splits a small fraction of signal jets into two jets or that it is more sensitive to hard gluon radiation.

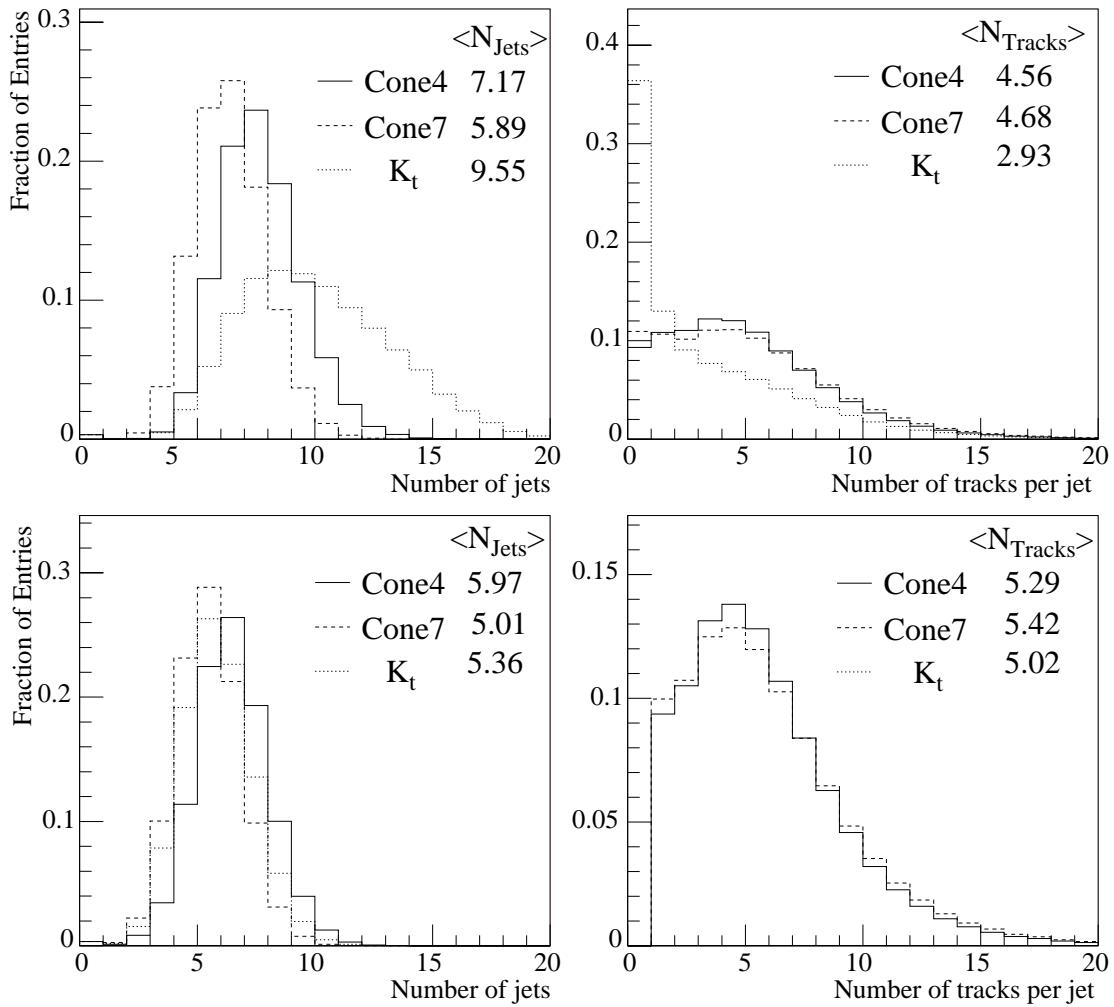


Figure 8.2: Number of reconstructed jets and number of tracks associated to these jets before (upper plots) and after (lower plots) the jet selection cuts for the three jet finding algorithms on the $t\bar{t}H$ data set.

Chapter 9

b-Tagging

The presence of b quarks in many interesting physics and background channels makes it desirable to have efficient labelling or *tagging* of reconstructed jets as either b jets or background jets (g , c or *light*). The potential Higgs discovery channel $t\bar{t}H^0(120)$, $H^0(120)\rightarrow b\bar{b}$ under consideration in this thesis is a good example for an analysis which strongly depends on an excellent b -tagging performance. The final state consists of 4 b jets which need to be identified as such to be able to reconstruct the Higgs Boson, where, at the same time, an efficient rejection of light jets in the background channels (e.g. $t\bar{t}$) is required.

Due to the relatively long lifetime of hadrons with b quarks as their constituents, jets stemming from a b quark have a different topology than jets from light quarks. The B hadron can travel several millimeters before it decays creating a signature of a jet with a reconstructable secondary vertex and tracks with high transverse and longitudinal impact parameters.

To be sensitive to these topological differences in b jets and light jets, a high-precision vertex detector like the ATLAS innermost pixel detector is necessary, which, in conjunction with the SCT and TRT, reconstructs tracks and their impact parameters with very high resolution. These tracks are along with the calorimeter based jets the basic ingredients for b -tagging. They are used to reconstruct the primary vertex, to calculate the impact parameters with respect to the primary vertex and to fit secondary vertices - all quantities which are very important for efficient b -tagging.

To facilitate the b -tagging process and the calculation of all these quantities, a general jet-tagging environment has been developed during this thesis work. It provides common interfaces and a common Event Data Model for the implementation of jet-tagging algorithms within the ATLAS Athena framework. Several well known b -tagging methods have been newly implemented into this jet-tagging environment and previously existing ones migrated. It is therefore now the default b -tagging environment in ATLAS.

One of the guiding design principles is a strong focus on modularity and defined interfaces using the advantages of the new ATLAS Event Data Model and object oriented C++. The benefit for the developer is modularity in terms of easy expandability of the tagging software with additional and different tagging algorithms. The user profits from a common look and feel of all algorithms and data classes and also from an easy configurable jet-tagging chain. The jet-tagging environment provides tools to perform basic tasks which are needed for the tagging process like track to jet association. It also allows not only to choose between the results from different tagging algorithms but also to combine the results into a single discriminating variable.

This chapter starts with a short overview of the general process of jet-tagging. A detailed

description of the software design is postponed to appendix B. b-tagging methods developed at earlier collider experiments have been implemented in this jet-tagging environment and are presented as well as common tasks which are part of the jet-tagging process. The second part of this chapter is dedicated to the performance of the b-tagging algorithms on the same data samples which have been used to study the primary vertex finder.

9.1 General Jet-Tagging Process

The input to the jet-tagging process are jets and tracks as reconstructed by the jet and track finding algorithms. The output of the jet-tagging process are again jets, but this time jets which carry additional tagging information. The tagging process in between can be subdivided into three categories: **preprocessing**, **actual tagging** and **post processing**.

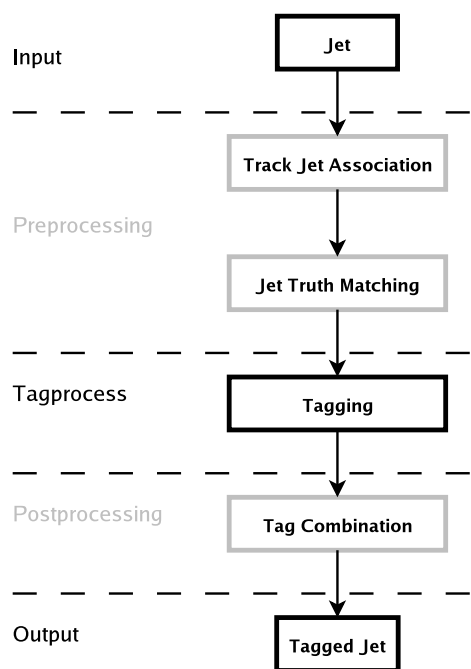


Figure 9.1: Information flow and execution order of the jet-tagging process.

steps. The construction of a single discriminating variable (i.e. post processing) is described last.

9.2 b-Tagging Methods

This section gives an overview of general (b-)tagging methods. It tries to be as general as possible because these methods are of course not restricted to the ATLAS detector and are used in other LHC experiments and have also been used in the past by e.g. the LEP experiments.

The methods can be divided into two groups. The first one is the one used and implemented during this thesis. It makes use of the geometrical difference of b jets and light jets due to the presence of B hadrons with their special properties. Common tagging algorithms in this group

The **preprocessing** steps include the association of tracks to the calorimeter based jets and - if run on Monte Carlo data sets - labelling of the jets with truth information to mark their origin for performance studies. The post processing covers the combination of tagging results from different algorithms. Its purpose is to provide the user with a default combination of the tagging results of certain tagging algorithms and to achieve optimal performance by combining several different single tags. The actual tagging process in between consists of a series of specific tagging algorithms which are executed one after the other and which add their specific tag information to the jet.

Preprocessing, tagging and post processing algorithms will all be explained in this chapter. The design and implementation of their software analogies is presented in appendix B. Different tagging methods are discussed first, followed by the preprocessing

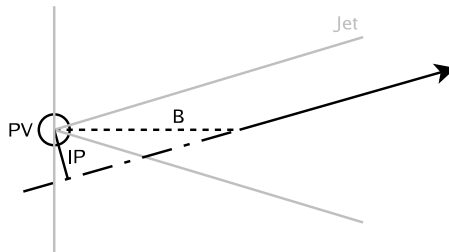


Figure 9.2: Impact parameter of a particle originating from a B hadron decay.

are so called impact parameter taggers and secondary vertex taggers. The second group is based on the fact that the B meson decays in about 10% of all cases semileptonically (e.g. $B \rightarrow l\nu D$) and the b jets therefore often contain (non isolated) leptons with a soft momentum spectrum at low p_t with respect to the jet axis. The taggers of this group are called soft lepton taggers. They were not used in this thesis but have been implemented in the general b-tagging framework by other people.

9.2.1 Impact Parameter Tagging

Impact parameter based b-tagging is the most common way of separating b jets from light jets. A track coming from the decay of a B hadron has a larger impact parameter than those coming from the primary vertex. In addition, the point of closest approach of such a track to the jet axis will more likely be in the hemisphere of the jet defined by the jet axis, the primary vertex and the plane transverse to the jet axis (see Fig. (9.2)). To take this into account, the *geometrical* sign of the impact parameter as it has been described in section 6.1 is redefined to a *lifetime* sign which is

- positive: if the point of closest approach of the track to the jet axis is in the hemisphere of the jet
- negative: otherwise

Particles which originate from the primary vertex will equally likely have impact parameters on both sides of the jet hemisphere whereas tracks from a secondary vertex mostly have a positive lifetime sign. This 3 dimensional topology is normally split into two projections, i.e. the transverse impact parameter in $r\phi$ and the longitudinal one in z . The idea behind this splitting is that the track resolution in $r\phi$ is better than the one in z direction and that the primary vertex resolution is also much better in the $r\phi$ plane which is both due to the design of the ATLAS detector.

The lifetime sign for the $r\phi$ plane and the z direction is calculated as

$$\text{sign}(d_0) := \text{sign}(\sin(\phi_{Jet} - \phi_{Track})d_0) \quad (9.1)$$

and

$$\text{sign}(z_0) := \text{sign}((\eta_{Jet} - \eta_{Track})z_0) \quad (9.2)$$

where the track parameters are given with respect to the primary vertex of the event. The impact parameter is divided by its error to give tracks with small measurement errors (i.e.:

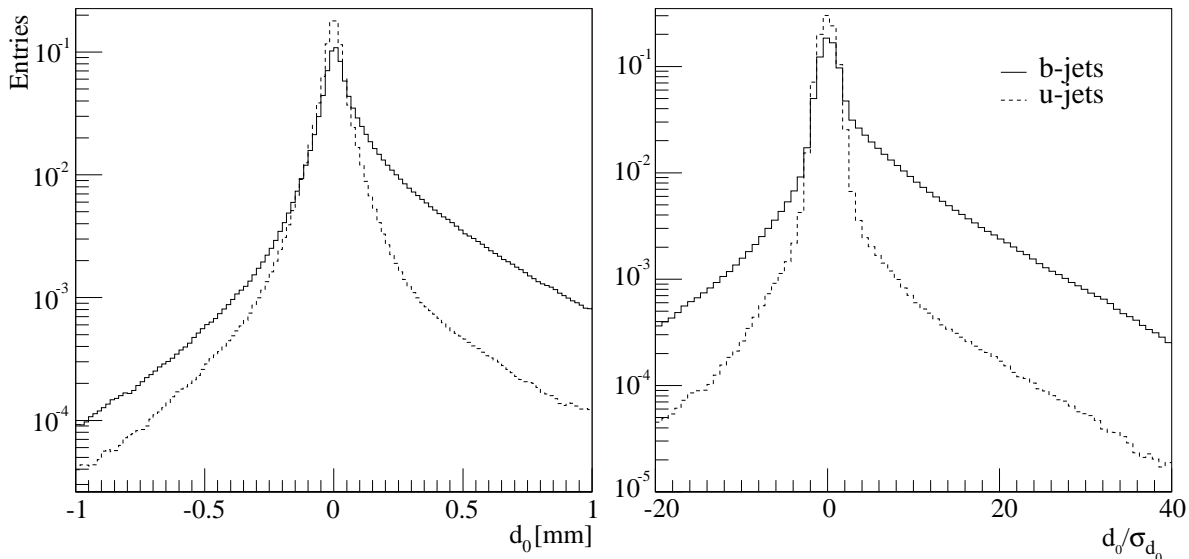


Figure 9.3: *Lifetime* signed impact parameter (left plot) and significance distribution (right plot) in the $r\phi$ plane for b jets (cont. line) and u-jets (dashed line).

better tracks) a higher weight. A new quantity - the significance s of a track - is then derived as

$$s := \frac{d_0}{\sigma_{d_0}}. \quad (9.3)$$

Figure (9.3) shows the *lifetime* signed impact parameters and significance in the $r\phi$ plane for b jets and light jets. The abundance of tracks with larger impact parameters for b jets compared to light jets is clearly visible. For the impact parameter based taggers the distribution of the significance in z and $r\phi$ serves as input (i.e. as the probability density function) to construct a discriminating variable (weight/likelihood).

The single weights of the z and $r\phi$ methods are usually combined into a more powerful discriminating combined weight.

9.2.2 Secondary Vertex Tagging

The secondary vertex taggers try to reconstruct the vertex caused by the decay of the B hadron in the b jet and use this information to separate b from light jets. Already the existence of a reconstructable secondary vertex in a jet is a strong indication that a jet originated from a b quark. In addition, vertices reconstructed in b jets have different topologies than those in light jets. The track multiplicity and mass of a b jet vertex is higher than for light jets and also the fraction of the total jet energy which is in the tracks of the secondary vertex is higher. The distance of the secondary vertex to the primary vertex is bigger for b jets and the quality of the vertex fit is also better.

The algorithm used by the b-tagging software to find secondary vertices is described in detail in [52].

9.3 Tagging Preparation

9.3.1 Association of Tracks to Jets

The input jets and tracks are reconstructed separately before the b-tagging starts. For the tagging process it is important to establish a connection between the jets which need to be tagged and the tracks which hold important tagging information. This track to jet association is done by a simple cone matching criterion. The distance between a track and a jet is defined by

$$\Delta R := \sqrt{(\eta_{track} - \eta_{jet})^2 + (\phi_{track} - \phi_{jet})^2} \quad (9.4)$$

Tracks and jets closest to each other are associated to each other, or in technical words, the track is added to the list of constituents of the jet and can later be used by tagging algorithms. If a track is further away than a certain cut value ΔR_{cut} then it is not associated to any jet. On the other hand it might also happen that one track is within ΔR_{cut} of two or more jets. In this case it has been added to the closest jet. The ΔR_{cut} was set to 0.7 for all studies in this thesis.

9.3.2 Truth Matching

Truth matching of jets is an important aspect when studying the performance of jet-tagging algorithms when running on Monte Carlo data sets. The goal is to label reconstructed jets with MC truth information to mark their origin. For the purpose of b-tagging this would mean labelling the jet as coming from b, c, gluon or uds (where uds are together referred to as light jets). The reference histograms for signal (b jets) and background (light jets) are filled according to the truth label of the jet.

The jet-tagging software provides two different truth label approaches. Both have in common a direct label of signal jets and an indirect label of background jets. This means that every jet which could not be flagged as signal is given a background jet label. The problematic aspect here is that true b jets which could not be correctly labelled as such will be given a background jet label. These wrongly labelled jets contaminate both: the background reference histograms and the background rejection performance. Additional “jet cleaning” measures can be applied to reduce the number of true signal jets in the background jet sample.

Cone Parton Truth Label One possibility to label a jet with truth is by comparing the jet direction and the direction of the truth particle the jet is meant to come from (e.g. b quark, tau lepton, c quark). The parton which is closest to the jet in measures of a cone around the jet will be assigned to the jet and the jet is labelled accordingly. The definition of the distance between jet and quark is the same as used for the jet-track association in Eq. (9.4). If no signal parton is within a certain distance ΔR_{cut} then the jet is labelled as background.

The variable of interest in this kind of truth matching is ΔR_{cut} which defines the maximum distance a parton can have to still be assigned to a jet. The smaller it is the more real signal jets might be mislabelled as background jets, the bigger it is some background jets might be labelled as signal jets. The default value in ATLAS is set to $\Delta R_{cut} = 0.3$.

For the cone matching one needs to decide how to treat b jets which come from gluon splitting. 6% of gluon splitting is into a pair of b quarks and it is a matter of definition if a b jet from $g \rightarrow b\bar{b}$ is labelled as gluon or b. To test the performance of the jet-tagging algorithms the so called *algorithmic* definition is used where a b jet from gluon splitting is truth labelled as b

(because it will have a b jet topology). The other approach is called *physics* definition where these jets are labelled as gluon because the very original parton was a gluon and not a b quark. In this thesis the algorithmic approach is used.

Track Truth Label Another way of labelling jets with truth information is by means of tracing back the true origin of a track which is part of the jet. During reconstruction each track is mapped to a particle from the truth collection. It is possible in Pythia to ask this true particle for all its ancestors and check if one of them was a B hadron. If yes, the whole jet is labelled as a signal jet. The disadvantage of this method is that it is difficult to directly label c jets by checking possible c hadron ancestors of a reconstructed track. Especially, because b jets contain D mesons (which contain c quarks) from the B decay. This is less of a problem for the cone match algorithm because one only looks for the flavor of the initial quarks (and not at a whole decay chain of hadrons with b or c quarks) and label priority is given to the b quark. The issue of gluon splitting is not present in this type of truth matching which does not know anything about the underlying quark nature of the event. In that sense b jets from gluon splitting will be labelled as b (if they contain a B hadron).

9.4 Discriminating Variables

A very important part of the tagging process is the construction of a final discriminating variable which can later be used to separate signal jets from background jets. The input to calculate this discriminant are single variables which are different for signal and background jets. The significance distribution used in the impact parameter based tagging is an example.

In the jet-tagging framework two similar approaches to construct a discriminant are used, namely the likelihood and weight. Software tools to calculate these quantities are provided. The weight technique can distinguish between 2 types of objects (e.g. b jet or light jet) whereas the likelihood can discriminate among many types (e.g. b jet, c jet or light jet). The range of the weight is between $-\infty$ and $+\infty$. The likelihood is always between 0 and 1. The following paragraphs define the mathematical model behind both methods.

9.4.1 Likelihood

The likelihood method can discriminate between n types of objects¹. For each variable i the probability density function $f_i^j(x_i)$ for each object class $j=1\dots n$ has to be known. Again, the significance distribution for b and light jets is an example. The probability $p_j^i(x_i)$ if an object with value x_i belongs to the event class $j=b, \text{ light}$ is given by

$$p_j^i(x_i) = \frac{f_i^j(x_i)}{\sum_{j=1}^n f_i^j(x_i)} \quad (9.5)$$

The pdfs $f_i^j(x_i)$ are normalised to unity. If there are $i=1, \dots, N$ discriminating variables, then the probability can be combined to one event quantity $P_j(x_1, \dots, x_N)$ which expresses the tendency if this object is of type j

$$P_j(x_1, \dots, x_N) = \prod_{i=1}^N p_j^i(x_i) \quad (9.6)$$

¹Examples of object types could be light jets and b jets.

and finally this quantity is normalised to the so called likelihood

$$L_j(x_1, \dots, x_N) = \frac{P^j(x_1, \dots, x_N)}{\sum_{j=1}^n P^j(x_1, \dots, x_N)}. \quad (9.7)$$

The likelihood can be interpreted as a probability of this object to be of type j as long as the input variables are uncorrelated. If they are correlated, the likelihood can still be used to discriminate between events but it is not a probability anymore.

9.4.2 Weight

Another possibility to combine variables to one single discriminating variable is by means of a weight. The same pdfs and nomenclature as for the likelihood are used. The weight method can only distinguish between two classes $s_i(x_i)$ therefore defines the pdf of variable i of the signal events and $b_i(x_i)$ that of the background events. The weight for variable i is then obtained by

$$w_i(x_i) = \frac{s_i(x_i)}{b_i(x_i)} \quad (9.8)$$

and the combined weight of $i=1, \dots, N$ discriminating variables is obtained as

$$W(x_1, \dots, x_N) = \sum_{i=1}^N \log \frac{s_i(x_i)}{b_i(x_i)} \quad (9.9)$$

As an example, Fig. (9.4) shows the weight and likelihood distribution used to calculate the performance of the 1D and 2D combined (i.e. 3D) impact parameter taggers for b jets and light jets. The distribution for b jets shows a clear enhancement toward higher values when compared to the one for light jets. A cut on these distributions determines the b jet selection efficiency and background rejection. The cut values are chosen to achieve a certain selection efficiency (usually 50, 60 and 70%) giving certain background rejection rates at these efficiencies. For the numbers presented in the following chapters only the weight distribution is used to calculate the background jet rejection rate at a given b jet selection efficiency. The likelihood can also be used but it is mathematically equivalent to the weight and therefore the results are expected to be the same.

9.4.3 Weight and Likelihood for the Secondary Vertex Tagger

The weight/likelihood given to a jet by the secondary vertex tagger is calculated in two steps where the second step is the normal weight/likelihood calculation using probability density functions as described in the previous section. The first step calculates a weight according to the reconstruction efficiency of secondary vertices in light and b jets. This probability is measured separately in truth matched light and b jets by counting the number of jets where a secondary vertex has been found divided by all reconstructed jets of a certain truth match type. If r_u and r_b denote the reconstruction efficiencies in light and b jets, respectively, then the weight added to the jet is (see also [52] for weight calculations)

1. $W_{add} = \log \frac{1-r_b}{1+r_b}$ if no secondary vertex was found,
2. $W_{add} = \log \frac{r_b}{r_u}$ if a secondary vertex was found.

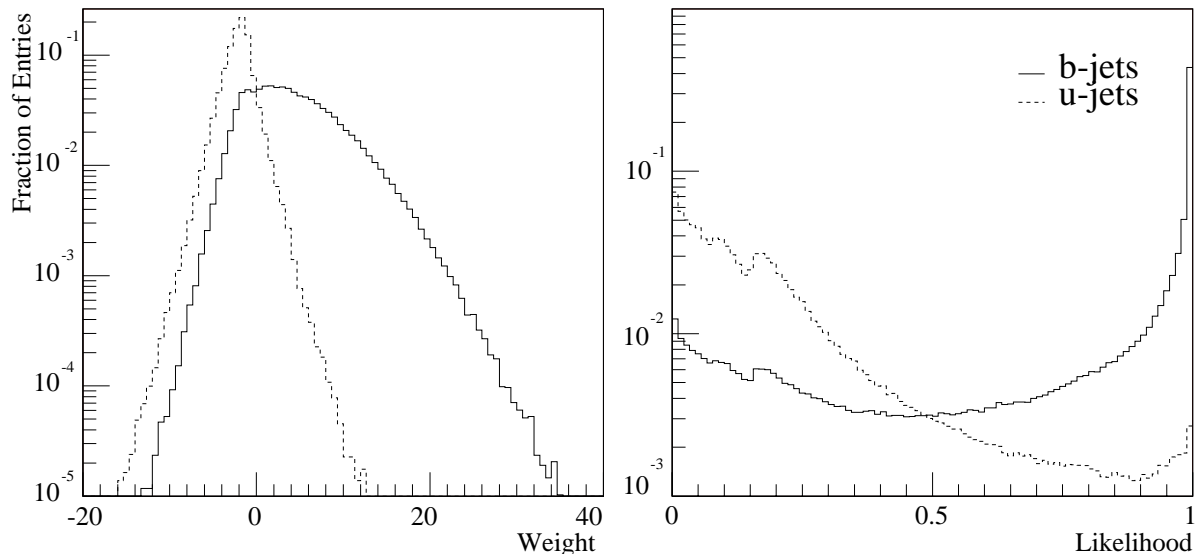


Figure 9.4: Weight/Likelihood for the combined 3D b-tagging algorithm on WH events.

The b jet/light jet likelihoods L_b/L_{light} need to be multiplied by

1. $L_b \cdot \frac{1-r_b}{1-r_b-r_u}$ and $L_{light} \cdot \frac{1-r_u}{1-r_b-r_u}$ if no secondary vertex was found,
2. $L_b \cdot r_b$ and $L_{light} \cdot r_u$ if a secondary vertex was found.

9.5 b-Tagging Performance

This section is dedicated to the performance of the b-tagging algorithms which have been presented in the previous sections. Common b-tagging performance variables are introduced and the track and jet selection cuts are presented. The section about reference histograms explains in detail which b-tagging methods (impact parameter, secondary vertex) and which variables have been used to calculate the weight and the final performance.

The b-tagging performance is studied on the same data sets which have been used to study the primary vertex finder.

9.5.1 Performance Variables: Efficiency and Rejection

The performance of b-tagging algorithms is measured in two connected quantities:

- light jet misidentification efficiency ϵ_u (or light jet rejection $R_u := 1/\epsilon_u$)
- at a given b jet selection efficiency ϵ_b

The selection efficiency is a measure for how many true b jets are identified as such. A 60% efficiency, for example, means that 60% of all b jets can be identified. The background rejection is a measure on how good light jets are rejected and are not misidentified as b jets. It is the inverse of the misidentification efficiency of light jets as b jets. A number of 100 for example

means that 1 light jet in 100 is misidentified as a b jet. The goal of every b-tagging software is to have a high selection efficiency while keeping the b misidentification rate of light jets as low as possible (i.e. a high rejection rate).

9.5.2 Track and Jet Selection Cuts

The track selection cuts used for b-tagging are given in Table (9.1). The distributions of the according variables are shown in Fig. (6.2) of the tracking chapter. The track selection cuts are

p_t	$>$	1. GeV/c
z_0	$<$	1.5 mm
d_0	$<$	1. mm
precision hits	\geq	9
pixel hits	\geq	2
b layer hits	\geq	1

Table 9.1: Track selection cuts for b-tagging.

similar to the ones used in the vertexing but are applied with respect to the primary vertex and hence tighter values can be used for the cut on the z variable. The cut on d_0 is looser because tracks with high impact parameter are not meant to be rejected since they carry relevant tag information. The track selection for the secondary vertex finder are listed in [52].

The jet selection cuts are as presented in chapter 8. For b-tagged jets there is one additional cut which requires at least one associated track in the jet: $N_{tracks} > 1$.

9.5.3 Tagging Methods and Reference Histograms

The performance of the following b-tagging algorithms has been studied:

- impact parameter based b-tagging in z direction (1D), $r\phi$ plane (2D) and z and $r\phi$ combined (3D)
- secondary vertex based b-tagging (SV)

The according names of the C++ tagging tools are: Lifetime1D, Lifetime2D, SecVtxBU. The 3D performance is obtained by combining the results of 1D and 2D and hence no separate implementation is needed. Figure (9.5) shows the significance distributions in z and $r\phi$ which are used as reference histograms by the 1D and 2D impact parameter taggers, respectively. The results of the 1D and 2D tags are combined to a more powerful weight using the combination techniques as presented in section 9.4 and the results obtained by this combination are labelled as 3D.

The secondary vertex based b-tagging method uses the following variables to construct a weight:

- vertex mass
- number of tracks used in the secondary vertex fit (track multiplicity)
- number of good two-track vertices

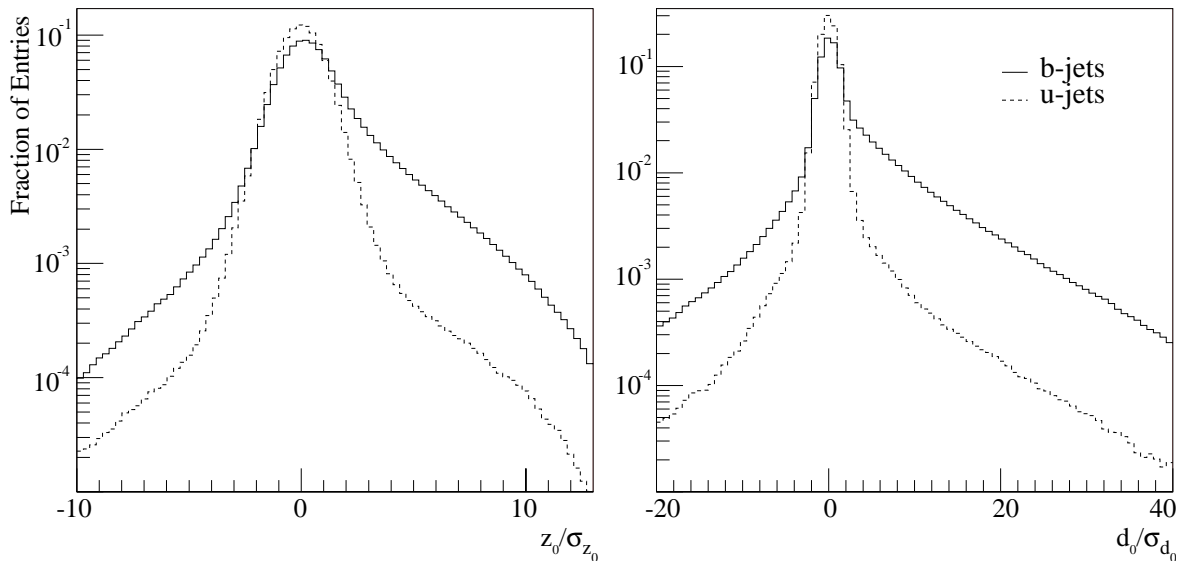


Figure 9.5: Reference histograms for the 1D and 2D impact parameter tagging algorithms for cone4 jets and truth matching using a cone of $\Delta R = 0.3$ around the reconstructed jet to associate b quarks.

- energy of the charged tracks used in the secondary vertex fit divided by the energy of the jet (charged energy fraction)

The distributions of these variables are shown in Fig. (9.6). The mass of the reconstructed secondary vertex in b jets is higher than in light jets. The average mass is close to $2 \text{ GeV}/c^2$ for b jets and a bit less than $1 \text{ GeV}/c^2$ for light jets. The number of tracks used to fit a secondary vertex is significantly higher in b jets than in light jets where most of the reconstructed secondary vertices have two tracks. The average in b jets is 3.5 tracks. The same is true for the number of secondary vertex candidates (which are later combined to the final secondary vertex). Light jets have mostly just one two track vertex which might be taken as a final secondary vertex whereas b jets have an average of 6 two track vertex candidates. The last variable is the energy fraction. In b jets the secondary vertex (i.e. the B meson) carries a significant amount of the energy of the jet which is directly related to the fragmentation function which is harder for b jets than for light jets. In light jets the average energy fraction is 0.15 and in b jets 0.7.

The reference histograms shown in this section use Cone4 jets as input and the cone truth labelling procedure described in section 9.3.2 with a cone size in $\eta\phi$ of $\Delta R = 0.3$. Input events have been $\text{WH}^0(120) \rightarrow l\nu b\bar{b}$, $\text{WH}^0(120) \rightarrow l\nu u\bar{u}$, $t\bar{t}H$ and $t\bar{t}$. The distributions for other jet finding algorithms and the track truth matching procedure are very much alike. The difference is that reconstructed tracks, which are always the same regardless of which jet finder or truth matching is used, might be associated to other jets with possibly different truth label. This works both ways and hence the final difference between the distributions is small. However, the usage of different jet finders and different truth matching has quite an impact on the performance variables. Given the very similar reference histograms this difference is due to the fact that the weight is calculated jet-wise. It makes a big difference for the overall weight of a jet if a track with high impact parameter is suddenly associated to another jet with different truth label.

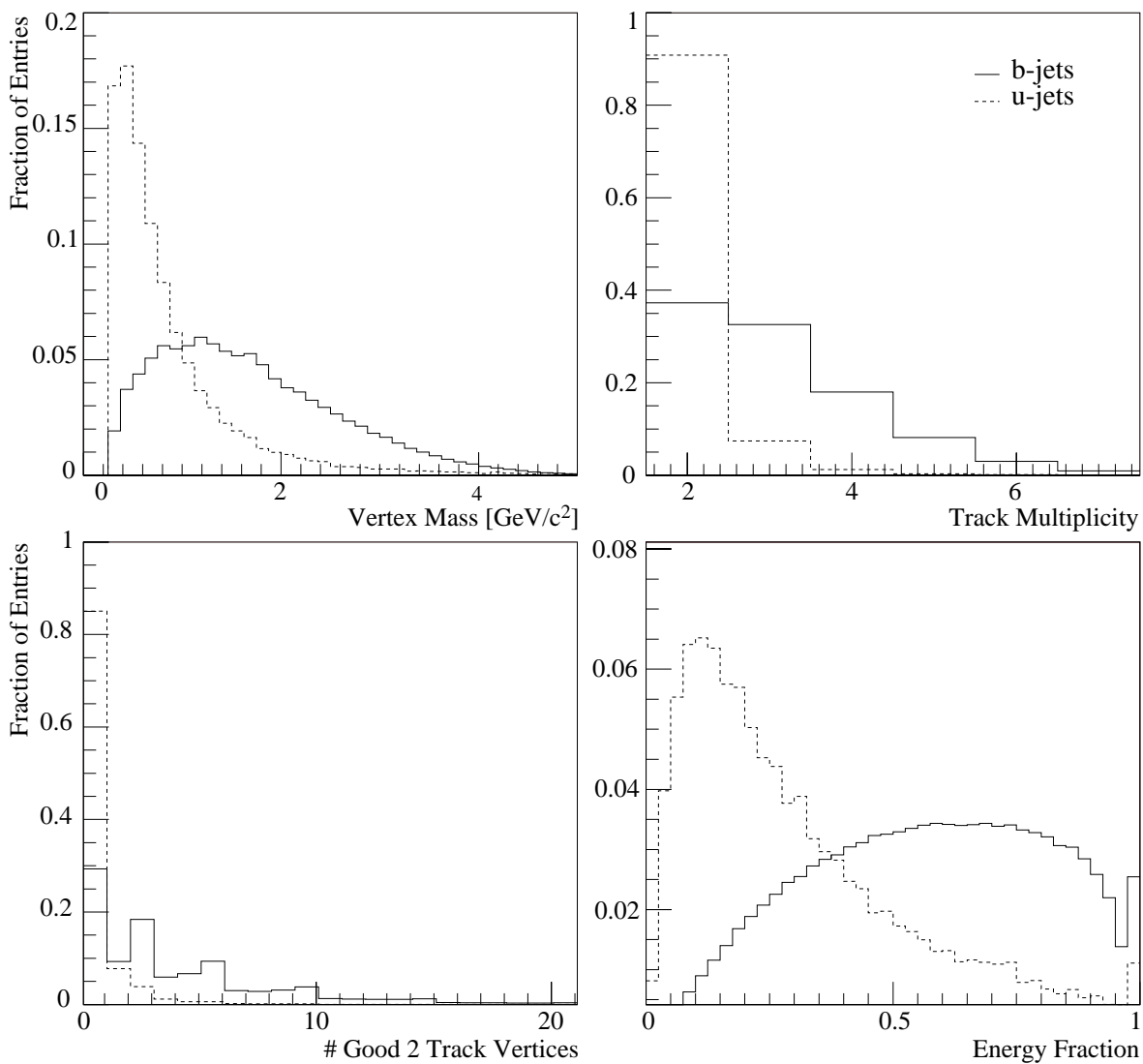


Figure 9.6: Reference histograms for the secondary vertex tagging algorithm for Cone4 jets and cone parton truth matching.

The reference histograms are “all inclusive” for jets with $p_t > 15$ GeV/c and $|\eta| < 2.5$. The performance of the jet-tagging algorithms depends on these variables and separate reference histograms for various η and p_t regions can improve it (as was the case in LEP, see e.g. [58]). However, very high statistics is needed to fill all the bins of the various reference histograms with a small statistical error and hence, for this thesis, it was preferred to use the same reference histograms for all η and p_t regions.

9.5.4 Performance on $WH^0(120) \rightarrow l\nu b\bar{b}$ and $WH^0(120) \rightarrow l\nu u\bar{u}$

The $WH^0(120) \rightarrow l\nu b\bar{b}$ and $WH^0(120) \rightarrow l\nu u\bar{u}$ samples are first used to study the impact of different truth matching and jet finding algorithms on the tagging performance of the impact parameter taggers. The set of truth matching, jet finding and tag combination which gives the best results is chosen for further studies of the influence of a displaced primary vertex and events with pile up.

Impact of Truth Matching and Jet Finding

In ATLAS, three different jet definitions are used. All of them are calorimeter based where two are reconstructed by a cone algorithm with a cone size ΔR of either 0.7 (Cone7 jets) or 0.4 (Cone4 jets) and one by a K_t algorithm (K_t jets). Two different truth matching strategies are in use as explained in section 9.3.2.

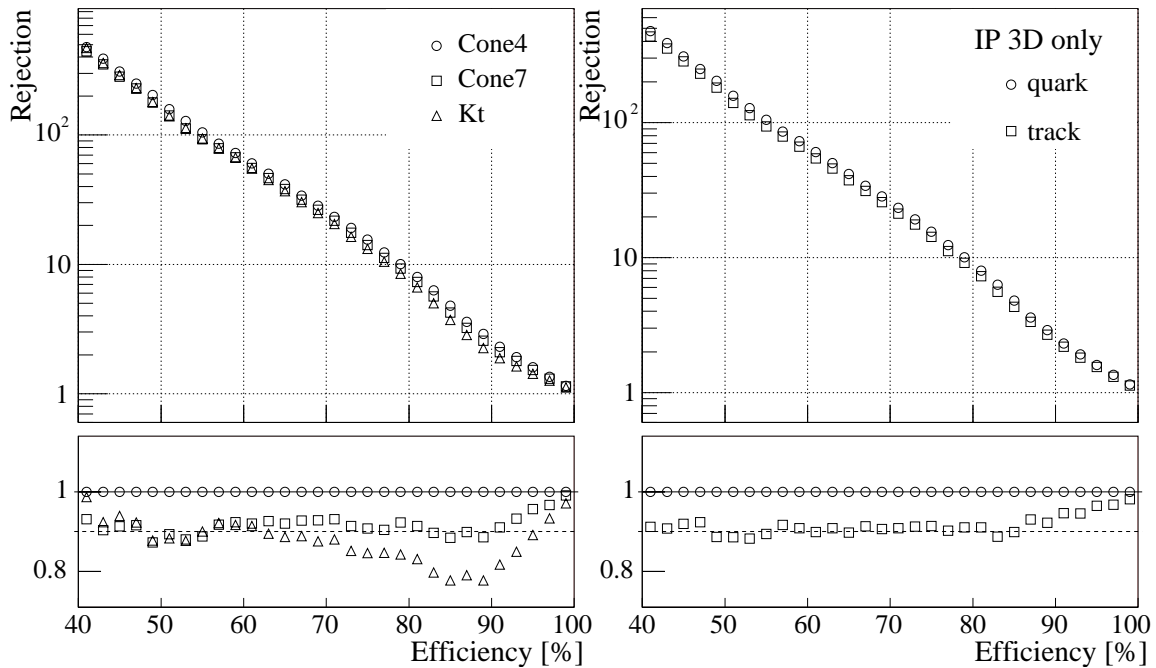


Figure 9.7: Impact of different truth matching and jet finding algorithms on the b-tagging performance on WH(120) samples. The Cone4 jets with standard cone parton truth matching serve as reference. The left plot shows the performance of Cone and K_t relative to Cone4. The right plot shows the performance of the track truth matching relative to the standard cone one for Cone4 jets.

The left plot in Fig. (9.7) shows the impact of different jet finders on the light jet rejection rate. The small plot below shows the Cone7 and K_t jet rejection rates divided by the Cone4 jet rate to better spot the differences. The performance is best with Cone4 jets and worst for K_t jets. For 60% b jet selection efficiency the Cone and K_t algorithms perform about 10% worse than the Cone4 one. The right plot shows the performance using Cone4 jets with cone parton truth matching and track truth matching algorithms. The small plot below shows the ratio of the two (track/parton). The parton truth matching algorithm achieves about 10% better rejection rates than the track truth due to the fact that the track truth matching algorithm mistags more b jets as light jets than the parton one does. This of course has direct impact on the rejection rate because true b jets are not labelled as such and hence contribute to the light jet mistagging rate and decrease the performance.

The best overall performance with the impact parameter taggers is achieved on Cone4 jets and quark truth matching. This combination will be used for all further studies.

Performance of the Impact Parameter Taggers

A comparison of the performance of the 1D, 2D and 3D impact parameter taggers is shown in Fig. (9.8). It shows the rejection as a function of the b jet selection efficiency for all jets with $p_t > 15$ GeV/c and $|\eta| < 2.5$. The left plot is a comparison of the performance of the 1D, 2D and combined 3D taggers concerning the light jet rejection. As expected from the track resolution plots in Fig. (6.3) the light jet rejection of the 2D tagger is better by an average factor of 5 compared to the 1D tagger. The combination of the two yields an increase in light jet rejection power of about 33% at 60% b jet selection efficiency and 30% at 50% b jet selection efficiency. The right plot shows the rejection power of the combined impact parameter tagger for the three common types of background jets: light, c and gluon. The rejection of light, i.e. uds jets, is the best. Jets coming from c quarks more often have a similar topology to the ones from b quarks and therefore the rejection power of c quarks is on average a factor of 5 smaller than for u quarks. Gluon jets play an interesting role as background jets since the splitting rate of gluons into bb is about 6% and hence 6% of all gluon jets will have a b jet topology. This of course limits the gluon jet rejection power.

Exact numbers for the rejection of light and c jets for all impact parameter taggers are shown in Table (9.2) for a b jet selection efficiency of 50%, 60% and 70%. For 60% selection efficiency the rejection of light jets is about 10/45/60 for the 1D/2D/3D taggers respectively.

Performance of the Secondary Vertex Tagger

The rejection rate of light jets and c jets can be dramatically improved when combined with a secondary vertex tagger. As explained earlier, the secondary vertex tagger does not only contribute to the final weight if a secondary vertex has been found in the jet but also if it is absent. The secondary vertex reconstruction efficiency is 65.79% in b jets and 2.92% in light jets. This information is directly used when constructing the weight of the secondary vertex tagger. Figure (9.9) shows the rejection rate as a function of the b jet selection efficiency for the combined 3D tagger alone and in conjunction with the secondary vertex algorithm. The rejection power increases by a factor of 2.5 for 60% and 3.5 for 50% b jet selection efficiency. Table (9.2) summarizes the results. The quoted errors are binomial.

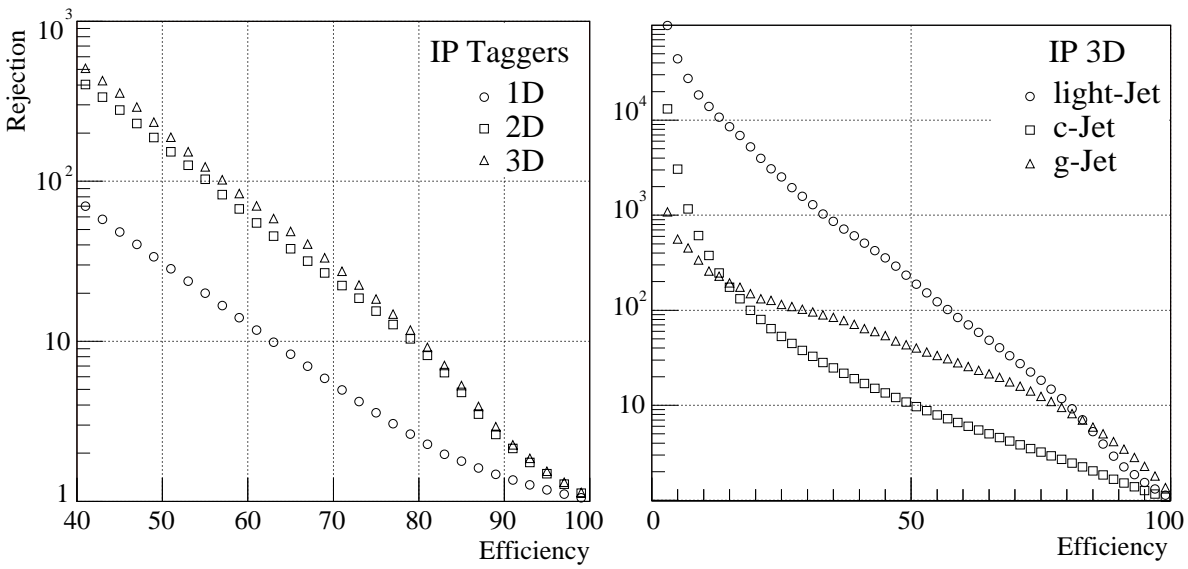


Figure 9.8: Left plot: Comparison of the light jet rejection performance of the 1D, 2D and 3D combined impact parameter taggers. Right plot: Rejection power of the combined tagger for jets labelled as light, c or gluon. Both are obtained using the WH(120) samples.

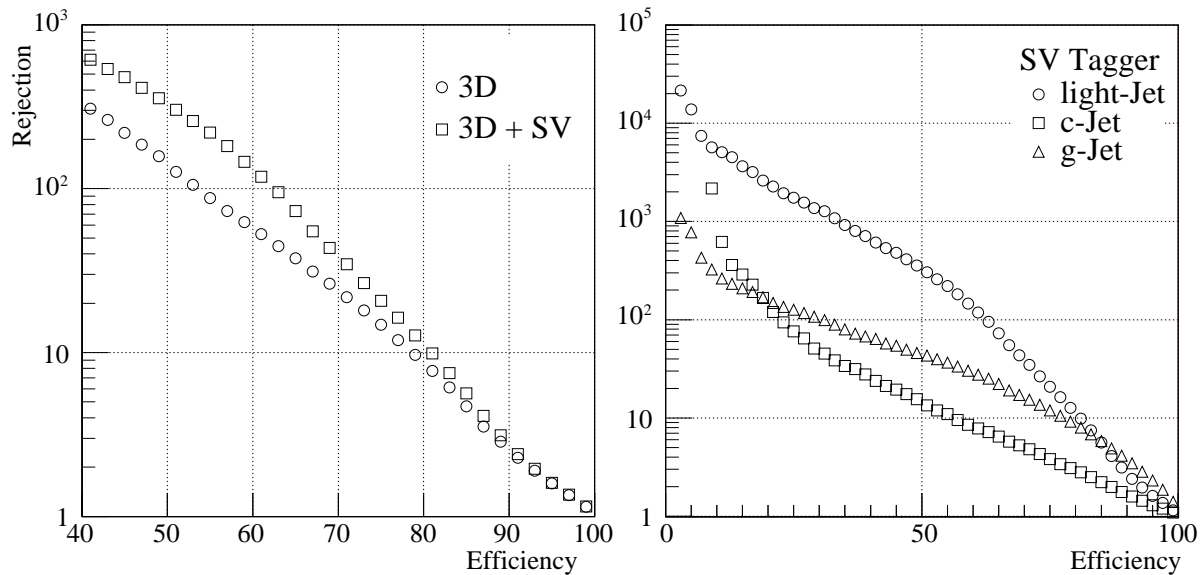


Figure 9.9: Left plot: Comparison of the light jet rejection performance of the 3D impact parameter tagger alone and combined with the secondary vertex tagger. Right plot: Rejection power of the SV+3D combined tagger for jets labelled as light, c or gluon. Both are obtained using the WH(120) samples.

	50%		60%		70%	
	R_u	R_c	R_u	R_c	R_u	R_c
1D	23.4 ± 0.27	7.3 ± 0.3	10.1 ± 0.07	4.3 ± 0.1	4.7 ± 0.02	2.8 ± 0.06
2D	122.8 ± 3.3	8.7 ± 0.4	45.5 ± 0.7	5.7 ± 0.2	18.7 ± 0.2	3.7 ± 0.1
3D	158.1 ± 4.7	11.4 ± 0.6	60.5 ± 1.1	6.8 ± 0.3	23.3 ± 0.3	4.2 ± 0.1
3D + SV	550.6 ± 30.9	14.2 ± 0.9	153.6 ± 4.5	8.3 ± 0.4	38.3 ± 0.6	5.0 ± 0.1

Table 9.2: Performance of the impact parameter and secondary vertex taggers on $WH^0(120) \rightarrow l\nu b\bar{b}$ and $WH^0(120) \rightarrow l\nu u\bar{u}$ events.

p_t and η Dependence

The performance of the tracking depends on p_t and η and this dependence effects directly the performance of b-tagging. Therefore it is expected that the b-tagging performance is better on jets with higher p_t (up to a certain limit) and on jets which are well contained within the Inner Detector (small η). The dependence of the 3D and 3D+SV algorithms on p_t and η is shown in Fig. (9.10). The best p_t region for b-tagging is therefore $70 \text{ GeV}/c < p_t < 150 \text{ GeV}/c$ and $\eta < 1$. The tracking performance decreases very slightly for tracks with $\eta < 0.5$ which also causes the b-tagging performance to slightly decrease again in the very central region. Jets with large transverse momentum are very collimated and are especially challenging for the track reconstruction which has direct impact on the b-tagging performance. There are also more tracks with larger impact parameters in light jets due to the higher momentum of the initial quark. Low p_t jets on the other hand are also harder to tag because the b quark is boosted less and the flight distance of the B hadron is shorter resulting in tracks with smaller impact parameters. The impact parameter resolutions are also worse for tracks with smaller transverse momentum.

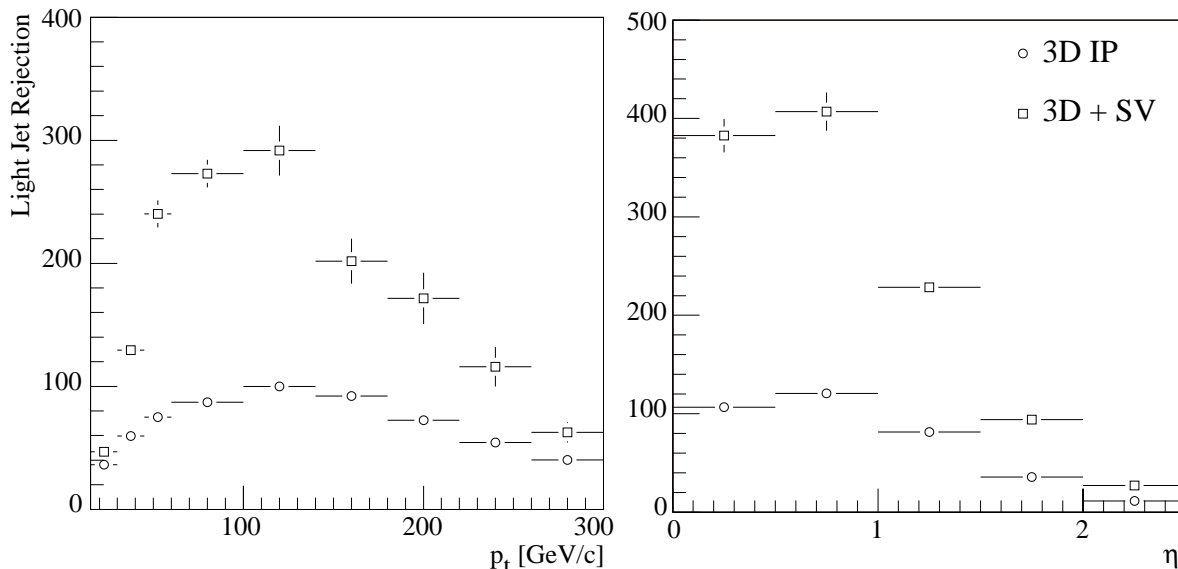


Figure 9.10: η and p_t dependence of the light jet rejection rate for the combined 3D and 3D+SV taggers.

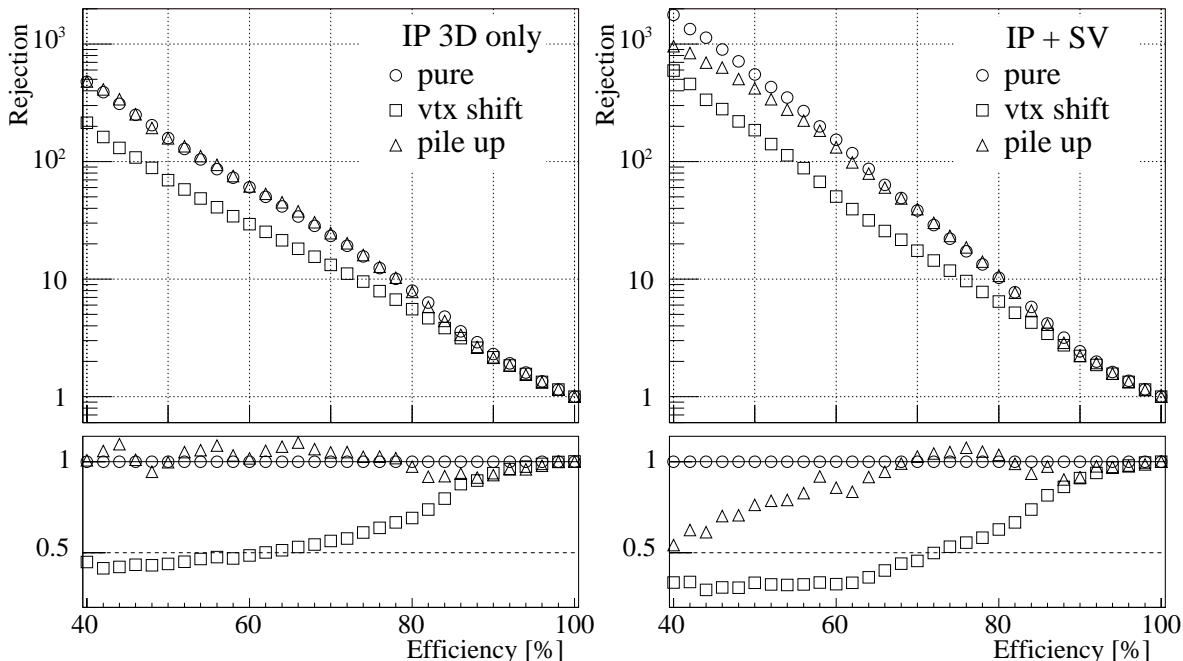


Figure 9.11: Left plot: performance of the 3D tagger on pure, pile up and shifted vertex WH(120) events. Right plot: performance of the combined 3D+SV taggers on these event types.

Displaced Primary Vertex and Pile Up

Figure (9.11) shows a comparison of the light jet rejection for the 3D tagger (left plot) and the 3D+SV tagger (right plot) for *pure* WH(120) events, events with a vertex shift of 1 cm in x direction and events with low luminosity pile up. Table (9.3) lists exact numbers and also holds values for the c jet rejection. The performance on events with shifted vertex however drops dramatically by up to 50%. This severe degradation is believed to be due to the underlying tracking software (iPatRec) which, by that time, was tuned to find and reconstruct tracks which come primarily from the ATLAS global origin and not emerge from as far as 1 cm off (in $r\phi$).

The resolution of impact parameters on pure, pile up and shifted vertex events is comparable (see Fig. (6.3)) but the number of reconstructed tracks in events with shifted vertex is lower than in the exact same events with central primary vertex. In other words, the track reconstruction efficiency is worse for events with a shifted primary vertex. This leads to a slightly worse reconstructed primary vertex in events with shifted vertex and - in conjunction with the lower track reconstruction efficiency - to a degradation of the b-tagging performance on these events. The tracking and vertexing performance on pile up events on the other hand is very similar to the one on pure events. Therefore the observed impact of low luminosity pile up on the b-tagging performance is less severe. The performance turns out to be equal when only the impact parameter taggers are used and about 15-20% less with the secondary vertex tagger turned on.

The degradation of tagging performance in samples with a shifted vertex is not a serious problem. Even though the primary vertex will not be exactly at ATLAS global (0,0,0) it will be known with a precision of $(\pm 15\mu\text{m}, \pm 15\mu\text{m}, \pm 5.6\text{cm})$ around its actual position. The reconstruction software will be given the beamspot position and hence can adjust itself accordingly.

	50%		60%		70%	
	R_u	R_c	R_u	R_c	R_u	R_c
vertex shift						
3D	69.4 ± 2.0	8.7 ± 0.55	29.3 ± 0.5	5.8 ± 0.3	13.2 ± 0.15	3.7 ± 0.14
3D + SV	184.9 ± 8.6	12.2 ± 0.9	50.3 ± 1.2	6.9 ± 0.4	17.4 ± 0.24	4.23 ± 0.17
pile up						
3D	157.5 ± 9.8	15.5 ± 1.9	61.5 ± 2.4	7.9 ± 0.7	24.5 ± 0.6	4.3 ± 0.25
3D + SV	419.9 ± 42.8	18.3 ± 2.6	131.7 ± 7.5	9.6 ± 0.9	39.3 ± 1.2	5.4 ± 0.4

Table 9.3: Performance of the 3D impact parameter and secondary vertex taggers on $WH^0(120) \rightarrow l\nu b\bar{b}$ and $WH^0(120) \rightarrow l\nu u\bar{u}$ events with pile up and vertex shift.

9.5.5 Performance on $t\bar{t}H^0$, $H^0 \rightarrow b\bar{b}$ and $t\bar{t}$ background

The $t\bar{t}H^0(120)$, $H^0(120) \rightarrow b\bar{b}$ channel is a potential Higgs Boson discovery channel which, with four b jets in the final state, strongly depends on a well performing b-tagging software. Compared to $WH^0(120) \rightarrow l\nu b\bar{b}$, $t\bar{t}H$ events are more realistic and busy events meaning they are more demanding on the detector and reconstruction performance itself (higher occupancy of the detectors, higher track multiplicity). Some aspects, however, are not necessarily a disadvantage for the b-tagging performance.

Figure (9.12) shows a comparison between $t\bar{t}H$ and WH events of variables which are important for b-tagging: jet and track multiplicities, jet transverse momentum and jet η . The average number of jets in $t\bar{t}H$ events is 7.5, in $WH \rightarrow b\bar{b}$ 3.5. $t\bar{t}H$ events on average have 65 reconstructed tracks, that is twice as many as for $WH^0(120) \rightarrow l\nu b\bar{b}$, and leads to a better resolution of the reconstructed primary vertex (see Table (7.9)). The average transverse momentum in $t\bar{t}H$ events is 60 GeV/c, in $WH \rightarrow b\bar{b}$ 44 GeV/c. The η distribution of both event types are very similar where $t\bar{t}H$ events have slightly more centralised jets (due to their higher transverse momenta). As shown in the last section, the b-tagging performance is better for jets with p_t around 100 GeV/c and $\eta < 1$ and, with also a better reconstructed primary vertex, we expect a better “all inclusive” performance of the b-tagging algorithms on the $t\bar{t}H$ sample.

The left plot in Fig. (9.13) shows the performance of the 3D impact parameter tagger alone and combined with the secondary vertex tagging algorithm. The right plot shows the rejection power of the 3D+SV taggers on the three background jet types: light, c and gluon. All plots use the Cone4 jet definition and the parton truth matching technique. Table (9.4) lists exact numbers for light jets and c jets.

The light rejection power of the 3D tagger is 190/70/27 and the use of the secondary vertex tagger improves it to 650/200/50 for 50/60/70% b jet selection efficiency. This is an increase in light jet rejection of a factor of about 3.5/2.8/1.9 for 50/60/70% b jet selection efficiency. The c jet rejection is 10/6/3.8 of the 3D tagger and 12/7/4.5 for the combined 3D+SV tagger, again on 50/60/70% b jet selection efficiency. Due to the more similar topology of c jets to b jets the secondary vertex tagger cannot improve the rejection power of c jets as much as for light jets. It is on average 15-20% better.

All the primary vertex and b-tagging studies have been done on data sets which were simulated using two Pixel layers in the Inner Detector. However, the analysis of the $t\bar{t}H$ sample has been carried out later where it was already clear that the final ATLAS detector will have 3 Pixel

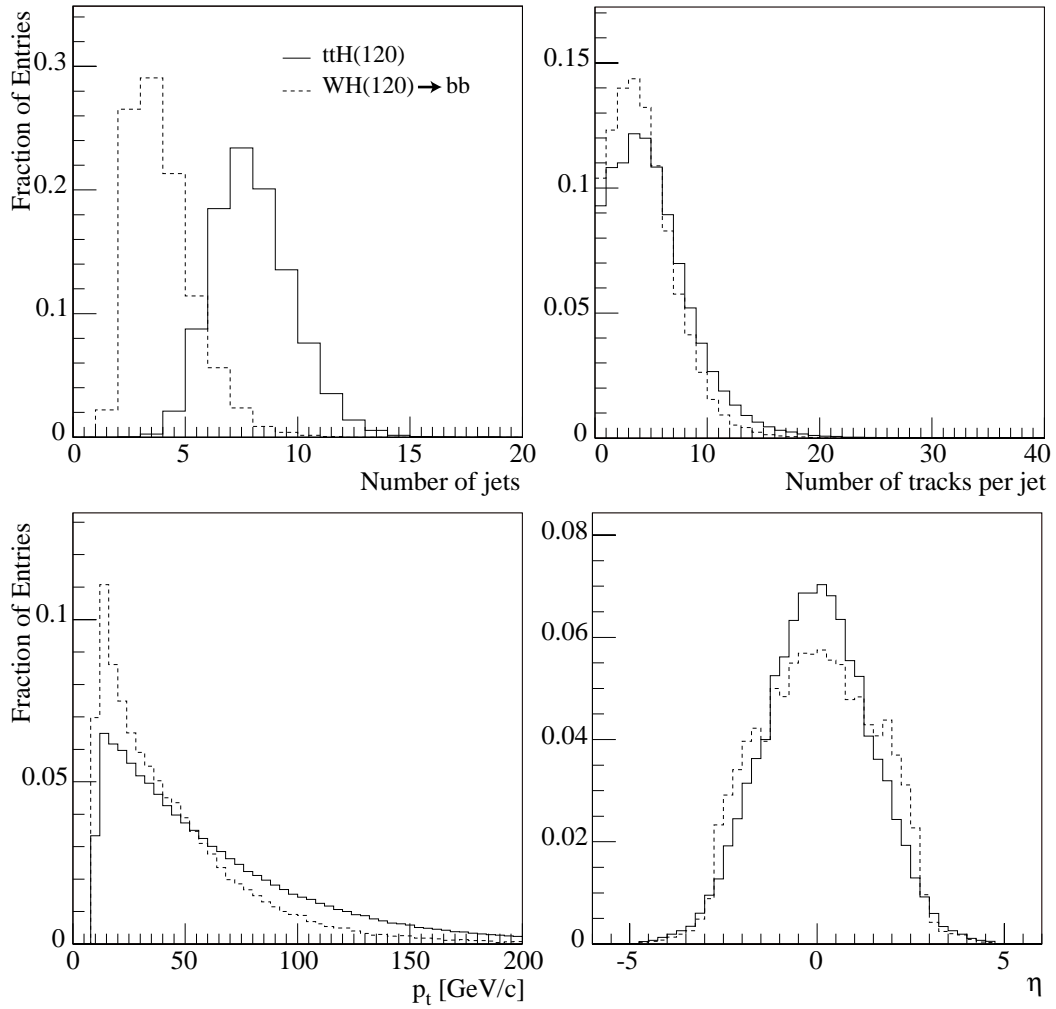


Figure 9.12: Comparison of jet quantities which have an impact on the b-tagging performance in $tt\bar{H}^0(120)$, $H^0(120) \rightarrow b\bar{b}$ (solid curve) and $WH^0(120) \rightarrow l\nu b\bar{b}$ (dashed curve) events. The jet type is Cone4.

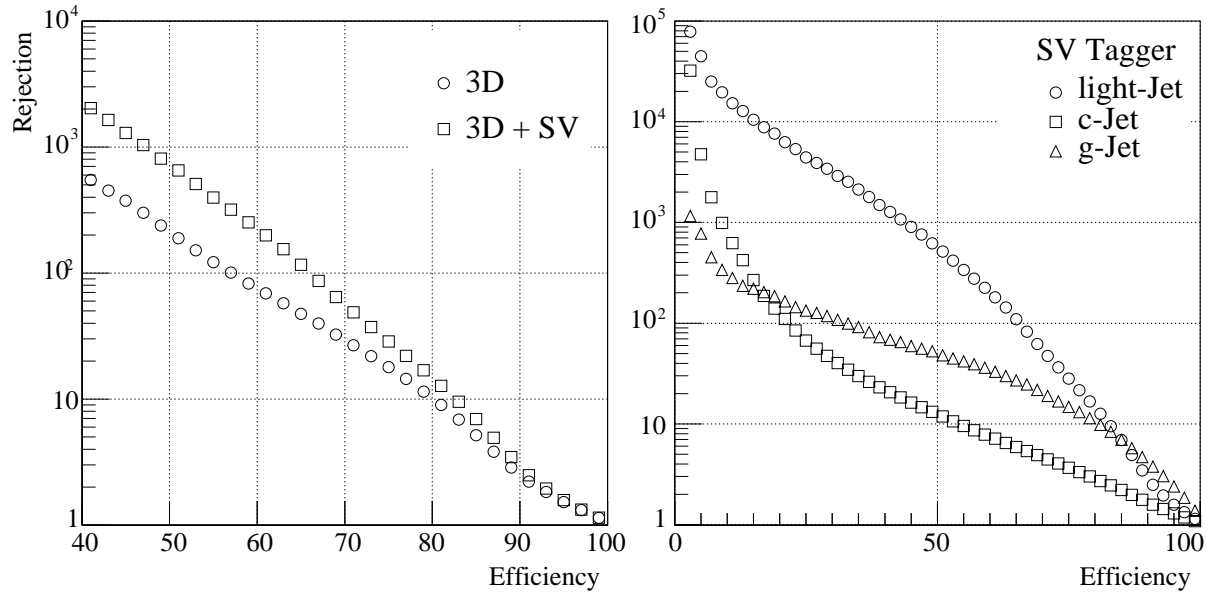


Figure 9.13: Left plot: Comparison of the light jet rejection rate of the 3D impact parameter tagger alone and combined with the secondary vertex tagger. Right plot: Rejection power of the SV+3D combined tagger for jets labelled as light, c or gluon. The plots are for the $t\bar{t}H^0(120)$, $H^0(120)\rightarrow b\bar{b}$ sample.

layers in the Inner Detector after all. Therefore, the b-tagging performance for the $t\bar{t}H$ sample has also been studied on the 3 Pixel layout. It has been shown in earlier studies on b-tagging in ATLAS that a 3 layer Pixel detector enhances the light jet rejection by around 20% [49]. Similar results are expected when comparing the performance on the $t\bar{t}H$ channel. The last row of Table (9.4) lists the light jet rejection performance of the 3D+SV b-tagging algorithms for the 3 layer layout. The performance is 701/225/53 for 50/60/70% efficiency and is better by about 10-15%. The improvement is not quite as good as observed in earlier studies but the number of Pixel layers is not the only difference between the two $t\bar{t}H$ samples. The version of Pythia [25] which is used by the ATLAS software to generate the $t\bar{t}H$ events has also changed from Pythia 6.221 to 6.323. It features a complete new scenario for multiple interactions where the parton shower model in the fragmentation process uses a new approach called “junction fragmentation” which lifts the restriction that only the first parton in the cascade could undergo initial and final state radiation. Now all subsequent partons are allowed to do so leading to a different event structure which affects the b-tagging performance.

	50%		60%		70%	
	R_u	R_c	R_u	R_c	R_u	R_c
3D	189.2 ± 3.3	9.6 ± 0.07	68.9 ± 0.7	6.0 ± 0.04	26.7 ± 0.17	3.8 ± 0.02
3DSV	650.0 ± 21.0	11.8 ± 0.1	198.6 ± 3.6	7.1 ± 0.05	48.8 ± 0.43	4.5 ± 0.02
3 layer						
Pixel 3DSV	701.2 ± 20.3	11.3 ± 0.2	225.3 ± 4.0	7.6 ± 0.09	53.4 ± 0.4	5.1 ± 0.03

Table 9.4: Performance of the 3D impact parameter and secondary vertex taggers on $t\bar{t}H^0(120)$, $H^0(120) \rightarrow b\bar{b}$. The last column also lists numbers for $t\bar{t}H$ samples produced with the 3 Pixel layer detector layout.

9.6 Summary

This chapter presented various b-tagging algorithms and their performances. To obtain these results a whole new modular and extendable b-tagging software environment has been developed as part of this thesis work.

Tagging algorithms under consideration have been a 1D and 2D impact parameter tagger which makes use of the z_0 and d_0 track impact parameters, respectively, a 3D tagger which combined the weight of the 1D and 2D tagger and a secondary vertex tagger which is combined with the 3D weight.

The performance section began with a comparison of rejection rates for the various jet finders (Cone7, Cone4 and K_t) and truth matching algorithms (parton cone, track). The combination of Cone4 jets with parton cone truth matching yields the best performance and they have been used for all further studies.

The performance of the tagging algorithms was looked at for WH with $H^0 \rightarrow b\bar{b}$ and $H^0 \rightarrow u\bar{u}$, $t\bar{t}H$ and $t\bar{t}$ events. For the first two the influence of pile up and a shifted primary vertex was also studied. Table (9.5) and Fig. (9.14) give a summary of the light jet rejection for all samples for the 3D and the 3D+SV taggers. The results can be directly related to the tracking/vertex finding performance on these samples. The performance on events with pile up was found to be comparable to that on pure events. The performance on events with a shifted primary vertex has been found to be degraded by 50%. This however is not a serious problem because the actual beamspot position and resolution will be known to the reconstruction algorithms and can be taken into consideration accordingly. In addition, a shift by 1 cm is very unlikely and can be seen as a worst case scenario.

The performance of the b-tagging software in general is very promising. Standard “expectations” of a light jet rejection of 100 for a b jet selection efficiency of 60% can be met easily with the tagging software on top of the present detector modelling inside the simulation. However, running on real data can and will degrade the performance because of various reasons. A big issue for the performance of the b-tagging on real data will be the residual misalignment of the detector and of course the challenge to obtain meaningful reference histograms, which, in the case of the studies presented here, are obtained by using truth information.

$\epsilon_b = 60\%$	3D		3D + SV	
	R_u	R_c	R_u	R_c
WH pure	60.5 ± 1.1	6.8 ± 0.3	153.6 ± 4.5	8.3 ± 0.4
WH pile up	61.5 ± 2.4	7.9 ± 0.7	131.7 ± 7.5	9.6 ± 0.9
WH vtx shift	29.3 ± 0.5	5.8 ± 0.3	50.3 ± 1.2	6.9 ± 0.4
t \bar{t} H Rome	68.9 ± 0.7	6.0 ± 0.04	198.6 ± 3.6	7.1 ± 0.05
t \bar{t} H CSC	75.3 ± 1.8	6.6 ± 0.06	225.3 ± 4.0	7.6 ± 0.09

Table 9.5: Summary of the b-tagging performance on all samples for 60% b jet selection efficiency. The numbers are for the Cone4 jet definition and the cone parton truth matching.

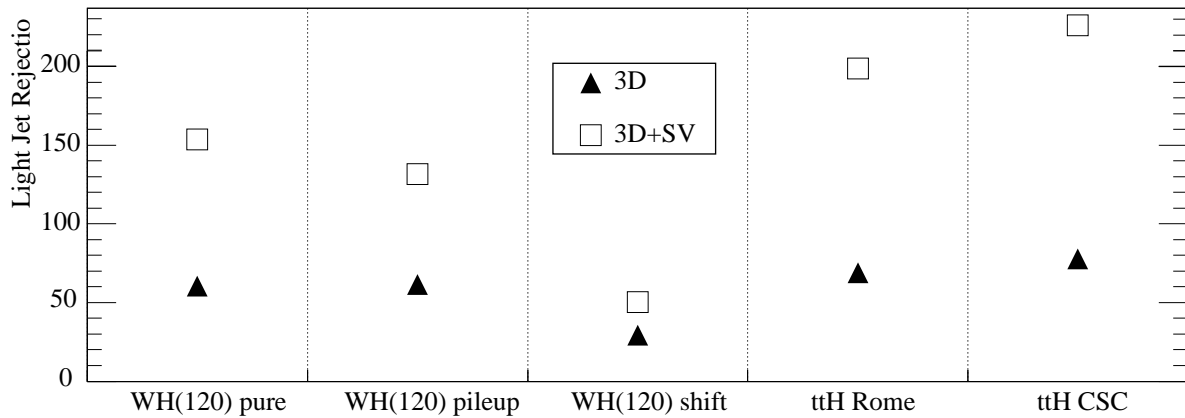


Figure 9.14: Summary of the b-tagging performance in terms of light jet rejection rates at 60% efficiency on all samples used for the 3D and 3D+SV tagging algorithms.

Chapter 10

Analysis of the Channel $t\bar{t}H^0$, $H^0 \rightarrow b\bar{b}$

The discovery of the Higgs boson is one of the major goals of the ATLAS experiment at the LHC. For a light Standard Model Higgs Boson, which is favoured by current EW data ($114 \text{ GeV}/c^2 < m_H < 199 \text{ GeV}/c^2$) [20], associate production with a top quark pair and later decay of the Higgs boson into a pair of b quarks is a very interesting and promising channel. This $t\bar{t}H^0(120)$, $H^0(120) \rightarrow b\bar{b}$ channel was first considered for ATLAS in [59]. It turned out that the reconstruction of the Higgs boson mass in this channel is mostly a combinatorial problem because the final state consists of 2 light and 4 b jets from the decay chains $t \rightarrow jjb$, $t \rightarrow l\nu b$ and $H \rightarrow b\bar{b}$. Two b jets out of four b-tagged jets need to be assigned to the Higgs decay. Without any hint about which two b quarks stem from the Higgs boson, the two correct pairs will only be assigned in 17% of all cases. In [60] it was therefore first suggested to fully reconstruct the whole event and assign two of the four b quarks to the $t \rightarrow Wb$ decays in order to reduce the combinatorial choices for the reconstruction of the Higgs boson.

This chapter re-evaluates the significance of the $t\bar{t}H$ channel in the ATLAS experiment for a Higgs mass of $120 \text{ GeV}/c^2$. The study is based on the analysis steps as presented in the Physics TDR [31]. It is based on fully simulated and fully reconstructed events but also uses results from fast simulation for comparison. The reconstruction algorithms for vertexing and b-tagging developed during this thesis are applied. For signal reconstruction, two different detector layouts were looked at. The difference between them is the number of pixel layers. The layout used for the study of the vertexing and b-tagging performance has 2 layers in the inner most Pixel Detector. The layout used for the final analysis of the $t\bar{t}H$ channel has 3 pixel layers. For convenience, the 2 layer layout is called “Rome” layout because it was used for studies in preparation of the ATLAS Physics Workshop in Rome, 2005. The 3 layer layout is called “CSC” layout because it is used for the Computing System Commissioning (CSC) production. It resembles the actual layout of the ATLAS detector concerning the number of pixel layers at the start up of data taking.

Final results of the $t\bar{t}H$ analysis are only calculated for the CSC layout because of lack of background events in case of the Rome layout. All results are compared to the ones given in the TDR related part of the thesis of J. Cammin [32] which represents a recent fast simulation based study of the $t\bar{t}H$ channel.

This chapter starts with a brief description of the signal and background channels, their

generation and cross sections. Event selection cuts and the reconstruction of the final state are then shown. Results are presented at the end followed by a conclusion.

If not indicated otherwise all plots shown are for the CSC samples. Numbers in tables will mostly state results obtained with CSC and Rome samples and - where applicable - they are compared to J. Cammins TDR style analysis.

10.1 Description of the Signal and Background Channels

In the $t\bar{t}H$ channel, the Higgs boson is produced via associate production with a pair of top quarks. The two top quarks decay in more than 99% of all cases into a W vector boson and a b quark [22]. Each W decays further either hadronically or leptonically. For this analysis the interesting channel is the semileptonic decay of the two tops where one W is forced to decay leptonically into $e^\pm\nu$ or $\mu^\pm\nu$. Without this lepton in the final state no suitable trigger condition would be present. The Higgs boson decays into a pair of b quarks and the Higgs mass was set to 120 GeV/ c^2 in all samples.

The main background arises from three sources which are in order of importance:

1. irreducible continuum $t\bar{t}b\bar{b}$ background from gluon and quark fusion
2. general reducible $t\bar{t}$ background, with additional jets from QCD initial and final state radiation
3. irreducible background mediated by electro-weak gauge bosons: $gg \rightarrow Z/\gamma/W \rightarrow t\bar{t}b\bar{b}$

In the generation of these background channels the two top quarks decay into Wb, one W decays into $l\nu$ (e^\pm or μ^\pm as in the signal) and the other W decays into light quarks. A summary of generated events for signal and background processes used in this study is shown in Table (10.1).

	Sample	$\sigma_{incl.}$ [pb]	$\sigma_{excl.}$ [pb]	Generator	Events	
					full	fast
CSC	$t\bar{t}H$	0.52	0.105	Pythia 6.323	90k	290k
	$t\bar{t}b\bar{b}$	8.2	2.4	AcerMC+Pythia 6.323	45k	
	$t\bar{t}$	833	247	MC@NLO+Herwig+Jimmy	350k	350k

Table 10.1: Cross sections and number of events for the CSC samples used in this analysis. $\sigma_{incl.}$ denotes the total production cross section of the process and $\sigma_{excl.}$ includes the branching ratios for e.g. $H \rightarrow b\bar{b}$ and $t\bar{t} \rightarrow l\nu b j\bar{b}$ ($l=e$ or μ).

The $t\bar{t}H$ signal is generated with Pythia [25]. The $t\bar{t}b\bar{b}$ background sample is done with AcerMC [61] to generate the hard process and is then interfaced to Pythia for initial and final state radiation and hadronisation. The $t\bar{t}$ background events are done with MC@NLO [62, 63] to calculate the hard process using matrix elements and the four vectors are interfaced to Herwig [64] for fragmentation/hadronisation. The underlying event of the $t\bar{t}$ sample is simulated by Jimmy [65]. The $t\bar{t}$ events contain a certain fraction of $t\bar{t}b\bar{b}$ events and when counting the final number of background events that survive all the selection cuts and reconstruction steps it is important to subtract these events again.

The $t\bar{t}H$ channel has an inclusive leading-order cross section of 0.52 pb at $E_{cm} = 14$ TeV [5]. The branching ratio of the Higgs boson into $b\bar{b}$ at $m_H = 120$ GeV/ c^2 is 70% and the branching ratio of $t\bar{t} \rightarrow l\nu b j\bar{b}$ with $l=e$ or μ is 29% which leaves an exclusive cross section of about 0.105 pb. The $t\bar{t}b\bar{b}$ irreducible background has an inclusive cross section of 8.6 pb (8.1 pb for gg fusion and 0.5 for qq fusion) and is one of the largest backgrounds because it also has 4 b quarks in the final state which make its suppression more difficult. Easier to reject than the $t\bar{t}b\bar{b}$ is the general $t\bar{t}$ background. It is very important because of its large inclusive cross section of 833 pb which has been calculated in next-to-leading-order (NLO) [6]. The electro-weak irreducible background is hard to reject because of the two extra b jets. However, it has a relatively small cross section of 0.9 pb and the decay into the two extra b quarks is resonant. It was shown in [32] that this background channel contributes about 10% to the overall reducible $t\bar{t}$ and irreducible $t\bar{t}b\bar{b}$ background and has been considered indirectly by enhancing the number of background events by 10%.

Particle masses and their widths are set as follows: $m_{top} = 175$ GeV/ c^2 , $m_W = 80.425$ GeV/ c^2 , $\Gamma_W = 2.124$ GeV, $m_Z = 91.19$ GeV/ c^2 and $\Gamma_Z = 2.495$ GeV. CTEQ6L is the standard set of structure functions and CTEQ6M is used with MC@NLO.

Rome samples have been simulated and digitised with Athena 9.0.4 and reconstructed with Athena 10.0.2. For CSC samples Athena 11.0.41 was used for all steps.

Characteristics of the Generated Samples

Figure (10.1) shows some characteristics of the generated samples in terms of transverse momentum and η distribution of the lepton from the W decay, the b quarks from the top decay and the b quarks from the Higgs decay. The plot shows the distribution for the CSC $t\bar{t}H$, $t\bar{t}b\bar{b}$ and $t\bar{t}$ samples. Table 10.2 gives a comparison also to the Rome samples and to the samples used by J. Cammin.

In the CSC samples, the average p_t of the lepton from the W decay is 59 GeV/ c for $t\bar{t}H$, 49 GeV/ c for $t\bar{t}$ and 56 GeV/ c for $t\bar{t}b\bar{b}$. The transverse momenta of the b quarks from the top decay are on average 79 GeV/ c , 71 GeV/ c and 77 GeV/ c in $t\bar{t}H$, $t\bar{t}$ and $t\bar{t}b\bar{b}$ samples, respectively. The p_t of the b quarks from the Higgs decay is on average 72 GeV/ c in the $t\bar{t}H$ sample whereas the two extra b's in the $t\bar{t}b\bar{b}$ sample which might fake the presence of the Higgs boson have an average transverse momentum of 41 GeV/ c .

Compared to the Rome samples and especially to the TDR samples small differences in the events produced with Pythia, i.e. $t\bar{t}H$ and $t\bar{t}b\bar{b}$, can be seen. The average transverse momentum of the lepton in the CSC sample is 5% higher than in Rome and TDR samples. The p_t of the b jets from top and Higgs decays are only very slightly higher by the order of 1%. The additional b jets in the $t\bar{t}b\bar{b}$ sample have a 7% higher average transverse momentum in the CSC sample than in the TDR samples which might make this background harder to reject in the CSC samples.

There are also differences in the transverse momenta of the lepton and the b quark in $t\bar{t}$ events where Rome samples turn out to have the highest average transverse momenta. CSC samples and TDR samples, even though the former uses MC@NLO and the latter Pythia, are very similar w.r.t. the p_t spectrum of the lepton and the b quarks.

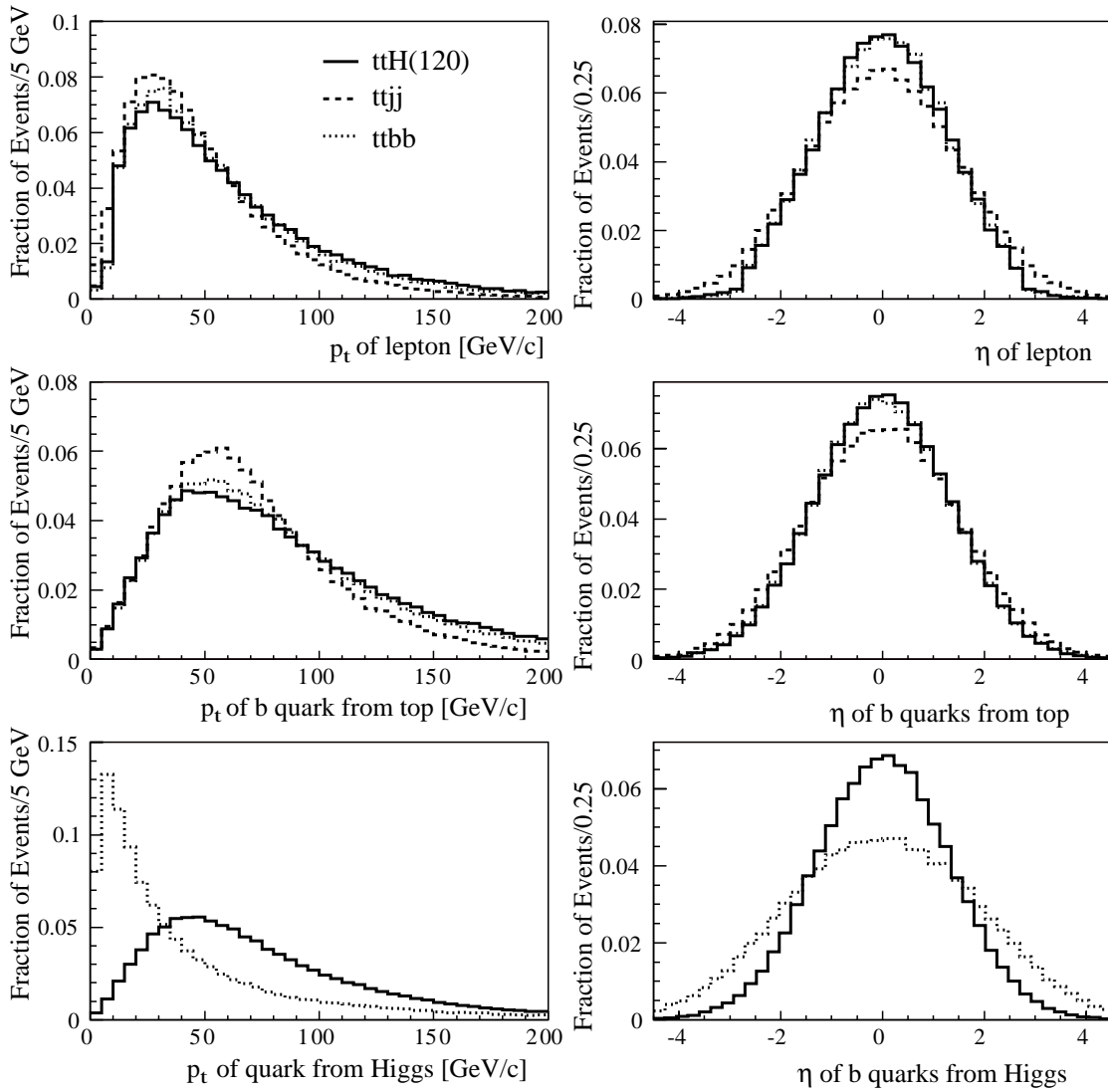


Figure 10.1: Event characteristic on generator level for signal and background processes for CSC samples. Solid lines denote $t\bar{t}H$ events, dashed lines $t\bar{t}$ events and dotted lines $t\bar{t}b\bar{b}$ events.

Mean p_t in [GeV/c]	lepton			b jets from top			b jets from Higgs	
	$t\bar{t}H$	$t\bar{t}$	$t\bar{t}b\bar{b}$	$t\bar{t}H$	$t\bar{t}$	$t\bar{t}b\bar{b}$	$t\bar{t}H$	$t\bar{t}b\bar{b}$
CSC	59	49	56	79	71	77	72	41
Rome	56	54		78	73		71	
Cammin/TDR	57	50	53	78	71	75	71	38

Table 10.2: Mean of the p_t distribution of the lepton from the W decay, the b quarks from the top decay and the b quarks from the Higgs decay on generator level.

10.2 Event Selection

The event selection cuts are based on the selection cuts used in the TDR analysis and, for full and fast simulation, consist of the following steps:

- at least 1 isolated lepton with $p_t > 20(25)$ GeV/c in case of muon(electron) and $\eta < 2.5$
- at least 6 reconstructed jets with $p_t > 20$ GeV/c and $\eta < 5$
- out of these 6 jets 4 must be tagged as a b jet with $\eta < 2.5$

In fast simulation muons and electrons are created directly from truth information and the only source of loss (i.e. that the selection cuts are not 100% efficient) are kinematic cuts and isolation criteria. b jets are labeled randomly as such where the standard setting is that for 60% selection efficiency there is 1% misidentification of light jets as b jets and 10% misidentification of c jets as b jets.

In full simulation the criteria to select reconstructed muons, electrons and b jets are a bit more complex. Lepton selection cuts have been chosen similar to the ones used by $H \rightarrow 4$ lepton analyses which heavily depend on efficient reconstruction and selection of 4 leptons per event. Electron candidates are required to have a reconstructed track in the Inner Detector and less than 8 GeV energy deposit in the calorimeter within a cone of 0.2 around the electron. In addition the so called isEM() flag [67] is required in a way that electron identification is only based on the calorimeters. Muon candidates are required to have a reconstructed track in the Inner Detector and the Muon Spectrometer. Isolation requires not more than 6 GeV energy deposit in the calorimeter within a cone of 0.2 around the muon candidate.

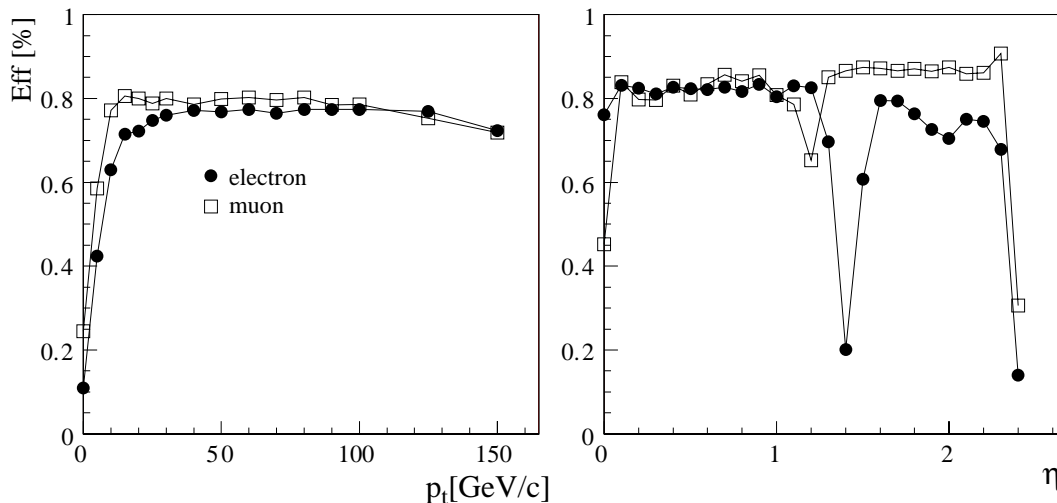


Figure 10.2: Reconstruction efficiency of electrons and muons for $t\bar{t}H$ CSC events in full simulation. The selection efficiency is very stable within the acceptance region of $p_t > 20$ GeV/c and $|\eta| < 2.5$ with some expected drops in η regions where the detector has certain imperfections like cracks.

With these cuts an average reconstruction efficiency of 74(78)% for electrons(muons) is achieved with a fake rate of 4.8(3.2)%. Figure (10.2) shows the selection efficiency for electrons and muons as a function of η and p_t . The p_t dependent selection efficiency is about

constant for electrons(muons) which have a p_t of more than 20(25) GeV/c. In η the selection efficiency is also rather constant within the acceptance region of $|\eta| < 2.5$. In the crack regions of the detector (i.e. regions with no modules) there are some expected drops in efficiency. Examples are the regions around $\eta = 0$ for muons where no muon chambers are present and the transition region around $\eta = 1.2$ between barrel detectors and endcaps which affects the quality of reconstruction for both muons and electrons.

The jet reconstruction in full simulation is done by the Cone4 jet finder algorithm (see chapter 8). b-tagging is done using the combined 1D, 2D and SV taggers as described in chapter 9. For a b jet selection efficiency of 60% a light jet rejection of 225 could be achieved in CSC samples and 190 in Rome samples.

The multiplicity of reconstructed jets and b jets after kinematic cuts is shown in Fig. (10.3). For all but the $t\bar{t}$ background, the multiplicity of reconstructed jets in the fast simulation is higher than for full simulation. Comparison to J. Cammins analysis on fast simulation yields on average 7.5 jets per event for the $t\bar{t}H$ signal events which is yet another 10(4)% higher than observed in this analysis for full (fast) simulation.

	# jets			# b jets		
	$t\bar{t}H$	$t\bar{t}b\bar{b}$	$t\bar{t}$	$t\bar{t}H$	$t\bar{t}$	$t\bar{t}b\bar{b}$
CSC full	6.8	6.2	4.7	2.2	1.7	1.1
CSC fast	7.2	6.5	4.7	2.2	1.8	1.1
Cammin/TDR	7.5					

Table 10.3: Average jet and b jet multiplicity in signal and background samples for CSC full and fast simulation and for Cammin/TDR.

10.3 Parton-Jet Matching

The $t\bar{t}H$ final state consists of 4 b and 2 light jets. Correct assignment to the according decays (i.e. assign the correct two b jets to the Higgs decay) is important to properly reconstruct the masses. To see how many and which reconstructed jets have been correctly assigned to a certain decay it is important to relate the true quarks from the underlying hard process to the reconstructed jets. This is done in the same way as for the measurement of the performance of the b-tagging algorithms. The only difference is the matching cone size which in accordance to J. Cammins analysis was set to 1.0.

The true quark and reconstructed jet which are closest to each other are matched. If a true quark is further away than 1.0 in ΔR (or another - closer - true quark has already been assigned) then the quark is unmatched. With this procedure on average about 73.0% of all input quarks can be matched to a jet. This is in good agreement with the quoted 72% in J. Cammins thesis.

10.4 Jet Energy Calibration

The reconstruction of the mass spectra of the hadronic W decay, the top decays and the Higgs decay depend on a good jet energy calibration. The H1 standard jet energy calibrating has been used for all jets as described in chapter 8.3.

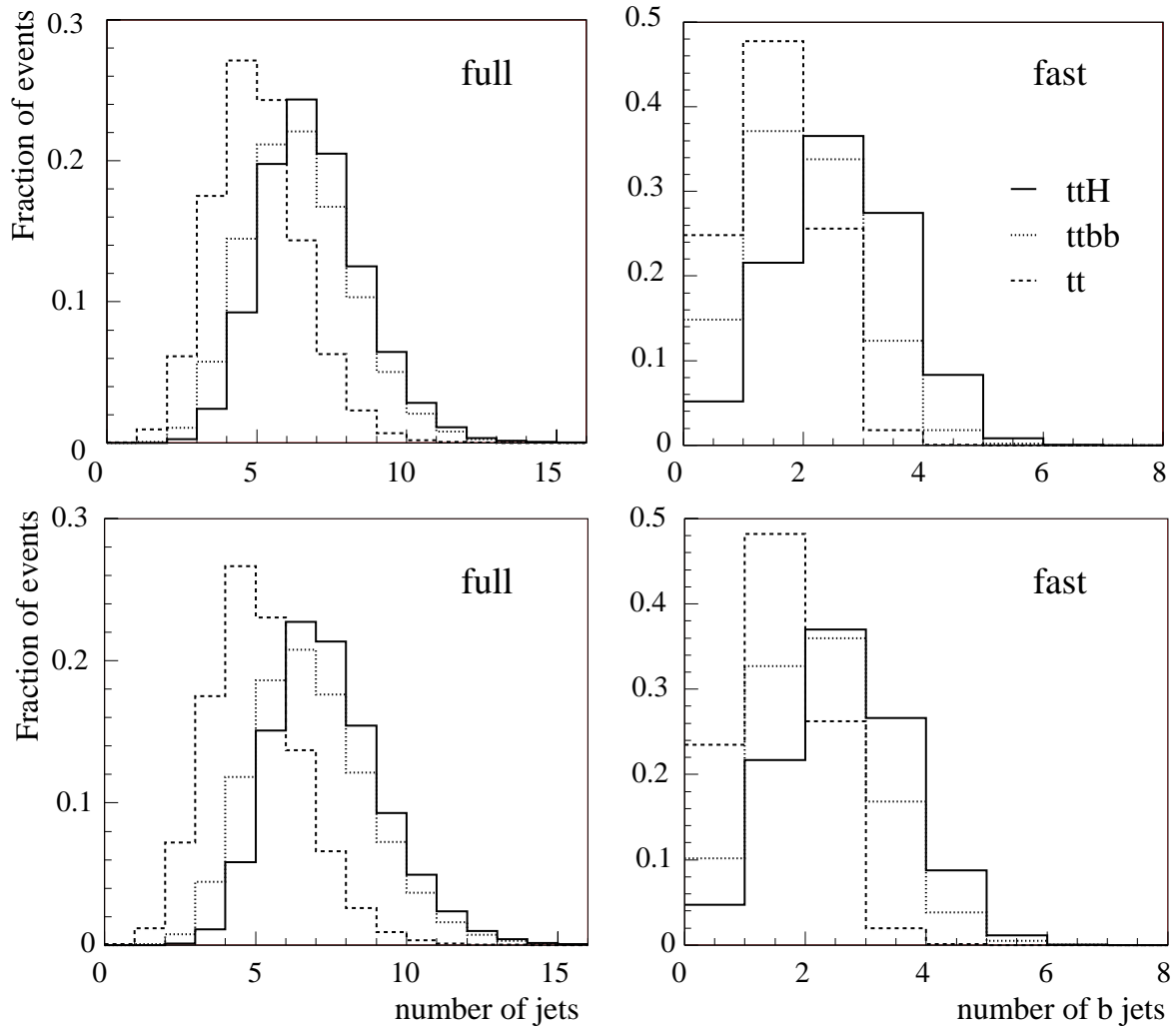


Figure 10.3: Upper plots: Number of reconstructed Cone4 jets with p_t bigger 20 GeV/c and η less than 5 in CSC full simulation for all jets (left plot) and b-tagged jets (right plot) in signal and background samples. Lower plots: same for the fast simulation. Notice that the general jet multiplicity is always a bit higher or equal in fast simulation compared to full simulation for all samples look at.

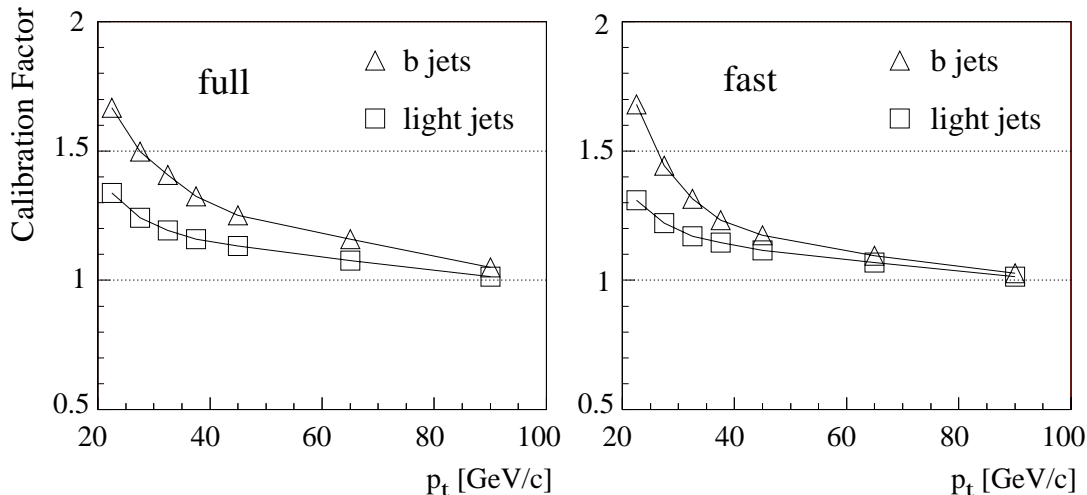


Figure 10.4: Jet energy calibration constants for light and b jets in full simulation (left plot) and fast simulation (right plot) as a function of the reconstructed transverse momentum of the jets.

It turned out that the Cone4 jets of the full simulation samples looked at have been wrongly calibrated with Cone7 calibration functions. No calibration functions for Cone4 jets existed at all at the time of this analysis and all b jets, which due to the possible presence of muons in the jet, need separate calibration functions, have also been treated as light jets. For the fast simulation it also turned out that the jet energy was not properly calibrated and that especially reconstructed b jets have too low energies.

Recalibrating all jets from scratch is a time consuming task and it was decided to follow a simpler but sufficient approach which was originally used in fast simulation [68]. The method determines p_t dependent calibration constants by comparing the reconstructed jet energy to the true energy of the quark that caused the jet. With this approach, new calibration functions have been computed for light and b jets for fast and full simulation. Figure (10.4) shows the calibration constants as a function of p_t . The corrections are largest for jets with low transverse momentum because of more “out of cone” energy due to less collimated jets.

The jet four momentum is scaled with these calibration constants before the jet selection (which applies a cut on the transverse momentum) is done. Figure (10.5) shows the ratio of the reconstructed jet energy to the energy of the truth matched quark ($\Delta R=0.2$) for full simulation and for light and b jets. The wrongly calibrated jets peak significantly below 1 (they are off by up to 13% in the case of b jets in full simulation) and the recalibrated ones have their peak around 1. In fast simulation the jets were better calibrated but still off by a few percent. Recalibration also shifted the reconstructed jet energy over true jet energy distribution of fast simulation jets to peak around 1. In Rome samples no additional corrections have been applied.

10.5 Reconstruction of the Final State

All events which pass through the event selection are passed on to the final state reconstruction. The full event is reconstructed in several steps as done in the physics TDR [31]. First, all $W \rightarrow l\nu$ and $W \rightarrow jj$ candidates are reconstructed. Then the two tops are simultaneously reconstructed

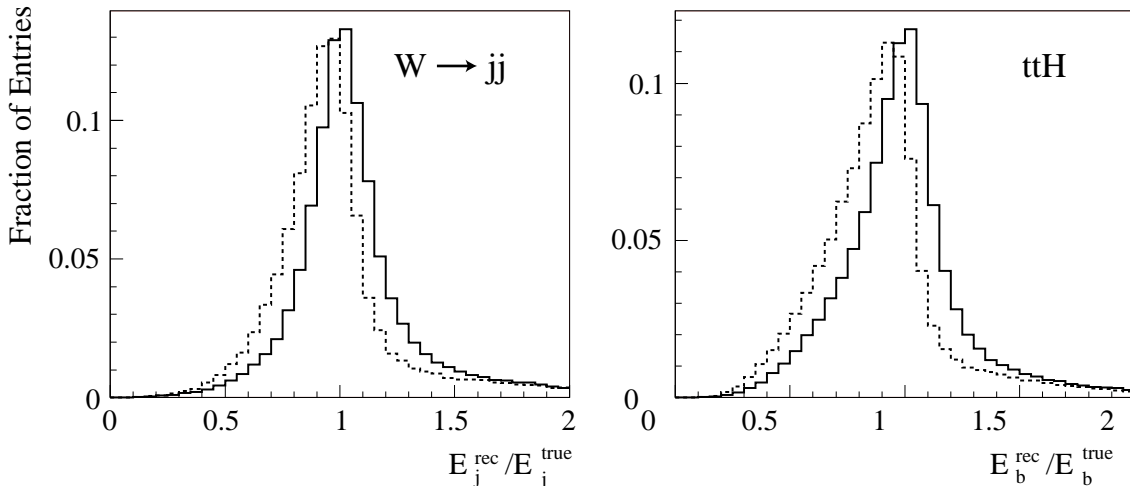


Figure 10.5: Single jet energy calibration of light jets from the $W \rightarrow jj$ decay (left plot) and from b jets from the top and the Higgs decay (right plot) for CSC full simulation. The continuous lines show re-calibrated jets. The dashed lines show the jet energy as given by the default calibration. The discrepancy is because default jet calibration in full simulation is based on Cone7 jets. In this analysis however, Cone4 jets were used.

by using the W candidates and two out of the four or more b jets. The remaining b jets are used to reconstruct the Higgs boson.

10.5.1 Reconstruction of $W \rightarrow l\nu$

The reconstruction of the leptonic W decay requires a reconstructed lepton and a neutrino. The four momentum of the neutrino can only be detected indirectly by means of missing momentum/energy in the event. This, however, is only possible in the transverse plane (i.e. for $p_x^\nu \equiv p_x^{miss}$ and $p_y^\nu \equiv p_y^{miss}$) but not in the longitudinal direction. The z component of the neutrino can be reconstructed by constraining the invariant mass of the reconstructed lepton-neutrino system to the mass of the W boson

$$m_W^2 = (E^\nu + E^l)^2 - (p_x^\nu + p_x^l)^2 - (p_y^\nu + p_y^l)^2 - (p_z^\nu + p_z^l)^2 \quad (10.1)$$

where the general solution of this equation is given by

$$(p_z^\nu)_{1/2} = \frac{\lambda}{2} \pm \frac{1}{2} \sqrt{\lambda^2 - 4\gamma} \quad (10.2)$$

and the following abbreviations are used

$$\begin{aligned} \lambda &= -\frac{2\beta p_l^z}{E_l^2 - p_l^{z2}} \\ \gamma &= -\frac{p_\nu^{t2} E_l^2 - \beta^2}{E_l^2 - p_l^{z2}} \\ \beta &= \frac{1}{2}(\alpha - p_\nu^{t2} + p_l^{z2}) \\ \alpha &= E_\nu^2 + 2E_\nu E_l + (p_\nu^z + p_l^z)^2. \end{aligned} \quad (10.3)$$

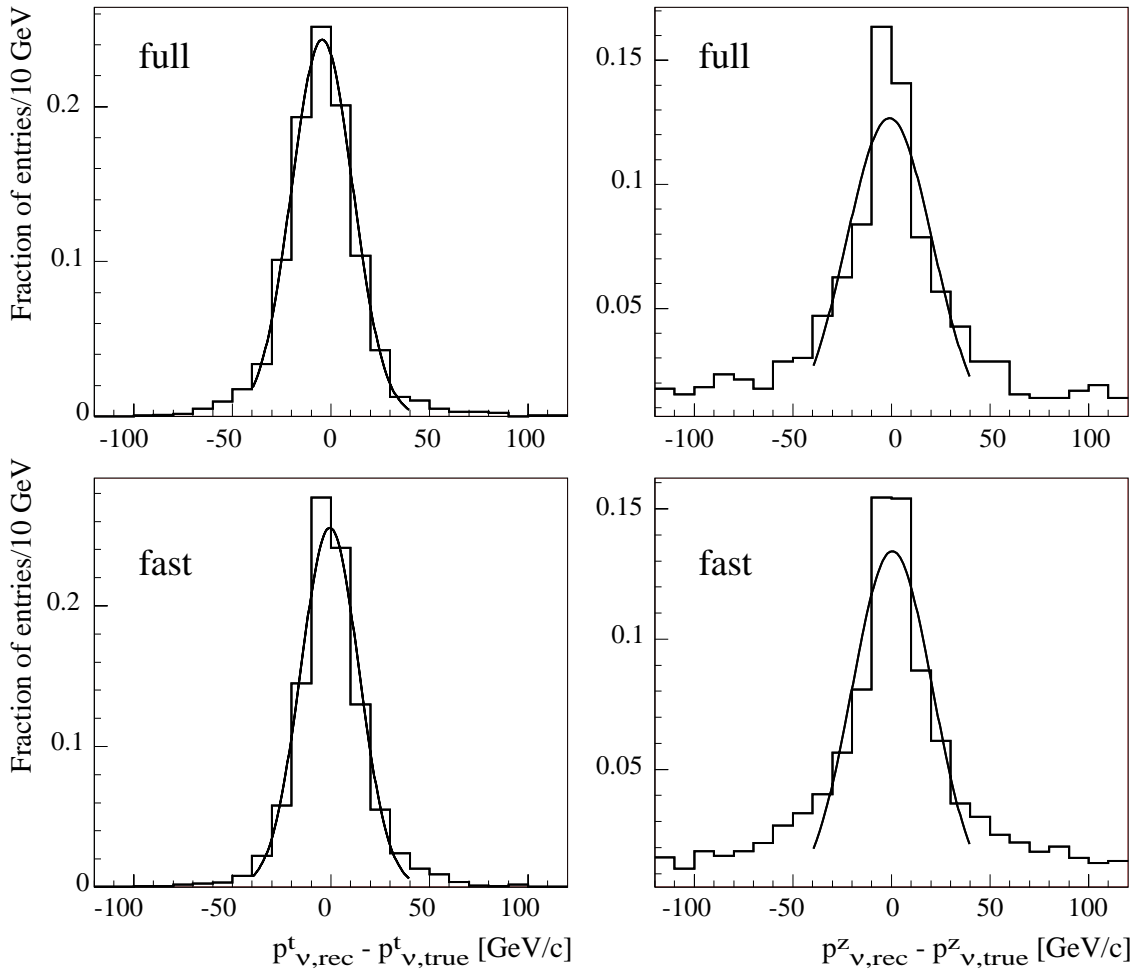


Figure 10.6: Reconstructed neutrino momenta in full (upper plot) and fast (lower plot) simulation for CSC samples. The left plots show the resolution of the transverse momentum, the right plots that of the longitudinal momentum. Exact numbers are listed in Table (10.4).

Depending on the discriminant $\lambda^2 - 4\gamma$ this equation has 0, 1 or 2 solutions. In case of two solutions both are kept until the simultaneous reconstruction of the two top quarks. In the case of no solution the longitudinal neutrino momentum is set equal to the z momentum of the lepton and the neutrino four-vector is scaled such that the invariant mass of the lepton-neutrino system is that of the W boson. The scaling factor S can be calculated as

$$s = m_W^2 / (2(E_l E_\nu - p_l^x p_\nu^x - p_l^y p_\nu^y - p_l^z p_\nu^z)) \quad (10.4)$$

and the rescaled neutrino momentum is given by

$$p_\nu = (sE_\nu, sp_\nu^x, sp_\nu^y, sp_\nu^z). \quad (10.5)$$

This procedure recovers all events where no solution was found but slightly degrades the quality of the top quark reconstruction which was observed to be about 5% in fully simulated CSC samples.

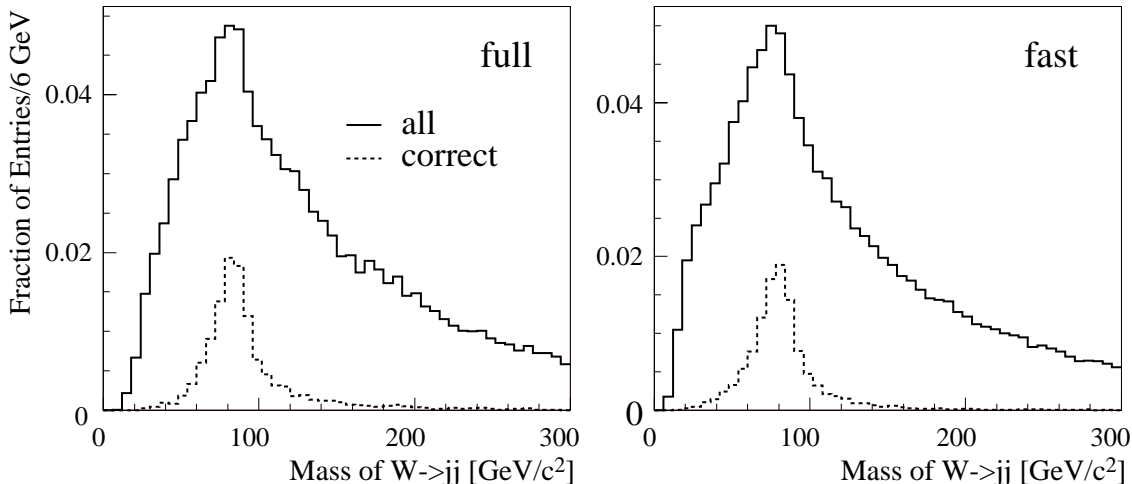


Figure 10.7: Mass spectrum of $W\rightarrow jj$ for all jet-jet pairs for the CSC signal sample. The dashed line shows the contribution of pairs with correct assignment to the true $W\rightarrow jj$ decay. The left plot is for full simulation, the right plot for fast simulation.

A good measurement of the missing transverse momentum is important to reconstruct the z component of the neutrino four-vector and to reconstruct the leptonic W decay. Figure (10.6) shows the resolution of the reconstructed neutrino momenta in p_t and p_z in the CSC signal sample on full and fast simulation for all events where at least one neutrino solution has been found. The resolution of the transverse component is about 15.0(14.6) GeV/c and the longitudinal resolution is about 21.3(20.4) GeV/c for full (fast) simulation. The z resolution degrades to 25.2 GeV/c for full and 22.3 GeV/c for fast CSC simulation if events without neutrino solution are included. These results are in agreement with J. Cammin where the transverse resolution is 15.8 GeV/c and the longitudinal resolution is 20.7 GeV/c.

Table 10.4 summarises the situation for CSC, Rome and Cammin/TDR samples. The resolution of the z component is always significantly worse compared to the transverse resolution because, in its calculation many quantities are involved (E_l , p_x^{miss} , p_y^{miss} , ...) each contributing to the measurement uncertainty.

in [GeV/c]	p_x		p_z	
	full	fast	full	fast
CSC	15.0	14.6	21.3	20.4
Rome	15.5	14.4	19.0	18.3
TDR/Cammin		15.8		20.7

Table 10.4: Resolution of the reconstructed neutrino momenta obtained by CSC, Rome and TDR/Cammin. Only events where a neutrino solution could be found are taken into account.

10.5.2 Reconstruction of $W\rightarrow jj$

The second W of the $t\bar{t}$ decay is reconstructed by calculating the invariant mass of all possible combinations of 2 reconstructed jets which have not been flagged as b jets. If the reconstructed

mass is in a mass window of $|m_{reco} - m_W| < 25 \text{ GeV}/c^2$ (with $m_W = 80.425 \text{ GeV}/c^2$) then the jet-jet pair is stored as a W candidate and the four momenta of the two light jets are rescaled such that the reconstructed W has the nominal W mass.

In CSC samples about 72.5(81.6)% of all selected events have a $W \rightarrow jj$ solution in full (fast) simulation within the mass window. The difference between full and fast simulation is due to the higher jet multiplicity in events processed by fast simulation. In J. Cammins thesis 80% of all selected events have a $W \rightarrow jj$ within the mass window which is in good agreement to CSC fast simulation.

The average number of found jj candidates within the W mass window is 2.6(2.9) in $t\bar{t}H$, 3.0(3.3) in $t\bar{t}b\bar{b}$ and 2.0(2.1) in $t\bar{t}$ for full (fast) CSC simulation. In the TDR this was 2.6 in $t\bar{t}H$, 3.0 in $t\bar{t}b\bar{b}$ and 1.6 in $t\bar{t}$. The $t\bar{t}H$ and $t\bar{t}b\bar{b}$ CSC full simulation is in good agreement with the TDR. The CSC $t\bar{t}$ full (and fast) simulation samples have more jj candidates than it was the case in the TDR which is thought to be due to the different generators used.

Figure (10.7) shows the distribution of m_{jj} for all jet-jet pairs (continuous line) and for the right combinations (dashed line) for full (left plot) and fast simulation (right plot). The distributions peak correctly at the nominal W mass which was not the case before the jet energy recalibration of section 10.4 has been applied.

All $W \rightarrow l\nu$, $W \rightarrow jj$ candidates and the 4 b jets are used simultaneously in the next step to find the best combination to reconstruct the two top quarks. The remaining b jets are used to reconstruct the Higgs boson.

10.5.3 Simultaneous Reconstruction of the 2 Top Quarks

The two top quarks are reconstructed simultaneously by trying to find the best combination of W candidates and b jets to minimise

$$\Delta^2 = (m_{l\nu b} - m_t)^2 + (m_{jjb} - m_t)^2. \quad (10.6)$$

The two reconstructed top quarks have to be within a mass window of 20 GeV/c^2 to the nominal top mass of 175 GeV/c^2 in order to be accepted.

Figure (10.8) shows the mass of the reconstructed top quark with decay $t \rightarrow l\nu b$ and Fig. (10.9) shows the mass of the reconstructed top quark with decay $t \rightarrow jjb$. The dashed lines show the reconstructed mass for those tops where, according to truth, the right combination of leptons/quarks was used. In analogy to the TDR and to J. Cammins analysis, the measurement error on the reconstructed top mass is estimated with a gaussian fit in the region 160-190 GeV/c^2 . For the leptonic top the mass is 174.4 GeV/c^2 with $\sigma = 10.1 \text{ GeV}/c^2$ for full simulation (left plot) and 174.7 with $\sigma = 9.2$ for fast simulation (right plot). For the hadronic top the mass is 174.7 with a σ of 7.6 for full and 174.6 with a σ of 7.4 for fast simulation. These results are in good agreement with the ones obtained by J. Cammin which yield 174.6, $\sigma = 8.6$ for the leptonic and 174.7 GeV/c^2 , $\sigma = 7.7 \text{ GeV}/c^2$ for the hadronic W decay.

Table 10.5 summarises the situation and also includes Rome samples.

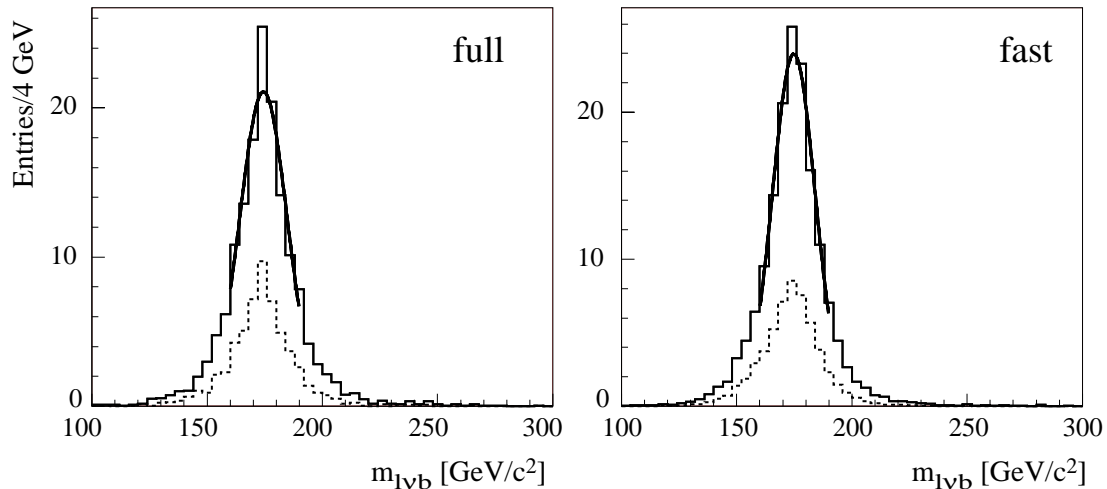


Figure 10.8: Reconstructed mass of $t \rightarrow l\nu b$ for CSC signal events for full simulation (left plot) and fast simulation (right plot). The dashed lines show the contribution of correctly reconstructed tops. The histograms are normalised to an integrated luminosity of 30 fb^{-1} .

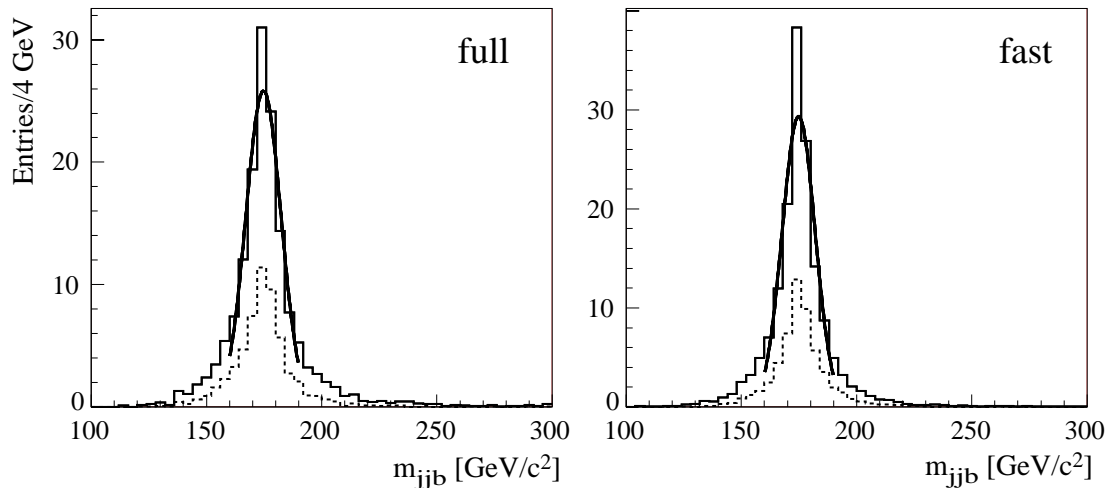


Figure 10.9: Reconstructed mass of $t \rightarrow jjb$ for CSC signal events for full simulation (left plot) and fast simulation (right plot). The dashed lines show the contribution of correctly reconstructed tops. The histograms are normalised to an integrated luminosity of 30 fb^{-1} .

Top mass in $[\text{GeV}/c^2]$	$t \rightarrow l\nu b$				$t \rightarrow jjb$			
	full		fast		full		fast	
	m	σ	m	σ	m	σ	m	σ
CSC	174.4	10.1	174.7	9.2	174.7	7.6	174.7	7.6
Rome	174.1	9.8	173.5	9.4	174.4	9.3	173.2	8.9
TDR/Cammin			174.6	8.6			174.7	7.7

Table 10.5: Resolution of the reconstructed top mass in $t\bar{t}H$ signal events obtained by CSC, Rome and TDR/Cammin.

10.5.4 Reconstruction of the Higgs Boson

The remaining b quarks are used to reconstruct the Higgs boson. If there are more than two b jets left then the two with highest transverse momentum are taken. The reconstructed Higgs mass needs to be in a mass window of around $\pm 20 \text{ GeV}/c^2$ of the expected Higgs mass (which is $120 \text{ GeV}/c^2$ for all samples looked at) in order for the event to be accepted.

Figure (10.10) shows the spectrum of the reconstructed Higgs mass for all events where a Higgs could be found (regardless if in mass window or not) for CSC fast and full simulation in signal events. The dashed line shows the contribution of reconstructed Higgs bosons where the right b quarks were used. 45% of all reconstructed Higgs bosons within the mass region are reconstructed with the correctly paired b jets. For cross checking of the jet energy recalibration, Fig. (10.11) shows the reconstructed Higgs mass obtained by using all events (regardless if they pass the selection cuts) which have two reconstructed b jets associated to the true b quarks from the Higgs decay. The peak of the gaussian distribution is at $118.0 \pm 17.3 \text{ GeV}/c^2$ for CSC full simulation and at $117.7 \pm 19.0 \text{ GeV}/c^2$ for CSC fast simulation. Without the recalibration the distributions were peaked at $100 \text{ GeV}/c^2$ and $107 \text{ GeV}/c^2$ for full and fast simulation, respectively.

The tails in Fig. (10.11) are due to a wrong association of reconstructed jets to the true b quarks from the Higgs decay. Because of final state radiation the jet direction of the reconstructed jet can be deflected far enough so that a correct association to the b quark is not possible. The tails toward larger values in the reconstructed Higgs mass spectrum is entirely due to events where the Higgs boson has been reconstructed using the wrong jets.

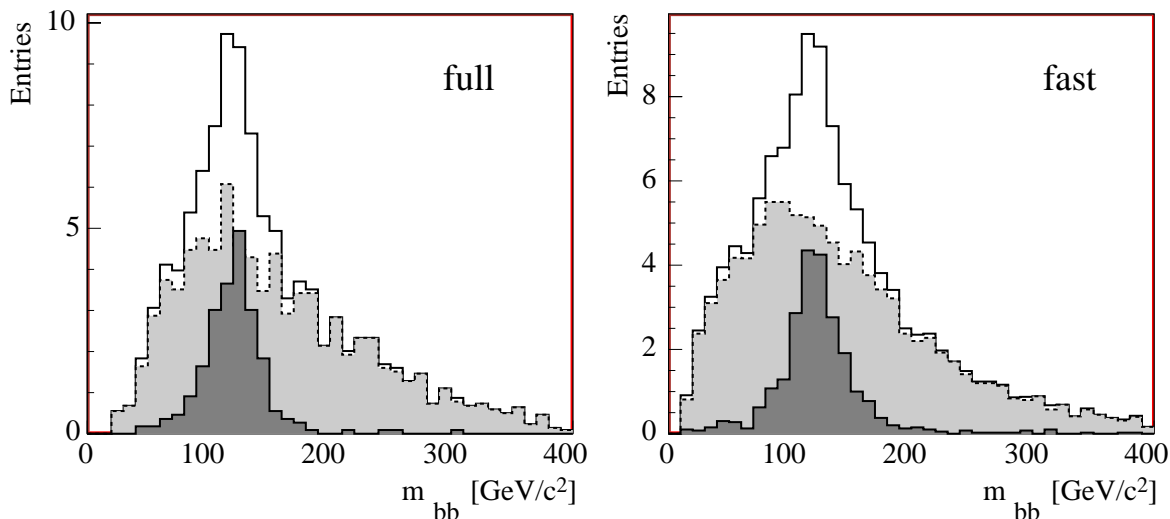


Figure 10.10: Reconstructed mass spectrum of the Higgs boson in the $t\bar{t}H$ signal events. The white histogram shows the masses of all Higgs bosons after the signal reconstruction process. The dark grey histogram shows the mass spectrum of correctly assigned b jets and the light grey histogram shows the contribution of the wrongly assigned b jets. The left plot is for CSC full simulation, the right plot for CSC fast simulation. The histograms are normalised to an integrated luminosity of 30 fb^{-1} .

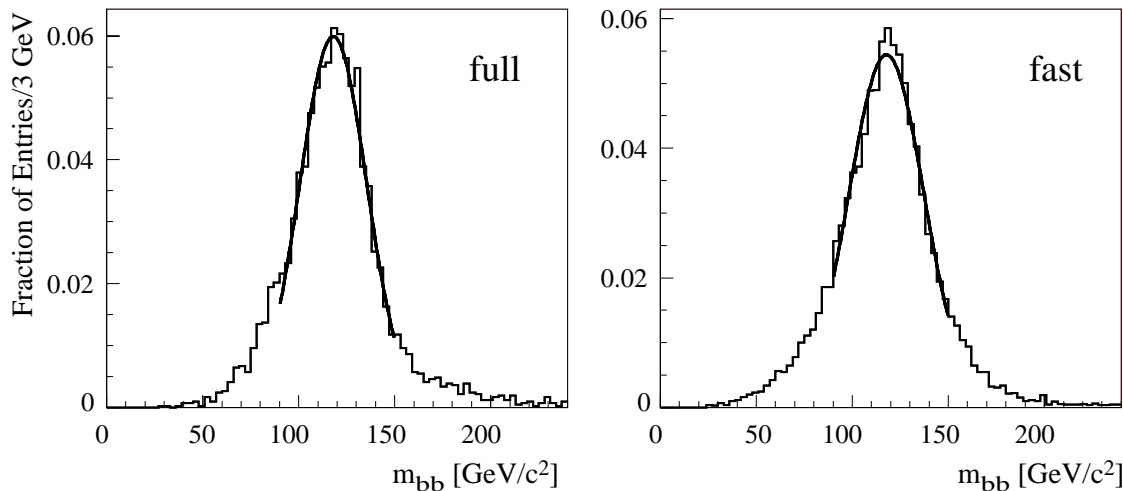


Figure 10.11: Mass spectrum of all events with correctly assigned b jets from the Higgs decay regardless if the full event could be reconstructed or not. The mean of the gaussian fit for fully simulated samples is at $118.0 \text{ GeV}/c^2$ with $\sigma = 17.3 \text{ GeV}/c^2$, that for fast simulation is at $117.7 \text{ GeV}/c^2$ with $\sigma = 19.0 \text{ GeV}/c^2$. These plot state the necessity of the recalibration of the jet energies in full and fast simulation. Without recalibration the peak of the full simulation was at $100 \text{ GeV}/c^2$ and the one for fast simulation at $107 \text{ GeV}/c^2$.

10.6 Results

This section presents results of the full CSC simulation using the vertexing and b -tagging reconstruction software as presented in earlier chapters and the event selection and reconstruction procedures as described in this chapter. A comparison to fast simulation using CSC settings and to J. Cammins thesis will be provided whenever possible. A comparison to Rome samples is not possible because the important $t\bar{t}b\bar{b}$ background was not accessible anymore at the time of this thesis.

10.6.1 Event Selection Cut Flow

The cut flow of the event selection steps is presented in Table (10.6) for CSC samples in fast and full simulation and, for the last two cuts, also for J. Cammins TDR style analysis.

The muon reconstruction efficiency in the full simulation is 35.6% for the $t\bar{t}H$ signal, 35.8% in the $t\bar{t}b\bar{b}$ and 34.2% in the $t\bar{t}$ samples. The electron reconstruction efficiency is 32.3%, 33.6% and 30.8% for the three data sets, respectively. The overall lepton reconstruction efficiency in full simulation is 67.3% for the signal, 68.7% for $t\bar{t}b\bar{b}$ and 64.6% for $t\bar{t}$. The fake rate of muons in full reconstruction was observed to be 3.2% and that of electrons 4.8%. The overall lepton selection efficiencies in the CSC fast simulation are comparable. The largest difference is in the selection efficiencies of muons in the signal $t\bar{t}H$ and background $t\bar{t}$ data sets where the full simulation accepts about 10% more events relative to the fast simulation. The cuts in full simulation are a compromise between high selection efficiency of the signal with a low lepton fake rate. It was found that tighter cuts on the muon selection do not decrease the fake rate of 3.2% accordingly to justify a loss of about 4% in signal selection efficiency.

in %	CSC full			CSC fast			TDR/Cammin		
	$t\bar{t}H$	$t\bar{t}b\bar{b}$	$t\bar{t}$	$t\bar{t}H$	$t\bar{t}b\bar{b}$	$t\bar{t}$	$t\bar{t}H$	$t\bar{t}b\bar{b}$	$t\bar{t}$
1 μ^\pm	35.6	35.8	34.2	31.2	32.7	33.2			
1 e^\pm	32.3	33.6	30.8	33.3	34.4	32.4			
1 lepton	67.3	68.7	64.6	64.4	67.1	65.6			
6 j, 1 l	45.6	35.5	17.1	47.2	37.9	18.6	46.2	36.9	15.4
6 j (4b), 1 l	4.9	1.4	0.036	6.2	2.9	0.062	3.8	1.5	0.01

Table 10.6: Percentage of events with reconstructed lepton, 6 jets and 4 b jets for the CSC samples and for TDR/Cammin for the $t\bar{t}H$ signal and the $t\bar{t}b\bar{b}$ and $t\bar{t}$ background for full and fast simulation.

The selection efficiencies for 6 jets and 1 lepton in full simulation are 45.6% for $t\bar{t}H$, 35.5% in $t\bar{t}b\bar{b}$ and 17.1% in $t\bar{t}$. In the CSC fast simulation they are 47.2%, 37.9% and 18.6%, respectively. In the TDR style analysis of J. Cammin 46.6% of $t\bar{t}H$, 36.9% of $t\bar{t}b\bar{b}$ and 15.4% of $t\bar{t}$ events have 6 jets and 1 lepton. These numbers are within the statistical uncertainties comparable. An exception is the jet rate in the $t\bar{t}$ background. It is 11% higher in the CSC full and 20% higher in the CSC fast simulation relative to the TDR analysis. A reason for this is that the $t\bar{t}$ background data set in J. Cammin's thesis has been generated with Pythia whereas in this analysis MC@NLO is used. In Pythia any additional jet can only come from the parton shower while in MC@NLO one additional jet is calculated correctly in next-to-leading order. Jets produced in the parton shower have a lower p_t spectrum than those calculated directly in the hard process and therefore the acceptance of events with 6 jets is higher in the CSC samples.

The most significant differences are in the final event selection efficiencies. In the CSC full simulation 4.9% of $t\bar{t}H$, 1.4% of $t\bar{t}b\bar{b}$ and 0.036% of $t\bar{t}$ events have 1 lepton and 6 jets where 4 are b jets. In CSC fast simulation it is 6.2%, 2.9% and 0.062%, respectively. J. Cammin's TDR style analysis yields 3.8%, 1.5% and 0.01% for the three event types. The difference of a factor two in the selection efficiencies of the $t\bar{t}b\bar{b}$ and $t\bar{t}$ backgrounds in CSC full and fast simulation can be understood by looking at the b-tagging performance. The light jet rejection in fast simulation was set to 100 for a b jet selection efficiency of 60%. For the same efficiency the b-tagging in full reconstruction achieves a light jet rejection of about 225 meaning that it more efficiently rejects background events leading to a better rejection in the full simulation of $t\bar{t}b\bar{b}$ and $t\bar{t}$ events. For the same reason, the selection efficiency of $t\bar{t}H$ signal events is 20% higher in the fast simulation compared to the full simulation.

The largest difference is between the selection efficiency of $t\bar{t}$ events in CSC fast simulation compared to J. Cammin's analysis. The background rate of $t\bar{t}$ is 6 times higher in the CSC fast simulation. Statistical uncertainties are rather small and the difference cannot be explained by statistical fluctuations. The reason for this difference is again believed to be caused by the use of very different generators in the two analyses. A recent paper published by CMS [66] underlines this and reports similar behaviour where a study of the background rejection on $t\bar{t}$ events with additional jets is performed. The selection rates for $t\bar{t}+2j$ is 2 to 5 times higher than that for the $t\bar{t}+1j$ jet.

Table 10.7 shows the expected number of events at 30 fb^{-1} for this cutflow for the CSC samples. At the end, 157(197) $t\bar{t}H$ events remain to be fully reconstructed in full (fast) simulation. In total 3463(6763) background events survive. Applying these event selection cuts, the signal to background ratio could be significantly increased by a factor of 96(62) for full (fast) simulation. The biggest improvement is due to the requirement of 4 b jets which increases the background

rejection by a factor of 36(25) for full (fast) simulation when going from the requirement of 6j1l to 6j1l4b.

in %	CSC full			CSC fast		
	$t\bar{t}H$	$t\bar{t}b\bar{b}$	$t\bar{t}$	$t\bar{t}H$	$t\bar{t}b\bar{b}$	$t\bar{t}$
All Events	3166	74776	6619886	3166	74776	6619886
1 μ^\pm	1128	26770	2264001	988	23333	2470010
1 e^\pm	1023	25161	2037608	1051	24578	2402593
1 lepton	2131	51419	4271460	2038	47865	4869729
6 j, 1 l	1443	26545	1132000	1494	28340	1231298
6 j (4b), 1 l	157	1055	2398	197	2132	4631

Table 10.7: Expected number of signal and background events at 30 fb^{-1} after the event selection.

10.6.2 Event Reconstruction Cut Flow

On the remaining events, the full event reconstruction is performed. Table 10.8 shows the cut flow after each reconstruction step w.r.t. the number of events that survived the event selection cuts. In the last row the absolute percentage of events which have a reconstructed Higgs boson is shown.

The leptonic W decay is reconstructed in 68.0% of all $t\bar{t}H$ events, 67.6% in $t\bar{t}b\bar{b}$ and 70.7% in $t\bar{t}$ events in the full simulation. The according numbers for CSC fast simulation are 76.8%, 74.4% and 78.9%, respectively. The reconstruction efficiency is better in fast simulation because the resolution of the missing energy is better and because the lepton fake rate is zero. The transverse missing energy in the event is taken as the transverse momentum of the neutrino and the longitudinal momentum is calculated using the constraint that the invariant mass of the lepton-neutrino system equals the W mass. A worse resolution of the missing energy leads to fewer events where a solution for the longitudinal momentum of the neutrino can be found (and hence no leptonic W is reconstructed). In addition, in the full simulation there is a lepton fake rate of a few percent. Especially in those events the reconstruction of the W fails more often because (due to the wrongly reconstructed lepton) a solution for the longitudinal momentum of the neutrino cannot be found and no leptonic W is reconstructed. It is possible to reduce the loss in selection efficiency in $t\bar{t}H$ event on full (fast) simulation by setting the longitudinal momentum of the neutrino to $(-p_z)$ of the lepton. This recovers all events with no neutrino solution but decreases the resolution of the reconstructed top mass and hence some of these events are later rejected in the simultaneous reconstruction of the $t\bar{t}$ pair.

The hadronic W is reconstructed in 72.5% of all $t\bar{t}H$ events, 70.7% in $t\bar{t}b\bar{b}$ and 60% in $t\bar{t}$ events in full simulation. The according numbers for fast simulation are 81.6%, 81.2% and 70.3%, respectively. The higher reconstruction efficiency in the fast simulation is directly related to the higher jet multiplicity compared to full simulation. In fast simulation there are on average 5-10% more reconstructed jets than in full simulation leading to more combinatorial choices when reconstructing the W boson out of all 2j pairs in the event.

The percentage of events with 2 reconstructed top quarks is 51.4% in $t\bar{t}H$ events, 47.4% in $t\bar{t}b\bar{b}$ and 32.1% in $t\bar{t}$ events in full simulation. The same numbers for the CSC fast simulation are 62.2%, 55.7% and 46.9%, respectively. Again, a larger fraction of events in fast simulation has two reconstructed top quarks. This is directly related to the higher reconstruction efficiency

in %	CSC full			CSC fast			TDR/Cammin		
	$t\bar{t}H$	$t\bar{t}b\bar{b}$	$t\bar{t}$	$t\bar{t}H$	$t\bar{t}b\bar{b}$	$t\bar{t}$	$t\bar{t}H$	$t\bar{t}b\bar{b}$	$t\bar{t}$
$W \rightarrow l\nu$	68.0	67.6	70.7	76.8	74.4	78.9			
$W \rightarrow jj$	72.5	70.7	60.0	81.6	81.2	70.3			
2 tops in mass window	51.4	47.4	32.1	62.2	55.7	46.9	47.3	46.6	31
Higgs in mass window	23.0	11.5	5.0	26.0	14.3	13.4	23.6	13.3	10
absolute % end	1.14	0.16	0.002	1.6	0.42	0.008	0.9	0.2	0.001
- double counted			0.001			0.0045			

Table 10.8: Percentage of events with reconstructed W 's, tops and Higgs boson with respect to those which passed the event selection cuts. For $W \rightarrow l\nu$ it actually is 100% but here the percentage with a neutrino solution is shown. The last column shows the absolute percentage which passes through all cuts and reconstruction steps.

of the leptonic and hadronic W 's in the previous step. For J. Cammins analysis 47.3% of $t\bar{t}H$ events, 46.6% of $t\bar{t}b\bar{b}$ and 31% of $t\bar{t}$ events remain. The differences between CSC fast simulation and J. Cammin are large and of the order of 30% for the $t\bar{t}H$ signal but arise from the fact that in the TDR style analysis of J. Cammins thesis leptonic W 's with no neutrino solution have been rejected which makes up for 25% of all events where as in this analysis they are included.

The final percentage of events which have a reconstructed Higgs boson is 23% in $t\bar{t}H$ events, 11.5% in $t\bar{t}b\bar{b}$ and 5% in $t\bar{t}$ in full simulation. The according numbers for the CSC fast simulation are 26%, 14.3% and 13.4%, respectively. For J. Cammins analysis 23.6% of $t\bar{t}H$ events, 13.3% of $t\bar{t}b\bar{b}$ and 10% of $t\bar{t}$ events remain. The higher top quark reconstruction efficiency in the CSC fast simulation propagates to the higher Higgs boson reconstruction efficiency compared to full simulation. In relative terms, however, in full and fast simulation about 43% of all $t\bar{t}H$ events with two reconstructed top quarks have a reconstructed Higgs boson. In $t\bar{t}b\bar{b}$ background events it is 24% for both cases. The Higgs reconstruction efficiency in $t\bar{t}$ background is (in relative terms to events with two top quarks) twice as high in fast simulation compared to full simulation. This is also observed in the fast simulation of J. Cammin. In his case the relative reconstruction efficiency of the Higgs boson compared to the previous level is in general higher: 50% for the $t\bar{t}H$ signal, 28% for $t\bar{t}b\bar{b}$ and 31% for $t\bar{t}$ which is comparable to the 29% of the CSC fast simulation.

In absolute numbers 1.14% of all $t\bar{t}H$ events, 0.16% of $t\bar{t}b\bar{b}$ and 0.001% in $t\bar{t}$ remain in the full simulation. For CSC fast simulation 1.6% of all $t\bar{t}H$ events, 0.42% of $t\bar{t}b\bar{b}$ and 0.0045% in $t\bar{t}$ remain. In the generation of $t\bar{t}$ samples events of the type $t\bar{t}b\bar{b}$ are not filtered out before the simulation. The $t\bar{t}$ sample is therefore “contaminated” with some $t\bar{t}b\bar{b}$ events. Because of their importance, the latter are simulated as an extra sample. The events in the $t\bar{t}$ sample which are actually of the type $t\bar{t}b\bar{b}$ (and therefore taken into consideration in the $t\bar{t}b\bar{b}$ sample) have to be subtracted from the final number of events.

At the end the background rejection of the CSC fast simulation is worse by a factor of 4.5 compared to the fast simulation of J. Cammin. This is in the same range as was observed by CMS. A bigger surprise is that on CSC full simulation samples the $t\bar{t}$ rejection is of the same level as in the TDR fast simulation despite the fact that after the event selection cuts 3.6 times more events were present in the CSC full simulation. The CSC full simulation loses particularly many events during the Higgs boson reconstruction where twice as many events are rejected compared to the CSC and TDR fast simulation. This effect has not been entirely understood.

	CSC full			CSC fast		
	$t\bar{t}H$	$t\bar{t}b\bar{b}$	$t\bar{t}$	$t\bar{t}H$	$t\bar{t}b\bar{b}$	$t\bar{t}$
$W \rightarrow l\nu$	107	713	1678	151	1586	3657
$W \rightarrow jj$	114	747	1438	161	1731	3258
2 tops in mass window	80	500	769	122	1189	2172
Higgs in mass window - double counted	36 ± 1	121 ± 14	136 ± 43 75 ± 32	51 ± 1	305 ± 23	622 ± 87 320 ± 66

Table 10.9: Expected number of events at 30 fb^{-1} after each reconstruction step. The last column shows the actual number of $t\bar{t}$ background events after events with additional b quarks which are already considered in the $t\bar{t}b\bar{b}$ background have been subtracted.

Table 10.9 shows the expected number of events at 30 fb^{-1} after the event selection and reconstruction process. The error on the final rate is purely binomial and obtained by $\sqrt{N\epsilon(1-\epsilon)}$, where ϵ is the selection efficiency and N the original number of events for each sample. In the full simulation 36 $t\bar{t}H$ events, 121 $t\bar{t}b\bar{b}$ and 75 $t\bar{t}$ events remain. In the fast simulation it is 51, 305 and 320, respectively.

10.6.3 Significance

Table (10.10) shows the results of the analysis for CSC full and fast simulation, the TDR style analysis of J. Cammin and latest results of CMS. The numbers are given for an integrated luminosity of 30 fb^{-1} .

The significance S/\sqrt{B} in this analysis is 2.45 for the CSC full simulation and 1.94 for the CSC fast simulation. The worse performance on CSC fast simulation is mostly due to the less efficient rejection of the $t\bar{t}$ and $t\bar{t}b\bar{b}$ backgrounds. This is because of the worse b-tagging performance in fast simulation compared to full simulation. However, because the b jet selection efficiency is 60% in both cases but the light jet background rejection is less and the jet multiplicity a bit higher in CSC fast simulation, also more signal events pass through the selection cuts. This combination gives an overall degradation in significance of 40% from full to fast simulation.

So far no absolute numbers for the analysis of J. Cammin have been quoted because the cross section of the $t\bar{t}$ background used in his analysis and in this one differs significantly. The TDR analysis used LO calculations which yield a cross section of 474 pb. In this analysis the NLO value of 833 pb is taken. The significance numbers in Table (10.10) have therefore been recalculated with this new cross section and yield 1.85 (compared to 2.0 which was the original result). The current analysis on CSC full simulation achieves a significance of 2.45 which is 30% better than J. Cammin's TDR style. The analysis on CSC fast simulation achieves comparable results.

The last columns of Table (10.10) show recent results published by CMS [66]. The study is based on an integrated luminosity of 60 fb^{-1} and yields a significance of 2.34. The number in Table (10.10) is 1.65 which is the rescaled value to an integrated luminosity of 30 fb^{-1} . The results of CMS seem to be far worse than the CSC full simulation results. However, the study of CMS is based on a more realistic scenario including pile up, misalignment, trigger efficiencies and systematic experimental uncertainties arising from the imperfect knowledge of

the detector response. The next section tries to estimate the influence of some of these effects on the significance of this analysis.

	CSC Full	CSC Fast	TDR	CMS
S/B	18.3%	8.16%		
S/\sqrt{B}	2.6	2.04		
$S/B + t\bar{t}b\bar{b}$ resonant	16.7%	7.4%	14.4%	4.1%
$S\sqrt{B} + t\bar{t}b\bar{b}$ resonant	2.45	1.94	1.85	1.65

Table 10.10: Signal over background ratios for the $t\bar{t}H$ channel as obtained in this analysis using fast and full simulation compared to the TDR results and to results from CMS [66]. The second row includes the missing resonant $gg \rightarrow Z/\gamma/W \rightarrow t\bar{t}b\bar{b}$ background which, in J. Cammins thesis, contributed about 10% to the overall background rate.

10.6.4 Uncertainties

This section estimates the effect of theoretical uncertainties, trigger, low and high luminosity pile up and misalignment on the final significance of the $t\bar{t}H$ channel.

Theoretical uncertainties come from the cross section of the $pp \rightarrow t\bar{t}H$ signal process which has been calculated in leading-order (LO) and is subject to variations depending on the choice of the factorisation scale. Next-to-leading-order (NLO) predictions have been calculated in [69] and results for LO and NLO are shown in Fig. (10.12). For the renormalisation scale used by Pythia the NLO correction to the $t\bar{t}H$ LO cross section is about 1.25 and the scale dependence in general is largely reduced in NLO prediction compared to LO. The cross sections of the background are already calculated in NLO and uncertainties due to the renormalisation scale are small. The increase in signal cross section by 25% directly increases the significance S/\sqrt{B} by 25% to 3.06 for the full simulation and to 2.4 for the fast simulation.

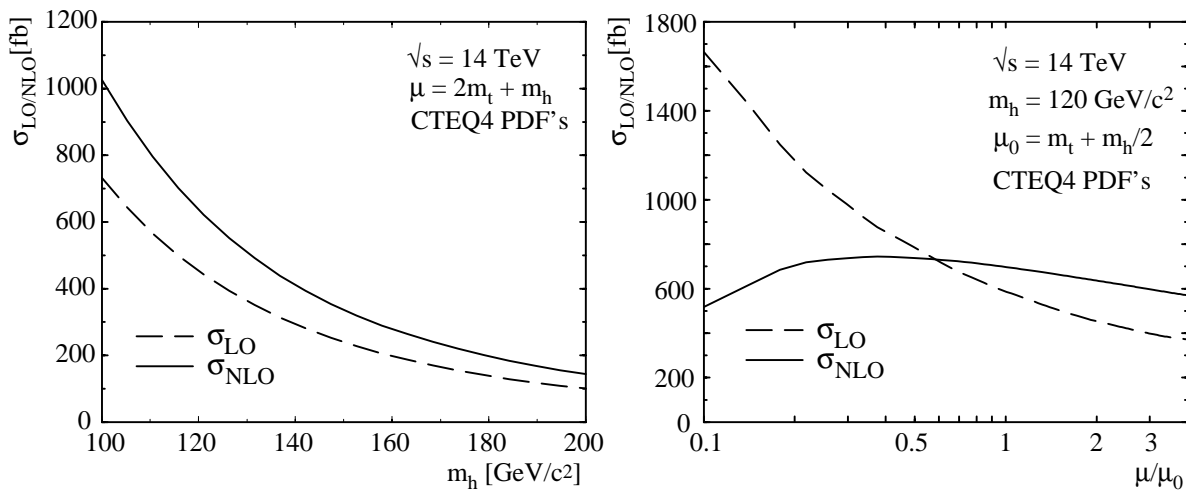


Figure 10.12: Scale dependence and NLO corrections for the $t\bar{t}H$ cross section. NLO corrections increase the cross section by about 20-30% over the whole renormalisation scale. The scale dependence is largely reduced by the NLO calculation. Both plots are from [69].

A simulation of the trigger system has not been used in this study. Earlier studies [31] state a 2% loss of significance S/\sqrt{B} if the p_t threshold is set to 25(20) GeV/c for electrons(muons) as is done by the e25i and μ 20i trigger menus. The degradation gets up to 8% if the selection criteria were raised to 35(25) GeV/c. A 2% decrease would mean a significance of 2.4 for the full simulation and 1.9 for the fast simulation (using the LO cross section for the $t\bar{t}H$ signal).

The influence of pile up on the significance is harder to estimate. The main influence on the significance is thought to come from any changes to the b-tagging performance and hence to a degradation of the background rejection. It was already noted that in the CSC fast simulation twice as many background events pass the requirement of 4b jets compared to the full simulation. The reason is seen in the better b-tagging performance of the full simulation. Any degradation will therefore raise the background rate and decrease the significance of the analysis.

It has been shown in this analysis that the tracking and vertexing performance in terms of (impact parameter) resolutions degrade very little at low luminosity pile up and that also the b-tagging performance only suffers very little. In earlier studies [49] the impact of low luminosity pile up on the tagging performance is given as 2-5% and has been found to be below 20% for high luminosity. Another influence at low and high luminosity, especially for the impact parameter taggers, is the misidentification of the primary vertex which results in impact parameters which are calculated with respect to the wrong primary vertex. In this analysis the misidentification rate at low luminosity pile up was found to be 2.8% for $WH \rightarrow l\nu b\bar{b}$ and 1.5% for $WH \rightarrow l\nu u\bar{u}$. The misidentification rate at high luminosity was studied in [52] and was found to be around 11% for both $WH \rightarrow l\nu b\bar{b}$ and $WH \rightarrow l\nu u\bar{u}$ events. This rate is expected to be less for the $t\bar{t}H$ sample due to the higher track multiplicity and higher average transverse momentum of tracks which makes it easier to identify the correct primary vertex.

To give a rough estimate of the influence of low and high luminosity pile up on the $t\bar{t}H$ analysis a b-tagging degradation of 10% for low and 25% for high luminosity is considered. It is not possible to directly relate the loss in b-tagging performance to the degradation of the significance. To get a first estimate the difference of a factor of 2 in background rejection between CSC fast and full simulation for a b-tagging degradation of 55% from $R_u = 225$ for full to $R_u = 100$ for fast simulation is taken. For low(high) luminosity the 10(25)% degradation in b-tagging would then lead to an increase of background events by about 18(45)% and hence, approximated that this directly propagates to the final rejection rate after the full event reconstruction, to a decrease of the significance of 8% for low luminosity and 17% for high luminosity.

The influence of misalignment on the b-tagging performance has been subject of earlier studies [70]. The expected alignment of the Pixel Detector after an initial running period corresponding to an integrated luminosity of about 100 pb^{-1} is estimated to be of the order of around $10 \mu\text{m}$ in $r\phi$ and $30 \mu\text{m}$ in z direction. After several years of data taking this is reduced to $5 \mu\text{m}$ in $r\phi$ and $15 \mu\text{m}$ in z . For an initial misalignment ($\sigma_{R\phi} = 10 \mu\text{m}$, $\sigma_Z = 30 \mu\text{m}$) the b-tagging performance of a 3D combined tagging algorithm was reduced by 8%. For the final alignment ($\sigma_{R\phi} = 5 \mu\text{m}$, $\sigma_Z = 15 \mu\text{m}$) the degradation is much smaller and is of the order of 2%.

Systematic detector uncertainties such as the jet energy scale, jet resolution or uncertainties in the tag efficiencies have not been taken into account.

Detailed studies of the $t\bar{t}H$ channel including the influence of the trigger system, low and high luminosity pile up, misalignment of the detector and systematic detector uncertainties are planned in ATLAS within the context of the next large scale Monte Carlo data production over the next months.

10.7 Summary

The Higgs boson discovery potential of the $t\bar{t}H$, $H \rightarrow b\bar{b}$ channel for a Higgs mass of $120 \text{ GeV}/c^2$ in the ATLAS experiment has been re-evaluated and compared to previous results by J. Cammins TDR style analysis and to CMS. For the study of the $t\bar{t}H$ signal a 2 and 3 layer Pixel detector layout has been looked at.

The overall results on fast simulation are in agreement with earlier results and on full simulation even better. A signal to background ratio S/\sqrt{B} of 2.45 could be achieved on full simulation and 1.94 on fast simulation compared to 1.85 for the TDR fast simulation and 1.65 for the CMS full simulation (the latter has been scaled to 30 fb^{-1} , it was given by CMS as 2.34 for 60 fb^{-1}).

Differences between the CSC fast and full simulation have been found where the biggest influence comes from the default setting of the b-tagging performance in the fast simulation. It is set to a light jet rejection of 100 for a b jet selection efficiency of 60%. For the same efficiency the full simulation achieves a rejection of 225. The rejection of the background is twice as good after the requirement of 4 b jets in the event in the full simulation. This underlines the need for efficient and well performing b-tagging algorithms as they have been implemented as part of this thesis work. Newer approaches implement a b-tagging parametrisation (dependent on η and p_t) into the fast simulation in order to achieve more comparable results. The comparison to J. Cammins TDR style analysis yields that for his samples the fast simulation rejects the $t\bar{t}$ background better than CSC fast and even full simulation. The reason for that is thought to be in the different generator used to simulate the $t\bar{t}$ background. In his case it is Pythia in leading-order where in this analysis it was MC@NLO in next-to-leading-order. The same was observed by CMS in [66] where additional jets in the $t\bar{t}$ background increased the number of events by a factor of 2 to 5.

In general, the fast simulation performs a bit better in terms of W and top reconstruction efficiencies but this is due to the higher jet multiplicity, the better resolution of missing energy in the event and the fact that there are no fake electrons/muons which cause the full simulation to less often find a solution for the longitudinal momentum of the reconstructed neutrino.

An estimate of the influence of theoretical uncertainties in the cross sections, trigger and low/high luminosity pile up has been done. The NLO corrections to the $t\bar{t}H$ cross section would increase the signal by about 25%. The use of the e25i and μ 20i trigger menus to select signal events reduce the significance by about 2%. The biggest degradation comes from a decrease of b-tagging performance due to low/high luminosity pile up. From pile up studies in this thesis and from earlier studies in ATLAS [49] it was estimated that the significance can decrease by about 8% for low and 17% for high luminosity. The influence of misalignment of the detector on the significance of the $t\bar{t}H$ channel has also been looked at. It has been reported in earlier studies [70] that the b-tagging performance degrades by about 2% considering the final misalignment of the Pixel Detector after a few years of data taking ($\sigma_{R\phi} = 5 \mu\text{m}$, $\sigma_Z = 15 \mu\text{m}$). The influence of misalignment on the b-tagging performance in the $t\bar{t}H$ channel is therefore rather small.

Including all these estimates would leave a final significance of about 1.96 instead of 2.45 for the full simulation using the LO cross section calculation for the $t\bar{t}H$ signal.

Chapter 11

Conclusion

This thesis covers the implementation and study of vertex finding and b-tagging reconstruction algorithms, a study of the e/γ part of the ATLAS trigger and the analysis of the potential Higgs discovery channel $t\bar{t}H^0(120)$, $H^0(120)\rightarrow b\bar{b}$ for which vertex finding and b-tagging are of high importance. This last chapter summarises the results and gives a conclusion.

Two vertex fitters, so called Billoir fast and full fitters, have been implemented. Both are linearised least square vertex fitters which rely on a local parametrisation of the track parameters to successfully fit a vertex. Their performance was compared using exclusive $H\rightarrow 4$ lepton decays and it was found that for the purpose of primary vertex finding the fast fitting method is as performant as the (slower) full Billoir mechanism. It therefore was decided to only use the fast vertex fitter for further studies.

The performance of the primary vertex finder was tested on $WH\rightarrow l\nu b\bar{b}$ and $WH\rightarrow l\nu u\bar{u}$ benchmark samples which are commonly used to study vertex finding and b-tagging algorithms. On pure events, i.e. events without pile up, a resolution of 12-14 μm in the transverse plane and around 45 μm in the longitudinal direction could be achieved which is a great improvement compared to the accuracy with which the collision point can be given by the LHC monitoring (which is around 15 μm in $r\phi$ and 5.6 cm in z direction). Running on more realistic data sets with shifted primary vertex and pile up did not reveal a significant decrease of the performance and yields resolutions of 13-15 μm in the transverse plane and 52 μm in z direction. In events with pile up it is important that the actual primary vertex is identified among uninteresting vertices arising from minimum bias collisions. The misidentification rate was found to be below 3% which is in accordance with earlier studies [52]. The performance of the primary vertex finder on $t\bar{t}H$ events was 10.6 μm in the transverse plane and 31.5 μm in the longitudinal direction. These results are better than on the $WH\rightarrow l\nu b\bar{b}$ and $WH\rightarrow l\nu u\bar{u}$ samples because of a higher track multiplicity in $t\bar{t}H$ events. In general, the performance of the primary vertex finder in conjunction with the Billoir fast vertex fitting method was found satisfactory and powerful enough to be used for the analysis of the $t\bar{t}H$ channel. The modular C++ implementation and the newly developed Event Data Model greatly facilitated the comparison of full and fast Billoir fitters and the study of the performance of the primary vertex finder in general.

During this thesis work, three different b-tagging algorithms have been implemented and tested: transverse and longitudinal impact parameter based tagging algorithms (1D and 2D) and a secondary vertex based tagging algorithm (SV). They have been studied separately and in conjunction of 1D+2D (so called 3D) and the 3D tag combined with the secondary vertex tagger. Input samples have been the same as for the primary vertex finder.

At 60% b jet selection efficiency the light jet rejection power of the combined 3D tagger on the $WH \rightarrow l\nu b\bar{b}$ and $WH \rightarrow l\nu u\bar{u}$ benchmark samples was found to be around 60 on pure samples and those with low luminosity pile up and dropped down to 29.3 if the primary vertex was shifted. The problem was identified as coming from the tracking software (iPatRec) which, at that time, was tuned to find tracks which emerge from the global ATLAS origin rather than one centimeter away. In conjunction with the secondary vertex finder the rejection power increased to 153.6 on pure samples, 131.7 on samples with pile up and 50.3 on samples with shifted primary vertex.

The performance on the $t\bar{t}H^0(120)$, $H^0(120) \rightarrow b\bar{b}$ channel for both, the Rome 2 layer Pixel and CSC 3 layer Pixel layout, has been studied. The light jet rejection rate is 190 for the 2 and 225 for the 3 layer Pixel layout for the combined 3D+SV at 60% b jet selection efficiency. This is better than on the $WH \rightarrow l\nu b\bar{b}$, $WH \rightarrow l\nu u\bar{u}$ benchmark samples due to the higher average momentum of the tracks and higher track multiplicity leading to a better reconstructed primary vertex and to a better resolution of the impact parameters.

The performance of the b-tagging software is very promising and is more than twice as good as the standard settings for fast simulation. Again, the modular design and implementation of the new b-tagging software chain along with the new common b-tagging Event Data Model which both have been developed as part of this thesis proved highly useful in the study of the various b-tagging algorithms and their possible combinations. This b-tagging software framework along with its Event Data Model is now used as default in ATLAS.

The primary vertex finding and b-tagging algorithms have both been applied in full reconstruction to the analysis of the $t\bar{t}H$ channel for a Higgs mass of 120 GeV/c². The goal was to re-evaluate the discovery potential of the $t\bar{t}H$ channel using the same analysis steps as described in the ATLAS Physics Technical Design Report but with the recent Computing System Commissioning detector layout and full simulation/reconstruction. Fast simulation has also been used for comparison. The results are compared to the TDR section of the rather recent study of J. Cammin which was done on fast simulation and to an analysis done by CMS on full simulation.

The analysis in this thesis first suffered from a wrong calibration provided in Athena of the jet energies. It was found that especially reconstructed b jets in fully simulated events had up to 13% less energy compared to the truth. This resulted in a reconstructed mass spectra of the Higgs boson that peaks at around 100 GeV/c² instead of 120 GeV/c². Correct jet energy calibration is also important because the assignment of reconstructed jets to the decays of the tops and the Higgs strongly depends on it. The wrong calibration thus lead to a wrong assignment of jets and overall results on the $t\bar{t}H$ channel were very bad. All light and b jets in fast and full simulation have therefore been separately recalibrated by applying a transverse momentum dependent scale factor to the full four momentum of the jet. These calibration functions had first to be determined by comparing the reconstructed jet energy in the $t\bar{t}H$ and background samples to the true energy.

After successful recalibration of the jet energies results in terms of signal to background ratios S/\sqrt{B} of 2.45 for the full simulation and 1.94 for the fast simulation could be reached (using the LO cross section of the $t\bar{t}H$ signal). In earlier studies on fast simulation by J. Cammin a ratio of 1.85 was achieved for the TDR style analysis. CMS published a ratio of 2.34 (for 60 fb⁻¹ which scales down to 1.65 for 30 fb⁻¹) in a recent study.

The biggest difference between CSC full and fast simulation is the default fast simulation setting of the b-tagging performance. It is set to a light jet rejection of 100 for a b jet selection efficiency of 60%. For the same efficiency the full simulation achieves a rejection of 225. The

rejection of the background is twice as good after the requirement of 4 b jets in the event in the full simulation compared to fast simulation. This underlines the need for efficient and well performing b-tagging algorithms as they have been implemented as part of this thesis work. The fast simulation performs a bit better in terms of W and top reconstruction efficiencies but this is due to the higher jet multiplicity, the better resolution of missing energy in the event and the fact that there are no fake electrons/muons which cause the full simulation to less often find a solution for the longitudinal momentum of the reconstructed neutrino.

The overall conclusion is that both, reconstruction algorithms and analysis techniques, are well performant in the ATLAS experiment within the realism applied to the simulated samples of interest. The discovery potential achieved is above 2 and hence, the $t\bar{t}H$ channel contributes to the overall discovery potential of a light Standard Model Higgs boson at the LHC. A significantly better performance than on fast simulation could be achieved. This is mostly due to the well performing b-tagging algorithms which are better by more than a factor of two of what is normally expected in ATLAS and also implemented in the fast simulation. A comparison to results from CMS yield that ATLAS performs better on the $t\bar{t}H$ channel but it needs also be stressed that the CMS study includes many effects and systematic uncertainties which were not possible to be considered in this analysis. Some of the effects have been estimated and it turns out that due to high luminosity pile up and trigger efficiencies the significance might be reduced by up to 20%.

Appendix A

Design of the Vertexing Software

This chapter describes the design of the vertex software and its Event Data Model. The design of the vertex software follows the approach of chapter 7 where the process of vertexing is split into two separate stages: vertex finding and vertex fitting. The fitters are purely mathematical tools which are used by the finders to calculate a vertex position. The idea is that a vertex finder can choose from a set of existing fitters and that the change from one fitter to another is simple. This can only be accomplished if the vertex software uses a common Event Data Model and if the vertex fitters inherit from a common interface. Both has been developed, implemented and tested during this thesis. In addition it is vital that the software makes explicit use of the existing common ATLAS Event Data Model in order to be fully integrated in the Athena framework.

The common interface of the fitters does not put any restriction on the number and type of data members a concrete implementation uses and hence the important requirement of individual configurability of different vertex fitting methods can also be guaranteed in this approach.

This chapter first introduces the vertex part of the ATLAS Event Data Model. It then presents the design of the vertex fitter interface and describes the concrete implementations of the full and fast Billoir vertex fitting methods of sections 7.2.3 and 7.2.4. The primary vertex finder as a client of the vertex fitters is presented at the end followed by a configuration chapter.

The vertex software is under constant improvement and has been enhanced recently with additional fitters such as the Kalman and adaptive vertex fitters. This chapter gives a snapshot of the vertexing software as it is in Athena release 11.0.41.

A.1 Terminology

During the two appendices about the design of the vertexing and b-tagging software and their Event Data Models the following format for classes and software related objects is used. All class names are written in **emphasis**. Names of configuration variables used for Python steering of classes are written in *italic*. Possible values of these configuration variables are written in “quotation marks” in case the variable is a string. The diagrams use the UML (Unified Modelling Language) [71]. Common computing terms in ATLAS will be explained briefly when appropriate. For further details the reader is invited to refer to the ATLAS online documentation pages [72] which are the most up to date documentation about the ATLAS software.

A.2 Event Data Model

The vertex Event Data Model defines the objects which are used by all vertex finders and fitters to store and pass on relevant vertexing information. It has been developed alongside and is part of the general ATLAS Event Data Model.

A vertex in an high energy physics event is normally understood as a point in space where a certain number of particles are produced. This can be the collision point of two particles or the decay point of an unstable particle. The most general vertex object is therefore only a position in space $V=(x,y,z)$ and the according class is called **Vertex**. Since vertices in high energy physics can never be given with infinite accuracy a more specialised vertex object can be derived by extending the first one with a 3x3 error matrix. The extended class is called **RecVertex**. Additional variables of interest are the fit quality χ^2 and the number of degrees of freedom (ndf) of the fit to a reconstructed vertex. The inheritance structure of these basic vertex objects and their data members is shown in Fig. (A.1). Additional information which is

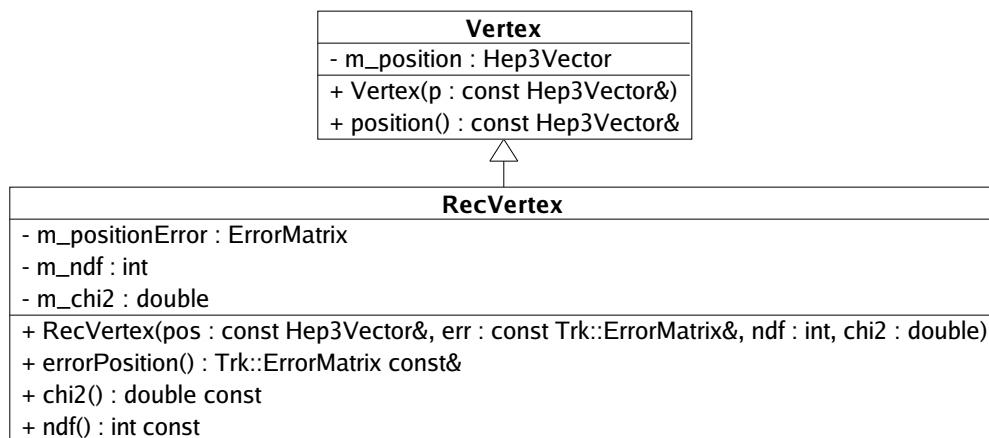


Figure A.1: .

The design of the Vertex and RecVertex classes. Default constructor, destructor and copy constructor/assignment operator are not shown.

stored in a vertex object is the sum of the transverse momenta of the tracks used in the vertex fit - this serves as a criterion to define the primary vertex in a pile up event - and also track related information like pointers to tracks used in the fit, the χ^2 contribution of each track to the vertex fit and the perigee of the track with respect to the fitted vertex. The track related information is stored in the object **VxTrackAtVertex**. The final vertex object is called **VxCandidate** and is shown in Fig. (A.2). The **VxContainer** is the top level object to store one or many **VxCandidate** objects (as in pile up there are more vertices in the event of which only one is the primary vertex) and it is the object which is written to StoreGate and eventually to persistent storage on disk.

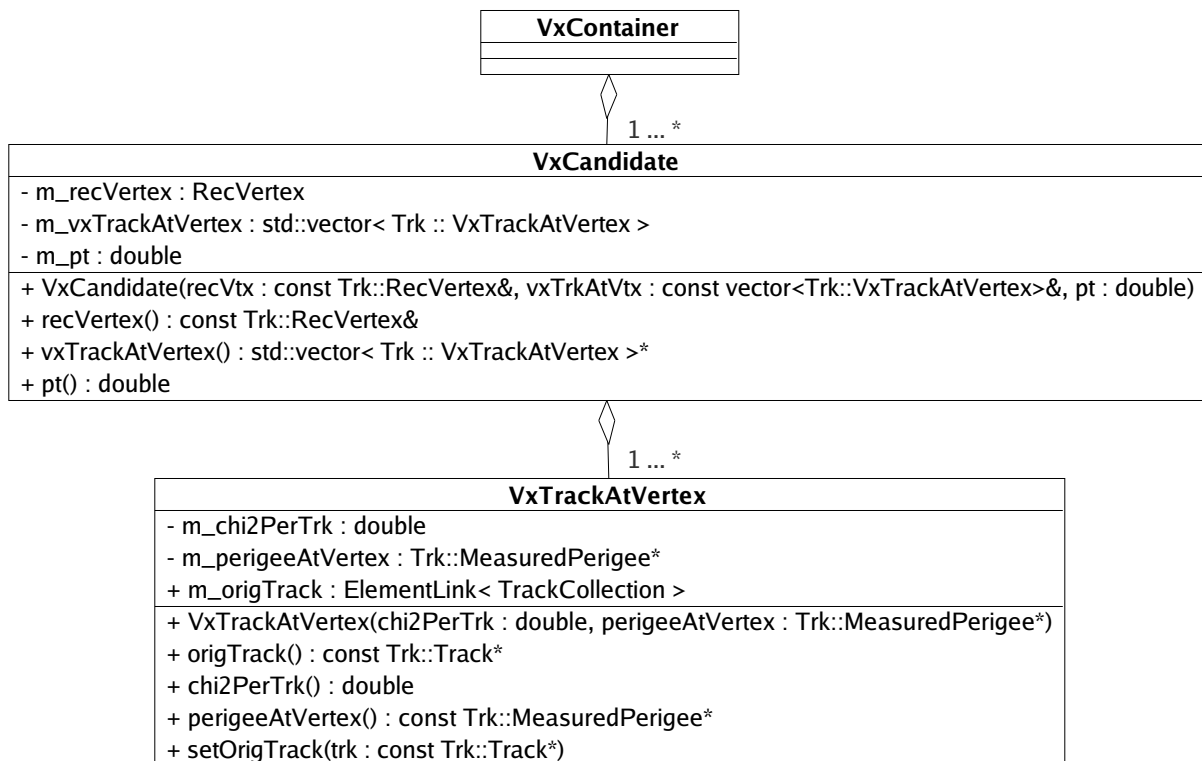


Figure A.2: The vertex EDM object `VxCandidate`. Default constructor, destructor and copy constructor/assignment operator are not shown.

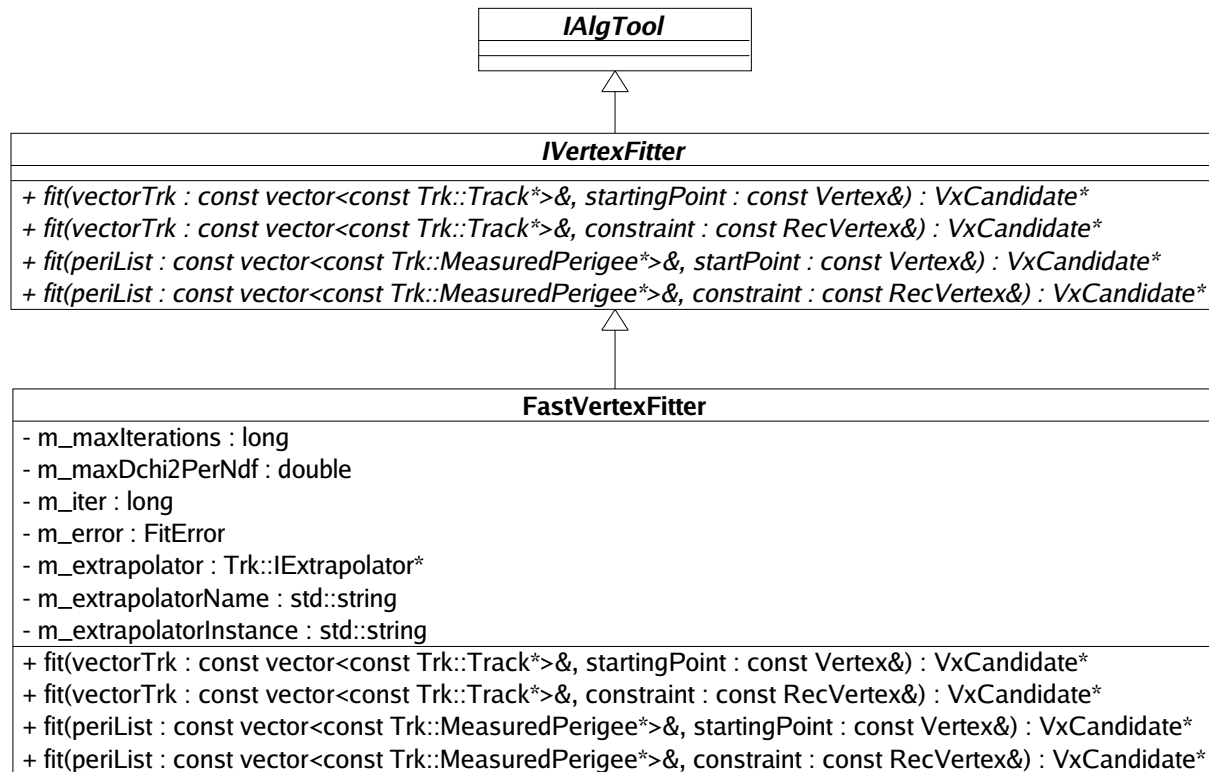


Figure A.3: Interface design of the vertex fitters.

A.3 Vertex Fitter Interface and Implementations

The common interface for all vertex fitters is shown in Fig. (A.3). It is specified in an abstract base class called `IVertexFitter` and supports exactly one method called `fit(...)` which is overloaded four times to serve different use cases: either the input is a list of `Tracks` or `MeasuredPerigees` with either a constraint or starting point for the fit. In all four cases a pointer to the fitted `VxCandidate` is returned. Every concrete implementation of a vertex fitter has to inherit the `IVertexFitter` interface.

The vertex fitters are tools which need to be called on demand and therefore `IVertexFitter` inherits from an Athena interface class called `IAAlgTool`, which guarantees that each concrete vertex fitter implementation behaves like an Athena `AlgTool`. `IAAlgTool` is an abstract base class which provides an interface that is especially designed for classes that need to be called on demand but still need the configurability of an Athena algorithm and all the services of the Athena framework.

With this design every vertex fitter looks the same for a client. Modularity with respect to the usage of different fitters is guaranteed because the client depends at compile time only on the interface while the concrete fitter implementation is chosen at run time. The steering of each tool is done from outside using the standard Athena approach by means of python [73] job option files. Configuration variables for the fast and the full fitter implementation are shown in section A.5.1. The class names of the concrete implementation of the full Billoir mechanism is called `FullVertexFitter`, the one of the fast method `FastVertexFitter`.

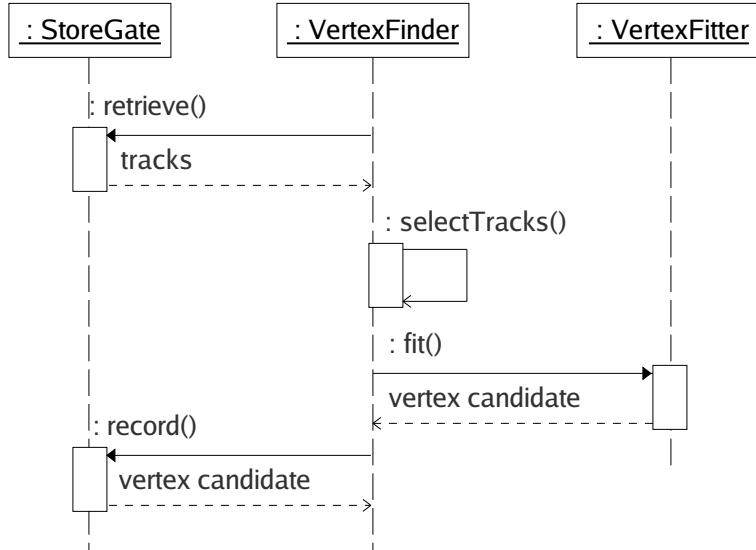


Figure A.4: Data flow between the primary vertex finder, the fitter tools and the transient event store (StoreGate).

A.4 Primary Vertex Finder

The primary vertex finder is a client of the fitter tools. Due to the modular design it can use either fast or full fit or any new fitter which might be implemented in the future. The flow of information between the primary vertex finder, the vertex fitter and StoreGate is shown in Fig. (A.4).

In the beginning the primary vertex finder needs to retrieve a vertex fitter tool. The only information it needs to have about the tool is its name which is given to the finder on construction of the algorithm. The actual name is defined in the according python job option file of the vertex finder (see section A.5.2). To change between different fitters is as easy as to change the name in the configuration file.

During execution the primary vertex finder algorithm reads tracks which have been reconstructed by the tracking software and stored in the Athena transient event store (StoreGate). It performs track selection cuts and passes a subset of all input tracks to the fitter tool. The tool performs its calculation and passes a `VxCandidate` object back to the finder algorithm. The finder performs an additional track selection based on the χ^2 a track contributed to the fit of the vertex and gives the selected tracks again to the fitter, which performs its calculations and again gives back a `VxCandidate` object. The final primary vertex is pushed into the `VxContainer` and written to StoreGate for further use by downstream algorithms and to be written to disk.

This schema is basically true for all types of input files. Only in case of events with pile up vertices the track selection procedure is more elaborate (see chapter 7.3.5) but the interplay between finder and fitter stays the same.

A.5 Configuration

A.5.1 Billoir Fast and Full Vertex Fitters

The vertex fitters are configured like all Athena AlgTools via python steering files. Possible configuration variables are shown in Table (A.1). The number of internal iterations a tool should perform is set by *maxIterations*. The default is set to 3. The maximum difference in χ^2/ndf between the iterations is given by *maxDchi2PerNdf*. The fitters make use of standard tracking tools to extrapolate the perigee to the vertex region. Different extrapolators exist and the type and instance can be chosen via the variables *ExtrapolatorName* and *ExtrapolatorInstance*. The fast and full fit use the standard preconfigured “Trk::Extrapolator” with the private instance name “TrackToVertexExtrapolator”.

Property	Meaning	Default Value
<i>maxIterations</i>	maximum internal iterations the fitter should do	3
<i>maxDchi2PerNdf</i>	maximum difference in χ^2 per ndf from one iteration to next	0.000001
<i>ExtrapolatorName</i>	name of the extrapolator tool	“Trk::Extrapolator”
<i>ExtrapolatorInstance</i>	name of the extrapolator instance	“TrackToVertexExtrapolator”

Table A.1: Configuration of the full/fast vertex fitter.

A.5.2 Primary Vertex Finder

The primary vertex finder is implemented as an Athena Algorithm and can also be configured through a python job option file. The name of the configurable properties, their meaning and default values are listed in Table (A.2). Most of the variables are self explanatory. The *useBeamConstraint* flag determines if the beam position should be used as an additional measurement in the fast/full fit method or not. The starting point of the vertex fit is always the beam position. The beam position itself does not have to be provided by the user but is taken from the beam condition database during run time. Its value is retrieved once per event since the position can change even during one fill. With the *chi2CutMethod* the user can choose how the algorithm should get rid of tracks after the first vertex fit depending on their χ^2 value. Two variations are available:

- Version 1:
 - remove all tracks with $\chi^2 > \text{maxChi2PerTrack}$
 - refit the vertex with the previous result as starting point
- Version 2:
 - remove tracks one by one starting with the one with highest $\chi^2 > \text{maxChi2PerTrack}$
 - refit the vertex with the previous result as starting point
 - repeat until all $\chi^2 < \text{maxChi2PerTrack}$

Property	Meaning	Default Value
<i>TrackName</i>	track input collection key	“Tracks”
<i>VxCandidatesOutputName</i>	vertex output collection key	“VxPrimaryCandidate”
<i>FitRoutine</i>	name of vertex fitter	“FastFit”
<i>useBeamConstraint</i>	beam constraint on/off (1/0)	0
<i>minPt</i>	minimum p_t of track	1 GeV
<i>maxZ0</i>	maximum z_0 of track	150 mm
<i>maxD0</i>	maximum d_0 of track	0.25 mm
<i>maxD0overSigmaD0</i>	maximum $\frac{d_0}{\sigma_{d_0}}$ of track	3.
<i>useSiHitCut</i>	check if track has 1 b-layer hit and at least 1 additional pixel hit (on/off)	1
<i>chi2CutMethod</i>	choose among different χ^2 track selection strategies	1
<i>maxChi2PerTrack</i>	maximum χ^2 a track can have to be kept after first fit	5.
<i>enableMultipleVertices</i>	looks for more than one vertex (pile up)	0
<i>clusterLength</i>	defines the cluster length in z direction	3. mm

Table A.2: Configuration of the primary vertex finder.

For the performance studies in this thesis version 1 has been. It was tested that for the fit of the primary vertex both approaches give very similar result. Version 1 is way faster since there is no refit of the vertex for each removed track and hence it was the chosen method.

A.6 Location of the Vertexing Software

The vertexing software is divided into several packages. The package for the Event Data Model is in

`Tracking/TrkEvent/VxVertex`

in the ATLAS Athena offline repository. The interface for the vertex fitters is in

`Tracking/TrkVertexFitter/TrkVertexFitterInterfaces`

Concrete implementations of the fast and full Billoir vertex fitters are located here

`Tracking/TrkVertexFitter/TrkVertexBilloirTools`

`Tracking/TrkVertexFitter/TrkVertexKalmanFitter`

Clients of the vertex fitters like the primary vertex finder and the b-tagging software are here

`InnerDetector/InDetRecTools/InDetPriVxFinderTool`

`PhysicsAnalysis/JetTagging/JetTagTools`

but many other clients exist which are not listed.

Appendix B

Design of the Jet-Tagging Software

The design of the jet-tagging software is based on the principles and ideas about the general process of jet-tagging given in chapter 9.1. The considerations of splitting the tagging process into several steps and the idea of a modular and expandable tagging procedure, where each tagging method is taken care by a separate algorithm, have to be translated and incorporated into the existing ATLAS Athena software and into a consistent C++ design.

On the Event Data Model side, the anticipated modularity requires a very flexible data object which stores all tagging relevant information: common tagging information which every tagger is required to produce (e.g. tagging likelihood) and specialised information which only a certain tagger calculates (e.g. impact parameter significance).

The keystone to meet all these requirements are common interfaces. The tagging algorithms need a common interface so they can be called one after the other by a higher level jet tag algorithm - without the need of deeper knowledge of the used tagger. The data classes need common interfaces so that the tagging algorithms can add their information and the user and tag combination tools can access them in a uniform way no matter which tagger produced them.

Configuration and steering of the whole tagging process and in particular individual configurability of tagging algorithms is another important requirement for a general jet-tagging environment. However, the use of common interfaces in algorithms and data classes does not put any restrictions on the number and type of data members a derived class can use - and hence each tagging algorithm can be configured individually using the standard Athena approach of python steering files to set these private data members.

This chapter starts with a description of the jet-tagging Event Data Model which was developed alongside the new ATLAS Event Data Model. It then presents the data flow of the jet-tagging environment and how the tagging process of tag preparation, tagging itself and post processing as presented schematically in Fig. (9.1) is implemented within a C++ and Athena context. Required interfaces of the tagging algorithms and all tools needed during the tagging (truth matching, jet track association) are presented.

The concrete implementation of the b-tagging algorithms is presented in section B.2.2 and their configuration is shown. Examples on how to run b-tagging and how to retrieve results end this chapter.

The computing terminology is in accordance with section A.1 of the vertexing appendix.

B.1 Jet-Tagging Event Data Model

The `JetTag` data object stores all relevant tag information which is produced during the jet-tagging process. Given the stringent requirements of modularity with respect to the varying number of tagging algorithms which are used and the implementation of new taggers (whose calculated information has to be stored somewhere) this data object has to be very flexible and expandable in design. Other relevant data which is needed for tagging also has to be stored in the `JetTag` object including

1. jet kinematics (momentum, energy) and particle identification information
2. a link to the original jet from the ESD¹ level
3. jet-track association

where in practise some of this information might be missing or might not be available.

The kinematic and particle identification information is stored in inherited data members. The link to the original jet and associated tracks is stored via the navigation scheme which is offered by the Athena framework. In principal these are just pointers to the according object with the possibility of a hierarchical navigation through them.

Kinematics and Particle Identification Information This information is stored in the `JetTag` object in inherited data members. The inheritance structure is shown in Fig. (B.1). The kinematics are provided via an `I4Momentum` interface and the concrete Cartesian implementation `P4PxPyPzE` was chosen for the `JetTag` object. Data members and access methods for particle identification, charge and other properties are given by inheritance from the `ParticleBase` class. The inheritance structure is the same for nearly all data objects which are stored on AOD² level. This is to provide a common look and feel to the users of AOD objects and to be able to develop common tools which act on these objects.

Link to original Jet and Track Jet Association A link to the original ESD Jet as well as the link to associated tracks is implemented using the concept of navigation. This functionality is given to the AOD objects via inheritance from the base class `INavigable`. In principal navigation is just a system of pointers to constituents of objects (i.e. a jet has cells) with the possibility of hierarchically going through the constituents.

Tagging information The information each tagging algorithm needs to store into the `JetTag` object can be divided into two categories

- **Mandatory information:** data which every tagger has to provide in order for the whole tagging chain to work (e.g. it has to be possible to combine tag results from different taggers)
- **Optional information:** individual tag information only used and needed for a specific tag tool

¹Event Summary Data: contains detailed reconstruction information.

²Analysis Object Data: contains a subset of information of the ESD and is the data format for physics analysis.

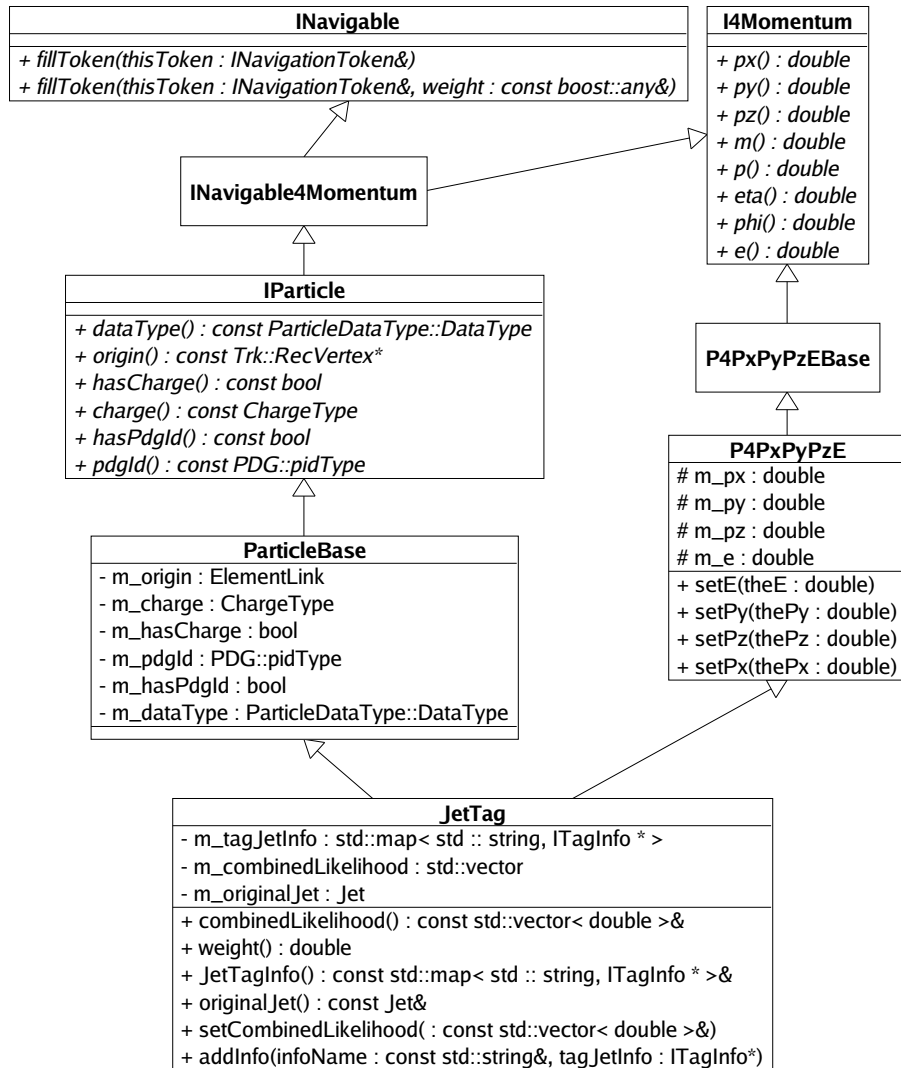


Figure B.1: Inheritance structure, data members and methods of the JetTag object. This inheritance structure is used for most AOD objects. It provides the AOD objects with common methods to retrieve kinematic and particle specific (e.g. charge) information. The methods of the JetTag object basically provide set and get methods for the weight/likelihood and to add and retrieve tag info objects.

Mandatory information is common information like a discriminating variable which is needed by the user to select tagged jets and during the tag combination process to construct a more powerful discriminant. Two discriminants (likelihood and weight) are supported and each tagging algorithm has to provide this information. Optional information is specific to a tagging algorithm. An example would be the signed impact significance for an impact parameter tagger or the vertex probability for a secondary vertex based tagger.

To guarantee flexible and individual “storage space” for every tagger and the possibility to add new taggers with their according information a design of so called info objects has been proposed (see Fig. (B.2)). The idea is that the `JetTag` object has a map of pointers to an abstract base class called `ITagInfo`. This base class provides a minimal interface which all info classes of different taggers have to use. This interface guarantees that all taggers can provide a likelihood/weight as their tag result and that these results can be accessed later by the user or other tools whose goal it is to combine the tag information to a more powerful one. The interface includes set and get methods for the tag likelihood and weight which are used by the taggers to set these values and by the user or other tools to retrieve the information. It contains an `infoType()` method which returns a unique string to identify the info object and relate it to a tag tool by which it was produced. To avoid ambiguities the instance name of a tag tool is used as the identifier. The info type data member (added via the `BaseTagInfo` class) can only be set when constructing an info object. This is to avoid that the string is accidentally set to another value later on and the link between tagger and info object is lost. The last method of the interface is there for the C++ copy constructor to assure the info objects are copied correctly when a whole `JetTag` object is copied/assigned.

With this design it is possible that all classes derived from `ITagInfo` have common set and get methods for the actual tag likelihood/weight and still can be enhanced to offer space for any individual information a certain tagger might produce. Likelihood and combiner tools profit from this design and offer the user a lot of flexibility with respect to which information from which taggers should be combined - without the need of retagging.

The only concrete implementation of an info class which is provided directly by the jet-tagging environment is the so called `TruthInfo` class (see Fig. (B.3)). It is a special type of info class used to store the result of the truth match between the reconstructed jet and the generated particles in the `McEventCollection`. This truth matching information is needed for performance studies no matter which tagging algorithms are run. Therefore it is provided by the environment and filled by default during the jet-tagging process (see section B.4).

The truth info class contains a string which is set by the truth matching tools. The string stores the truth match of the jet which is either B for b jet, C for c jet or N/A for light jets. The choice of a string in stead of an enum leaves greater flexibility for future use of this class. In addition to that the class contains two data members which store the closest distance in ΔR of the jet (as defined in Eq. (9.4)) to a c and a b quark. This information is often needed when studying the performance of jet-tagging algorithms (“jet cleaning”).

The `TruthInfo` approach also addresses the problem that in an analysis on real data, there is no truth information available and that no AOD object should offer direct space to store truth information. This is solved here by not appending any `TruthInfo` object to the map of `ITagInfo` objects in the `JetTag` object on real data.

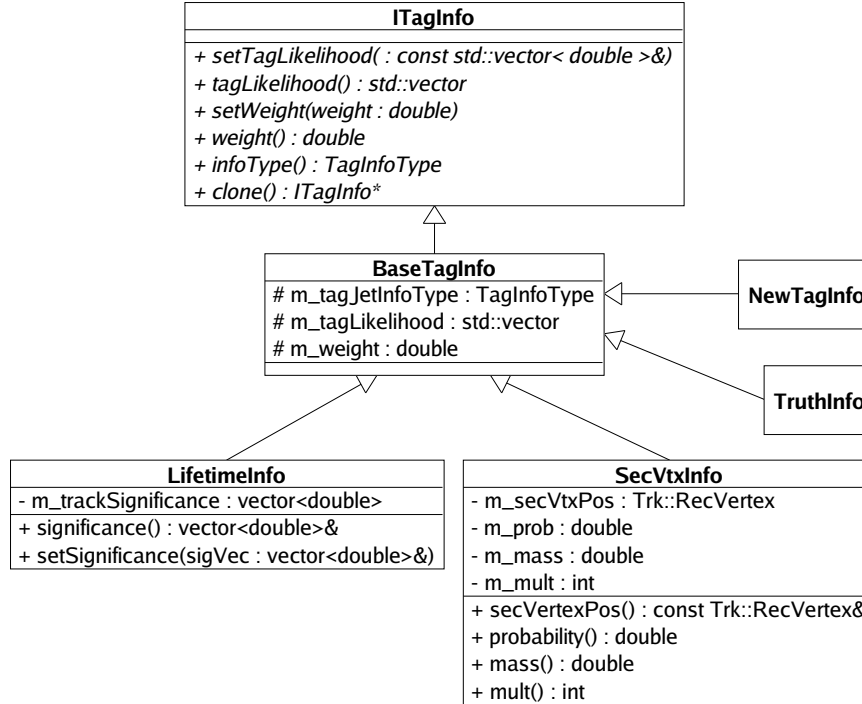


Figure B.2: Inheritance structure of the info objects. All info objects are required to inherit from one common base class to give them a common interface which can be used by other tools (e.g. LikelihoodTool) to retrieve this information. Additional tag specific information can be implemented in the derived classes.

B.2 Algorithms and Data Flow

This section describes the design of the algorithmic part of the framework and the info flow between algorithms and the Event Data Model.

B.2.1 Jet-Tagging Process

The jet-tagging process is split into several steps and is shown in Fig. (B.4) as a UML sequence diagram. The top level algorithm `JetTagBuilder` is called once per event by the Athena framework. It retrieves the primary vertex position and the jets.

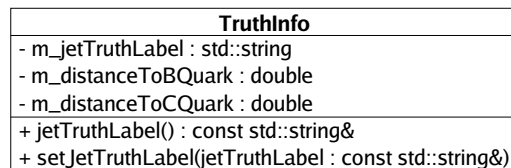


Figure B.3: Jet-tagging `TruthInfo` class to store relevant truth matching information. In addition to the truth label the distance in ΔR to the closest *c* and *b* quark can be stored. This info is often needed for so called “jet cleaning” purposes when measuring the performance of jet-tagging algorithms.

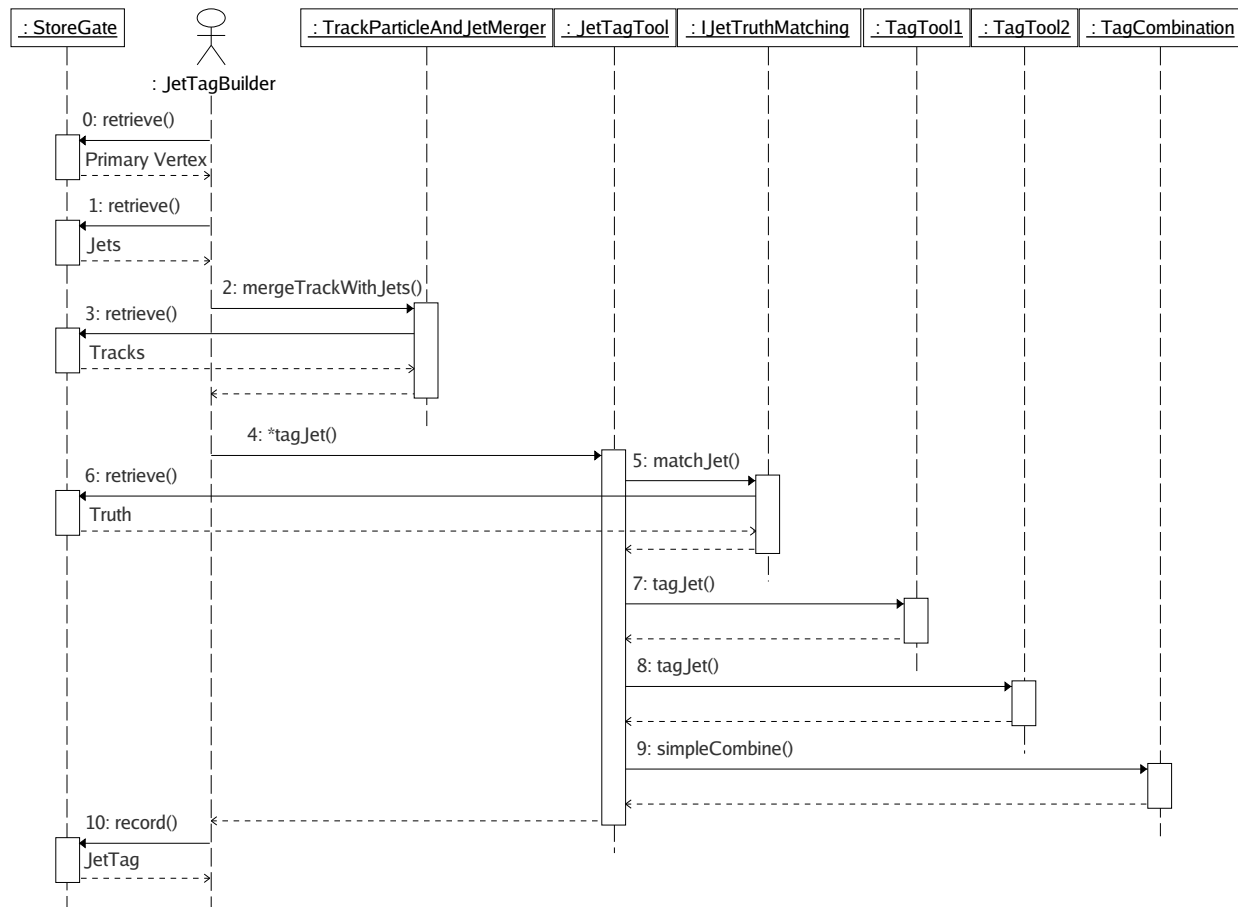


Figure B.4: Sequence diagram of the jet-tagging process. The tagging process is split into several levels. A top level algorithm (`JetTagBuilder`) uses a `JetTagTool` which subsequently calls all tagging tools. See text for a detailed explanation.

The first tool called is the `TrackParticleAndJetMerger` which gets the tracks from `Storegate` and associates them to the jets. Then the `JetTagBuilder` does not call the tagging algorithms itself but calls a `JetTagTool` for every input jet. This extra layer is typical for the execution process of algorithms in Athena because it makes it possible that the `JetTagTool` can be used by other tools/algorithms to tag a jet. The top level `JetTagBuilder` is de facto only the default Athena algorithm to execute the jet-tagging during standard event reconstruction. The actual set of jet tag tools and the question if truth matching is to be enabled are determined at run time. In case of simulation, the `JetTagTool` calls an `IJetTruthMatching` tool which labels each jet with truth information. There are several truth matching tools available and they all have a common interface and hence the `JetTagTool` only needs to know about the interface. After the truth matching, the `JetTagTool` calls a sequence of tag tools (`TagTool1`, `TagTool2`, ...) which all append their specific info object to the `JetTag` object. After all tools have been called the `JetTagTool` calls a `TagCombination` tool which combines the tag information of a predefined set of tag tools so that the `JetTag` object itself has a default weight and likelihood. The completed `JetTag` object is pushed into the `JetTagContainer` which is written once per event to the transient event store (to be used by other algorithms) and to the persistent event

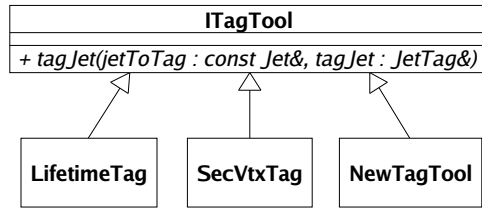


Figure B.5: Interface structure of the tagging algorithms. The `ITagTool` base class specifies one methods which has to be implemented by all derived tagging algorithms. The `JetTagTool` uses exactly this method to call all the tagging tools.

store.

B.2.2 Individual Tag Tools

For the above scheme to work, the individual tag tools need to have a common interface. This interface method is the only thing which the `JetTagTool` needs to know to call a tagger. This makes it possible that different numbers of taggers can be run in any desired order. Due to the common interface of the info objects the results of a subset or all of the taggers can be combined with hindsight.

Figure (B.5) shows the interface of the base class `ITagTool` from which all concrete tag implementations need to inherit. It is minimalistic and supports only one method which all taggers have to implement and which is called by the `JetTagTool`. As input it takes an ESD `Jet` object and a reference to a `JetTag` object. Every tag tool subsequently adds its specific tag results to the `ITagInfo` map of the `JetTag` object.

B.2.3 Reference Histograms

To construct a discriminating variable a tagging environment needs reference histograms as input. Within the jet-tagging environment the `LikelihoodTool` (see paragraph B.3) takes care of reading the histograms from disk and using them for the calculation of the discriminating variable (e.g. likelihood or weight). The names of the histograms need to be the same as used in the configuration of the `LikelihoodTool`.

In general the jet-tagging environment itself does not directly support the production of reference histograms. However, it also does not hinder a tag tool to offer this feature and it is up to a concrete implementation of a tag tool to do so or not.

Section B.5 shows job option snippets which demonstrate how the reference histogram input files can be modified. The section about the likelihood tool shows how the histogram files are read in.

B.3 Implementation of Helper Tools

The jet-tagging framework provides a couple of helper tools to fulfil the following tasks:

- association between tracks and jets
- truth matching

- likelihood/weight calculation
- combination of the results of different taggers

A brief description of these tools is given in this section. They are all implemented as Athena AlgTools and can hence be called on demand by the jet-tagging software.

Jet-Track Association Tool The association of tracks to a jet is done as described in section 9.3.1. This procedure requires knowledge of all tracks and all jets at the same time and hence the association cannot be done jet by jet during the tagging process but has to be done in the top level algorithm (e.g. the `JetTagBuilder`) before calling the `JetTagTool` for every jet. In principal this association could be done once and for all by a previous algorithm. However, it is possible that a `TauJetBuilder` wants to use a different configuration for the association than e.g. a `BJetBuilder`.

The association tool is called `TrackParticleAndJetMerger`. It offers only one method:

```
JetCollection* mergeTrackWithJets(const JetCollection*,
                                const INavigable4MomentumCollection*)
```

The input is the original `JetCollection` and the `TrackParticleContainer` and the output is a new `JetCollection` which has tracks associated to the jets.

Truthmatch Tools Truth matching is done as described in section 9.3.2. The two different matching strategies are implemented in two different tools, namely the `JetQuarkLabel` tool and the `JetTrackTruthMatching` tool. They inherit a common interface from a base class and hence can be interchanged easily. The method to match a jet is

```
bool matchJet(const Jet& myJet);
```

It is called by the `JetTagTool` once per jet. The information is stored in a `TruthInfo` object which is appended to the `JetTag` object as a normal info object with the identifier "TruthInfo". If the method return false the jet will be labelled as light by default. For the cone matching method the distance to the closest b and c quarks are also stored. This information is needed for "jet cleaning" purposes when reference histograms or performance plots are generated using the same input sample as source for b and light jets (e.g. $t\bar{t}H$ sample). In that case jets matched as light jets are very often b jets and one has to reject them by checking how close in ΔR true b and c quarks are.

Likelihood Tool The construction of a weight or likelihood out of one or several probability density functions (reference histograms) and their combination is an often needed task during jet-tagging. The jet-tagging framework offers various tools for that reason.

In addition to calculating weights/likelihoods the likelihood tools handle the reading in of histograms - a service which eases the life of every tagger. A very detailed description of the likelihood tools is replaced by an example on how the tool is typically used. Starting point is that every tagger has its own instance of the `LikelihoodTool` and uses it in 3 steps.

At the beginning of the run, during the initialisation phase, it will retrieve a `LikelihoodTool` and tell it to read in the reference histogram file


```
void readInHistosFromFile(const std::string& refFileName);
```

where the string `refFileName` is a reference to the real input file which needs to be established in job options file.

Every time the tag tool is called by the `JetTagTool` it calculates some discriminating variable(s) (e.g. significance) and assigns them to the tool via

```
void setLhVariableValue(const std::string& lhVariable,
                       std::vector<double>& value);
void setLhVariableValue(const std::string& lhVariable,
                       double value);
```

Every variable used in the likelihood needs to have a unique name. As many variables as wanted can be given to the tool. In case one type of variable appears more than once per jet (e.g. the significance of each track) a vector of values can be given to the tool.

After all variables of a tagger are calculated and passed on to the likelihood tool then one can calculate a weight or likelihood by calling

```
std::vector<double> calculateLikelihood();
double calculateWeight();
```

The first method returns a vector of (pre)likelihoods. It is a vector which consists of an entry for every object category which one wants to discriminate (in the case of b-tagging this is normally two: b and light jet). The first entry is some kind of signal probability of the object (i.e. jet) and the others are background probabilities. It is important to say that this is not the final likelihood for a certain tagger. Out of generality that this information might be combined with that of other taggers later on a so called "pre likelihood" or probability is stored. The combiner tool has to be used to get the real likelihood for the jet.

The `calculateWeight()` method just returns one value: the weight of the jet. It does not need to be a vector nor a "pre weight" since there are no normalisation issues and weight combination is simply additive.

The likelihood tool can be configured to only use a subset of variables to calculate the likelihood or weight. A secondary vertex based b-tagging tool, for example, might use four variables to construct a discriminator (vertex mass, probability, multiplicity and energy fraction) which all have been given to the tool via the `setLhVariableValue(...)` method described above. The user, however, might decide to use only two of them to calculate the discriminating variable of this tagger. Without the need of changing the code one can tell the likelihood tool to only use a subset of taggers via job option steering:

```
LHToolOfTagTool1 = Service ("ToolSvc.LHToolOfTagTool1")
LHToolOfTagTool1.useTheseLhVariables = [ 'mass', 'probability' ]
```

where "LHToolOfTagTool1" is the instance name of the private likelihood tool used by the tagger.

Combiner Tool The combiner tool needs to be used to retrieve likelihood information for one tagger and to combine likelihood information from various taggers. It is not needed for the weight.

The `CombinerTool` offers two methods. The first is to retrieve the proper likelihood for a single tagger

```
std::vector<double> simpleCombine(const Analysis::ITagInfo*) const;
```

It takes the pointer to the info object of the tagger (stored in the `JetTag` object) and returns the likelihood.

The second method can be used to combine tagging results from a list of tag tools.

```
std::vector<double> simpleCombine(  
    const std::map<std::string, ITagInfo*>&,   
    const std::vector<std::string>&          ) const;
```

It takes the whole map of info objects and a list of tagger names and returns the combined likelihood. The first entry is always the signal likelihood of the jet, i.e. in the case of b-tagging if this jet is of the type b jet.

B.4 Access to Tagging Results

Tagging information is stored in a `JetTagContainer` which can be read in by another algorithm the standard Athena way. In this example we read in a collection with the key "JetTagCollection" which was produced by some `JetTagBuilder` (this could be the `BJetBuilder`) and retrieve its tag information.

In the execute method of a (user analysis) algorithm the `JetTagContainer` can be read in as follows:

```
const JetTagContainer *jetTagContainer( 0 );  
m_storeGate->retrieve( jetTagContainer, "JetTagContainer" );  
log << MSG::DEBUG  
    << "Number of Jets in event: " << jetTagContainer->size() << endreq;
```

where `m_storeGate` is a pointer to the Athena StoreGate service. After these lines the pointer `jetTagContainer` will point to the `JetTagContainer` of the current event and a line with the number of jets in the event will be displayed.

The tagging information for each jet is obtained by a loop over the `JetTag` objects in the `JetTagContainer`

```
JetTagContainer::const_iterator jetTagItr = jetTagContainer->begin();  
JetTagContainer::const_iterator jetTagItrE = jetTagContainer->end();  
  
for ( ; jetTagItr != jetTagItrE ; ++jetTagItr )  
{  
    const JetTag* myJet = *jetTagItr;  
    // do something  
}
```

In the following we assume that we are in the loop over the jets acting on one `myJet` object. At the end of the tag process the `JetTagBuilder` uses the `CombinerTool` to assign a default combination of taggers to the final `JetTag` object. This information can be retrieved by typing

```
log << MSG::DEBUG  
    << "signal likelihood of this jet is: " << myJet->lhSig() << endreq;
```

because the `lhSig()` method returns the first element of the `JetTag` likelihood vector. In analogy for the weight one can do

```
log << MSG::DEBUG
    << "signal weight of this jet is: " << myJet->weight() << endreq;
```

To retrieve the likelihood/weight for a certain tagger one needs to retrieve the info map of the `JetTag` object and get hold of the corresponding info object. The key of the info object in the map is the same as the name of the info object which itself has been derived from the instance name of the tagger which added this info object to the `JetTag` object (one should remember this is to avoid ambiguities between taggers and info objects). The following lines show how to retrieve the likelihood and weight of the a jet tag tool named "TagTool1".

```
const std::map<std::string, ITagInfo*> jetTagInfo = myJet->JetTagInfo();
ITagInfo* tagTool1 = jetTagInfo->find("TagTool1")
vector<double> likelihood = m_combinerTool->simpleCombine(tagTool1);
log << MSG::DEBUG <<
    "TagTool1 signal likelihood of jet:" << likelihood[0] << endreq;
log << MSG::DEBUG <<
    "TagTool1 signal weight      of jet:" << tagTool1->weight() << endreq;
```

Notice that due to the common interfaces no casting is needed to retrieve this information. The above lines work in the same way for any info object which inherits from `ITagInfo` by just changing the key in the `find` method of the map to the name of the other info object.

In the next example the `CombinerTool` is used to combine results from `TagTool1` and `TagTool2`.

```
vector<string> combineTheseTaggers;
combineTheseTaggers.push_back("TagTool1");
combineTheseTaggers.push_back("TagTool2");
vector<double> likelihoodComb =
    m_combinerTool->simpleCombine(jetTagInfo, combineTheseTaggers);
log << MSG::DEBUG
    << "Comb signal likelihood of jet:" << likelihoodComb[0] << endreq;

ITagInfo* tagTool2 = jetTagInfo->find("TagTool2")
log << MSG::DEBUG << "Comb signal weight of jet:" << tagTool1->weight()
    + tagTool2->weight() << endreq;
```

Notice that this time the whole info map is passed as a pointer to the `CombinerTool` along with a vector of tagger names to be combined. To have a combined weight the weights of the `TagTool1` and `TagTool2` info objects just need to be summed.

B.5 Changing the Reference Histogram Input Files

The Athena histogram service (`THistSvc`) use “reference” names to find the input files. This has the advantage that the input files can be changed via python job options and the actual source code where the likelihood tool reads in the reference histograms stays untouched.

In general two reference histogram input files are used, one for the signal histograms “JetTagRefFileSig”, and one for the background ones “JetTagRefFileBkg”. The files have to be added to the list of input files for the histogram service to know where they are. In this example we use the file names SigHisto.root for the signal histograms and BkgHisto.root for the background histograms.

```
theApp.Dlls += [ "RootHistCnv" ]
THistSvc = Service( "THistSvc" )
THistSvc.Input += [
    "JetTagRefFileSig DATAFILE='<fullpathtofile>/SigHisto.root' OPT='OLD'",
    "JetTagRefFileBkg DATAFILE='<fullpathtofile>/BkgHisto.root' OPT='OLD'"
]
```

The connection to the real files can also be automatised (i.e. the fullpathtofile does not need to be known) if the reference histograms are located in the share folder of an (arbitrary) Athena package which has been compiled already (or is part of the release used). The absolute path to the files can then be found using the a predefined python FindFile() method

```
dataPathList = os.environ[ 'DATAPATH' ].split(os.pathsep)
dataPathList.insert(0, os.curdir)
from AthenaCommon.Uutils.unixtools import FindFile
JetTagsigname = FindFile( 'HbbRefHistos.root', dataPathList, os.R_OK )
JetTagbkgname = FindFile( 'HuuRefHistos.root', dataPathList, os.R_OK )
```

and in the connection is then made by using the python string, e.g.:

```
"JetTagRefFileSig DATAFILE='" +JetTagsigname+ "' OPT='OLD'",
```

B.6 Location of the Jet-Tagging Software

The jet-tagging package is divided into 4 packages, all located under

PhysicsAnalysis/JetTagging

in the ATLAS Athena offline repository. Names and contents of the packages are as follows:

JetTagInfo contains the ITagInfo base class and the BaseTagInfo class which implements the interface classes and adds needed data members.

JetTagEvent contains the JetTag object and the JetTagContainer classes.

JetTagTools holds the tag tool interface class ITagTool and the likelihood and combiner tools along with smaller helper classes (e.g. histogram helpers).

JetTagAlgs is a container package where concrete implementations of JetTagBuilders and JetTagTools should go.

Other helper tools described in B.3, e.g. truth match and jet-track association tools are in the package

PhysicsAnalysis/AnalysisCommon/ParticleJetTools

Bibliography

- [1] <http://lcg.web.cern.ch/LCG>
- [2] O. Brüning (ed.), P. Collier (ed.), P. Lebrun (ed.), S. Myers (ed.), R. Ostojic (ed.), J. Poole (ed.), P. Proudlock (ed.), LHC Design Report v.1 : the LHC Main Ring, CERN-2004-003-V1.
- [3] O. Brüning (ed.), P. Collier (ed.), P. Lebrun (ed.), S. Myers (ed.), R. Ostojic (ed.), J. Poole (ed.), P. Proudlock (ed.), LHC Design Report v.2 : the LHC Infrastructure and General Services, CERN-2004-003-V2.
- [4] M. Benedikt (ed.), P. Collier (ed.), V. Mertens (ed.), J. Poole (ed.), K. Schindl (ed.), LHC Design Report v.3 : the LHC Injector Chain, CERN-2004-003-V3.
- [5] B. Mellado, G. Unal, Sau Lan Wu, SM Higgs Production Cross-Sections and Branching Ratios for the ATLAS Higgs Working Group, ATL-COM-PHYS-2004-062.
- [6] R. Bonciani, S. Catani, L. Mangano, P. Nason, NLL Resummation of the Heavy-Quark Hadroproduction Cross-Section, Nucl. Phys., B 529 (1998) 424-450.
- [7] ATLAS Collaboration, ATLAS Inner Detector Vol 1., Technical Design Report, CERN/LHCC/97-16.
- [8] ATLAS Collaboration, ATLAS Inner Detector Vol 2., Technical Design Report, CERN/LHCC/97-17.
- [9] ATLAS Collaboration, ATLAS Liquid Argon Calorimeter Performance, Technical Design Report, CERN/LHCC/96-41.
- [10] ATLAS Collaboration, ATLAS Tile Calorimeter Performance, Technical Design Report, CERN/LHCC/96-42.
- [11] ATLAS Collaboration, ATLAS Muon Spectrometer, Technical Design Report, CERN/LHCC/97-22.
- [12] ATLAS Collaboration, ATLAS Magnet System, Technical Design Report, CERN/LHCC/97-18.
- [13] ATLAS Collaboration, ATLAS Detector and Physics Performance, Technical Design Report, CERN/LHCC/99-14.
- [14] Bureau International des Poids et Mesures, <http://www.bipm.fr/fr/si/>.

- [15] http://en.wikipedia.org/wiki/Planck_units.
- [16] B. Greene, *The Elegant Universe*, Vintage Books, USA 2000.
- [17] E. Lohrmann, *Hochenergiephysik*, Teubner Studienbücher Physik, Stuttgart.
- [18] F. Halzen, A. Martin, *Quarks and Leptons*, John Wiley & Sons, New York.
- [19] The Super-Kamiokande Collaboration, Y. Fukuda et al, Evidence for oscillation of atmospheric neutrinos, *Phys.Rev.Lett.* 81 (1998) 1562-1567.
- [20] C. Parker, Precision Tests of the Standard Model, talk at ICHEP 06, Moskau.
- [21] ALEPH Collaboration, DELPHI Collaboration, L3 Collaboration, OPAL Collaboration and The LEP Working Group for Higgs Boson Searches, Search for the Standard Model Higgs boson at LEP, *Phys. Lett. B* 565 (2003) 61-75.
- [22] W.-M. Yao et al., *J. Phys. G* 33, 1 (2006).
- [23] U. Egede, The search for a standard model Higgs at the LHC and electron identification using transition radiation in the ATLAS tracker, CERN-THESIS-98-001.
- [24] J.F. Gunion, H.E. Haber, G.L. Kane and S. Dawson, *The Higgs Hunters Guide*, Addison-Wesley, 1990.
- [25] T. Sjöstrand, P. Eden, C. Friberg, L. Lönnblad, G. Miu, S. Mrenna and E. Norrbin, PYTHIA 6.2 Manual, *Computer Physics Commun.* 135 (2001) 238.
- [26] B. Andersson and M. Ringner, Bose-Einstein correlations in the Lund model, *Nuclear Physics B*513, 627-644 (1998).
- [27] F. Canelli for the CDF and D0 Collaborations, Top Quark Mass Measurements, talk at ICHEP 06, Moskau.
- [28] M. Spira, A. Djouadi, D. Graudenz and P.M. Zerwas, Higgs boson production at the LHC, *Nucl. Phys. B*453:17-82, 1995.
- [29] Z. Kunszt, Associated production of heavy Higgs boson with top quarks, *Nucl. Phys. B*247:339, 1984.
- [30] D.A. Dicus and S. Willebrock, Higgs boson production from heavy quark fusion, *Phys. Rev. D*39:751-757, 1989.
- [31] ATLAS Collaboration, ATLAS Detector and Physics Performance, Technical Design Report, CERN/LHCC/99-15.
- [32] J. Cammin, Study of a Light Standard Model Higgs Boson in the ttH Channel with ATLAS at LHC and Decay-Mode Independent Searches for Neutral Higgs Bosons with OPAL at LEP, PhD Thesis, March 2004.
- [33] S. Asai et al, Prospects for the Search for a Standard Model Higgs Boson in ATLAS using Vector Boson Fusion, *Eur. Phys. J., C* 32 (2004) s19-s54.

- [34] H.P. Nilles, Supersymmetry, supergravity and particle physics, Phys. Rep. 110 (1984) 1-162.
- [35] ZEUS Collaboration, C. Horn et al., Searches for R-parity violating Supersymmetry at ZEUS.
- [36] ALEPH Collaboration, V. Büscher, P. Morawitz, P. Williams, Searches for R-parity violating Supersymmetry at LEP 2, CERN-OPEN-99-331.
- [37] G.F. Giudice and R. Rattazzi, Theories with Gauge-Mediated Supersymmetry Breaking, Phys.Rept. 322 (1999) 419-499.
- [38] A.H. Chamseddine, R. Arnowitt and P. Nath, Locally Supersymmetric Grand Unification, Phys. Rev. Lett. 49, 970974 (1982).
- [39] <http://cern.ch/atlantis>.
- [40] J. Couchman, F. Crijns, J. Drohan, E. Jansen, P. Klok, N. Konstantinidis, Z. Maxa, D. Petrusca, G. Taylor, C. Timmermans, The ATLANTIS Visualisation Program for the ATLAS Experiment, CHEP 2004
- [41] ATLAS Collaboration, ATLAS High Level Trigger, Data Acquisition and Controls, Technical Design Report, ATLAS TDR-016.
- [42] An Object Oriented Data Analysis Framework, <http://root.cern.ch/>.
- [43] A. Wildauer et al, The e/γ Analysis Framework, ATL-COM-DAQ-2004-010.
- [44] A. Ventura, Muon Event Filter, talk in ATLAS Trigger and Physics Week, March 21, 2006.
- [45] I. Gavrilenko, Description of Global Pattern Recognition Program (XKalman), ATL-INDET-97-165, Geneva, CERN, 25 Apr 1997.
- [46] R. Clift, A. Poppleton, IPATREC: inner detector pattern-recognition and track-fitting, ATL-SOFT-94-009, Geneva, CERN, 14 Jun 1994.
- [47] N.C. Benekos, R. Clift, M. Elsing, A. Poppleton, ATLAS Inner Detector Performance, ATL-INDET-2004-002, Geneva, CERN, 04 Dec 2003.
- [48] F. Akesson, T. Atkinson, M.J. Costa, M. Elsing, S. Fleischmann, A. Gaponenko, W. Liebig, E. Moyse, A. Salzburger, M. Siebel, ATLAS Tracking Event Data Model, ATL-COM-SOFT-2006-005.
- [49] S. Correard, V. Kostyukhin, J. Lévêque, A. Rozanov, J.B. De Vivie de Régie, b-tagging with DC1 data, ATL-PHYS-2004-006, Marseille, 26 Nov 2003.
- [50] P. Billoir, R. Frühwirth and M. Regler, Nucl. Instr. and Meth. A241 (1985) 115.
- [51] P. Billoir and S. Qian, Nucl. Instr. and Meth. A311 (1992) 139-150.
- [52] V. Kostioukhine, Secondary Vertex Based b-Tagging, ATL-PHYS-2003-033.
- [53] U. Baur, R.K. Ellis and D. Zeppenfeld, QCD and Weak Boson Physics in Run II, Fermilab-Pub-00/297.

- [54] J.E. Huth et al., Proceedings of Research Directions For The Decade: Snowmass 1990, July 1990, edited by E.L. Berger (World Scientific, Singapore, 1992) p. 134.
- [55] S. Catani, Yu.L. Dokshitzer, M.H. Seymour, B.R. Weber, Longitudinally-Invariant k_{\perp} -Clustering Algorithms for Hadron-Hadron Collisions, CERN-TH.6775/93, Geneva, 1993.
- [56] J.M. Butterworth, J.P. Couchman, B.E. Cox, B.M. Waugh, KtJet: A C++ Implementation of the K_{\perp} Clustering Algorithm, MAN/HEP/2002/02, October 2002.
- [57] W. Braunschweig et al., Desy Internal Report (1989), DESY 89-022.
- [58] J. Abdallah et al., DELPHI Collaboration, b-tagging in DELPHI at LEP, Eur. Phys. J., C 32 (2004) 185-208.
- [59] D. Froidevaux, E. Richter-Was, Is the channel $H \rightarrow b\bar{b}$ observable at the LHC?, Z. Phys. C67 (1995) 213.
- [60] ATLAS Collaboration, E. Richter-Was, M. Sapiński, Search for the SM and MSSM Higgs boson in the $t\bar{t}H$, $H \rightarrow b\bar{b}$ channel, Acta Phys. Polon. B30 (1999) 1001-1040, ATL-PHYS-98-132.
- [61] The AcerMC Manual, <http://borut.web.cern.ch/borut/>.
- [62] S. Frixione and B.R. Webber, Matching NLO QCD computations and parton shower simulations, JHEP 0206 (2002) 029.
- [63] S. Frixione, P. Nason and B.R. Webber, Matching NLO QCD and parton showers in heavy flavour production, JHEP 0308 (2003) 007.
- [64] G. Corcella, I.G. Knowles, G. Marchesini, S. Moretti, K. Odagiri, P. Richardson, M.H. Seymour and B.R. Webber, HERWIG 6.5, JHEP 0101 (2001) 010.
- [65] J.M. Butterworth, Jeffrey R. Forshaw, M.H. Seymour, Multiparton interactions in photoproduction at HERA, Z.Phys.C72:637-646, 1996.
- [66] CMS Collaboration, Search for $H \rightarrow b\bar{b}$ in association with a $t\bar{t}$ pair at CMS, CMS NOTE 2006/119.
- [67] https://twiki.cern.ch/twiki/bin/view/Atlas/ElectronGamma_IsEM
- [68] E. Richter-Was and P. Bruckman, How well can we reconstruct continuum background \rightarrow b-jet calibration for the ATLFast fortran framework, ATL-PHYS-2002-025, 10 June 2002.
- [69] S. Dawson, L.H. Orr, L. Reina, D. Wackerth, NLO QCD predictions for associated $t\bar{t}H$ production in hadronic oscillations, Nucl. Phys. B 116 (2003) 207-211.
- [70] A. Rozanov, Alignment and b-tagging, Presentation at the ATLAS Software Workshop, September 2003, CERN, Geneva.
- [71] The Unified Modeling Language, <http://www.uml.org>.
- [72] <https://uimon.cern.ch/twiki/bin/view/Atlas/WorkBookAthenaFramework>.
- [73] The Python Programming Language, <http://www.python.org>.

Curriculum Vitae

Name: *Andreas Wildauer*
Date and place of birth: *January 17th 1976, Innsbruck, Austria*
Nationality: *Austrian*
Marital status: *single*

Education

September 2006 Ph.D. (Doctor Rerum Naturalium)
Innsbruck University
based at CERN in the “Austrian Doctoral Student Programme”
Supervisor: Prof. Dr. Dietmar Kuhn, Dr. Markus Elsing (CERN)
Thesis on “Primary Vertex Finding, b-Tagging and Analysis of the
Channel $t\bar{t}H$, $H \rightarrow b\bar{b}$ in the ATLAS Experiment”

January 2003 Master of Science (Magister Rerum Naturalium)
Innsbruck University
Supervisor: Prof. Dr. Gerald Rudolph
Diploma Thesis on “Bose-Einstein Correlations in Multi-Hadronic Z
Decays”

1996 - 2003 Study of physics at Innsbruck University.

1986 - 1995 Bundes(real)gymnasium Innsbruck Sillgasse, Matura Juni 1995.

1992 - 1993 Exchange student at Castro Valley High School, California, USA.

1982 - 1986 Primary school in Innsbruck-Arzl.

Personal Data

Private Address	Les Marronniers Rue de la Ramaz 01630 Sergy France	Office Address	CERN, Office 40-3D-06 1211 Geneva 23 Switzerland email: andreas.wildauer@cern.ch
-----------------	---	----------------	---